Autonomous Optical Inspection of Large Scale Freeform Surfaces

Lyngby, Rasmus Ahrenkiel

Publication date:
2019

Document Version
Publisher's PDF, also known as Version of record

Autonomous Optical Inspection of Large Scale Freeform Surfaces

Rasmus Ahrenkiel Lyngby

Kongens Lyngby 2018
PhD-2018-486

Technical University of Denmark
Department of Applied Mathematics and Computer Science
Richard Petersens Plads, building 324,
2800 Kongens Lyngby, Denmark
Phone +45 4525 3031
compute@compute.dtu.dk
www.compute.dtu.dk

PhD-2018-486
ISSN: 0909-3192

Summary in English

It is estimated that 80% of wind turbine blade failures can be back-tracked to defects which were introduced during production. Blades that are nonconforming to the intended design of their outer geometry are likely to underperform concerning aerodynamic lift, and can, therefore, cause their turbines to have a lower than nominal power output. Furthermore, small, usually discrete, surface aberrations can lead to turbulence in the boundary flow around the blade. This turbulence reduces the lift even more and can lead to surface erosion, which potentially can cause blade failure within a few years after installment. Consequently, geometric quality inspection in the production is vital to the performance and expected lifetime of a blade, and thus also to the business cases of the blade manufactures, owners, and operators.

This thesis studies how the geometric inspection of blades can be automated, through the development and construction of a novel autonomous robotic scanner system. The studied scanner modality is optically based and relies on a structured light camera-projector system, which samples point clouds from the blade's surface. Experiments demonstrate the system's capabilities in measuring the outermost 20 meters of 55 meter long blades. The Modular Freeform Gauge approach is used to study the scanner system's metrological performance. Additionally, the thesis considers the interaction between light and materials, with the purpose of selecting the optimal parameters, such as the coding strategy, for the structured light scanner.

Summary in Danish

Det er blevet vurderet, at 80% af de fejl som forårsager svigt i vindmøllevinger blev introduceret under vingernes fremstilling. Vinger, som ikke overholder det hensigtsmæssige design af deres ydre geometri, er i risiko for at have et underydende aerodynamisk løft, og kan derfor forårsage, at deres respektive turbiner præsterer dårligere end forventet. Endvidere kan små, ofte diskrete, overflade afvigelser føre til turbulens i grænselaget omkring vingen. Dette begrænser løftet yderligere, og kan føre til overfladerosion, som potentielt kan forårsage vingens svigt allerede få år efter dens installation. Derfor er geometrisk kvalitetsinspektion i produktionen vital for vingens ydeevne og forventede levetid, og altså også for vingeproducenternes, -ejernes og -operatørenes forretningsmodel.

I denne afhandling studeres det hvordan den geometriske inspektion af vinger kan automatiseres igennem udvikling og konstruktion af et nyt autonomt robotskannersystem. Den undersøgte skanner er optisk, og bygger på et kameraprojektorsystem med struktureret lys. Den måler vingeoverfladen i form af tætte punktskyer. Systemet er demonstreret på de yderste 20 meter af tippen på en 55 meter lang vinge. Skanneres metrologiske ydeevne er undersøgt ved brug af "modular freeform gauge" tilgangen. Derudover studerer afhandlingen interaktionen imellem lys og materialer, med det formål at vælge de optimale parametre, såsom kodningsstrategi, for den strukturerede lysskanner.

Preface

This thesis was prepared at the Section for Image Analysis and Computer Graphics, under the Department of Applied Mathematics and Computer Science, at the Technical University of Denmark (DTU). It was done to fulfill the requirements for obtaining a doctor of philosophy degree (Ph.D.) in applied mathematics with an emphasis on computer vision.

The scientific project was done as an Industrial Ph.D., with Siemens Gamesa Renewable Energy (SGRE) being the industry partner and DTU being the academic partner. Funding was provided partly by the Innovation Fund Denmark and partly by SGRE. The project was a part of the Manufacturing Academy of Denmark (MADE) framework, through which FORCE Technology was also a partner.

The experimental and developmental work were conducted at DTU's campus in Kgs. Lyngby, Denmark, at FORCE Technology's workshop in Brøndby, Denmark, and at SGRE's production site in Aalborg Øst, Denmark. For the majority of the project's duration, this involved weekly travels across Denmark.

The academic supervision was handled by Ph.D. Henrik Aanæs (former Associate Professor) for the first year, after which it was handed over to Professor Anders Bjorholm Dahl. Henrik Aanæs continued as co-supervisor. The industrial supervision was handled by Ms. Ewa Nielsen, with Mr. Søren Rahmberg as co-supervisor.

The work and contributions contained in this thesis seek to develop an automated inspection system for finding geometric defects on wind turbine blades. As indicated by the thesis' title, the lessons learned and the results are poten-

tially relevant for other applications, which also concern large-scale metrology on freeform surfaces.

Reading Guide

The thesis is intended to be read from Chapter 1, which defines the project's scope and provide insight into blade manufacturing and the consequences of geometric defects. Chapter 2 forms a solid background, which is useful when analyzing optical based 3D scanners, by presenting a theoretical overview of cameras, lenses, material properties, and light propagation. This background is put to use in Chapter 3, which presents the developed optical blade scanner system, along with a demonstration of its capabilities. Chapter 4 studies the metrological measuring uncertainty of the system. The thesis' novel contributions are highlighted and referenced as needed. The list of publications is found on page xi and their full text is located in the back starting from page 81, after the list of references. Citations follow the American Psychological Associations (APA) format given as (Author surname(s), year), for example (Lyngby, 2018). Page 73 lists the citation references.

Helsingør, 3-August-2018

Rasmus Ahrenkiel Lyngby

Acknowledgments

A project of the kind that leads to this thesis is seldom a one-person endeavor. First and foremost, I would like to praise my supervisors, Anders Bjorholm Dahl, Henrik Aanæs, Ewa Nielsen and Søren Rahmberg. Their always insightful suggestions, comments, and guidance helped me overcome even the most impenetrable obstacles, and was paramount to the project. Their willingness and positivity was a constant source of inspiration, both on an academic and personal level. Thanks for taking the time to proof-read my half-finished manuscripts. I would especially like to thank Ewa for keeping the project on track with her pragmatic approach to project managing, for her restless drive and aid in making sure that I had the tools that I needed, and for weeding away unimportant stuff, stay focused and cut red tape.

Thanks to the Innovation Fund Denmark and Siemens Gamesa Renewable Energy (SGRE) for funding the project. Thanks to Heine Bach, Mads Kelter-Wesenberg, and Lasse Eisgruber for hosting me in their respective departments at SGRE, for the interest that they took in the project, and for continuous allocation of the funds needed to have me around. Special thanks to Heine Bach and Rasmus Larsen for instantiating the project. Thanks to the Manufacturing Academy of Denmark (MADE) for providing a framework for the project. Thanks to Dorthe Wiederholt Andersen, Manja Gildhoff Jensen, and Fie Victoria Fogh Rasmussen for taking care of the bulk of the administrative paperwork generated by the various project stakeholders. Thanks to Lonnie Kragelund Pedersen and Camilla Stokbro Petri for their help during the hardware procurement process within SGRE.

Thanks to my co-authors: Alessandro Dal Corso, Anders Bjorholm Dahl, Carsten

Gundlach, David Bue Pedersen, Eythor Runar Eiriksson, Ewa Nielsen, Heine Bach, Henrik Aanæs, Jakob Andreas Bærentzen, Jakob Wilm, Jannik Boll Matthiassen, Janus Nørtoft Jensen, Jeppe Revall Frisvad, Jonathan Dyssel Stets, Knut Conradsen, Leonardo De Chiffre, Mads Brix Doest, and Sebastian Hoppe Nesgaard Jensen. Especially thanks to Jannik for our close collaboration on the gonioreflectometer development, to Jonathan, Eythor, and Jakob Wilm for insightful discussions related to 3D scanning, and to Leonardo both for teaching me geometrical metrology and for his deep involvement in estimating the measurement uncertainty of the developed blade scanner.

Throughout the mechanical design, construction and assembly of the blade scanner, the contributions by FORCE Technology were significant. Though I was involved in all aspects of the design process, the design and construction of the machine would never have been possible without Christian Brandt Lauritzen, Peder Bent Hansen, and Thomas Aaboe Jensen from FORCE. Especially thanks to Christian for his deep involvement in the project. Thanks for taking ownership of problems, help to solve them, and participate in cozy late night development and construction sessions. He vastly exceeded expectations and went the extra mile for the project. The ideas, skills, and experiences put forward by the technicians at FORCE greatly enhanced the machine's design and were instrumental to its build quality, why I would also like to thank them.

Thanks to Klaus Liltorp for his help with obtaining the CMM measurements needed for estimating the blade scanner's measuring uncertainty.

Thanks to the blue-collar colleagues in the production at SGRE for always aiding the project, and for showing a positive attitude towards the project, even when my 600 kg scanner system blocked their way, so they had to walk a detour. Thanks to Rasmus Ladevig for hosting me, providing space for working, and allocating assistance for cranes etc. during the development, implementation and test phases of the blade scanner's control algorithm. Thanks to Ib Aage Olesen, and his colleagues, for their help during the algorithm development. Thanks to Lene Lang Sørensen, Søren Grønhøj Hval, Peter Bach, and their colleagues for moving the blade scanner around the factory site, and for pulling blades in and out of storage. Thanks to Frede Frederiksen from Skagen Sandblæseri & Skibsservice, and his team, for giving me space to measure and provide help during the acquisition of the blade dataset, and for his good and contagious mood.

Thanks to Martin Hertz Sørensen, Lars Vestergaard Poulsen, Jesper Roemer Smith Christophersen, Anders Skjoeth Binderup, Christian Norre Andersen, and Ove Andersen for their help, explanations, and insightful discussions about wind turbine blade manufacturing, blade quality, blade inspection, and associated topics. Also thanks for contributing to an exciting, relaxed and fun working environment. Also thanks to the rest of my colleagues at SGRE.

Thanks to George Vogiatzis and his group at Aston University for hosting me during my external stay.

Thanks to my colleagues at the Image Analysis and Computer Graphics Section for interesting daily academic discussions, their friendliness, and all the fun that they brought. They were never too busy to lend an ear and provided insightful comments and suggestions on numerous occasions.

I have been fortunate to meet several persons who wanted me the best, and who ultimately provided me with the confidence and inspiration to pursue a Doctor of Philosophy. While it would be too extensive to mention all of them here, I would like to highlight a select few. Thanks to Gertrud Borberg Stenius, Bent Pagh, Zheng-Hua Tan, Zhanyu Ma, and Thomas Moeslund.

Last, but not least, I would like to thank my family for their unlimited support: my parents for all their love and affection, and continuous encouragements. To my wife Louise, and our daughters Alba and Flora, for being a source of strength, bringing meaning to my life, and bearing with me on all those days where I did not come home and on all the evenings where I was absent during the past three years. I love you.

With the number of people involved in the project, there are most likely some persons that I have forgotten to acknowledge, and for that, I am deeply sorry.

List of Contributions

The contributions, which are included in this Thesis, are listed below. They are listed according to their appearance in the thesis. There are 10 in total, of which five are peer-reviewed publications, one is under review, one is a pending patent application, and three are technical reports. Further down, after the included contributions, two contributions are listed, which are not included in the thesis, but which were also made during the PhD project.

Contributions Included in the Thesis

A. **Lyngby, R. A.**, Wilm, J., Eiríksson, E. R., Nielsen, J. B., Jensen, J. N., Aanæs, H., & Pedersen, D. B. (2017). In-line 3d print failure detection using computer vision. In Special interest group meeting: Additive manufacturing, Euspen. (Lyngby et al., 2017)

B. Stets, J. D., Dal Corso, A., Nielsen, J. B., **Lyngby, R. A.**, Jensen, S. H. N., Wilm, J., . . . Aanæs, H. (2017). Scene reassembly after multimodal digitization and pipeline evaluation using photorealistic rendering. Applied optics, 56 (27), 7679–7690. (Stets et al., 2017)

C. Nielsen, J. B., Eiríksson, E. R., **Lyngby, R. A.**, Wilm, J., Frisvad, J. R., Conradsen, K., & Aanæs, H. (2015). Quality assurance based on descriptive and parsimonious appearance models. In Material appearance modeling. (J. B. Nielsen, Eiríksson, Lyngby, Wilm, Frisvad, et al., 2015)

D. **Lyngby, R. A.**, Matthiassen, J. B., Frisvad, J. R., Dahl, A. B., & Aanæs, H. (2018). Using an industrial robot arm for measuring BRDFs. Techni-

cal University of Denmark. Technical Report. Kgs. Lyngby, Denmark. (Lyngby, Matthiassen, Frisvad, Dahl, & Aanæs, 2018)

E. Nielsen, J. B., Stets, J. D., **Lyngby, R. A.**, Aanæs, H., Dahl, A. B., & Frisvad, J. R. (2017). A variational study on BRDF reconstruction in a structured light scanner. In International conference on computer vision workshop (ICCVW 2017) (pp. 143–152). IEEE. (J. B. Nielsen, Stets, et al., 2017)

F. **Lyngby, R. A.**, & Dahl, A. B. (2018a). Make geometry inspection of wind turbine blades great again with robots. Technical University of Denmark. Technical Report. Kgs. Lyngby, Denmark. (Lyngby & Dahl, 2018a)

G. **Lyngby, R. A.**, Nielsen, E., & Bach, H. (2018). Visual inspection arrangement. Patent application. Application number 18171466.8 - 1022. European Patent Office. (Lyngby, Nielsen, & Bach, 2018)

H. **Lyngby, R. A.**, & Dahl, A. B. (2018b). Snags on surfaces: Detecting geometrical defects on wind turbine blades. Technical University of Denmark. Technical Report. Kgs. Lyngby, Denmark. (Lyngby & Dahl, 2018b)

I. **Lyngby, R. A.**, Aanæs, H., Nielsen, E., & Dahl, A. B. (2018). Autonomous surface inspection of wind turbine blades for quality assurance in production. In 9th european workshop on structural health monitoring (EWSHM). BIND. (Lyngby, Aanæs, Nielsen, & Dahl, 2018)

J. **Lyngby, R. A.**, Nielsen, E., De Chiffre, L., Aanæs, H., & Dahl, A. B. (2018). Development and metrological validation of a new automated scanner system for freeform measurements on wind turbine blades in the production. Precision Engineering. In Press. (Lyngby, Nielsen, De Chiffre, Aanæs, & Dahl, 2018)

Other Contributions

K. Jensen, J. N., **Lyngby, R. A.**, Aanæs, H., Eiríksson, E. R., Nielsen, J. B., Wilm, J., & Pedersen, D. B. (2017). Photogrammetry for repositioning in additive manufacturing. In Special interest group meeting: Additive manufacturing, Euspen. (J. N. Jensen et al., 2017)

L. Nielsen, J. B., Eiríksson, E. R., **Lyngby, R. A.**, Wilm, J., Jensen, J. N., Aanæs, H., & Pedersen, D. B. (2017). Picprint: Embedding pictures in additive manufacturing. In Special interest group meeting: Additive manufacturing, Euspen. (J. B. Nielsen, Eiríksson, Lyngby, Wilm, Jensen, et al., 2017)

Acronyms

ADC	Analog to Digital Converter
BRDF	Bidirectional Reflectance Distribution Function
BSSRDF	Bidirectional Scattering-Surface Reflectance Distribution Function
BTCP	Binary Temporal Coded Pattern
CAD	Computer-Aided Design
CAN	Controller Area Network
CCD	Charge Coupled Device
CMM	Coordinate Measuring Machine
CMOS	Complementary Metal-Oxide Semiconductors
CNC	Computer Numerical Control
DTU	Technical University of Denmark
FDM	Fused Deposition Modeling
GUM	Guide to the Expression of Uncertainty in Measurements
HAWT	Horizontal-Axis Wind Turbine
iGPS	Indoor Global Positioning System
IMU	Inertial Measurement Unit
IR	Infrared
ISO	International Organization for Standardization
LAN	Local Area Network
LEP	Leading Edge Protection
MADE	Manufacturing Academy of Denmark
MFG	Modular Freeform Gauge
MLI	Multiple Laser Line
NA	Not Available
Ph.D.	Doctor of Philosophy
PTCP	Phase Temporal Coding Pattern
SBP	Single Binary Pattern
SGRE	Siemens Gamesa Renewable Energy
SI	International System of Units
SL	Structured Light
SLI	Single Laser Line
SVBRDF	Spatially Varying Bidirectional Reflectance Distribution Function
VDE	Verband der Elektrotechnik Elektronik Informationstechnik
VDI	Verein Deutscher Ingennieure
WTB	Wind Turbine Blade

Contents

Chapter 1

Introduction

The production of electricity is undergoing a drastic changeover from fossil fuels to renewable energy. The year 2017 was thus the most productive for wind turbines ever recorded. In Denmark, wind turbines provided 45.8% of the total consumed electricity and 4.4% worldwide (BP, 2018; O. K. Jensen, 2018). With many new turbines being put into service, wind power is projected to be an even greater contributor to the global power generation in the future.

1.1 Scope

In addition to developing new and bigger turbines, manufacturers continuously optimize the supply chain to bring down production costs, while increasing quality, in an effort to maximize the revenue and power output per turbine. The wind turbines blades are instrumental to this effort. A significant portion of the coming turbines is going to be huge and placed on the ocean, where wind, precipitation and servicing difficulties increase the demands on quality and durability. Designers carefully design wind turbine blades through an extensive engineering process which builds upon decades of experience. Any deviation away from the intended geometry can lead to a drop in the performance of the turbine and its life expectancy (Dalili, Edrisy, & Carriveau, 2009). In a talk given at the European Workshop on Structural Health Monitoring (EWSHM) on July

11, 2018, Dr. H. Friedmann, Woelfel Engineering GmbH, assessed that 80% of blade failures could be traced back to defects which were introduced during production.

With relatively small per-turbine profit margins (Bolinger & Wiser, 2012), complaints and warranty costs can easily make the difference between gaining or losing money for turbine manufactures. Siemens Gamesa Renewable Energy (SGRE) and the Technical University of Denmark (DTU) launched this Ph.D. project as an effort to develop the methodology needed to create a detailed and accurate digital model of the surface of wind turbine blades, which can be used for assuring its geometrical quality. Furthermore, such a model can act as an enabler for Industry 4.0 production and design methods, as described by Hermann, Pentek, and Otto (2016).

1.2 Wind Turbine Blade Basics

We begin with a brief introduction to wind turbines to set the Ph.D. project into context. For an in-depth description, the interested reader is directed to the Wind Energy Handbook (Burton, Jenkins, Sharpe, & Bossanyi, 2011).

In the *Oxford English Dictionary*, the term "wind turbine" is defined under "Wind" as follows:

> **wind** **turbine** *noun*, a turbine driven by wind; an apparatus designed to generate electricity when a large vaned wheel is rotated by the wind.

Many different kinds of wind turbines exist, but this thesis is concerned with the three-bladed Horizontal-Axis Wind Turbine (HAWT), which is the most common type (Schubel & Crossley, 2012). All further uses of the term "wind turbine" is synonymous with HAWT.

A wind turbine consists of four distinct component types. The foundation anchors the turbine to the ground for onshore turbines and to the seabed for offshore turbines. The tower is fastened to the foundation and lifts the turbine up into the wind and provides clearance for the blades to turn. On top of the tower sits the nacelle which holds all the power generating components and most of the mechanics and electronics needed to operate the turbine. In front of the nacelle sits the rotor, which is composed of a central hub with three blades attached. A shaft from the rotor drives the generator, either directly or through a

gearbox. Figure 1.1 shows an offshore wind turbine with the main components indicated.

Figure 1.1: Photo from an offshore wind farm showing seven Siemens Gamesa SWT-6.0-154 HAWTs. Each of these turbines has a rotor diameter of 154 meters with 75 meter blades and a nominal power output of 6 MW. (A) shows the visible part of the foundation, (B) is the tower, (C) is the nacelle, and (D) is the blade. Picture provided by Siemens Gamesa Renewable Energy (http://www.siemensgamesa.com/en-int/products-and-services/offshore/wind-turbine-swt-6-0-154).

Figure 1.2 shows a blade with a cross-section highlighted, and the airfoil shape that corresponds to the highlighted cross-section. The airfoil shape lets the blade produce an aerodynamic force when wind flows around it. Bernoulli's principle can describe this relation. Because the blades are attached to the nacelle hub, a centripetal force acts on the blades orthogonal to the aerodynamic force, and the blades make a circular motion, which drives the generator. The amount of power generated by the generator is proportional to the amount of lift created by the blades. In an unobstructed wind field, the amount of lift versus drag generated by a blade depends on its size, the shape of its airfoil, its angle of attack, the smoothness of its surface, the wind velocity and the air density (Schubel & Crossley, 2012).

1.2.1 Manufacturing Principle

While different embodiments of design and manufacturing techniques exist (Veers et al., 2003), overall, two types of production methods are used to manufacture wind turbine blades. Either, the blade is molded in one piece or in several parts which are joined together through a second bonding process. Both methods rely on virtually the same vacuum infusion molding process with epoxy resin. The post-molding processes are also similar, except for the second bonding, which is why only the one-piece molding technique is described here. Specifically, this description is based on the IntegralBlade® method (Stiesdal, 2011) used by SGRE.

Blades are made of composite materials organized in a sandwich structure, which typically contains some combination of wood, foam, fiberglass and carbon fiber joined together by epoxy or polyester resin (Veers et al., 2003). This kind of material is difficult to model compared to conventional materials, such as steel or aluminum, but provides structural properties that could not have been achieved by one single material (Jureczko, Pawlak, & Mężyk, 2005).

The blades are mostly hand made. The craftsmen stacks mats of either carbon fiber or fiberglass into a mold. The mats can either be prepped with resin before layup or infused with resin after layup. Different types of mats with different fiber directions are used to provide the right load bearing and strength characteristics where needed. At certain positions, balsa wood or foam is interlaced with the fiber mats to act as a low weight filler. This process is referred to as

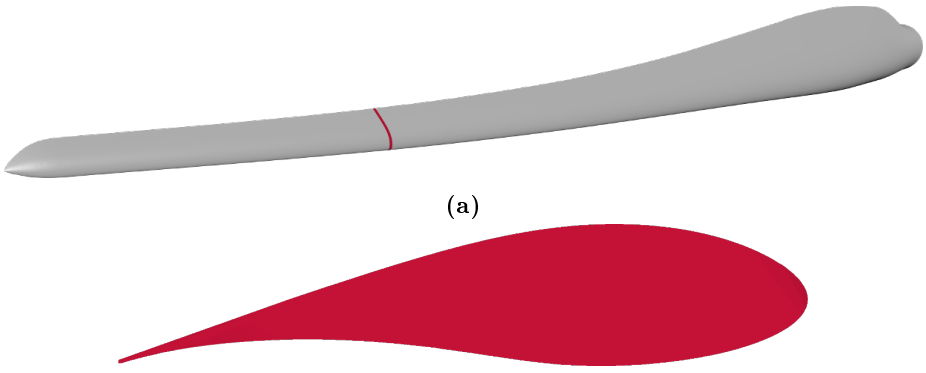

(a)

(b)

Figure 1.2: Cross-sectional view of a blade which illustrate its airfoil shape. (a) shows the blade with a cross-section highlighted in red and (b) shows the airfoil shape of the cross-section.

"packing" and is illustrated in Figure 1.3. After packing, the mold is sealed, and the air is pumped out to form a vacuum. The vacuum sucks in resin, which flows along specific resin channels in the mold and infuses the composite layers. The blade is then "baked" by heating the mold to around 80°C to increase the curing process. The resin's hardening process is itself exothermic. Therefore, the temperature of the mold is controlled to avoid overheating the materials.

The blade is removed from the mold after it has cooled. Excess materials from the infusion process, such as the now hardened resin channels, are removed, and a drill is used to make holes for rotor attachment. The surface is sanded, and a filler is added to give the blade a smooth undercoat, which provides the base for the primer. After priming, the blade is painted with a white base paint, and a protective coating is added to the leading edge, called leading edge protection (LEP), which prevents erosion and enhances air dispersion for increased laminar airflow around the profile. Finally, any extra gadgets, such as vortex generators, and individual customer required markings are added, and the blade is ready to be shipped.

1.2.2 Geometrical Blade Quality

The blade production process only rarely introduces defects, and it is generally a very stable process. However, if it introduces a defect, the consequences can be fatal for the turbine's production and its operational lifetime resulting in considerable costs for the turbine's manufacturer and operator. Geometrical quality inspection is vital to prevent turbine malfunction. Due to the generally small number of defects, the inspection process needs to have a high sensitivity, extensive coverage, and a low uncertainty, to catch the mistakes.

Before discussing the factors which influence the geometrical quality of blades and their related tolerances, we highlight the scope by stating a set of delimitations. There are many kinds of tolerances assigned to blades, but those that concern structural integrity, load bearing capability and assembly are not considered. Instead, our focus is solely on those tolerances which deal with the outer geometry, or surface topography, of the blade. Thus, we do not consider internal geometry. Though the micro-level structure of the blade surface, such as surface roughness, has implications for the laminar airflow and erosion, this thesis only concerns macro-level surface structure and geometry. Measuring micro-level structures, which are usually on a scale below 50 μm and often below 10 μm (De Chiffre, Hansen, Andreasen, Savio, & Carmignato, 2015), and macro-level structures require significantly different equipment. The general modality might be the same, such as light, but the level of magnification needed is vastly different, e.g. a camera with a standard lens versus a microscope.

(a) The lower part of the mold before material is added.

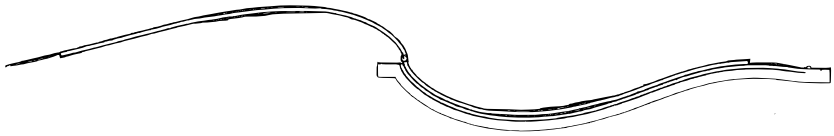

(b) Fiberglass is packed together with wood and foam into the lower mold with the top layers sticking out over the side.

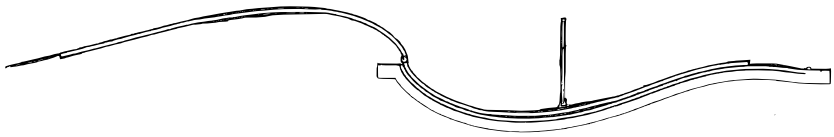

(c) A central beam of fiberglass-lined wood is placed inside the mold.

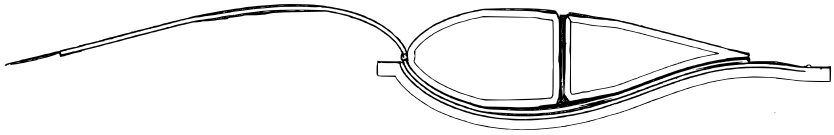

(d) Two mandrels are placed to fill the cavity on either side of the beam.

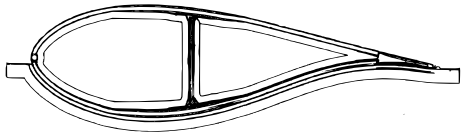

(e) The top layers are folded back onto the mandrels and tugged into the trailing edge.

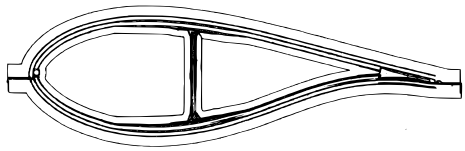

(f) The top mold is added and the assembly is sealed.

Figure 1.3: Illustration of the IntegralBlade® packing and molding technique as seen in profile. After packing, the blade is infused with epoxy resin. The mandrels are pulled out of the root end after demolding. Figure adapted from illustration made by (Stiesdal, 2011).

We now shift our attention towards an explanation of the geometrical quality within the Thesis' scope. The following two types of geometrical defects are considered: those with a large spatial extent and those with a small spatial extent, as viewed over the surface. Here, a large spatial extent is defined as being larger than a millimeter; thus super-millimeter. A small spatial extent is defined as being smaller than a millimeter, thus sub-millimeter. That is, an artifact which reaches over more than a millimeter across the surface is said to have a large spatial extent. Figure 1.4 illustrates this definition. Generally, defects with a large extent are smooth, such as hills and valleys, whereas defects with a small extent are discrete, such as cracks and steps. Large extent defects can, for example, be surface indentations originating from a too tightly closed mold lid, or an airfoil shape which is too thick due to a worn mold. Small extent defects can be steps from misaligned mold sections, pinholes from air bubbles in the paint or cracks from the resin curing process.

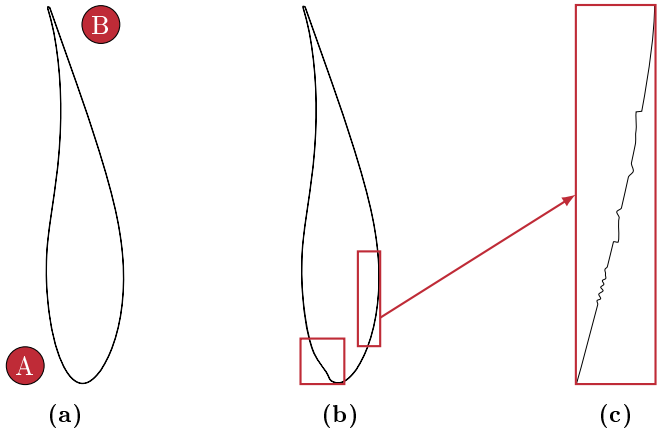

Figure 1.4: Illustration of geometrical errors on a blade airfoil. (a) illustrates an intended airfoil shape where (A) marks the leading edge and (B) marks the trailing edge. An example of a deformation with a large spatial extent near the leading edge is illustrated in (b). (c) illustrates a closeup view of the surface with deformations that have small spatial extent.

The airfoil shape of wind turbine blades is optimized to provide the correct balance between lift and drag within a certain range of wind speeds. Defects with a large spatial extent change the shape of the airfoil and can thus lead to lower power output, due to a reduced lift and increased drag. Defects with a small spatial extent can break the laminar airflow in the boundary layer prematurely. This breakage will increase drag and can lead to damaging surface erosion (Holmes, Obara, & Yip, 1984; Keegan, Nash, & Stack, 2013). In a

relatively short amount of years in operation, a surface pinhole, with an initial diameter of a few hundred microns, can erode into a hole which penetrates all the way through the laminate and into the blade's internal cavity. Such a damage hampers the structural integrity of the blade and is likely to result in blade failure if not repaired. The risk is most pronounced if the defect is located close to the leading edge and near the blade tip where the turning radius, and thus the wind speed, is most significant.

Traditionally in geometrical metrology, tolerances are assigned by segmenting a given component into simple features. These simple features allow one to specify straightness, flatness, roundness, etc. for each of the segments, and their mutual positions, as defined by ISO 1101:2017 (2017). The geometry of a blade is freeform in nature (Savio, De Chiffre, & Schmitt, 2007). It is difficult to decompose a freeform shape into simple geometric components and thus use traditional definitions of geometrical tolerances. Instead, the quality of the geometry is defined based on the 3D computer-aided design (CAD) model of the blade and a local smoothness measure.

At any given point, the surface is allowed to deviate only by a certain amount from the intended model. This requirement concerns defects with a large spatial extent. The tolerance is specified as a surface profile not related to a datum, as defined by ISO 1101. The tolerance zone defines the radius of a sphere centered on the nominal surface. The measured surface must be within this sphere. It usually varies across the blade surface.
The smoothness tolerance is specified as the ratio between the height or depth of a local surface extremum and the length of the gradient leading up or down to the respective peak or valley. It concerns defects with a small spatial extent. Note that this definition of smoothness considers a much larger scale than that of surface roughness as defined by ISO 4287:1997 (1997).

The precise definitions of the tolerances and their exact values vary across manufacturers and are considered trade secrets. Consequently, we can not state them here. However, it can be said that the tolerances are usually on the scale of a few millimeters for the geometrical deviations and a few hundred micrometers for the local smoothness ratio.

Most production processes influence the quality. Some primarily affect geometrical deviations, such as the packing and infusion, while others, such as surface treatment and painting, fundamentally impacts the local smoothness. Figure 1.5 presents an overview of the process chain, together with dependent processes and suggestions for where on the chain geometrical metrology could be applicable.

The mold is made from several sections, each formed as a negative cast of

a positive plug, which is fabricated through Computer Numerical Controlled (CNC) milling. A protective coating is applied to the inside of the mold to make it more durable. The mandrels, which are also part of the casting process, are sculpted to fit the cavity inside the blade and are pulled out of the root end after demolding. The alignment of the mold sections, the geometrical tolerances which govern the plugs and the mandrels, and the thickness of the protective coating all influence the blade's geometry. The geometrical inspection could be performed directly on the mold, but this inspection would not be able to detect any defect which is introduced after casting.

The layup of the materials, during packing, influences the blade's thickness, density, stiffness, *etc.*, which is why it impacts the fit of the mold lid and the resin flow during the infusion process. Tolerances on the flow of the resin, the sealing of the mold, and the pressure of the vacuum can lead to resin underfilling and trapped air, which leaves indentations in the blade surface. Over- or under-heating during the baking process can influence the resin's solidification process, which in turn can affect the geometry. The trimming of excess material might cause problems if too much or too little material is removed. In the rare event that defects have been introduced up until demolding and trimming, the blade undergoes a rectification process, which can also influence the final geometry. The geometrical inspection could be performed here, as the following procedures primarily concern local smoothness.

The blade undergoes various surface treatments, including sanding and plastering. These treatments remove and add material to the blade's surface, respectively, why they also impact the final geometry. The geometry can be inspected here, which would capture all shape-related defects. Finally, the painting process adds the final exposed surface. This layer mostly influences the surface's local smoothness.

Only by inspecting at the very end of the process chain, can the combined effects of all the various tolerances, added throughout the chain, be measured. This thesis is concerned with this final geometry inspection.

1.2.3 Current Trends in Geometrical Quality Inspection

To the extent of our knowledge, most companies rely on manual inspection by trained expert operators for assessing the geometrical quality. Trained quality controllers inspect the blade's shape with a set of profile templates, which are laser-cut from cross-sections of the blade CAD model. The templates are held against the leading edge, and their fitness is used as a measure of the geometrical quality. As illustrated in Figure 1.6, the local smoothness is investigated

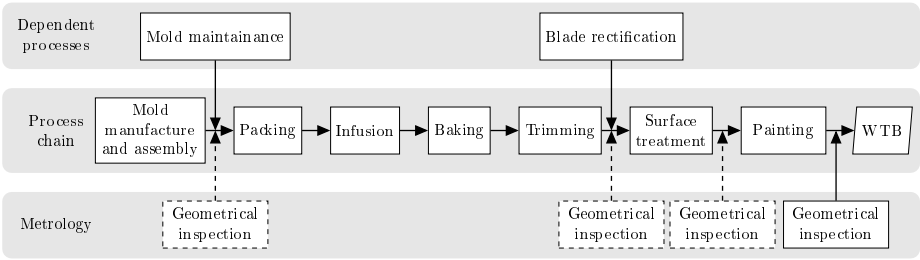

Figure 1.5: Overview of the production chain. The middle row lists all consecutive manufacturing processes required to make a wind turbine blade (WTB). The top row lists dependent processes, which are only executed when needed, *e.g.* the mold does not have to be maintained for every blade. The bottom row lists places, along the chain, where geometrical metrology could sensibly be applied. Here, the dashed boxes indicate suggestive inspection positions and the solid box indicates the position where this thesis actually applied inspection. The reason is explained in the text. Diagram inspired by De Chiffre (2012).

by looking for odd reflections of light from the surface. Light is shined perpendicular to the surface with a flashlight. Small bumps will reflect the light upwards, which is then notified by the operator. The operators can also see small holes, which will form a shadow. While manual inspection provides a decent sensitivity, it is slow, relatively expensive and somewhat cumbersome.

Recent contributions have sought to improve the inspection method by introducing automated inspection systems based on geometry measuring technologies. Fu, Fan, Huang, and Hu (2014) presented a low-cost system comprised of a liner drive stage with two laser-line scanners. They placed the blade over the drive stage and a 3D model acquired by moving the sled under the blade in its full length. The measurement uncertainty was not documented, but they demonstrated the system on a small 2-meter blade for household turbines. A system composed of a 3D structured light scanner, a laser-based tracker system, an industrial robot arm, and a linear drive stage was proposed by Petryna, Künzel, and Kannenberg (2014). This system can scan a small 12-meter blade, but again, the measurement uncertainty was not documented. Shmueli, Eder, and Tesauro (2015) developed a method for measuring fracture mode displacements in the trailing edge by stereo-photogrammetry. This study focused on a narrow application and did not provide a detailed blade surface model. The use of a coherent laser radar was proposed by Talbot, Wang, Brady, and Holden (2016). They demonstrated its use on a 1.65×0.5-meter workpiece, which simulated a cross-section of a real 44-meter blade. Thus, the study did not address the issue

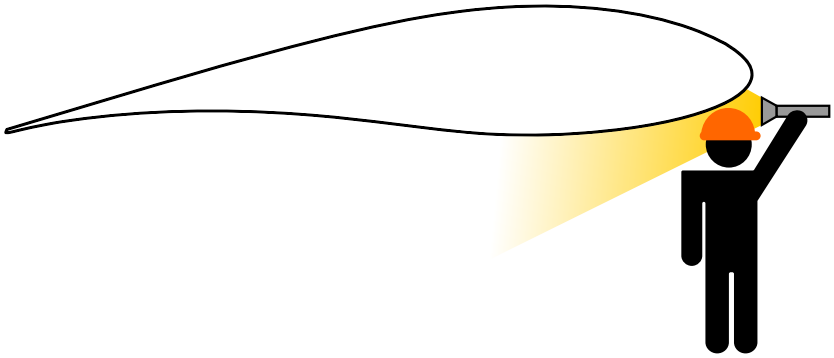

Figure 1.6: Illustration of manual quality inspection for detecting defects with a small spatial extent on a blade surface. An operator points a flashlight almost parallel to the surface. Small surface defects are likely to form a hill, which will reflect the light into the eyes of the operator, or a valley, which will form a shadow.

of moving the laser system as needed to cover a full blade, but merely stated that it should be possible. The measuring repeatability was investigated, but the paper did not document traceability and measurement uncertainty.
These recent contributions covered significant groundwork and provided a foundation which can be built upon. However, no prior studies which demonstrate a method for scanning a full blade have been published. Nor has a technique for establishing traceability for blade measurements been demonstrated. Inspired by the promising results shown by Petryna et al. (2014), we decided to base the inspection system, developed in this thesis, on a 3D scanner and laser tracker. This combination turned out to be a good choice as documented by the results presented in Chapter 3 and Chapter 4.

1.3 Thesis Outline

The thesis continues by describing how camera-based 3D scanners work in Chapter 2. It focuses on the conditions that affect measuring accuracy and precision, and the considerations that should be taken into account when selecting a 3D scanner for industrial use. Then, a detailed description of the proposed blade scanner system is provided in Chapter 3, including a description of its mechanical design, its control loop, and its safety features. The thesis then finishes by describing a method for establishing a traceable measuring uncertainty of such a scanner system in Chapter 4.

The contributions and publications made during the execution of the Ph.D. project are highlighted and explained where appropriate. All contributions are included as appendices.

Chapter 2

Measuring Geometry Through Light

This chapter describes how a stereo camera setup is used to measure geometry, and how such a setup is influenced by light and material properties. The contributions described in this chapter are concerned with utilizing knowledge about light propagation for different kinds of quality inspections, and with measuring how materials reflects and scatters light. Contribution A is a conference proceeding paper, which develops a simple computer vision system, with cross-polarized light source and camera, to conduct automatic online failure mode detection in additive manufacturing. Contribution B is a journal paper, which presents an extensive pipeline for quantitatively measuring the quality of a rendered scene, which contains materials with difficult radiometric models, such as glass. The pipeline uses a novel gonioreflectometer, made from an industrial robot arm, for measuring the radiometric models of the not-so-difficult scene materials. Contribution C is a conference proceeding paper, which presents ideas on how radiometric models could be used in various, more classical, types of quality inspection. The gonioreflectometer itself is documented in the technical report in Contribution D. This contribution describes how the gonioreflectometer can be used to accurately measure radiometric properties of flat material samples, and how the material's reflectance can be modeled. Contribution E is a conference proceeding paper, which presents a method for measuring radiometric properties with a stereo camera and projector setup, specifically a structured light

scanner, together with an investigation of how the system parameters influence the quality of reconstructed radiometric models.

A camera senses the world through light. Any measurement acquired through a camera is susceptible to the radiometric environment in which it was obtained. This includes light source and material properties, but also the camera itself. When targeting an industrial geometrical metrology application, it is important to have a good overview of the factors which influence measurement quality, and a thorough approach for estimating measurement uncertainty, which is traceable back to the definition of the meter unit. Chapter 4 deals with the subject of traceability, while this chapter covers the measuring principle and its sensitivity to radiometric properties. A solid theoretical background is important for choosing the best 3D scanner, with respect to performance and cost, for a given task, and for understanding the limitations of the technique. Because of that, we start with a general explanation of the camera and lens system, followed by an outline of the structured light scanning approach, and conclude with an overview of how a medium distorts light and how to model this behavior. This is by no means a full explanation of the concerned physical phenomenons. Our mission is, however, not to write a self-contained book on the subject, as it mostly serves as an introduction to the thesis' core topic of blade 3D scanning. The chapter merely conveys enough information to understand the presented arguments, and to choose a suited 3D scanner in Chapter 3.

The chapter is structured as follows: First, a general overview of geometrical measurement systems is presented. Then, the triangulation process is described in detail, including details on how a camera and a lens works. This is followed by a description of how pixel correspondences between two cameras are established in a structured light (SL) scanner. Finally, light, as a physical phenomenon, is explained, together with how it interacts with materials, and how this interactions influences an SL scanner.

2.1 Measuring Geometry in General

A large number of geometrical measurement techniques, based on many different measurement principles, exist. From the simple manually operated devices for measuring length, such as calipers, over to the advanced laser based interferometers, all of these systems have different advantages, limitations, and costs. Figure 2.1 illustrates a sample of the more commonly used geometrical measurement techniques (De Chiffre et al., 2015).

When talking 3D measurements in modern manufacturing, the coordinate mea-

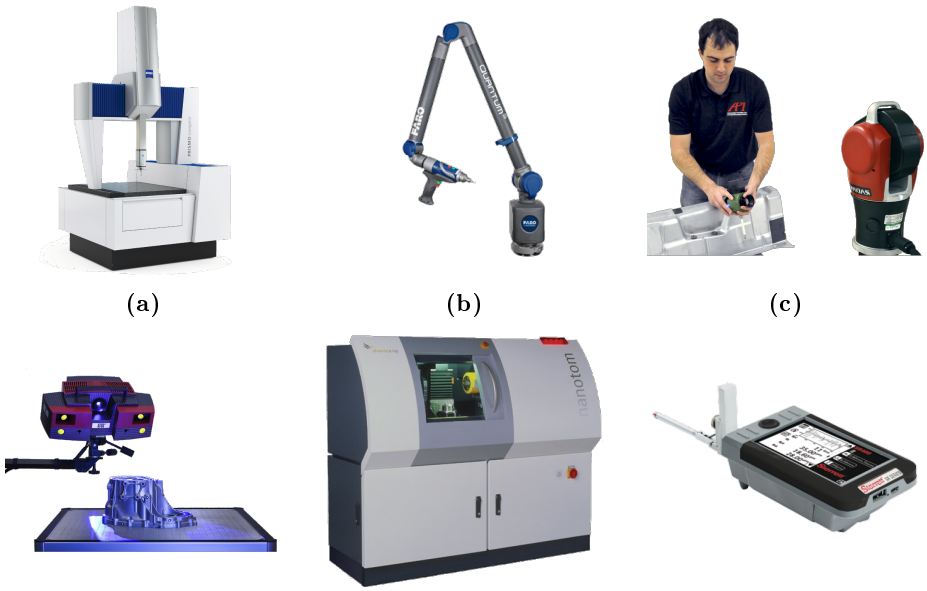

(a) (b) (c)

(d) (e) (f)

Figure 2.1: Examples of various types of commercially available measurement systems. (a) is a Zeiss touch probe CMM, (b) is a manually operated Faro CMM, (c) is an API laser tracked touch probe, (d) is a GOM structured light 3D scanner, (e) is a GE computed tomography scanner, and (f) is a Starret surface roughness tester. Images are from the respective manufactures webpages.

suring machine (CMM) is the primary tool. Figure 2.1a shows a conventional touch-probe Zeiss Prismo CMM. Figure 2.1b shows a FARO FaroArm, which is a manually operated CMM. A CMM consists of a measuring probe, which measures 3D points, either optically or through touch, and a locomotion system, which moves the measuring probe over the measured surface. CMMs always measure one point at a time. If an area is to be covered with measurements, the CMM can be used in scanning mode, where the measuring probe is passed over the surface continuously, while sampling points with a given frequency. CMMs can also be a hybrid between optical based techniques and touch probe techniques. As an example, a laser tracker can be used to measure the position of a touch probe, which is moved manually around in space by an operator, such as the API vProbe measuring probe and Radian Laster tracker shown in Figure 2.1c. CMMs are generally very accurate, but tend to be slow when measuring many points, and their reach is relatively limited.

Area measuring scanners are usually not touch based. Instead, a signal, such as x-ray, visible light or sound, is reflected off of the surface, or scattered through it, to sample measurements covering an area at a time. These techniques can quickly measure a relatively large surface area, but with a lower accuracy than CMMs. This thesis focuses on SL based 3D scanners, which samples 3D measurements through triangulation.

2.2 Triangulation

Using a stereo camera, 3D surface points can be measured through triangulation. The position of a 3D point, located on the surface of the measured object, is triangulated based on its observed angles, as seen by two cameras. In fact, all camera pixels potentially correspond to angles of surface points, which is why each pair of camera images can be used to cover an area with 3D measurements. To speed things up, the triangulation is often implemented as a constrained optimization problem based on epipolar geometry. However, for the sake of completeness, and as a way of presenting the general idea, we will take a step back and first outline the triangulation principle, before describing the specificities of a stereo camera setup.

2.2.1 The triangulation principle

Figure 2.2 shows a triangle $\triangle ABC$ with altitude h. Knowing the angles $\angle A$ and $\angle B$, and the length of the baseline $|AB|$, the position of vertex C, in the

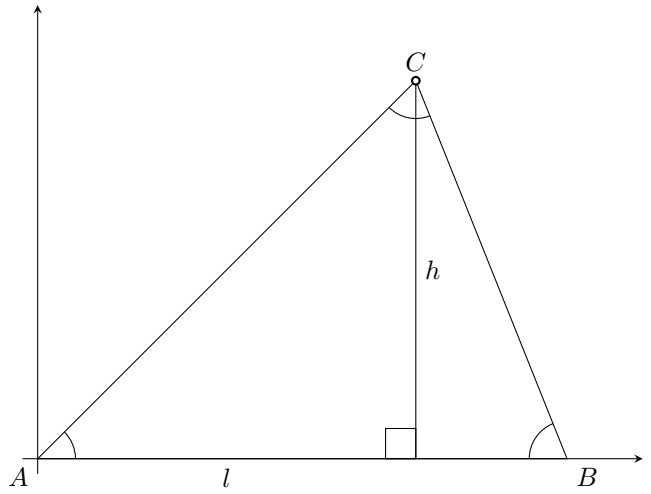

Figure 2.2: An illustration of the triangulation principle. The vertex A coincides with the origin of the coordinate system. The position of vertex C can be triangulated from the angles $\angle A$ and $\angle B$, and the length of the baseline $|AB|$.

coordinate frame with origin at A, is given as

$$\mathbf{c} = \begin{bmatrix} c_\mathrm{x} \\ c_\mathrm{y} \end{bmatrix} = \begin{bmatrix} l \\ h \end{bmatrix} \tag{2.1}$$

where l and h can be computed from the law of sines by

$$\begin{aligned} \angle C &= \pi - (\angle A + \angle B) \\ \frac{|AC|}{\sin(\angle B)} &= \frac{|AB|}{\sin(\angle C)} \Leftrightarrow |AC| = \frac{|AB|}{\sin(\angle C)} \sin(\angle B) \\ \frac{|BC|}{\sin(\angle A)} &= \frac{|AB|}{\sin(\angle C)} \Leftrightarrow |BC| = \frac{|AB|}{\sin(\angle C)} \sin(\angle A) \\ \cos(\angle A) &= \frac{l}{|AC|} \Leftrightarrow l = |AC| \cos(\angle A) \qquad (2.2) \\ \sin(\angle A) &= \frac{h}{|AC|} \Leftrightarrow h = |AC| \sin(\angle A) \qquad (2.3) \end{aligned}$$

If C is located in 3D space, the triangle $\triangle ABC$ is located on a 2D plane embedded into the 3D space, given that three non-coincident points located in a 3D space always spans a 2D plane. The z-axis coordinate of C's position, c_z,

can be computed from the angle of the slope of the plane, by forming another triangle on a new plane, which is perpendicular to the first one.

A brief account of the workings of a digital camera is presented, before explaining the details of how C's position is estimated using cameras. This is used as an introduction to a condensed derivation of the pinhole camera model, which is a key component of any stereo setup. Moreover, camera knowledge is important for understanding the following discussions about SL scanners, and their sensitivity to the radiometric properties of scanned materials.

2.2.2 The Camera

The following description is generally based on Gonzalez and Woods (2008) and Moeslund (2009). A modern digital camera is composed of two main components: a lens, which focuses light, and the image sensor, which converts the light signal into an electric signal. The image sensor is a rectangular integrated circuit, divided into a number of square cells, called pixels. The pixels integrate the energy received by incoming photons, over a given period of time, defined by the shutter speed, and stores it as electrical energy. Two types of sensors exist. It can either be based on charge coupled devices (CCD) or complementary metal-oxide-semiconductors (CMOS). In both sensor types, each pixel has a MOS capacitor, which accumulates an electric charge when exposed to light. In the CCD, after exposure, each row of capacitors act as a shift register where the charge of the capacitors are iteratively transferred to their neighbor capacitors, until they reach an analog to digital converter (ADC), sitting at the end of the row. Hence we have a charge-coupled device.
In a CMOS sensor, each pixel is equipped with its own ADC for individually reading the pixel values. More electronics are needed per pixel, which takes space on the circuit die. However, the manufacturing technique is significantly cheaper than that used for CCD's.

We believe that the slight performance difference between CCD and CMOS is insignificant for most applications. CCD's are generally perceived as having a better signal-to-noise ratio, at the expense of a higher power consumption and higher price. However, the gap seems to be narrowing (Hain, Kähler, & Tropea, 2007; Murari, Etienne-Cummings, Thakor, & Cauwenberghs, 2009), and CMOS sensors generally have higher frame rates, are smaller, uses less energy and are cheaper than CCD sensors. Thus, for the 3D scanning application

The lens focuses light onto the image sensor, such that all light rays reflected from a given world point, which is incident into the lens, hit the same point on the image sensor. A simplified camera lens is illustrated in Figure 2.3.

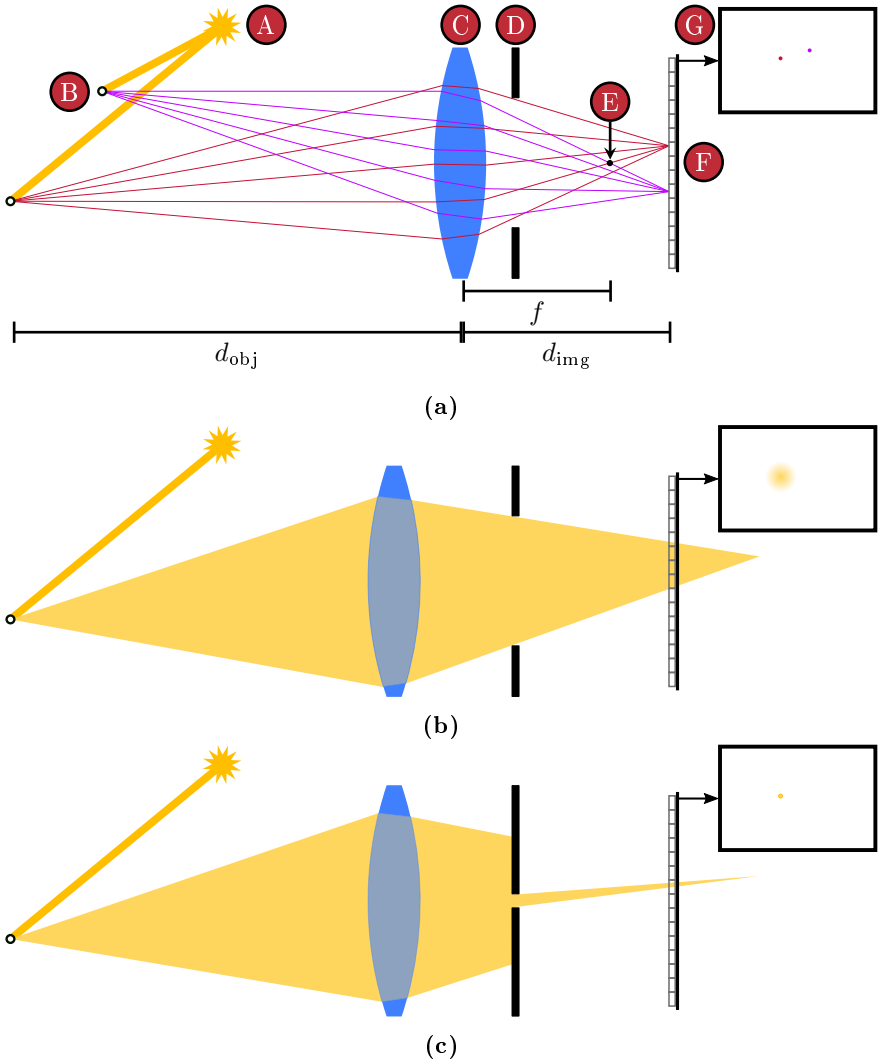

Figure 2.3: The working principle of a lens and aperture. (a) illustrates light rays being scattered at two points and focused onto an image sensor by the lens. Only a small number of scattered light rays are shown for simplicity. (A) is the light source, (B) is a scattering point, (C) is the lens, (D) is the aperture, (E) marks the focal point, (F) is the image sensor, and (G) is the image sampled by the sensor. The effect of moving the lens away from the sensor is shown in (b). The point spreading can be narrowed by closing the aperture, as seen in (c).

In Figure 2.3a, light is emitted from a source and scattered at two points. The precise nature of the scattering depends on the wavelength, polarization, parallelity and direction of the incident light rays, in combination with the radiometric material properties. This is covered in more detail further down in Section 2.4. Light is refracted when it enters the lens and again when it exits. Due to the convex shape of the lens, the different rays scattered from a single point encounter different surface normals when they hit the lens, causing them to be refracted in different directions through the lens. The result is a focusing of the rays. Thus, the lens re-gathers the incident rays, which were scattered, and focuses them onto a single point on the image sensor. The lens can be said to integrate incident light rays over a given solid angle, or section of a hemisphere. By doing so, it increases the radiance measured by a given pixel, as compared to if it had received only the direct straight ray.

Parallel light rays entering the lens perpendicularly to its plane intersect at a certain point, after being refracted. This point is called the focal point, and the distance from the center of the lens to this point is called the focal length, f. For a simple lens, this is a fixed property, which depends on the shape of the lens, and relates to its angle of view. As illustrated in Figure 2.3c, an object is in focus if the light rays converge within the area of one pixel. Assuming an approximation called the thin lens model (Hecht, 2016), the lens-to-sensor distance, d_{img}, at which an object located d_{obj} meters away from the lens is in focus, is related to the focal length by

$$\frac{1}{d_{\text{obj}}} + \frac{1}{d_{\text{img}}} = \frac{1}{f}\,. \tag{2.4}$$

For the stereo camera setup considered in this thesis, the focal length, f, and the distance between the lens and the image sensor, d_{img}, is in the range $[20, 50]$ mm. The distance between the lens and the object, d_{obj}, is in the range $[250, 1000]$ mm. Inserting a realistic combination of values into Equation 2.4, for example $d_{\text{obj}} = 350$ mm and $d_{\text{img}} = 35$ mm, yields $1/f = 1/350 + 1/35 \implies f = 31.8$ mm, which is relatively close to 35 mm. Thus, with values in the stated ranges, the image formation happens closely behind the focal length. For practical reasons, this knowledge is used to make the following simplification

$$\frac{1}{d_{\text{obj}}} + \frac{1}{d_{\text{img}}} \approx \frac{1}{d_{\text{img}}} \implies \frac{1}{d_{\text{img}}} = \frac{1}{f} \Leftrightarrow f = d_{\text{img}}\,, \tag{2.5}$$

which basically states that the distance from the lens to the image forming plane is identical to the focal length. Therefore, in the pinhole model, we speak only of the focal length, instead of the lens to sensor distance.

The aperture, whose effect is illustrated in Figure 2.3c, limits the number of directions which are integrated onto the image sensor. By doing so, the radiance

on the sensor is reduced, but the depth of focus, or depth of field, is increased. The depth of focus is defined as the range at which points are in focus. The narrower the aperture, the larger the depth of focus, but also the lower the radiance. Thus, there is a trade-off between having objects at a wide range in focus, and the amount of light which hits the sensor, and therefore the signal to noise ratio.

Actual optical systems, used on most consumer and industrial grade cameras, are compound lenses, which are constructed with multiple consecutive lens elements. This allows the lenses to do optical zoom, by varying the focal length, and to compensate for a type of error called chromatic aberration, where light with different wavelengths is refracted differently by the lens. Thus, the above description is greatly simplified, but the general observations apply.

The lens quality can influence the image quality. Impurities in the glass and tolerances in the shape of the lens can lead to image distortions. Electrical noise in the sensor leads to noise in the sampled pixel intensities. These effects propagate and lead to uncertainties in angles measured by cameras, which further causes uncertainties in the positions of triangulated points.

2.2.3 The Pinhole Camera Model

This brief derivation of the pinhole camera model follows Hartley and Zisserman (2003) and Heikkila and Silven (1997), with elements from Aanæs (2014). The goal is to form a model, which relates the positions of points in 3D space to the locations of their projections onto the 2D image plane. The lens is modeled as a hole with an infinitesimal diameter, only big enough to let a single ray of light pass, *i.e.* the direct ray. Thus, this model does not take depth of focus into account. Figure 2.4 shows a schematic of this situation, as seen from above, for a single point. A 3D point, C, with position $\mathbf{c} = [c_\mathrm{x}\ c_\mathrm{y}\ c_\mathrm{z}]^\mathrm{T}$, is projected, through a pinhole, onto the image plane at point Q, with position $\mathbf{q} = [q_\mathrm{x}\ q_\mathrm{y}]^\mathrm{T}$. Note that the focal length is set equal to the sensor-to-lens distance, as per the thin lens approximation. The two triangles on either side of the pinhole are similar. Therefore, the ratio between the lengths of their catheti are identical, thus

$$\frac{q_\mathrm{x}}{f} = \frac{c_\mathrm{x}}{c_\mathrm{z}} \Leftrightarrow q_\mathrm{x} = \frac{c_\mathrm{x}}{c_\mathrm{z}} f\,. \tag{2.6}$$

The same relation holds for the y-axis

$$\frac{q_\mathrm{y}}{f} = \frac{c_\mathrm{y}}{c_\mathrm{z}} \Leftrightarrow q_\mathrm{y} = \frac{c_\mathrm{y}}{c_\mathrm{z}} f\,. \tag{2.7}$$

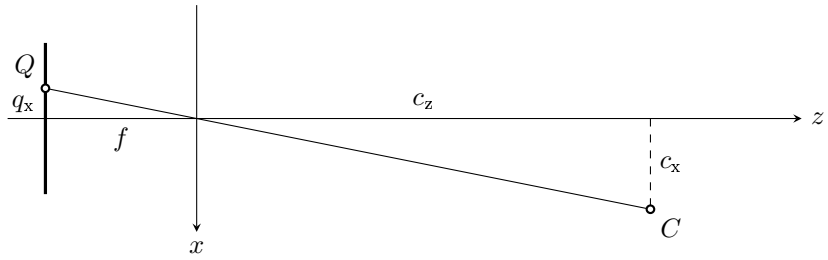

Figure 2.4: Illustration of the pinhole model as seen from above (y-axis not included). The point C, located at $\mathbf{c} = [c_x\ c_y\ c_z]^T$, is projected onto the image sensor at the point Q, located at $\mathbf{q} = [q_x\ q_y]^T$. The pinhole is located at the origin. Note that the y-axis points down through the paper. The coordinate system's orientation follows that usually adopted for cameras.

By introducing homogeneous coordinates, the projection of C onto Q can be written using linear algebra. In homogeneous coordinates, a vector $\mathbf{v} = [v_x\ v_y]^T$ is assigned a scale s such that $\mathbf{v}_h = [sv_x\ sv_y\ s]^T$ and $[\mathbf{v}^T\ 1]^T = \mathbf{v}_h/s$. The focal length can be different for the x-axis and y-axis, either due to rectangular pixels, a tilt between the lens and the sensor, or imperfections in the lens. This is compensated by introducing a scaling factor, α, on the focal length in the y-axis. A skew coefficient, β, is introduced to counteract a non-orthogonal pixel grid, which causes a skewness between the x- and y-axis. The optical axis usually intersect the image plane in its center. Per convention, the image origin is located in the top left corner. Therefore, a translation, $[\Delta_x\ \Delta_y]^T$, is added which moves the image plane origin. Combined, the projection can then be written as

$$\begin{bmatrix} sq_x \\ sq_y \\ s \end{bmatrix} = \begin{bmatrix} f & \beta & \Delta_x \\ 0 & \alpha f & \Delta_y \\ 0 & 0 & 1 \end{bmatrix} \begin{bmatrix} c_x \\ c_y \\ c_z \end{bmatrix} \tag{2.8}$$

$$\Rightarrow\ \mathbf{q}_h = \mathbf{A}\mathbf{c}\,, \tag{2.9}$$

where $\mathbf{q}_h$ is homogeneous and $\mathbf{A}$ is termed the intrinsic matrix, as it defines the parameters which describe the internals of the camera.

A camera may not be aligned with the reference coordinate system. To accommodate cameras which are offset from the origin, a rotation $\mathbf{R} \in \mathbb{R}^{3\times3}$ and translation $\mathbf{t} \in \mathbb{R}^3$ is introduced, such that the complete model for projecting a world 3D point, onto a 2D image plane in a camera, which does not align with

the coordinate system, is given by

$$\mathbf{q}_\mathrm{h} = \mathbf{A}[\mathbf{R}\ \mathbf{t}]\mathbf{c}_\mathrm{h} \tag{2.10}$$
$$= \mathbf{P}\mathbf{c}_\mathrm{h}\,. \tag{2.11}$$

The matrix $[\mathbf{R}\ \mathbf{t}]$ is called the extrinsic matrix, as it defines the parameters describing the external setting of the camera. The pinhole camera model is defined by the matrix $\mathbf{P}$, called the camera matrix.

In order to more precisely model a real camera, with an actual lens, a non-linear transformation is added (Brown, 1966, 1971). The shape of a lens can lead to radial lens distortion, where the apparent magnification changes with the distance from the lens' center. It moves the position of projected points on the image sensor in the radial direction relative to the lens. The points can be remapped using a power series which models the movement

$$\begin{bmatrix} x' \\ y' \end{bmatrix} = (1 + k_1 r^2 + k_2 r^4 + k_3 r^6) \begin{bmatrix} x \\ y \end{bmatrix}\,, \tag{2.12}$$

where $[x\ y]^\mathrm{T}$ is the position of the points projected onto the sensor and $[x'\ y']^\mathrm{T}$ is the location where the point would have been projected had it not been for radial distortion. The distance from the point to the optical axis is given by $r = \sqrt{x^2 + y^2}$. The optical axis is usually located at the image center and sits orthogonal to the image plane. The constants k_1, k_2 and k_3 are radial distortion coefficients. Note that r^2 is the base variable of the series. Consequently, the series only contain the even powers which are $(r^2)^1 = r^2$, $(r^2)^2 = r^4$ and $(r^2)^3 = r^6$. Tangential distortion can occur if the lens elements are misaligned. A correction function can be added, which yields the following combined mapping to account for lens distortions

$$\begin{bmatrix} x' \\ y' \end{bmatrix} = (1 + k_1 r^2 + k_2 r^4 + k_3 r^6) \begin{bmatrix} x \\ y \end{bmatrix} + \begin{bmatrix} 2p_1 xy + p_2(r^2 + 2x^2) \\ 2p_1(r^2 + 2y^2) + 2p_2 xy \end{bmatrix}\,, \tag{2.13}$$

where p_1 and p_2 are tangential distortion coefficients.

2.2.4 Estimating the Model Parameters

For a given camera, with a given optical system, the parameters of the pinhole camera model can be obtained through a process known as camera calibration. It usually involves capturing a series of photographs of either a flat checkerboard or circles aligned in a grid. By knowing the actual 3D position of the checkerboard corners or circle centers, relative to one of the corners or centers, the images provides a set of corresponding 2D and 3D points. The model parameters can be estimated from a non-linear optimization, which seeks to minimize the re-projection error of the 3D points onto the 2D points (Z. Zhang, 1999).

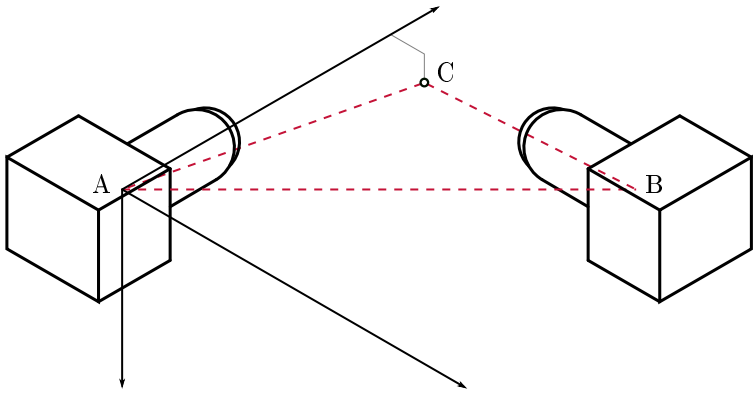

Figure 2.5: Illustration of a stereo vision setup. Two cameras observe a point in 3D space whereby a triangle is formed. The mutual displacement between the cameras, $|AB|$, and the orientation of the camera at B relative to that at A, can be obtained through calibration. The angles $\angle A$ and $\angle B$ to the point C can be measured by the cameras and used to compute C's position. Note that the coordinate system aligns with the position and orientation of the camera at A.

2.2.5 Triangulating With a Stereo Camera Setup

Imagine that a camera is placed at both vertex A and vertex B, and that they observe vertex C. Figure 2.5 illustrates this setup in 3D. As illustrated through the triangulation principle, the observation angles to C, from each of the cameras, can be used to compute the position of C. Without loss of generality, the frame of reference is chosen such that the coordinate system coincides with the position and orientation of camera A.

From camera calibration, a pinhole model of camera A and B is obtained, including lens distortion. The respective camera matrices are labeled $\mathbf{P}^{(\mathrm{A})}$ and $\mathbf{P}^{(\mathrm{B})}$.

Each of the cameras adds two constraints on the 3D position of the point C, one from the x-coordinate and one from the y-coordinate of the projection, respectively. Let $\mathbf{P}_i$ be a vector corresponding to the i'th row of $\mathbf{P}$, such that $\mathbf{P}_i \in \mathbb{R}^{1\times 3}$ and $\mathbf{P}_{i,j} \in \mathbb{R}^{2\times 3}$. Ignoring the lens distortion for now, the projection, $\mathbf{q}$, is given by the pinhole model in Equation 2.11. It is used to impose a

constraint on C's position, $\mathbf{c}$, as follows

$$\begin{aligned} \mathbf{q} &= \frac{\mathbf{P}_{1,2}\,\mathbf{c}}{\mathbf{P}_3\,\mathbf{c}} \\ \Rightarrow \quad \mathbf{q}(\mathbf{P}_3\,\mathbf{c}) &= \mathbf{P}_{1,2}\,\mathbf{c} \\ \Rightarrow \quad \left((\mathbf{P}_3^{\mathrm{T}}\,\mathbf{q}^{\mathrm{T}})^{\mathrm{T}} - \mathbf{P}_{1,2}\right)\mathbf{c} &= 0\,. \end{aligned} \tag{2.14}$$

The constraints imposed from each of the cameras can be stacked into a matrix, $\mathbf{B} \in \mathbb{R}^{4\times 4}$,

$$\mathbf{B} = \begin{bmatrix} \left(\mathbf{P}_3^{(A)\mathrm{T}}\,\mathbf{q}^{\mathrm{T}}\right)^{\mathrm{T}} - \mathbf{P}_{1,2}^{(A)} \\ \left(\mathbf{P}_3^{(B)\mathrm{T}}\,\mathbf{q}^{\mathrm{T}}\right)^{\mathrm{T}} - \mathbf{P}_{1,2}^{(B)} \end{bmatrix}, \tag{2.15}$$

from which $\mathbf{c}$ can be estimated by solving the linear problem $\mathbf{Bc} = \mathbf{0}$, subject to $||\mathbf{c}|| = 1$ to avoid the trivial solution. The vector $\mathbf{0} \in \mathbb{R}^4$ is the 0-vector. Now, the non-linear lens distortion is added, by splitting $\mathbf{B}$ into two matrices, and applying them consecutively, with the non-linear mapping in between. The final position of C is then estimated through a least squares optimization (Hartley & Zisserman, 2003).

In an actual implementation, the above optimization is conducted for multiple points at a time, which returns a so called point cloud. The question is now: how does the system knows which points in the two cameras belong together? This is covered by the following section.

2.3 The Correspondence Problem

Up until this point, it has been assumed that the location of C's projections, into the two cameras, were known. Actually, the correspondence between pixels in two cameras are never known *a priori*. Accurately establishing pixel correspondences between two, or more, cameras is a registration problem, and sits at the core of much stereo vision research, from the early days (Lucas, Kanade, et al., 1981) up until today (Huang, Matzen, Kopf, Ahuja, & Huang, 2018).

There are two general approaches for establishing correspondence: passive and active (Dhond & Aggarwal, 1989). The passive approach relies exclusively on ambient light. Correspondences are generated from some form of correlation measure between pixel intensity values, or extracted image features. In the active approach, the stereo system emits its own light. A number of different correspondence approaches are used, depending on the nature of the emitted

light. They might be identical to those used for passive stereo, or utilize some form of structure imposed on the light or its source. Passive stereo requires the measured workpiece to be textured in order to assign pixel correspondences. In many industrial applications, the workpiece is untextured, which is very much the case for wind turbine blades, and thus active techniques are preferable (Maas, 1993). Therefore, only the most common active stereo techniques are covered here (Van der Jeught & Dirckx, 2016).

Various flavors of active techniques exist, but it seems that the SL techniques are commonly used in metrological applications (Savio et al., 2007). In SL, a light projector emits a spatial light pattern with a certain ordering. It is commonly line(s), dots, or waves (Eiríksson, Wilm, Pedersen, & Aanæs, 2016; Salvi, Pages, & Batlle, 2004). The pattern is observed by both cameras, and used to assign pixel correspondence. A projector is essentially a reversed camera, where the image sensor is replaced by a display. Therefore, it can be calibrated similarly to the cameras, using the pinhole model. Thus, it is possible to construct a stereo setup containing only a calibrated light source and a calibrated camera, though a setup containing multiple cameras are believed to be more robust and easier to calibrate (Maas, 1990, 1993).

Different pattern strategies have been proposed (Batlle, Mouaddib, & Salvi, 1998) to overcome problems with ambient light, inter-reflections, surface discontinuities, surface texture, and sub-surface scattering. Four commonly used strategies are described here, including their advantages and disadvantages (Geng, 2011). It is a key parameter of an active stereo setup, and thus relevant to take into account when selecting a 3D scanner.

2.3.1 Line Scanning

In line scanning, a line, often from a laser source, is projected onto the surface. By segmenting the line in each of the camera images, correspondence is relatively straight forward to assign (Levoy et al., 2000). It can be done either by finding intersections between epipolar lines, where a point in one camera forms a line in the other, and the laser line, or through a simple row scan given that the images are corrected such that they appear to originate from fronto parallel cameras (*i.e.* cameras with parallel image planes). The resulting 3D points are all located on the line, which is why either the object, or the stereo setup, has to be moved to capture the full geometry.

If a projector is used, a number of lines can be projected and triangulated simultaneously. This yields an area covering point cloud, but complicates the correspondence problem. The lines has to be separated from each other, which

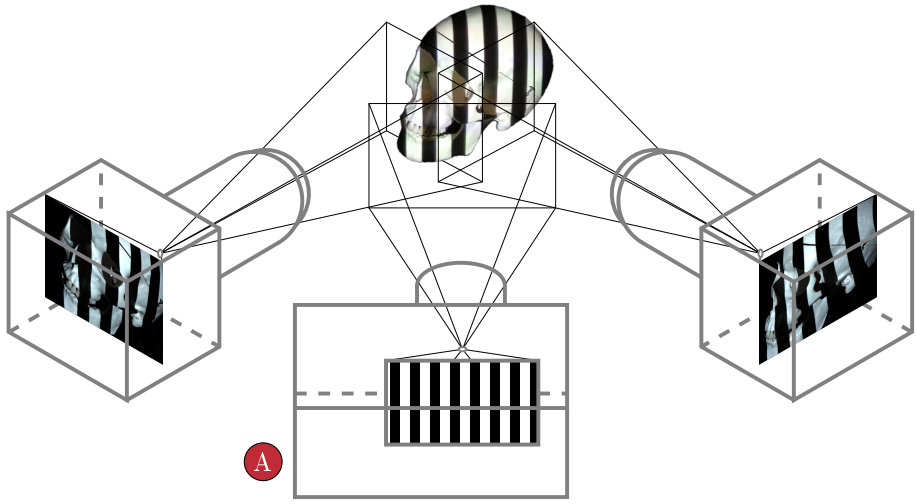

Figure 2.6: Illustration of a single gray code pattern being projected, by a projector (A), onto a skull, and then observed by two cameras in a stereo setup. In the subsequent patterns, each stripe is divided into two, with the left half being black and the right being white.

can be difficult, especially if the geometry is complex.

Line scanning is, in general, fairly precise and fast. Only a single image needs to be captured by each of the cameras. The resulting point cloud is relatively sparse. Additionally, problems with keeping track of the lines across images from multiple cameras can lead to wrong matches between the lines, which in turn results in outliers.

2.3.2 Gray Coding

The problem of identifying each line in a multi-line projection, can be solved by projecting a series of consecutive patterns, which, when combined, assign a binary code to each line. Patterns forming a Gray Code (Breckman, 1956; Frank, 1953) are often used due to their good robustness against noise (Inokuchi, 1984). Each pattern contains a number of dark and illuminated stripes. Often, black and white stripes are used, but color can be used for enhancing contrast, depending on the material (Benveniste, Cem, et al., 2010). Figure 2.6 shows a single pattern, from a sequence, being projected onto a skull.

The largest possible contrast between neighboring lines is achieved by using a

binary pattern. This is advantageous in situations where the surface is textured or very light absorbent, or if the surface is illuminated by ambient light which has to be outshined. In situations where the surface is translucent, light from the illuminated strips can "bleed" into the dark stipes. If parts of the surface is convex, inter-reflections can illuminate dark stripes. These effects can be counteracted, to some extend, by using a different code than Gray code (Gupta, Agrawal, Veeraraghavan, & Narasimhan, 2011). The resolution of the triangulated point cloud depends on the number of edges in the highest frequency pattern, and thus the resolution of the projector.

2.3.3 Phase Shifting

A binary pattern only uses the two extremes of the projectors dynamic range. In phase shift coding, the full dynamic range is utilizes by projecting patterns containing all possible shades of gray. The patterns form spatial sine waves, as illustrated in Figure 2.7a, which are phase-shifted across the surface. The general setup is identical to that shown in Figure 2.6, but each pixel-row in the pattern forms a sine wave. The intensities measured by a single camera pixel, which covers a part of the surface, sampled during the phase-shifting, will form a time-discrete sine signal. The frequency of this sine is directly correlated with the frequency of the projected sine pattern, and its phase is correlated with the depth of the surface, relative to the projector. The phase will wrap around as the depth increased, which results in arbitrary phase values. Phase-unwrapping is applied to circumvent this issue and make the phase values directly correlate with the depth, either by projecting multiple sine patterns with different frequencies (Wust & Capson, 1991), or by also projecting a series of gray coded patterns (Krattenthaler, Mayer, & Duwe, 1994). The depth of the surface can be directly deduced from the unwrapped phase. This is, however, often unrobust, which is why the unwrapped phase is commonly used as identifying codes for assigning correspondence (Sansoni, Carocci, & Rodella, 1999).

The resolution of the point cloud depends on the resolution of the cameras, as the coding strategy does not rely on discrete line edges. The depth granularity is generally higher than that obtained with Gray coding, as cameras generally has higher resolutions than projectors. This strategy is less sensitive to light bleeding and inter-reflections (Gupta & Nayar, 2012), and generally provides better precision and accuracy (Eiríksson et al., 2016), than Gray coding.

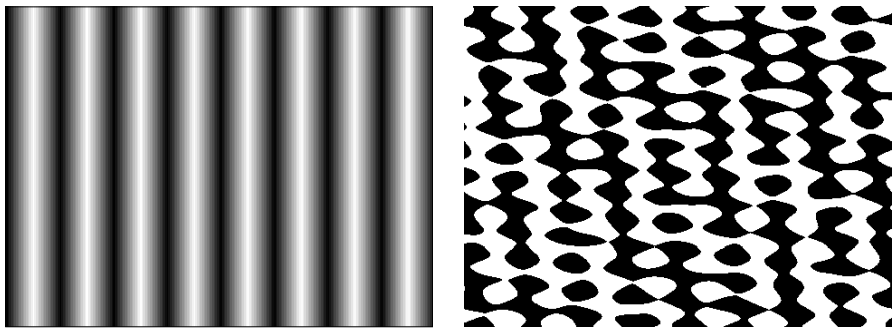

(a) (b)

Figure 2.7: Example of a sine-wave pattern used for phase shifting (a), and a random phase, fixed frequency pass-band pattern used as unstructured light (b).

2.3.4 Unstructured Light

It has been indicated, that better correspondence robustness against inter-reflections, light bleeding and depth continuities can be achieved by using an unstructured pattern (Couture, Martin, & Roy, 2014). Unstructured patterns (Claus, 1988) are still a form of structured light, but with the structure having some form of random element. For example, a "pattern" can be completely random white noise (Kushnir & Kiryati, 2007), or constructed from a set of spatial frequencies with random phase (Couture, Martin, & Roy, 2011), as illustrated in Figure 2.7b. The method is similar to Gray coding, as a number of patterns are projected, imaged, thresholded, and then used to assign a depth depending code to each pixel. Correspondence is typically established through a correlation measure (Claus, 1988; Maas, 1993), dynamic programming (L. Zhang, Curless, & Seitz, 2002), or based on hashing (Couture et al., 2011).

2.4 Modeling the Interaction Between Light and Matter

No matter which coding strategy is used, the projected patterns are susceptible to the radiometric properties of the surface's material(s). As a consequence, it is important to consider the material-light interaction. Different levels of abstraction can be used, when describing this interaction, but, in the end, it all boils down to effects taking place at a quantum level. Light can be modeled as

an electromagnetic wave, which interacts every time it encounters an atom. This level of abstraction is, however, too detailed for what is needed here. Instead, we will look at a more general level, where multiple quantum effects combine to yield the observed behavior. However, be aware, that most of the following sentences could be ended with ", due to quantum effects.". We will refrain from using it but once, where it was deemed necessary. This section is based on the books by Callister and Rethwisch (2013) and Hecht (2016).

When light proceeds from one medium into another, a part of the light can be reflected at the boundary, a part of it can be transmitted through the medium, and a part of it can be absorbed by the medium (Callister & Rethwisch, 2013). The sum of the ratios between the incoming irradiance, I_0, and the reflected radiance, I_R, the transmitted radiance, I_T, and the absorbed radiance, I_A, is given by

$$\frac{I_0}{I_\mathrm{R}} + \frac{I_0}{I_\mathrm{T}} + \frac{I_0}{I_\mathrm{A}} = 1\,. \tag{2.16}$$

Therefore, under normal circumstances, reflection, transmission, and absorption accounts for the total dissemination of energy. A ray of light has a direction and an orientation. The fraction of light being reflected, transmitted and absorbed depends on the angle between the incident light and the surface, the orientation of the light, and the wavelength, and thus the color, of the light, as described by the Fresnel equations (Hecht, 2016).

2.4.1 Polarization

Adopting the transverse wave model, electromagnetic waves, such as light, is constituted of an electric wave and a magnetic wave. The two waves are orthogonal and oscillate in-phase in a direction orthogonal to the direction of propagation. The light wave's orientation, or polarization, is defined as the vibration direction of the electric wave (Hecht, 2016). Polarization orientation influences refraction. Light emitted from an unpolarized source, *i.e.* the light rays have random orientations, will generally become partially polarized when reflected from a dielectric medium, such as glass, water or most plastics. When an incident light ray hits the surface at a specific angle, which depends on the refractive index of the involved media, called Brewster's angle, the reflected light is completely polarized. Only the light rays which are polarized parallel to the surface that is orthogonal to the surface normal, are reflected (Hecht, 2016). As an effect, specular reflections are often partly polarized parallel to the surface, and completely polarized exactly at Brewster's angle. This is why car drivers often wear vertically aligned polaroid sunglasses. Sunlight is unpolarized, but blinding specular reflections from the road are primarily horizontally polarized,

due to the roads horizontal orientation, and thus the sunglasses remove the glares. Conducting materials generally reflect all polarizations equally.

Other than sunglasses, knowledge about lights polarization can be used for a number of things. For example, it can be exploited to remove glares from images, which cause saturated pixels, by placing a polaroid filter in front of the lens. This was exploited in Contribution A, where a polarized light source was used, in combination with a polaroid camera filter, to remove specular highlights from images of additively manufactured plastic components. The goal was to develop a simple camera-based system for in-process failure mode detection. The detection was based on comparisons between a segmented image of the manufactured part, at a given time during the manufacturing process, and a rendering of what the outline of that part should look like at that time. The light source and camera were polarized 90° relative to each other in order to suppress specular reflections while enhancing diffuse reflection. We also placed them spatially close together, which minimized the amount of shadow observed by the camera. In combination, these two design choices made it easier to readily segment the component, and avoided saturated pixels. The paper demonstrated that a simple system, composed of a camera and a light source, can be used to detect certain types of failure modes during additive manufacturing. It was argued that it is advantageous and feasible to use such a system, even for cheap hobby machines based on fused deposition modeling (FDM).

So, what exactly is specular and diffuse reflection, and how do they relate to transmission, reflection and absorption? This is covered below.

2.4.2 Diffuse and Specular Light

Specular highlights are caused by direct reflections. They occur when light is reflected off of a surface directly towards the observer, and are as such not different from the general reflection phenomenon described above. Diffuse light is actually an artifact of micro structure on the surface, and light being scattered below the surface, and is also described by the Fresnel equations.

If a surface is not smooth, but instead distorted with small hills and valleys, the angle between the surface and an incident light ray depends on where the ray hits the surface. This influences the direction of the reflected light ray, and an observer will thus perceive the light as being scattered by the surface. The observer does not directly observe the micro structure, but instead perceives the irradiance to be scattered, yielding a radiant intensity in multiple directions. Figure 2.8 illustrates the principle. The scattering effect is proportional to how pronounced the micro structure is.

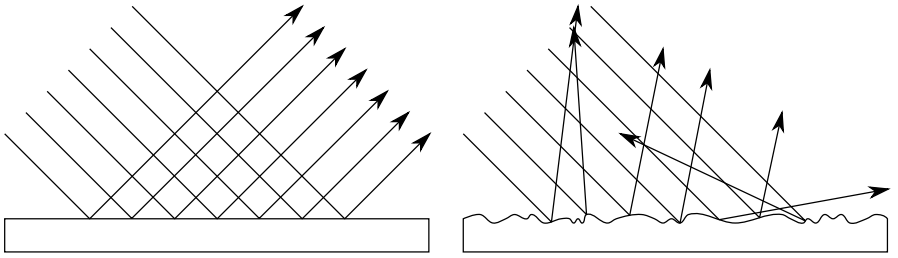

Figure 2.8: Illustration of specular reflection (a) and diffuse reflection (b). The arrows illustrate incident rays of light, which are reflected off of the surface.

For dielectric materials, the diffuse light caused by micro structure has the same color as the incident light. This is because no absorption occurs when light is reflected by a dielectric medium. Instead, most of the perceived color of an object, under white light illumination, comes from subsurface scattering (Hanrahan & Krueger, 1993).
In the situation where a given material consists of only one medium, *i.e.* it is homogeneous, its radiometric behavior can be accounted for by the effects described thus far. If the material is not homogeneous, *i.e.* it contains impurities, the effects take place every time light encounters an interface. This is illustrated in Figure 2.9. The result is, that a light ray is reflected, transmitted and absorbed multiple times as it propagates through the material. The reflection and transmission makes the ray change direction, and the absorption makes the transmitted light change color. The effects also cause the light to be attenuated. Some of the light will, by chance, be reflected back out of the surface, after having "bumped" around inside the material. The color and radiance of this re-reflected light will have changed, compared to that of the incident light. How much depends on the material parameters, such as purity, absorption coefficient and refractive index, and the light's wavelength, irradiance, polarization, and incidence angle.

Most materials generate both specular reflection, diffuse reflection and subsurface scattering, when excited by light (Hecht, 2016). Thus, the effects illustrated in Figure 2.8 and Figure 2.9 combine to give the perceived appearance of a material. Figure 2.10 shows an example of this. Dielectric materials, such as glass, most plastics, and air, tend to reflect most of the visible wavelengths, whereas conducting materials, such as metals, absorbs some wavelengths, due to quantum effects (Hecht, 2016). As a result, specular reflections tend to be white for dielectric materials and colored for conducting materials. As stated above, the color of a dielectric material originates from absorption of certain wavelengths

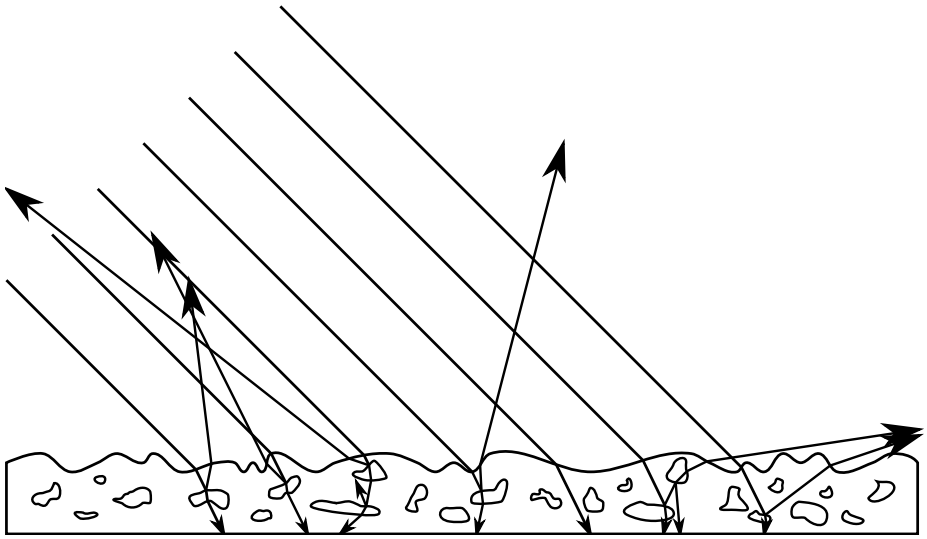

Figure 2.9: Illustration of subsurface scattering. Impurities, made from a medium with a different refractive index than the primary one, is placed below the surface. The black arrows illustrate incident rays of light, and their paths through the media. To avoid clutter, only the transmitted, or refracted, part of the rays are shown at the surface. The first reflection and refraction, below the surface, is also illustrated. Note that, at each boundary, a light ray is, of course, both reflected, transmitted and absorbed. An observer will perceive the light rays as being scattered by the material.

during subsurface scattering. The absorption causes certain wavelengths to be attenuated more than others, which is why the light reflected back out of the surface will be missing those wavelengths, thus resulting in a change of color, compared to the incident light.

The failure mode detection in Contribution A was based on comparing photographic and rendered segmentation masks. As a consequence, it could only detect defects which distorted the manufactured object's boundary. With knowledge about the scene's composition, and a model of the plastic's radiometric behavior, the manufactured object can be rendered photorealistically. By comparing this rendering directly with the acquired photographs, internal defects can be detected. A study of the precision of rendered images was done by Contribution B. It developed a method, with an associated pipeline, for quantitatively judging the realism of physically based rendering techniques, on a pixel-to-pixel basis. The considered scenes contained glass objects, which are

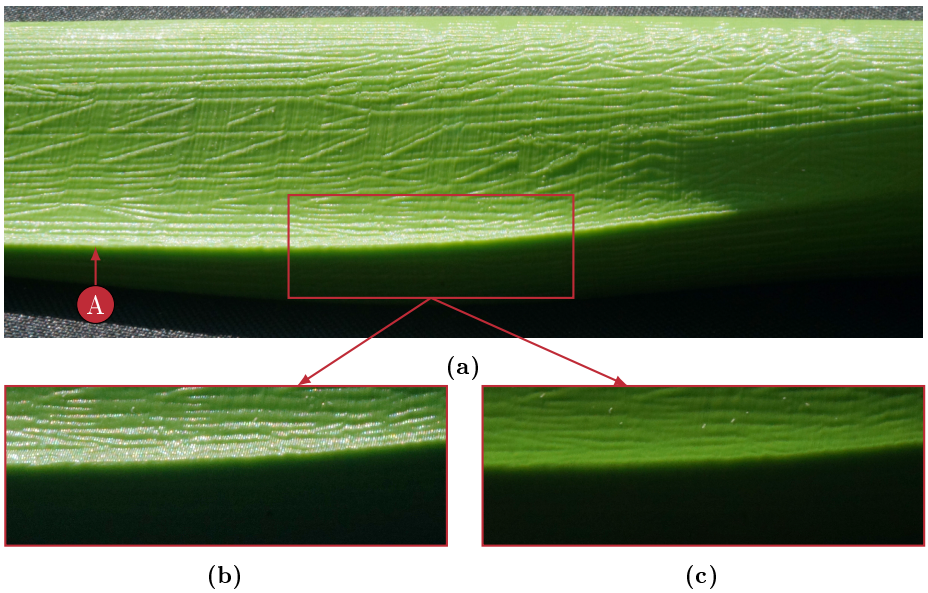

Figure 2.10: Photograph of an additively manufactured plastic component, illuminated by direct sunlight. (a) shows an unfiltered view of the component. Specular reflections are seen as shiny, white highlights, and diffuse reflections are seen as the green color. Subsurface scattering can be seen as a hazy glow on the side which faces away from the sun, right below the edge which is marked A. A horizontal polaroid filter is applied in (b) and a vertical polaroid filter is applied in (c). Notice how the vertical filter removes most of the specular reflections, but leaves the diffuse, including subsurface scattering.

considered difficult to model, due to the radiometric behavior of glass. Having a quantitative method for accurately measuring the precision of a rendering technique is important, if that technique is to be used for quality inspections, as could have been done in Contribution A. We will now turn our attention towards how the interaction between light and material is modeled in physically based renderings. Then, the following section describes how the interaction can be measured, before concluding with a description of how such measurements were used to analyze the behavior of the blade surface paints.

2.4.3 The Bidirectional Reflectance Distribution Function (BRDF)

As indicated above, the microstructure on a surface often exhibits some level of randomness. The same applies to the composition of the material below the surface. As a result, the perceived radiance of a surface can be regarded as probabilistic with respect to the material composition and the surface structure. However, for a given material sample, with a given surface and composition, the radiance can be regarded as deterministic, as long as the sample does not change its structure, or composition, over time. A given incident light ray, with a given wavelength and irradiance on the surface, which enters the surface at a given position, and with a given angle, relative to the surface, will cause a given set of reflected light rays, each with a given wavelength, radiance, exit position, and direction. This relation can be modeled by what is known as a reflectance distribution function.

The simplest of these functions are the bidirectional reflectance distribution function (BRDF) (Nicodemus, 1965). It assumes that a ray reflected in a given direction, relative to the surface, only depends on the angles of the incident rays. Thus, it ignores the existence of subsurface scattering, and instead perceives diffuse light as an independent phenomenon which occurs directly on the surface. As such, this model is best for describing the behavior of opaque materials, *i.e.* materials which either have no subsurface scattering, or which quickly attenuate subsurface scattered rays.

The irradiance of an incoming light ray is defined as

$$E = \frac{\partial \Phi}{\partial A} \quad [\mathrm{W/m^2}]\,, \tag{2.17}$$

where Φ is the radiant flux, measured in watts, and A is area, measured in square meters. It describes the flux received by the surface, per unit surface area, in the limit where the surface area tends to zero. The radiance is defined as

$$L = \frac{\partial \Phi}{\partial A_{\mathrm{proj}} \partial \Omega} \quad [\mathrm{W/sr/m^2}]\,, \tag{2.18}$$

where A_{proj} is the area of the surface when projected onto a detector, such as a camera or an eye, and Ω is the solid angle of the reflected light ray. The BRDF is defined as the ratio between the reflected radiance and the incident irradiance, thus

$$f(\lambda_{\mathrm{i}}, \boldsymbol{\omega}_{\mathrm{i}}; \lambda_{\mathrm{r}}, \boldsymbol{\omega}_{\mathrm{r}}) = \frac{\partial L(\lambda_{\mathrm{r}}, \boldsymbol{\omega}_{\mathrm{r}})}{\partial E(\lambda_{\mathrm{i}}, \boldsymbol{\omega}_{\mathrm{i}})} \quad [\mathrm{sr}^{-1}]\,, \tag{2.19}$$

where λ_{i} and λ_{r} are the wavelengths of the incident and reflected light, respectively, and $\boldsymbol{\omega}_{\mathrm{i}} \in \mathbb{R}^2$ and $\boldsymbol{\omega}_{\mathrm{r}} \in \mathbb{R}^2$ are the spherical directions of the incident

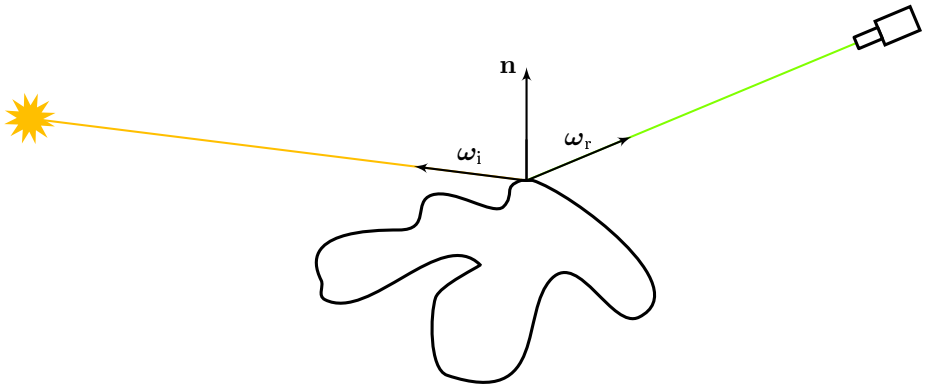

Figure 2.11: Illustration of the vectors used in the BRDF model. $\boldsymbol{\omega}_i$ is oriented towards the light source, $\boldsymbol{\omega}_r$ is oriented towards the camera, and $\mathbf{n}$ is the surface normal. Both $\boldsymbol{\omega}$s are defined relative to the normal.

and reflected rays, respectively (Nicodemus, 1965; Weyrich, Lawrence, Lensch, Rusinkiewicz, Zickler, et al., 2009). $L(\lambda_r, \boldsymbol{\omega}_r)$ is the radiance in the direction $\boldsymbol{\omega}_r$ for wavelength λ_r, and $E(\lambda_r, \boldsymbol{\omega}_i)$ is the irradiance received from direction $\boldsymbol{\omega}_i$ with wavelength λ_i. Figure 2.11 illustrates the vectors.

The BRDF describes how much of the incident light, coming from one direction, is reflected into another, possibly same, radiant direction. The BRDF is written as a differential quantity to emphasize, that we are talking about light received and emitted from directions with solid angles in the limit, as those angles approach zero, *i.e.* there is no such thing as *exactly* one direction (Weyrich et al., 2009). Naturally occurring BRDFs are positive, $f(\lambda_i, \boldsymbol{\omega}_i; \lambda_r, \boldsymbol{\omega}_r) \geq 0$, obey Helmholtz reciprocity, $f(\lambda_i, \boldsymbol{\omega}_i; \lambda_r, \boldsymbol{\omega}_r) = f(\lambda_r, \boldsymbol{\omega}_r; \lambda_i, \boldsymbol{\omega}_i)$, and conserve energy, which means that the integration of the BRDF over all $\boldsymbol{\omega}_r$, for a given $\boldsymbol{\omega}_i$, is less than, or equal to, one (Weyrich et al., 2009).

The BRDF model is insufficient for describing the appearance of materials with extensive subsurface scattering, such as colored glass, but it adequately describes the appearance of many types of paints, including those used for wind turbine blades.

In case one wants to explicitly model subsurface scattering, other reflectance functions are available, such as the bidirectional scattering-surface reflectance distribution function (BSSRDF), defined as

$$f(\lambda_i, \mathbf{x}_i, \boldsymbol{\omega}_i; \lambda_r, \mathbf{x}_r, \boldsymbol{\omega}_r) = \frac{\partial L(\lambda_r, \mathbf{x}_r, \boldsymbol{\omega}_r)}{\partial \Phi(\lambda_i, \mathbf{x}_i, \boldsymbol{\omega}_i)} \quad [\mathrm{sr}^{-1}\mathrm{m}^{-2}], \tag{2.20}$$

where $\mathbf{x}_i \in \mathbb{R}^2$ is the surface position where the light ray enters the surface, and $\mathbf{x}_r \in \mathbb{R}^2$ is the position where the ray exits the surface (Nicodemus, Richmond, Hsia, Ginsberg, & Limperis, 1977; Weyrich et al., 2009). Such a function would be needed to model unpainted blades, as the solidified epoxy-fiberglass composite is translucent. This thesis exclusively considers the final inspection of the finished, painted blade surface, which can be adequately modeled by a BRDF.

2.4.4 Utilizing Reflectance Distribution Functions

Appearance models, such as reflectance distribution functions, are used primarily in Computer Graphics, when trying to create realistic renderings, but they are starting to see applications in other fields. As an example, Contribution C presented ideas for using appearance models outside of Computer Graphics. Specifically, it was speculated that parsimonious models, *i.e.* models with few parameters, could be useful to quality inspection in additive manufacturing, metal casting, and wind turbine blade production, and for 3D content acquisition, such as SL stereo vision.

The reflectance distribution function, of a measured object's material, influences the performance of an SL scanner. Specular reflections can cause camera pixels to be saturated, in which case it is impossible to assign correspondence when using gray-level methods, such as phase coding. Interreflections, either from other objects or other pars of the same object, can illuminate dark areas of binary patterns, causing them to be thresholded incorrectly. They can also change the measured intensities of gray-level patterns, causing the phase to be wrongly decoded. Subsurface scattering can transport light from illuminated areas, and into areas which should be dark, causing effects similar to those caused by interreflections.

This makes it difficult to readily assign pixel correspondences. As outlined in Section 2.3, various coding strategies have been developed to limit the problems. Thus, a sensible coding strategy can be selected, based on the knowledge of the material's reflectance function. In addition, some of the effects, e.g. specular highlights, can be avoided through the design of the camera and projector setup, if the general geometry of the object to be measured is known *a priori*. The reflectance function can also be used to measure the orientation, or surface normal, of a surface directly, through a technique known as shape from shading (Woodham, 1980).

2.5 Measuring a BRDF

BRDFs are usually measured with a devise called a gonioreflectometer. It is a highly specialized device, which can measure correspondence between irradiance and radiance, for a given sample, by moving a detector, a light source, and potentially the sample, around. A gonioreflectometer is needed to measure the blade BRDFs, and to measure the BRDFs needed in Contribution B. Further, having such a device enables the possibility to conduct research within subjects such as material appearance, 3D reconstruction accuracy as a function of reflectance, and the utilization of reflection distribution functions in Computer Vision.

Instead of building a gonioreflectometer from scratch, it was decided to make one out of an industrial robot arm. As described by Contribution D, a six DoF industrial robot was used to move a camera around a flat material sample, capturing photographs, while the sample was illuminated from different angles by a purposely built light arc. It was not feasible to densely sample all combinations of directions, as it would have taken too long time, even with the automated robot system. Instead, a relatively sparse set of incident-reflected directions were sampled, and the full BRDF was reconstructed using a statistical method, based on a dataset of previously measured BRDFs (J. B. Nielsen, Jensen, & Ramamoorthi, 2015). The system is able to measure isotropic BRDFs of flat samples.

As mentioned previously, other than measuring the blade BRDFs, the gonioreflectometer was used to measure the BRDFs used in Contribution B. The constructed scenes contained a checkerboard backdrop, made of paper glued onto a plate, and a white tablecloth, made of fabric. It was decided to model these materials as having BRDF reflectance, and measure them using our constructed gonioreflectometer. This assumption turned out to provide a relatively realistic appearance in the renderings, but it is believed, that an even better appearance could have been obtained if the tablecloth had been modeled as a BSSRDF.
The pipeline, developed in the paper, included scanning the scene with an SL scanner. Having two cameras and a projector, this setup actually measures two combinations of incident and reflected light directions. If an additional light source is added, the scanner can be used to estimate BRDFs, thus removing the need for a gonioreflectometer entirely, given that BRDF models are retained. This idea is presented below.

2.5.1 Measuring BRDFs with a Structured Light Scanner

Adding an additional light source to a SL scanner, with a projector and two cameras, allows the system to estimate BRDFs, cf. J. B. Nielsen, Jensen, and Ramamoorthi (2015). Contribution E investigated how various parameters in the setup, and uncertainties associated with these parameters, influenced the precision of the reconstructed BRDFs, through simulation.

An SL scanner system was simulated, with the additional light source. The simulation created rendered images of a Gray coded pattern sequence, projection onto a given object, represented as a triangular mesh. Additionally, it also created images of the object fully illuminated by the projector, and by the light source, respectively. The triangle mesh, including surface normals, was reconstructed through the images, using triangulation. From the estimated surface normals, the incident and reflected directions of all vertices, relative to the two cameras, could be computed. The associated reflected radiances could then be estimated from the fully lit images. This yielded four pairs of reflection observations per vertex. By rotating the object, the direction of the surface normals, relative to the cameras, were changed, and thus each rotation yielded four new vertex observations. This allowed us to estimate the BRDF of each vertex independently, using the reconstruction method developed by J. B. Nielsen, Jensen, and Ramamoorthi (2015). Thus, the estimated BRDFs varied over the object's surface, which is termed a spatially varying BRDF (SVBRDF) (Weyrich et al., 2009). Through the simulation, it was discovered, that the vertex positions and estimated surface normals had a large impact on the reconstructed BRDF, but that the reconstruction was mostly invariant to object geometry and light source properties.

The benefit of measuring BRDFs with an SL scanner, is the faster and simpler acquisition, as compared to the gonioreflectometer. However, as the positions of the cameras and light sources are fixed, the range of the observed angles between incident and reflected light is limited. This can lead to problems for some types of materials, where the bias introduced by the statistical reconstruction model gets too much weight, and thus yields a reconstructed BRDF which does not resemble the actual BRDF, and thus has a high uncertainty.

2.6 Blade BRDFs

The blade surface contains two types of paint. Most of the blade is covered with one type, which we call the base paint, and the leading edge is covered with LEP,

which is smoother. We measured the two corresponding BRDFs with our robot gonioreflectometer and used them to asses the complexity of the blade reflection. Figure 2.12a shows a photograph of the two paints and their measured BRDFs. As seen, the paints have a gray hue, when compared against the near to perfectly white material Spectralon® . Spectralon is a unique material, fabricated by Labsphere, which has an almost perfect Lambertian reflection. The material is almost perfectly diffuse, which means that an incident ray is scattered almost uniformly across the hemisphere.

Judging from the BRDFs shown in Figure 2.12, the measurements seem to indicate that the surface reflections resembles a Phong reflection model (Phong, 1975), meaning that the surface is well suited for optically based measurement techniques. Both paints are relatively "shiny", but with the LEP having a more focused specular reflection than the base paint. As the blade's leading edge is convex, interreflections should not be a problem. Thus, the BRDF does not seem to impose any special requirements on the coding strategy. However, the specularity of the LEP could cause some problems with saturation. As described above, it can be avoided through polaroid filters, or by positioning the scanner at an angle, relative to the surface, such that the direct reflections do not shine back into the cameras.

(a)

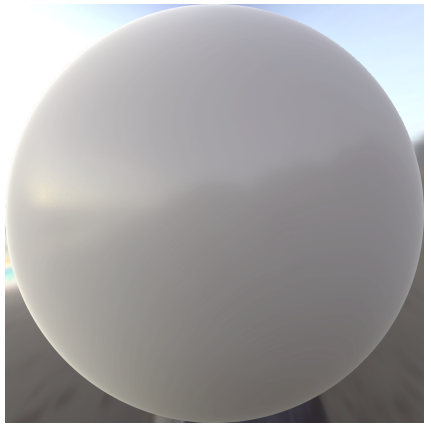

(b)

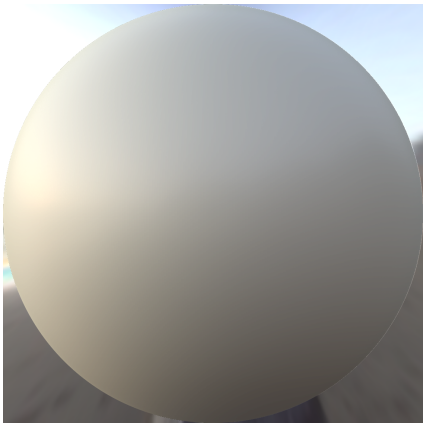

(c)

Figure 2.12: Illustration of the measured BRDFs for the two blade surface paints. A photograph of the two paints, together with Spectralon® are shown in (a). The left hand side is a photograph of the Spectralon, which exhibits a near to perfect Lambertian reflection (Weyrich, Lawrence, Lensch, Rusinkiewicz, Zickler, et al., 2009). Therefore, it is as close to white as possible. The right hand side is a photograph of the wind turbine blade surface, where a subtle horizontal line separates the LEP from the other paint. Note that both paints are relatively gray. (b) shows the measured BRDF for the specular paint, rendered on a sphere inside an environment map, and (c) shows the BRDF for the diffuse paint, rendered under the same conditions as the specular.

Chapter 3

Geometrical Quality Inspection of Large Freeform Components

This chapter focuses on describing the developed wind turbine blade measuring, or blade scanner, system. Most of the innovations introduced by our blade scanner system are based on requirements raised by the turbine blade manufacturer, namely SGRE, which was stated during interviews with company representatives. This chapter opens with a highlight of these requirements in Section 3.1. The measuring system, which is the payload, was selected based on a thorough benchmark of available commercial products, based on the knowledge described in Chapter 2. It is composed of an SL 3D scanner and a positioning system. Section 3.2 describes the scanner benchmarking, its outcome, and the details of the selected scanner and positioning system.

A locomotion system carries the measuring system and moves it over the blade surface. The 3D scanner is mounted on a six-axis industrial robot arm, which in turn is mounted on a robotic drive platform. The design and implementation of this locomotion system are described in Section 3.3. To test the system in a real production setting, and acquire data from real turbine blades, it has to comply with the Danish law for machinery: "Maskindirektivet" (Directive 2006/42/EC, 2006; DS/EN ISO 12100:2011, 2011). Therefore, a rather exten-

Figure 3.1: Photograph of the blade scanner system. The red steel frame is the robotic drive platform. The robot arm is wrapped by a white protective sock. The scanner system can be seen inside the black and yellow marked protective cage. Figure borrowed from Contribution J.

sive safety system had to be implemented, which is described in Section 3.4. Section 3.5 describes the control system, which is responsible for autonomously steering the scanner correctly. A photograph of the scanner system is shown in Figure 3.1.

The scanner system, in itself, is the major contribution included in this chapter. The specific scientific novelties are entailed in the following contributions: Contribution F is a technical report that describes the control algorithm and associated feedback loop. Contribution G is a patent application for the system idea, and specifically the application of the locomotion system, which has been filed with the European Patent Office. Two proof-of-concept methods for detecting surface defects from the blade scans are presented in Contribution H. Contributions I and J are shared among this chapter and Chapter 4. Both contributions present the scanner system and its measuring precision, but with a different focus. The precision part is described in Chapter 4. Note that the technical reports focus on the technical aspects of the presented work, and as such, they do not contain full accounts of its relation to state of the art. An overview of previous work was given in Section 1.2.3.

Table 3.1: Overview of the requirements for the blade scanner system. Table adapted from Contribution I.

Requirement	Description
Sensitivity	The system must be sensitive enough to measure defects with both a small and a large spatial extend.
Measuring Time	The time required to survey a leading edge must be lower than the corresponding manual inspection time.
Cost	The cost over the system's life time, including component depreciation and maintenance, must be lower than the total cost of the corresponding manual inspection.
Applicability	The system must be directly deployable in the current production facility, without changing the setup.
Safety	The system must be safe for humans to operate and be around.

3.1 Requirement Specification

The manufacturer's demands formed the basis for the scanner system's design. A series of interviews were conducted with key personnel from SGRE in order to establish requirements and expectations for a blade scanner system, which would make it practically applicable for geometry inspections in the production. While the details of the interviews, and most of the corresponding specific requirements, cannot be published, due to confidentiality, the overall observations can.

As indicated in Contribution I, the requirements are concerned with how easy it is to apply the scanner system in the current production setup, and with how precisely and quickly the system can measure a blade. The requirements are summarized in Table 3.1. The table does not state the obvious, which is that the system must be capable of autonomously scanning a blade.

The sensitivity is defined here as the system's ability to measure defects with both a small spatial extent, that is local smoothness, and a large spatial extent, *i.e.* shape as per the geometric design model. The requirement states, that the resolution of the scanner must be high enough to resolve small scale defects and that the measuring uncertainty should be low enough not to mask out the imperfections. This requirement is treated explicitly in Section 3.2.

The point of replacing manual inspection processes with automated ones is to save money. In our case, the saving is expected to come from a better product

quality due to a higher potential for statistical quality control based on the quantitative measurements returned by the scanner system and from a reduction of person-hours. As described in Chapter 1, a better surface quality will result in less rework, fewer warranty cases with broken or under-performing blades, and generally better performing wind turbines. However, the immediate cost saving comes from the reduction of working hours. SGRE would like to see a saving very soon after they implement the scanner system, and therefore it is essential that the inspection cycle time, that is the time it takes to measure an entire leading edge, is lower than the time needed for the manual inspection. While we can not state the manual inspection time, it can be said that our interviews indicated a maximum inspection time on the order of a couple of hours. Note that the current inspection takes a good deal longer than that. If the system's inspection time is on par with the manual inspection time, the immediate cost saving will only be that of salary. If, however, the inspection time is further reduced, the subsequent processes can get started faster, potentially resulting in a reduced takt-time for the entire blade. For the same reason, it is vital that there is a balance between component and maintenance cost, and the money saved on salary and the earnings gained from reduced takt-time. As indicated above, having a detailed 3D representation of the leading edge from all manufactured blades can potentially enable implementations of various Industry 4.0 technologies, which might increase the cost savings and earnings even more, but this is pure speculation as no hard evidence is available.

The manufacturer would like their production setup to be as agile and flexible as possible, and therefore they are very reluctant to make permanent changes to the general layout of the production facilities. The demand for a specific blade type varies rather significantly, and they need to be able to switch their production accordingly quickly. As a consequence, permanent, or semi-permanent, installations, such as rails on the floor, should be avoided as much as possible. This has implications for the design choices made in Section 3.2 and 3.3.

Last, but not least, the scanner system must be safe for the operator and any bystander. As stated above, this is not just a manufacturer requirement but is demanded by Danish and European legislation (BEK nr 693 af 10/06/2013, 2013; Directive 2006/42/EC, 2006). Therefore, if we want to test the scanner system on real blades (we do), we have to comply with the national safety requirements for machinery. This requirement is treated explicitly in Section 3.4.

On a side note, through the aforementioned interviews, it was found that the optimal position for geometric inspection, in the production chain, is right after final assembly when the blade is practically ready to be shipped to the customer. The choice of inspection location has implications for how the blade is mounted during scanning, and in which areas of the factory the blade is located. All further descriptions about the production environment and blade mounting are

thus valid for the final steps of the production chain only.

3.2 The Measurement System

The measurement system is composed of an SL based 3D scanner and a six DoF positioning system. The positioning system is used to locate and orientate the point clouds, returned by the scanner, in a global reference frame. Thus, the registration, or stitching, is done directly by the tracker system.

A purposely developed scanner could have been used, but it was important for the industrial partner, SGRE, to use a commercial product. By using a commercial scanner, it is easier to scale the developed blade scanner system and maintain it. Therefore, a benchmark of the scanner market was done to find the most well-suited scanner and supplier. The same was true for the positioning system.

3.2.1 The 3D Scanner

A rather comprehensive market benchmark was carried out, which included 12 different suppliers and 14 different scanners. A requirement specification based on the blade manufacturer requirements was sent to each of the scanner suppliers. Then they returned with their take on the problem and provided a solution.

The proposed scanners had different projection strategies, including some based on a single laser line (SLL), multiple laser lines (MLL), single binary pattern (SBP), binary temporal coded patterns (BTCP), such as gray coding or unstructured light, and some based on phase temporal coding patterns (PTCP), i.e. projection of sinusoidal patterns. Table 3.2 gives an overview of the proposed scanners. Note that the information contained in the table was valid as of December 20, 2015, but likely has changed since. As an example, AICON has since been acquired by Hexagon.
In the table, point spacing, scan area, focus distance, and focus depth are given in millimeters. Some of the SLL scanners move the laser line spatially to cover an area. In that case, the size of the covered area is documented under "Scan area". For the SLL scanners that do not move the line, only the length of the line is given and thus not an area. As all the scanners are camera based, the point-to-point distance depends on the resolution of the camera, but also the focal length and range to the surface. The scan time is given in seconds. The

wavelength is given in color or nanometers (depending on what information was available from the supplier). The weight is given in kilograms. Most of the suppliers were able to change individual settings of the scanners, such as focus distance, but the values documented here are the supplier's suggestions. All information contained in the table has been acquired through email correspondences or phone calls with the suppliers. If a supplier either could not or would not share a particular value, it is labeled as not available (NA) in the table. It would have been beneficial also to know the scanners measuring uncertainty, but most suppliers do not give this information, partly because no accepted standard procedure exists. For the same reason, the uncertainty stated by two different suppliers cannot be compared directly, as they possibly have used different methods.

Some of the scanners have unique traits that are difficult to document in a table. As an example, the Surphaser SLL scanner can rotate 360° horizontally and 180° vertically which enables it to scan its entire nearby surroundings, such as a room, from one position. These features were taken into account when the optimal scanner was selected.

Based on the specifications, and the companies' apparent commitment to the project, AICON, Artec, Creaform, API, GOM, and ZEISS were chosen for testing. The suppliers were invited to either do a live demonstration and test at the blade production site or to receive a surface sample for them to scan. Artec, Creaform, API, and GOM received samples and a measurement plan. ZEISS decided to come to the production site.

Four flat surface samples, each with a base paint, LEP, artificially created defects, and exposed fiberglass composites, were created, one for each supplier. Figure 3.2 shows an example of a sample. The suppliers were asked to measure the sample from at least three different angles, with the same distance, as illustrated in Figure 3.3. By having sample measurements from the same angles and distances, it should be possible to benchmark the scanners against each other directly from their measurements. ZEISS brought their laser line scanner to the production site, where they conducted analyses directly on a real blade.

The ZEISS T-SCAN had to be moved smoothly over the surface to cover an area with the desired resolution. At the blade production site, heavy machinery such as cranes and trucks induce low-frequency vibrations in the floor when operated. These vibrations propagate to the relatively flexible blades and put them into low amplitude oscillations. In the T-SCAN's measured point clouds, the oscillations were visible as waves in the surface due to its relatively long scan time. This kind of waves can also be present as naturally occurring surface features, and therefore they are difficult to filter away without masking actual defects. The ZEISS Comet performed well during tests, but ZEISS did not rec-

Table 3.2: Overview of scanner specifications

Supplier	Name	Type	Point spacing [mm]	Scan area [mm^2]	Focus distance [mm]	Focus depth [mm]	Scan time [mm]	Wavelength [nm]	Weight [kg]
AICON	SmartScan	BTCP	0.111	320× 320	800	NA	6.0	Blue	4
API	RapidScan	BTCP	0.150	300× 300	350	100	6.0	IR	3.5
Artec	Space Spider	SBP	0.200	180× 140	500	100	0.1	Blue	1
Creaform	Metrascan 3D	MLL	0.100	210× 210	300	200	NA	Red	2.75
FARO	Cobalt	BTCP	0.244	375× 220	500	NA	1.0	Blue	17
GOM	ATOS Triple Scan	BTCP	0.111	535× 400	800	320	2.0	Blue	13
GOM	Core	BTCP	0.120	300× 230	440	NA	2.0	Blue	2.9
Hexagon	T-SCAN	SLL	0.075	125	150	100	6.25 [m/s]	658	1
NextEngin	3D Scanner	MLL	0.200	130× 95	NA	NA	120	650	3
ShapeGrat	Scanhead	SLL	0.200	300× 300	500	100	15	670	7.5
Surphaser	400HP	SLL	0.189	1360× 1360	1000	110000	270.0	1550	11
ZEISS	Comet	BTCP	0.100	382× 254	800	200	1.2	658	NA
ZEISS	T-SCAN	SLL	0.075	125	150	100	6.25 [m/s]	658	1
3dDigital	Optix 400	MLL	0.065	250× 200	375	100	NA	450	3

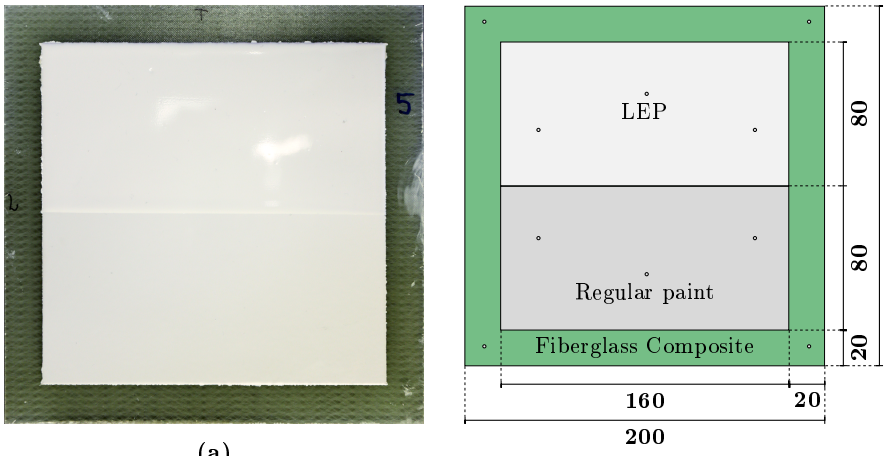

Figure 3.2: The flat surface sample which was send to potential scanner suppliers for testing. (a) shows a photograph and (b) shows an annotated drawing. All values are in mm. The dots seen in (b) indicate positions where small, discrete imperfections were introduced.

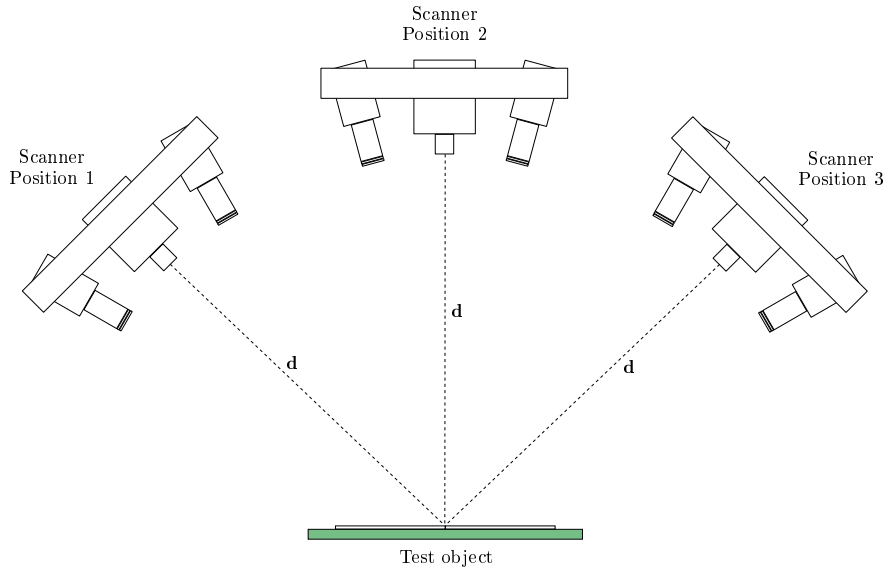

Figure 3.3: Schematic indicating three different scan positions at the same distance from the sample

Figure 3.4: Photograph of the RapidScan 3D scanner (to the right) and the vProbe active target (to the left), sitting inside a padded protective cage. The combined weight is 8 kg.

ommend this scanner for the task, due to its sensitivity to ambient light. Of the other suppliers, only API followed the supplied measurement plan, which made it impossible to compare the returned measurements directly. The scanners from Artec and Creaform returned point clouds with good resolution and accuracy. Both scanners were initially designed for hand-held operation, which means that they have to be swept continuously across the surface to attain their specified resolution. Both AICON's and API's scanners performed well, but it turned out that AICON's scanner could not be controlled programmatically. API based their scanner on infrared (IR) light, which meant that they could scan with high accuracy in normal ambient visible light. This ability is an important feature, as the production site has ambient lighting at 600 lux at the floor level.

Finally, API's RapidScan was chosen. It's performance, robustness against ambient light, and relatively low cost, as well as an extraordinary high commitment from their engineering team, made the difference. It is shown in Figure 3.4.

3.2.2 The Positioning System

Multiple technologies were considered for tracking the scanner's position. Common for all of them were that they could deliver positions with six DoF, thus providing both position and orientation. Nikon's indoor global positioning system (iGPS) is a laser-based system, were a set of laser light transmitters, or satellites, are placed around the measuring volume, and a receiver is situated at

the scanner. While this system has proved its worth, and accuracy, in many industrial applications, it was just too costly under the budget given for the blade scanner. Further, the laser emitters would have to be put up, and their positions re-calibrated, before every inspection session to avoid making permanent changes to the production facilities. A similar system, but one which relied on radio and audio signals, from GamesOnTrack was also considered. It required that small audio emitters were put up. The system had a positioning uncertainty of 10 mm, which was deemed way too large. Ideally, we would like an uncertainty which is on par with the measurement uncertainty of the scanner, or smaller. As we initially did not know the actual scanner's uncertainty, we assumed it to be equal to the point-to-point distance which was reported to be 150 μm by API. Inertial measurement units (IMU) were also considered, but it was deemed that their positioning uncertainty would increase above a tolerable level too quickly.

In the end, we settled on a laser tracker solution, coupled with an active target. This combination provides the laser tracker's low positioning uncertainty, combined with a small orientation uncertainty produced by the active target. A laser tracker measures the distance to a mirror, which reflects its laser light, based either on interferometry or temporal phase coding. A feedback controller keeps the tracker aimed at the mirror, by maximizing the irradiance of the reflected light, through continuous adjustments of two rotational actuators, which are coupled to the laser source. A passive target is just the mirror, while an active target contains electronics, and possible mechanics, which allows its orientation to be measured. This solution can quickly be calibrated before a blade scanning session. It only needs a line of sight in one, narrow direction, which is the direction from the tracker to the target.

Two laser tracker suppliers were considered, namely API and Hexagon. Both suppliers did trial tests, with their tracker systems, at the production site. While both presented powerful measurement systems, API was selected in the end. For our application, the positioning uncertainty of the two pieces of equipment was on par, but API's OmniTrack II laser tracker and vProbe active target had a more extended range of 80 meters, and they were less expensive. The combined OmniTrack and vProbe system has a positioning uncertainty of 75 μm, when measuring under 7 meters from the tracker, 115 μm when measuring between 7 and 15 meters from the tracker, and 40 μm + 5 μm/m at longer ranges. One-third of a blade's length is to be scanned, which means that the uncertainty is on par with the RapidScan's expected measuring uncertainty, even for the longest blades. The vProbe can be seen in Figure 3.4.

The laser tracker is placed close to the blade tip, where it has an unobstructed view under the leading edge towards the blade scanner. The vProbe is mounted close to the scanner, and the transformation between them, labeled $\mathbf{T}^{\mathrm{SA}}$ in

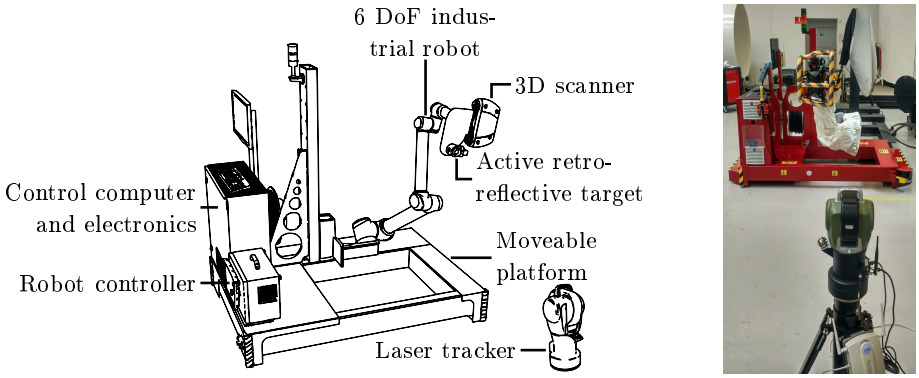

Figure 3.5: Illustration of the blade scanner system. A drawing of the system, with annotations, is shown in (a). This drawing is from Contribution F, where it is adapted from Contribution I and J. The system is seen, together with the laser tracker, and a blade tip in (b).

Contribution F, is computed by Hand-Eye calibration, using the same procedure as described in Contribution D.

3.3 The Locomotion System

Figure 3.5 shows the blade scanner system. In addition to the measurement system, it is composed of six axis industrial robot arm, a drive, or moveable, robotic platform, and a control system.

The design evolved through an iterative process conducted in close cooperation with FORCE Technology. One of the early drawings is shown in Figure 3.6. It had, besides an early version of the innovative drive platform, two telescopic axes and a rotational axis for positioning the scanner. It thus only had three DoF, disregarding the platform. During the design process, we found that a robot arm provided enhanced flexibility, and in the end would make it easier to position the scanner correctly. As a result, the general design is inspired by the one presented by Petryna et al. (2014), but with the robotic drive platform as the major novel invention.

The control system is also radically different. Petryna et al. (2014) measured a small 12-meter long blade in a fixed position and therefore the elastic deformations were not an issue for the measurement process. Their acquisition

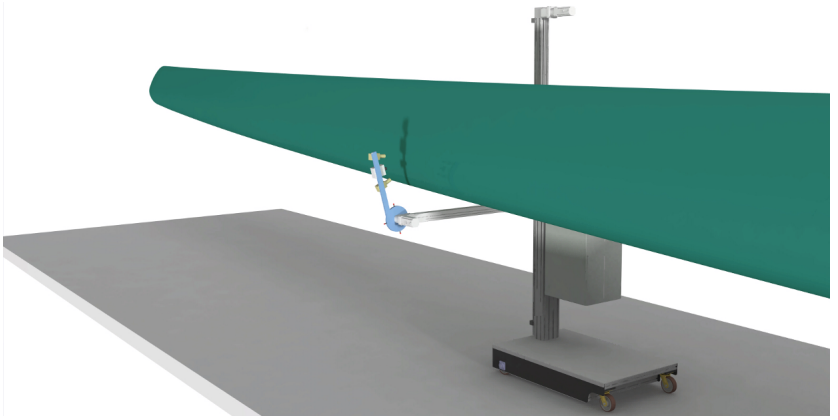

Figure 3.6: Rendering of an early version of the blade scanner system design. The six axis industrial robot is yet to be introduced. Instead, the scanner was, in this design, moved by two telescopic axis and a rotational axis, which in turn was moved by the platform.

trajectory could be hard-coded. Our blade scanner is autonomous and designed for measuring large blades of various sizes. Though the general orientation of the blades is similar between measuring sessions, tolerances in their position can cause a rather large elastic deformation. Therefore, the scanner adapts to the blade geometry, by feeding the blade scans back into the controller. The control algorithm is Contribution F. As noted in the introduction to this chapter, the design is patent pending at the European Patent Office. The application is Contribution G.

The drive platform was constructed from steel beams by FORCE Technology. It is designed as a frame, with a rectangular hole in the middle, to allow for the robot's "elbow" to sweep closely over the floor. The combined weight is just above 600 kg. Its weight and wide footprint make it a stable, and any vibrations, *e.g.* induced by robot movements, are quickly dampened. It is equipped with two drive wheels in the front, driven by FESTO EMMS-ST stepper motors. The motors are controlled through FESTO CMMS-ST-C8-7-G2 motors controllers, and they are communicated with through a FESTO CPX-CEC-C1-V3 Codesys controller. The Codesys controller is connected to the motor controllers through a controller area network (CAN) bus, and to the control PC via a local area network (LAN). Two follow wheels sit at the back of the drive platform.

The RapidScan-vProbe assembly, as seen in Figure 3.4, weighs about 8 kg. This low weight allowed us to choose the UR10 industrial robot from Universal Robots, as it has a lift capacity of 10 kg. It can be made collaborative (ISO/TS

15066:2016, 2016), which means that it does not have to be in a safety cage. We further elaborate on the safety aspect in Section 3.4. The UR10 was selected due to its adequate performance, relatively easy, and well-documented control interface, and low cost. It communicates with the control PC through LAN. While the intended robot trajectory is relatively simple, it spans a large portion of the robot's work envelope and requires movement of all robot joints. The UR10 has a cylindrical volume, extending above and below its base, where most of its kinematic singularities lurk. We mounted the robot with a 45° tilt, relative to the platform, which pointed the singularity regions away from its intended working region. The robot mount is fastened to a steel plate, which is bolted onto a tower. The plate can be moved up and down, which allows the robot's base height to be adjusted manually. It is prepared for installing a FESTO spindle axis, which could automatically change the height. Such an axis is needed if larger blade types are to be scanned in the future.

3.4 The Safety System

When an operator mans the blade scanner, (s)he will typically stand behind the computer monitor and will be able to walk freely in front of the machine. As stated above, the machine weights more than 600 kg, and it has a gearing factor of 300 between the drive motors and the wheels. If the operator, or any bystander, is unlucky and trips in front of the machine, a situation can arise where the machine crushes the person. The machine's safety system ensures that such a situation, or similar dangerous situations, cannot occur.

The design of the safety system follows DS/EN ISO 12100:2011 (2011) and associated standards. It is centered on a Pluto A20 programmable safety controller from ABB. All the safety-related sensors feed into the Pluto controller, which can emergency stop the FESTO motor controllers and the UR10 robot controller. The main emergency stop button is located on the UR10's teach pendant, which sits at the right-hand side of the operator. The emergency stop function follows DS/EN ISO 13850:2015 (2015). All connections between safety components are duplicated. If an emergency stop occurs, the machine has to be reset, using a Smile 11 RB reset button from ABB, which is placed at the rear end of the machine.

Figure 3.7a shows an RSL410 safety laser scanner from Leuze, which sits at the far front corner of the blade scanner, and stops the system if any obstacle, human or not, comes too close. It covers 270°, which corresponds to the machine's front and the side of the machine which is on the far side of the blade, relative to the operator. Thus, it covers both the machines drive direction, and the

(a) (b)

Figure 3.7: Photographs of the safety laser scanner (a) and safety handle to circumvent the scanner (b).

part which is outside the operator's visible area when standing at the control computer. The blade scanner is not designed to drive backward, which is why a safety scanner is not needed on its rear end. Figure 3.7b shows an ABB JSHD4 safety handle, mounted on the front of the machine, which can be used by the operator to "mute" the safety scanner. By holding its button in a fixed position, the safety scanner is circumvented, and the operator can step directly in front of the machine and inspect either the blade or the scanner system. If the button is released, and the safety scanner was activated, the machine goes directly into an emergency stop. The handle has two accompanying ABB MKey switches, which are visible at the bottom of Figure 3.7b. With the switches, the Pluto safety controller can detect if somebody removes the handle from its parking position.

The UR10 is certified to be a collaborative robot following ISO/TS 15066:2016 (2016), if its tool, combined with its acceleration and speed, is not considered dangerous. Its controller knows the weight of its tool based on which it can compute the expected torque on each of the motors in the arm, throughout its motion. Using sensors, it can sense and determine if the measured torques do not match the expected torque, in which case it goes into a safeguard stop. As seen on Figure 3.8, the tool, which is the RapidScan and vProbe, was put into a padded safety cage. In addition, the acceleration and velocity are relatively low, in order to protect the measurement equipment. Therefore, it is argued that the robot can safely be operated in a collaborative mode.

Figure 3.8: Photograph of the blade scanner which shows the safety cage put around the RapidScan and vProbe.

Figure 3.9: Photograph of one of the safety guides, which are attached to the side of the machine.

A safety guide, or bumper, is attached to both sides of the machine, which prevents the operator, or bystanders, from getting their feet crushed under the machine. The dimension of the guide follows DS/EN ISO 13857:2008 (2008). Figure 3.9 shows one of the guides.

An electrical schematic of the safety system is shown in Figure 3.10. The names of the components are defined in the text above, with the exception of the BT51, which is an ABB BT51 safety relay. It is used to duplicate the number of output emergency signals from the Pluto safety controller and to the motor controllers. When the system is in normal condition, all emergency stop signals will be in high (on) mode. If an emergency stop occurs, the signals drop to a low (off) mode. The transition from high to low ensures that the emergency stop is automatically activated in case of electrical failure where a signal is lost.

In addition to the already mentioned components, the blade scanner also has an indication light-audio tower. It is placed on top of the robot tower and is used to signal the state of the machine. A green light indicates that power is on, constant yellow indicates that the drive platform is engaged and ready to drive, and flashing yellow indicates that the platform is driving. Flashing red light indicates that something sits within the warning zone of the safety scanner, and constant red indicates that the machine is emergency-stopped. A pulsating

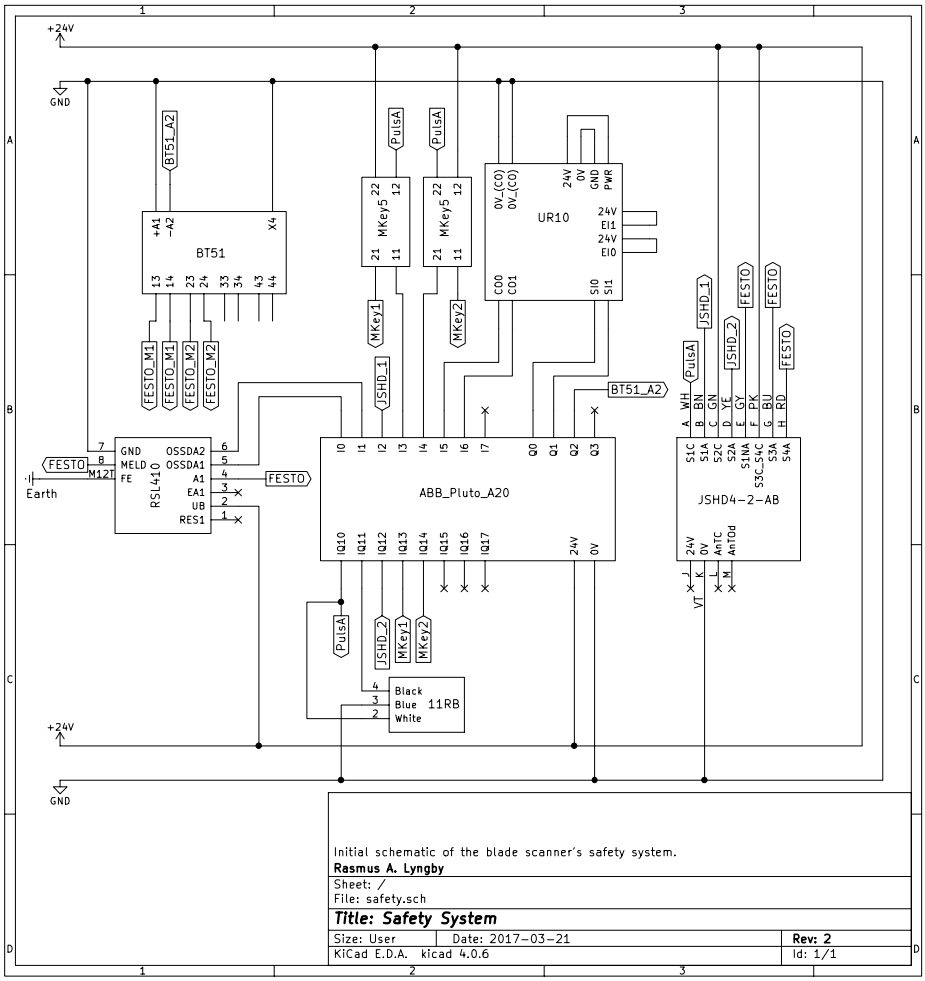

Figure 3.10: Electrical schematic of the blade scanner's safety system. All components are described in the text.

audio signal accompanies the flashing red light to warn both the operator and the obstacle, that an emergency stop is about to happen. The electrical wiring and software control of the indication tower is completely decoupled from the safety system. The control computer operates it via the FESTO Codesys controller.

3.5 The Control System

The control system is running on a computer, which is connected to the different components via LAN. The system is implemented in the Python programming language, version 2.7. Python might seem like a strange language to implement such a control system, but it has several benefits. It has a good selection of modules, which includes `numpy` for numerical computations, `urx` for controlling robots from Universal Robots, `OpenOPC` for controlling the FESTO Codesys controller, and `socket` for creating and connecting to sockets, which can be used for LAN communication. In addition, it is relatively easy to get going fast in Python, as much of the trivial boiler-plate code, which is often needed in compiled languages such as C++, can be avoided. As often said, there is no such thing as a free lunch, and the price we pay for Python's compatibility and simplicity is execution speed. Python is an interpreted language, which makes it slower to execute than compiled languages. However, it supports the execution of compiled code through Python extensions. Most of the high-level functionality can thus be implemented in Python, and computational bottlenecks can be implemented in C or C++, compiled, and instantiated from Python when needed.

Qt is a cross-platform application framework, in which graphical user-interfaces and multithreaded applications, among others, can be made. Bindings for Python are available (Summerfield, 2008), and Qt was selected for handling multithreading, and potentially, as future work, a graphical user interface. Qt instantiates an independent thread per hardware component. Figure 3.11 presents an overview of the threads and their mutual communication paths.

Communication problems related to incompatibility between the USB controller in the control computer and the USB driver for the RapidScan meant that a standalone program, running on a different and compatible computer, was needed in order to interface with the scanner. Due to the nature of the RapidScan and OmniTrack application programming interfaces, it was chosen to make the standalone program in C++. The program interfaces with the RapidScan via USB, and with the OmniTrack via LAN over WiFi. The OmniTrack, in turn, communicates with the vProbe via an in-built WiFi connection. A wired LAN network is used to communicate between the central control computer and the

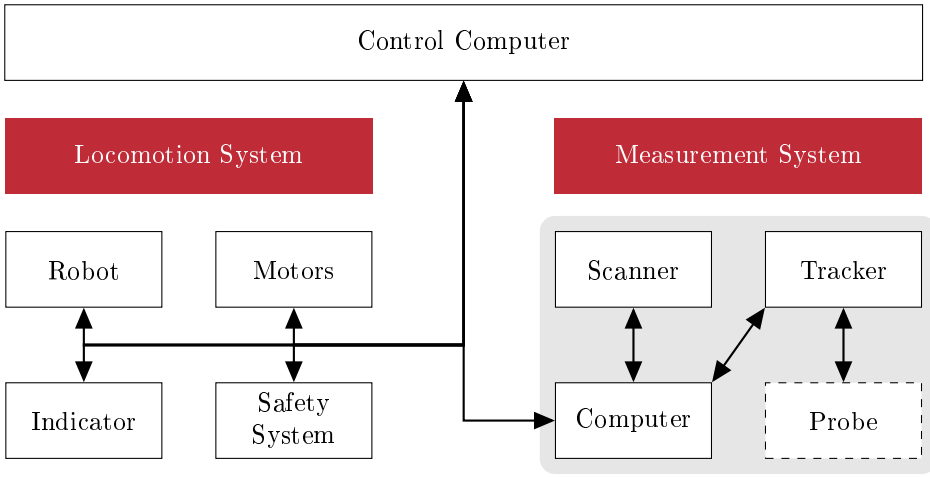

Figure 3.11: Overview of the control system. The white, non-dashed blocks indicate independent processes running on the control computer, each of which corresponds to an underlying physical resource. The blocks inside the gray enclosure runs on a separate computer, which communicates with the main control computer through LAN. The vProbe, labeled probe, does not have its own process, as it communicates directly with the laser tracker, which in turn delivers six DoF positions to the seperate measurement system computer.

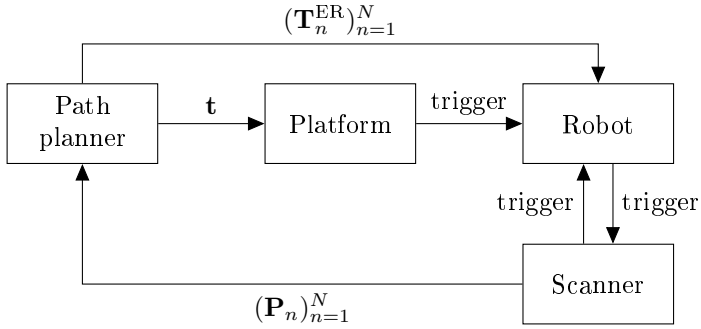

Figure 3.12: Flowchart showing the feedback control loop. $\mathbf{T}_n^{\mathrm{ER}}$ are transformations from the robot's base to its tool, i.e. robot poses, and $\mathbf{P}_n$ are point clouds acquired by the 3D scanner. "Trigger" signifies that a trigger signal is send once a process finishes. The *Path planner* "lives" inside the control computer. Platform is here synonymous with the drive motors, coupled with a function which converts the relative position in $\mathbf{t}$ to motor rotations. The figure is from Contribution F, in which it is adapted from Contribution J.

standalone computer. A simple TCP/IP based protocol, based on sockets, was developed for this communication, with which commands are sent from the control computer and raw data returned from the standalone computer.

The blade scanner works autonomously. A feedback loop takes in just measured geometry to plan the blade scanner's next movement. The loop is illustrated in Figure 3.12. Contribution F describes the control algorithm in detail. When a given blade is to be scanned, a forklift is used to move the scanner system from storage to the blade. Thus, the blade is usually measured *in situ*. With the forklift, the scanner system is placed under the blade where the measurements should start, and roughly aligned with the leading edge. A rough estimate of the distance between the floor and the leading edge, at the start position, is typed into the control system, which then initiates a robot movement to get an initial scan of the leading edge. If successful, the robot's initial acquisition trajectory is built up by iteratively placing the scanner at the edge of the just acquired geometry, making new scans at every edge. The process stops once enough of the geometry has been captured to make a curve with full arc-length, as specified by the operator, and then the primary scanning process is started, as described in Contribution F. The scan sequence stops once the tip of the blade has been reached, which is detected as a steep drop in the number of points acquired per curve.

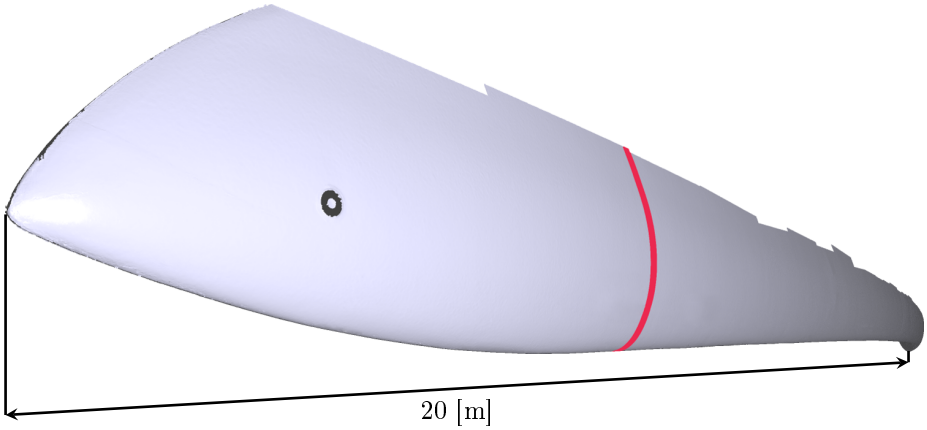

Figure 3.13: Rendering of all the point clouds from a leading edge scan of one blade. The surface has not been reconstructed so the rendering is made purely from individual vertices. A profile curve is marked in red for enhancing the 3D perception of the figure. The figure is from Contribution J.

3.6 Example of defect detection

So far, the blade scanner system has been used to create a dataset consisting of the outermost 20 meters of the leading edge from 23 individual 55 meter long blades. One of the blades was scanned twice, one was scanned three times, and one was scanned four times. The four repetitions are used to evaluate the measurement uncertainty in Contribution J, as described in Chapter 4. Each of the blade scans contains just above 500 individual point clouds, which adds up to more than 380 000 000 individual points in total. The clouds and their position in the global coordinate frame defined by the OmniTrack are saved in a binary format and take up 4.5 GB on the hard drive per blade. Figure 3.13 shows a rendering of the point clouds from one of the scan repetitions of the blade which was scanned four times. The tip part of another scan is shown up-close in Figure 3.14. As seen, the transition between the base paint and the LEP is clearly noticeable. From a simple visual judgment, the lightning connector is also captured with rather good detail.

In addition to the blade dataset, another dataset with 26 repeated scans of a four-meter-long blade tip was also made. Both datasets are proprietary, owned by SGRE, and can not be published, as the blade geometry is considered a trade secret. The datasets were used for optimizing the robustness of the scanner system and its control algorithm, and for evaluating its performance. When

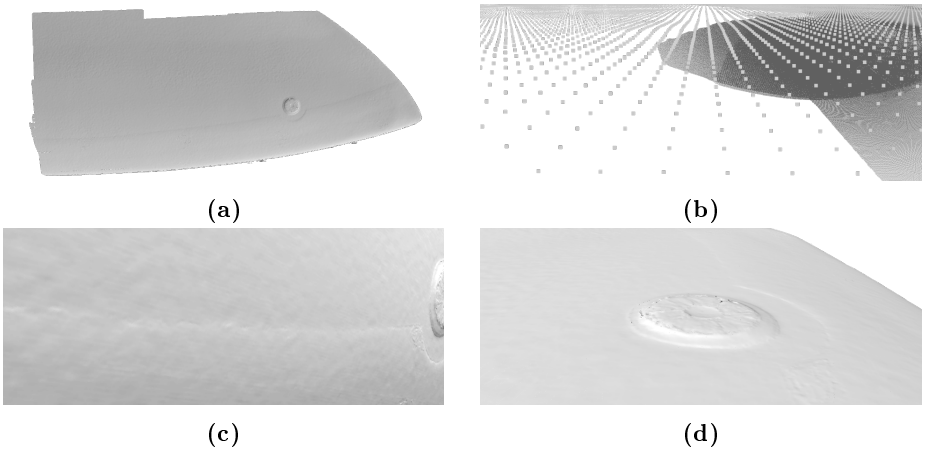

Figure 3.14: Up-close renderings of the tip from one scan sequence. The tip, scanned in two curve passes, is shown in (a). It has a length of approximately 0.5 m. A closeup of the point cloud is shown in (b). The point-to-point distance is around 200 μm. The transition between the base paint layer and the LEP is shown in (c). The lightning connector is shown in (d).

starting a blade scan from scratch, the setup and measuring system validation time is 20 minutes. The leading edge scan sequence takes, on average, just short of 1.5 hours.

Contribution H investigates the potential of detecting defects from the blade scans. It presents two proof-of-concept methods, one which concerns local smoothness and one which concerns shape deviations. The first method measured the size of the transition between the base paint and the LEP. The second method aligns 0.5 meters of measured leading edge point clouds, acquired with the blade scanner, to the blade's digital design model, and computes the deviation between the two.

Chapter 4

Estimating the Measuring Precision

When talking of measuring precision in this thesis, we are thinking of it in a geometrical metrological sense. Usually, *accuracy* is defined as how well the mean of a set of repeated measurements approaches the "true" value of the measurand, and *precision* is defined as the standard deviation of the measurements. Note that it does not make sense, as such, to talk about the true, or real, value of a measurand. The "true" value can never be obtained and therefore does not exist, other than in a philosophical sense. There exist only estimates. The uncertainty of the estimation, that is how well it approximates this philosophical "true" value, is obtained through a statistical analysis of repeated measurements of the workpiece. Different measurement techniques generally can achieve different levels of uncertainty. A length measurement obtained with a caliper, for example, will, usually, have a bigger uncertainty than a length measurement made with a CMM. The measurand's material properties also influence the uncertainty. If we would like to measure the length of a bath sponge, we would have to be careful about the amount of force that our measurement equipment exerts on the sponge, as even a small force can deform the material. Materials also change with temperature and the general conditions of the environment, such as humidity. This change happens for both the measurand's material, but also for the material of the measurement equipment itself. Thus, when reporting such a measurement, it is essential also to document the conditions under which the analysis was acquired. Failing to do so makes the measurement invalid because

it would be impossible to redo the measurement for validation purposes.

Accurately documenting the measuring conditions can seem overwhelming at first, but luckily there exists the guide to the expression of uncertainty in measurement (GUM) (ISO/IEC Guide 98-3:2008, 2008). This guide describes the general method for estimating measurement uncertainty, including influencing conditions. The general idea is that the uncertainty of any geometrical measurement must be traceable, through a chain of calibrations, back to the definition of the meter unit, as defined in the International System of Units (SI). SI defines the meter as "*... the length of the path traveled by light in vacuum during a time interval of 1/299 792 458 of a second.*" (Giacomo, 1984). It is realized through a laser system (Quinn, 2003), and this is where the calibration chain starts. A good introduction to the approach, and other techniques employed in geometrical metrology, is found in the book by De Chiffre et al. (2015). The information contained in this chapter is generally based on the methodologies described in that book and the relevant ISO standards.

Measuring something is regarded as sampling from a random variable. Usually, the outcomes of the random variable are assumed to follow a normal distribution, with a given mean μ, and a standard deviation σ. The GUM defines uncertainty of measurement as the standard deviation, multiplied with a coverage factor, k. The coverage factor is added to ensure that enough of the possible outcomes are contained within the uncertainty region. The actual standard deviation is called the standard uncertainty, and the result after applying the coverage factor is called the expanded uncertainty. Many industrial applications use a coverage factor of $k = 2$, which ensures that 95.45% of the possible outcomes are contained within $\mu \pm \sigma k$. In more demanding applications, such as astronomy and experimental physics in general, a coverage factor of $k = 6$ is often used, which contains more than 99.9999998% of the possible outcomes. The coverage factor is usually decided by whoever defined the need to measure. In an industrial setting, measurements are used to check if a given component is within the tolerance zone defined by its designer. The designer will in this scenario usually also have specified the coverage factor, which is multiplied onto the standard uncertainty of the measurement equipment. In doing so, (s)he defines with what level of confidence conformance to the tolerance zone must be guaranteed.

Estimation of measurement uncertainty, following the GUM, usually involves doing an uncertainty budget. Here, all the uncertainty contributions coming from all the influencing factors are listed and added together to yield the final standard uncertainty. We assume that the random variables associated with the contributing factors are independent. Had that not been the case, the correlation between the variables would have to be taken into account when added together. If a variable does not follow a normal distribution, the variable's variance is multiplied by a correcting factor b. The factor is chosen such that the

distributions integral from $\mu - b\sigma^2$ to $\mu + b\sigma^2$ is equal to the integral of a normal distribution from $\mu - \sigma^2$ to $\mu + \sigma^2$, which is roughly equal to 68% of the distributions total area. As an example, a correction factor is used when measurement uncertainties which are taken from a data-sheet, which, per definition, are always assumed to be uniformly distributed. This kind of uncertainty contributor is called a *Type B* contributor. A *Type A* contributor is a random variable that is estimated from data. Two independent, normally distributed random variables can be added together by summing their variances. Thus, the resulting standard deviation from combining a contributor, with standard uncertainty σ_1, with another contributor, with uncertainty σ_2, is $\sigma_{\text{combined}} = \sqrt{\sigma_1^2 + \sigma_2^2}$ when the variables are independent. The details and definitions can be found in the GUM.

4.1 Estimating Uncertainty Through VDI/VDE guide 2634

There are different approaches to estimating the measurement uncertainty of a measuring device. Contribution I uses a light-weight approach to study the measurement uncertainty of the blade scanner. It follows the procedure from the VDI/VDE guide 2634 (VDI/VDE 2634 Part 2, 2012) to estimate the RapidScan's measurement uncertainty. The method uses a calibrated ball bar reference standard and a calibrated flat plane reference standard, as shown in Figure 4.1. We measured the two reference standards with the scanner, in different positions, and used the point clouds for estimating the measurement uncertainty. The result defines two uncertainties from the sphere, and one from the flat plane. From the study, it was evident that a larger measurement uncertainty is to be expected from curved surfaces than from flat surfaces. Though the GUM dictates the use of standard deviations to indicate uncertainty, VDI/VDE calls for the maximum values to be used. Using the maximum value, we observed an uncertainty in the range from 0.98 mm to 1.4 mm for the sphere surface measurements, 0.68 mm for length measurements, and 0.23 mm for flat surface measurements.

The procedure is relatively easy to carry out, and it gives a ball-park estimate of the uncertainty. It does, however, not consider the contributions from the material, which makes up the blade surface, or the contributions from workpiece deformations due to effects from the environment. Nor does it consider contributions from the positioning uncertainty of the laser tracker when registering overlapping point clouds.

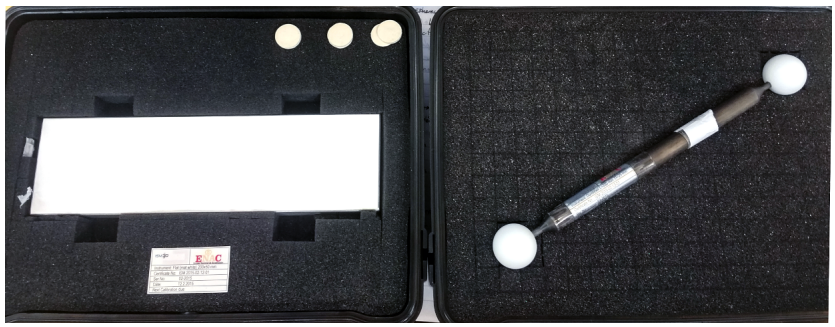

Figure 4.1: Photograph of the calibrated ball bar reference standard to the right, and the calibrated flatness reference standard to the left.

4.2 Estimating Uncertainty Through the Modular Freeform Gauge approach

Contribution J conducts a much more thorough study of the blade scanner's measurement uncertainty, including the uncertainty of the leading edge measurements. Note that there is a distinction between the two. The approach that we followed allows one to estimate the uncertainty of the scanner system when it is used to measure blade surfaces, isolated from the uncertainty contributions of the blade's elastic deformations. The deformations should, of course, be taken into account when the system is used to measure real blades. Therefore, the approach includes contributions from the blade deformations into the scanner system's measurement uncertainty.

A calibrated modular freeform gauge, which had a shape similar to the leading edge, was used to calibrate a CMM. Then, a section was cut out of a blade, as shown in Figure 4.2, and calibrated with the same CMM. The blade scanner system measured the then calibrated blade section. Finally, a real blade was measured by the scanner system. Each step in the process is equivalent to a link in the traceability chain, all the way back to the definition of the meter. The chain is illustrated in Figure 4.3.

The study provided a novel application of the Modular Freeform Gauge MFG method for establishing freeform measurement uncertainty for large components, such as blades. From the study, the blade scanner was found to have an expanded measurement uncertainty of 663.5 μm (k=2). This is fairly good when considering that the measured part of the object is 20 meters long and flexible.

The final expanded measurement uncertainty can be seen as two times the stan-

Figure 4.2: Photograph of a blade section, which includes the leading edge, being cut out from a blade.

dard deviation of a 3D spherical normal distribution assigned to the location of each point in the acquired point clouds. Thus, it directly says something about the smallest geometrical features which can be measured on the surface of the blade. However, the results of the flatness measurements in Contribution I indicates, that the distribution might be smaller in the direction along the scanners viewing direction. With a maximum deviation of 230 μm for planar measurements, the scanner should be able to resolve relatively small features, such as the LEP transition, when considered a single, isolated point cloud. This transition is also visible in the point clouds seen in Figure 3.14c. Because of that, we speculate that a significant portion of the measurement uncertainty is contributed to uncertainties in the positioning of the scanner, coming from the laser tracker system. This observation seems to be supported by the results obtained in Contribution H. In the future, it would, therefore, be interesting to study how the estimated measurement uncertainty changes if post-acquisition optimization of the registration between overlapping point clouds is introduced.

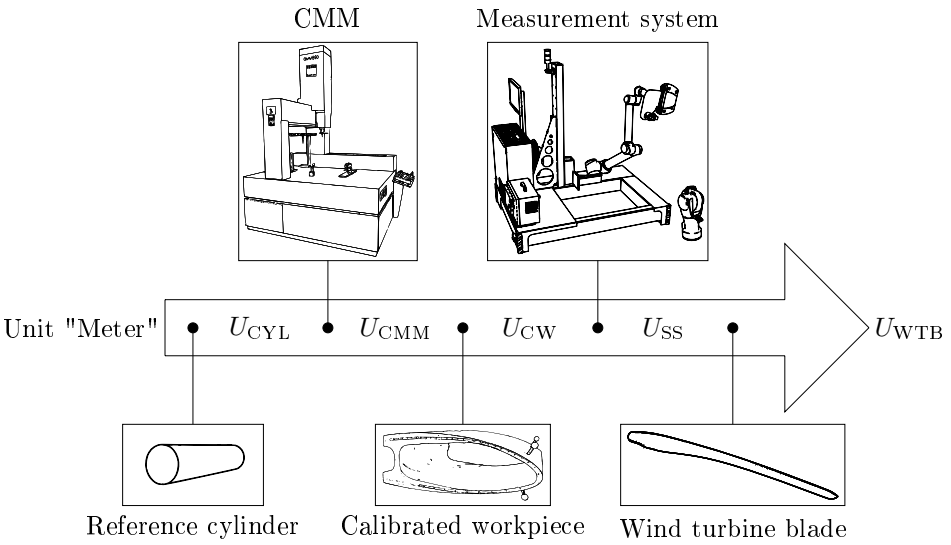

Figure 4.3: Schematic of the traceability chain established in Contribution J. U_{CYL} is the uncertainty of the MFG, U_{CMM} is the uncertainty of the CMM, U_{CW} is the uncertainty of the blade section, or workpiece, U_{SS} is the uncertainty of the scanner system, and U_{WTB} is the uncertainty of the wind turbine blade measurements. Figure from Contribution J.

This thesis developed and studied an approach for automating the geometry inspection process for wind turbine blades. Defects in the outer geometry of a blade, such as a deviating shape or small irregularity on the surface, can cause the turbine's power output to be lower than nominal and lead to blade failure during operation. Some defects are so severe that the blade has to be taken down for refurbishment, or replacement, which can quickly destroy the turbine's business case. Even though defects are rare, it is essential to find, locate, and repair them before the blade leaves the factory. Current inspection processes rely on trained experts who manually, and meticulously, study the entire surface in detail. This process has become exhaustive, time-consuming, and expensive as blades have grown longer to become the giants that we see today. Consequently, blade manufactures look toward autonomous inspection methods, which can deliver the same kind of sensitivity as the current inspection process, but faster and cheaper.

It is not easy to autonomously measure blades with the required speed, resolution, and precision. Wind turbine blades are large and flexible freeform components. Methods and procedures for measuring this kind of workpiece are still open research topics. This thesis studied the problem of measuring blades with a 3D SL scanner, mounted on an autonomous robot system.

The precision of an optical measurement system is subject to influences from the radiometric properties of the measurand's surface. These influences must be taken into account when a good overview of precision dependencies is required. A study of material's interaction with light, which focused on the measuring and use of BRDFs, was undertaken by Contributions B, C, D and E. A gonioreflectometer was developed from a common industrial robot and used for measuring the BRDFs of the blade's two paint types. Through this study, we concluded that the blade's surface was well suited for optically based measurement techniques. The parameters of the optical system, *i.e.* the camera and lens, also influence precision. Contribution A studied how knowledge about light, material properties, and the optical system can be utilized when constructing an inspection system for situations where the inspected component has challenging radiometric properties. As described in Chapter 2, the analysis of the blade's two paint types was used to select the best-suited commercial SL scanner for measuring the blade surface.

Through Chapter 3 and 4, and Contributions F, G, H, I and J, it was found that the proposed optical blade scanner system could measure the leading edge of blades fast and precise. The system was able to measure 20 meters of the tip of a 55-meter long blade with an average point spacing of 250 μm, yielding just below 400 million vertices, within 1.5 hours. The expanded measurement uncertainty was estimated to 670 μm (k=2). It was found through an extensive metrological validation, which used a novel application of the MFG method.

The method allowed us to get an estimate that was valid for the outer third of the blade. Finally, we demonstrated that the measured point clouds could be used for defect detection.

The thesis studied how a detailed and precise 3D model of wind turbine blade's outer geometry can be acquired quickly and precisely, and how such a model can be used for geometric quality inspection. We believe that this objective has been met and that the thesis has contributed to the scientific field.

Bibliography

Aanæs, H. (2014). *Lecture notes on computer vision*. Department of Applied Mathematics and Computer Science.

Batlle, J., Mouaddib, E., & Salvi, J. (1998). Recent progress in coded structured light as a technique to solve the correspondence problem: A survey. *Pattern recognition*, *31*(7), 963–982.

BEK nr 693 af 10/06/2013. (2013). Bekendtgørelse om indretning m.v. af maskiner. *Lovtidende A*, *693*.

Benveniste, R., Cem, Ã. et al. (2010). A color invariant based binary coded structured light range scanner for shiny objects. In *2010 international conference on pattern recognition* (pp. 798–801). IEEE.

Bolinger, M., & Wiser, R. (2012). Understanding wind turbine price trends in the us over the past decade. *Energy Policy*, *42*, 628–641.

BP. (2018). Statistical review of world energy. Retrieved June 23, 2018, from https://www.bp.com/en/global/corporate/energy-economics/statistical-review-of-world-energy/renewable-energy/wind-energy.html

Breckman, J. (1956). Encoding circuit. US Patent 2,733,432. Google Patents.

Brown, D. C. (1966). Decentering distortion of lenses. *Photogrammetric Engineering*, *32*(3), 444–462.

Brown, D. C. (1971). Close-range camera calibration. *Photogrammetric Engineering*, *37*(8), 855–866.

Burton, T., Jenkins, N., Sharpe, D., & Bossanyi, E. (2011). *Wind energy handbook*. John Wiley & Sons.

Callister, W. D., & Rethwisch, D. G. (2013). *Materials science and engineering: An introduction*. Wiley New York.

Claus, M. (1988). Experience with indusurf in 3d measurement of industrial surfaces. *International Archives ISPRS, Kyoto*.

Couture, V., Martin, N., & Roy, S. (2011). Unstructured light scanning to overcome interreflections. In *Computer vision (iccv), 2011 ieee international conference on* (pp. 1895–1902). IEEE.

Couture, V., Martin, N., & Roy, S. (2014). Unstructured light scanning robust to indirect illumination and depth discontinuities. *International Journal of Computer Vision*, *108*(3), 204–221.

Dalili, N., Edrisy, A., & Carriveau, R. (2009). A review of surface engineering issues critical to wind turbine performance. *Renewable and Sustainable Energy Reviews*, *13*(2), 428–438.

De Chiffre, L. (2012). *Modelling and Testing in Metal Cutting*. Department of Manufacturing Engineering, Technical University of Denmark. Kgs. Lyngby, Denmark.

De Chiffre, L., Hansen, H. N., Andreasen, J. L., Savio, E., & Carmignato, S. (2015). *Geometrical Metrology and Machine Testing*. Department of Manufacturing Engineering, Technical University of Denmark. Kgs. Lyngby, Denmark.

Dhond, U. R., & Aggarwal, J. K. (1989). Structure from stereo-a review. *IEEE transactions on systems, man, and cybernetics*, *19*(6), 1489–1510.

Directive 2006/42/EC. (2006). on machinery, and amending Directive 95/16/EC (recast). *OJ L*, *157*, 24–86.

DS/EN ISO 12100:2011. (2011). *Maskinsikkerhed - Generelle principper for konstruktion - Risikovurdering og risikonedsættelse*. Danish Standards Foundation and International Organization for Standardization. Copenhagen, Denmark,

DS/EN ISO 13850:2015. (2015). *Safety of machinery – Emergency stop function – Principles for design*. Danish Standards Foundation and International Organization for Standardization. Copenhagen, Denmark,

DS/EN ISO 13857:2008. (2008). *Safety of machinery – Safety distances to prevent hazard zones being reached by upper and lower limbs*. Danish Standards Foundation and International Organization for Standardization. Copenhagen, Denmark,

Eiríksson, E. R., Wilm, J., Pedersen, D. B., & Aanæs, H. (2016). Precision and accuracy parameters in structured light 3-d scanning. *The International Archives of Photogrammetry, Remote Sensing and Spatial Information Sciences*, *40*, 7.

Frank, G. (1953). Pulse code communication. US Patent 2,632,058. Google Patents.

Fu, H.-L., Fan, K.-C., Huang, Y.-J., & Hu, M.-K. (2014). Innovative optical scanning technique and device for three-dimensional full-scale measurement of wind-turbine blades. *Optical Engineering*, *53*(12), 122411.

Geng, J. (2011). Structured-light 3d surface imaging: A tutorial. *Advances in Optics and Photonics*, *3*(2), 128–160.

Giacomo, P. (1984). The new definition of the meter. *American Journal of Physics*, *52*(7), 607–613.

Gonzalez, R. C., & Woods, R. E. (2008). *Digital image processing: 3rd edition.* Pearson.

Gupta, M., Agrawal, A., Veeraraghavan, A., & Narasimhan, S. G. (2011). Structured light 3d scanning in the presence of global illumination. In *Computer vision and pattern recognition (cvpr), 2011 ieee conference on* (pp. 713–720). IEEE.

Gupta, M., & Nayar, S. K. (2012). Micro phase shifting. In *Computer vision and pattern recognition (cvpr), 2012 ieee conference on* (pp. 813–820). IEEE.

Hain, R., Kähler, C. J., & Tropea, C. (2007). Comparison of ccd, cmos and intensified cameras. *Experiments in fluids*, *42*(3), 403–411.

Hanrahan, P., & Krueger, W. (1993). Reflection from layered surfaces due to subsurface scattering. In *Proceedings of the 20th annual conference on computer graphics and interactive techniques* (pp. 165–174). ACM.

Hartley, R., & Zisserman, A. (2003). *Multiple view geometry in computer vision.* Cambridge university press.

Hecht, E. (2016). *Optics: Fifth edition.* Pearson Education Limited.

Heikkila, J., & Silven, O. (1997). A four-step camera calibration procedure with implicit image correction. In *Computer vision and pattern recognition, 1997. proceedings., 1997 ieee computer society conference on* (pp. 1106–1112). IEEE.

Hermann, M., Pentek, T., & Otto, B. (2016). Design principles for industrie 4.0 scenarios. In *System sciences (hicss), 2016 49th hawaii international conference on* (pp. 3928–3937). IEEE.

Holmes, B. J., Obara, C. J., & Yip, L. P. (1984). Natural laminar flow experiments on modem airplane surfaces. *NASA Technical Paper*, *2256*.

Huang, P.-H., Matzen, K., Kopf, J., Ahuja, N., & Huang, J.-B. (2018). Deepmvs: Learning multi-view stereopsis. In *Proceedings of the ieee conference on computer vision and pattern recognition* (pp. 2821–2830).

Inokuchi, S. (1984). Range imaging system for 3-d object recognition. *ICPR, 1984*, 806–808.

ISO 1101:2017. (2017). *Geometrical product specifications (GPS) – Geometrical tolerancing – Tolerances of form, orientation, location and run-out.* International Organization for Standardization. Geneva, Switzerland.

ISO 4287:1997. (1997). *Geometrical Product Specifications (GPS) – Surface texture: Profile method – Terms, definitions and surface texture parameters.* International Organization for Standardization. Geneva, Switzerland.

ISO/IEC Guide 98-3:2008. (2008). *Uncertainty of measurement – Part 3: Guide to the expression of uncertainty in measurement (GUM).* International Organization for Standardization. Geneva, Switzerland.

ISO/TS 15066:2016. (2016). *Robots and robotic devices – Collaborative robots.* International Organization for Standardization. Geneva, Switzerland.

Jensen, J. N., Lyngby, R. A., Aanæs, H., Eiríksson, E. R., Nielsen, J. B., Wilm, J., & Pedersen, D. B. (2017). Photogrammetry for repositioning in additive

manufacturing. In *Special interest group meeting: Additive manufacturing*, Euspen.

Jensen, O. K. (2018). Både vind og sol slog rekord i 2017 - leverede 45,8 procent af strømmen. Retrieved June 23, 2018, from http://energinet.dk/Omnyheder/Nyheder/2018/01/09/Baade-vind-og-sol-slog-rekord-i-2017-leverede-459-procent-af-stroemmen

Jureczko, M., Pawlak, M., & Mężyk, A. (2005). Optimisation of wind turbine blades. *Journal of materials processing technology*, *167*(2-3), 463–471.

Keegan, M. H., Nash, D., & Stack, M. (2013). On erosion issues associated with the leading edge of wind turbine blades. *Journal of Physics D: Applied Physics*, *46*(38), 383001.

Krattenthaler, W., Mayer, K., & Duwe, H. (1994). 3d-surface measurement with coded light approach. In *Proceedings of the 17th meeting of the austrian association for pattern recognition on image analysis and synthesis* (pp. 103–114). R. Oldenbourg Verlag GmbH.

Kushnir, A., & Kiryati, N. (2007). Shape from unstructured light. In *3dtv conference, 2007* (pp. 1–4). IEEE.

Levoy, M., Pulli, K., Curless, B., Rusinkiewicz, S., Koller, D., Pereira, L., ... Ginsberg, J., et al. (2000). The digital michelangelo project: 3d scanning of large statues. In *Proceedings of the 27th annual conference on computer graphics and interactive techniques* (pp. 131–144). ACM Press/Addison-Wesley Publishing Co.

Lucas, B. D., Kanade, T. et al. (1981). An iterative image registration technique with an application to stereo vision.

Lyngby, R. A., Aanæs, H., Nielsen, E., & Dahl, A. B. (2018). Autonomous surface inspection of wind turbine blades for quality assurance in production. In *Ewshm-9th european workshop on structural health monitoring*. BINDT.

Lyngby, R. A., & Dahl, A. B. (2018a). *Make geometry inspection of wind turbine blades great again with robots*. Technical University of Denmark. Technical Report. Kgs. Lyngby, Denmark.

Lyngby, R. A., & Dahl, A. B. (2018b). *Snags on surfaces: Detecting geometrical defects on wind turbine blades*. Technical University of Denmark. Technical Report. Kgs. Lyngby, Denmark.

Lyngby, R. A., Matthiassen, J. B., Frisvad, J. R., Dahl, A. B., & Aanæs, H. (2018). *Using an industrial robot arm for measuring brdfs*. Technical University of Denmark. Technical Report. Kgs. Lyngby, Denmark.

Lyngby, R. A., Nielsen, E., & Bach, H. (2018). Visual inspection arrangement. Patent application. Application number 18171466.8 - 1022. European Patent Office.

Lyngby, R. A., Nielsen, E., De Chiffre, L., Aanæs, H., & Dahl, A. B. (2018). Development and metrological validation of a new automated scanner system for freeform measurements on wind turbine blades in the production. *Precision Engineering*. In Press.

Lyngby, R. A., Wilm, J., Eiríksson, E. R., Nielsen, J. B., Jensen, J. N., Aanæs, H., & Pedersen, D. B. (2017). In-line 3d print failure detection using computer vision. In *Special interest group meeting: Additive manufacturing*, Euspen.

Maas, H.-G. (1990). Digital photogrammetry for determination of tracer particle coordinates in turbulent flow research. In *Close-range photogrammetry meets machine vision* (Vol. 1395, 13951E). International Society for Optics and Photonics.

Maas, H.-G. (1993). Robust automatic surface reconstruction with structured light. *International Archives of Photogrammetry and Remote Sensing*, *29*, 709–709.

Moeslund, T. B. (2009). *Image and video processing*. Institut for Medieteknologi, Aalborg Universitet.

Murari, K., Etienne-Cummings, R., Thakor, N., & Cauwenberghs, G. (2009). Which photodiode to use: A comparison of cmos-compatible structures. *IEEE Sensors Journal*, *9*(7), 752–760.

Nicodemus, F. E. (1965). Directional reflectance and emissivity of an opaque surface. *Applied optics*, *4*(7), 767–775.

Nicodemus, F. E., Richmond, J., Hsia, J., Ginsberg, I., & Limperis, T. (1977). Geometric considerations and nomenclature for reflectance, volume 161 of monograph. *National Bureau of Standards (US)*, *1*.

Nielsen, J. B., Eiríksson, E. R., Lyngby, R. A., Wilm, J., Frisvad, J. R., Conradsen, K., & Aanæs, H. (2015). Quality assurance based on descriptive and parsimonious appearance models. In *Material appearance modeling*.

Nielsen, J. B., Eiríksson, E. R., Lyngby, R. A., Wilm, J., Jensen, J. N., Aanæs, H., & Pedersen, D. B. (2017). Picprint: Embedding pictures in additive manufacturing. In *Special interest group meeting: Additive manufacturing*, Euspen.

Nielsen, J. B., Jensen, H. W., & Ramamoorthi, R. (2015). On optimal, minimal brdf sampling for reflectance acquisition. *ACM Transactions on Graphics (TOG)*, *34*(6), 186.

Nielsen, J. B., Stets, J. D., Lyngby, R. A., Aanæs, H., Dahl, A. B., & Frisvad, J. R. (2017). A variational study on brdf reconstruction in a structured light scanner. In *International conference on computer vision workshop (iccvw 2017)* (pp. 143–152). IEEE.

Petryna, Y., Künzel, A., & Kannenberg, M. (2014). Fault detection and state evaluation of rotor blades. In *Ewshm-7th european workshop on structural health monitoring*.

Phong, B. T. (1975). Illumination for computer generated pictures. *Communications of the ACM*, *18*(6), 311–317.

Quinn, T. (2003). Practical realization of the definition of the metre, including recommended radiations of other optical frequency standards (2001). *Metrologia*, *40*(2), 103.

Salvi, J., Pages, J., & Batlle, J. (2004). Pattern codification strategies in structured light systems. *Pattern recognition*, *37*(4), 827–849.

Sansoni, G., Carocci, M., & Rodella, R. (1999). Three-dimensional vision based on a combination of gray-code and phase-shift light projection: Analysis and compensation of the systematic errors. *Applied optics*, *38*(31), 6565–6573.

Savio, E., De Chiffre, L., & Schmitt, R. (2007). Metrology of freeform shaped parts. *CIRP annals*, *56*(2), 810–835.

Schubel, P. J., & Crossley, R. J. (2012). Wind turbine blade design. *Energies*, *5*(9), 3425–3449.

Shmueli, J., Eder, M. A., & Tesauro, A. (2015). A versatile stereo photogrammetry based technique for measuring fracture mode displacements in structures. *Precision Engineering*, *39*, 38–46.

Stets, J. D., Dal Corso, A., Nielsen, J. B., Lyngby, R. A., Jensen, S. H. N., Wilm, J., ... Aanæs, H. (2017). Scene reassembly after multimodal digitization and pipeline evaluation using photorealistic rendering. *Applied optics*, *56*(27), 7679–7690.

Stiesdal, H. (2011). Method for manufacturing a composite. EU Patent 08009395.8. European Patent Office.

Summerfield, M. (2008). *Rapid gui programming with python and qt : The definitive guide to pyqt programming*. Upper Saddle River, NJ: Prentice Hall.

Talbot, J., Wang, Q., Brady, N., & Holden, R. (2016). Offshore wind turbine blades measurement using coherent laser radar. *Measurement*, *79*, 53–65.

Van der Jeught, S., & Dirckx, J. J. (2016). Real-time structured light profilometry: A review. *Optics and Lasers in Engineering*, *87*, 18–31.

VDI/VDE 2634 Part 2. (2012). *Optical 3-D measuring systems: Optical systems based on area scanning*. Verein Deutscher Ingennieure and Verband der Elektrotechnik Elektronik Informationstechnik. Düsseldorf, Germany.

Veers, P. S., Ashwill, T. D., Sutherland, H. J., Laird, D. L., Lobitz, D. W., Griffin, D. A., ... Zuteck, M., et al. (2003). Trends in the design, manufacture and evaluation of wind turbine blades. *Wind Energy*, *6*(3), 245–259.

Weyrich, T., Lawrence, J., Lensch, H. P., Rusinkiewicz, S., Zickler, T., et al. (2009). Principles of appearance acquisition and representation. *Foundations and Trends® in Computer Graphics and Vision*, *4*(2), 75–191.

Woodham, R. J. (1980). Photometric method for determining surface orientation from multiple images. *Optical engineering*, *19*(1), 191139.

Wust, C., & Capson, D. W. (1991). Surface profile measurement using color fringe projection. *Machine Vision and Applications*, *4*(3), 193–203.

Zhang, L., Curless, B., & Seitz, S. M. (2002). Rapid shape acquisition using color structured light and multi-pass dynamic programming. In *3d data processing visualization and transmission, 2002. proceedings. first international symposium on* (pp. 24–36). IEEE.

Zhang, Z. (1999). Flexible camera calibration by viewing a plane from unknown orientations. In *Computer vision, 1999. the proceedings of the seventh ieee international conference on* (Vol. 1, pp. 666–673). Ieee.

CONTRIBUTION A

In-line 3D Print Failure Detection Using Computer Vision

Conference	Special Interest Group meeting on Dimensional Accuracy and Surface Finish in Additive Manufacturing
Organizer	euspen
Venue	KU Leuven, Leuven, BE
Submission date	July 05, 2017
Presentation Date	October 11, 2017
DOI	N/A

This contribution develops a method for detecting failure modes which occurs during the print process in consumer grade FDM 3D printers using a simple vision system. By combining a polarized light source with a cross-polarized camera, the unwanted sub-surface scattering effects are minimized and the workpiece segmentation is enhanced. My primary contribution to this paper was leading the development of the system, including segmentation and failure mode detection, and writing the text.

Joint Special Interest Group meeting between euspen and ASPE
Dimensional Accuracy and Surface Finish in Additive Manufacturing,
KU Leuven, BE, October 2017
www.euspen.eu

In-line 3D print failure detection using computer vision

R.A. Lyngby[1], J. Wilm[1], E.R. Eiríksson[1], J.B. Nielsen[1], J.N. Jensen[1], H. Aanæs[1], D.B. Pedersen[2]

[1]*Department of Applied Mathematics and Computer Science, Technical University of Denmark*
[2]*Department of Mechanical Engineering, Technical University of Denmark*

raly@dtu.dk

Abstract

Here we present our findings on a novel real-time vision system that allows for automatic detection of failure conditions that are considered outside of nominal operation. These failure modes include warping, build plate delamination and extrusion failure. Our system consists of a calibrated camera whose position and orientation is known in the machine coordinate system. We simulate what the object under print should look like for any given moment in time. This is compared to a segmentation of the current print, and statistical detection of significant deviation. We demonstrate that this methodology precisely and unambiguously detects the time point of print failure.

Failure detection, computer vision, fused deposition modeling (FDM)

1. Introduction

Even with today's rapid development of additive manufacturing processes and techniques, in-line quality control remains as one of the key technical challenges within the field [1]. Although the topic is rapidly gaining interest in the research community, the efforts have so far mostly concerned industrial metal based 3D printers [2,3]. Many of the most popular commercially available 3D printers rely on the Fused Deposition Modeling (FDM) method. Their popularity is not least due to their low cost, which has made rapid prototyping available to small businesses, research laboratories and even consumers. Despite the popularity of FDM based systems, and their continuous development, these systems remain error prone and print jobs fail from time to time. The relatively long cycle time of these systems means that they usually operate unsupervised, which is why failures are often only detected after significant amounts of time and material has been lost. An in-line quality control system could potentially surveil the process and either stop the printing process to save time and material, or mitigate the failure to restore the print quality. However, the cost of such a system needs to be reasonably low to allow for feasible integration into low cost printing systems.

Inspired by [4], and based on our personal experience with FDM printers, we have identified three failure modes which seem to be common and symptomatic of these systems. They are:

- Workpiece warpage
- Build plate delamination
- Extrusion failure

The purpose of this paper is to explore if a computer vision system composed of only one camera and one light source can utilize relatively simple, and well known, analysis techniques to detect these failure modes.

In [4], an in-line computer vision system was presented which uses differential imaging between consecutive video frames and BLOB detection to identify the three failure modes. As their method concerns relative changes between added layers, it implicitly assumes that each layer is added correctly at first, without warpage. It further assumes that the build process does not fail when putting down the first layer. Except for the detection of extrusion failure, these two assumptions limit the sensibility of the method as well as its scalability to other failure modes.

A different idea was proposed in [5]. There, a camera array of five cameras was used to capture images of the workpiece from multiple angles. The images were saved and compared pixel-wise against images of the finished workpiece, captured after the printing process had finished. The comparisons were then used, post-manufacturing, to determine if the print had failed during manufacturing. While this approach has obvious limitations and issues, the general idea of comparing a current workpiece state against a model of that state has good potential. Our approach continues this line of thought. We use the workpiece CAD model to synthesize the expected workpiece states based on knowledge of the build plate geometry, obtained through photogrammetry.

The paper starts by detailing our approach of failure mode detection in section 2. Section 3 presents results obtained from a proof-of-concept system based on our approach, which are discussed in Section 4. Finally, Section 5 concludes the paper.

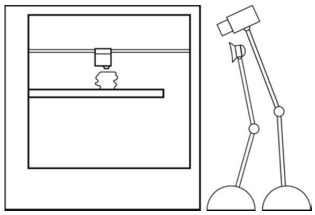

Figure 1. Illustration of the experimental printer/camera setup. A camera and a light source are positioned with good overview of the build plate.

2. Failure mode detection

Assume that we have a printer/camera system setup as illustrated on Figure 1. A color camera captures an image, $\boldsymbol{A}$, of the illuminated workpiece after each new layer is added. Using the workpiece CAD model, and perspective projection, an expected image of the workpiece geometry, $\boldsymbol{B}$, is rendered for each of the captured images. The failure modes defined in Section 1 can be jointly detected by comparing the image of the actual workpiece with that of the rendered workpiece. Note, however, that the current version of our method is not able to distinguish between the three failure-modes. Instead, it simply detects if there is *Matter Out Of Place* (MOOP).

As argued in the following sections, the interactions between light, scene and workpiece makes it difficult to render a photorealistic view of the workpiece. Inspired by [4], we overcome this issue by segmenting the workpiece, in both the captured and rendered image, and compare their segmentation masks, $s(\boldsymbol{A})$ and $s(\boldsymbol{B})$. This simplifies the error estimation to an elementwise logical exclusive disjunction between two sparse matrices with elements from the Boolean domain:

$$\boldsymbol{D} = s(\boldsymbol{A}) \oplus s(\boldsymbol{B}) \tag{1}$$

with $\boldsymbol{A}, \boldsymbol{B} \in \mathbb{B}^{N \times M \times 3}$ and $s(\boldsymbol{A}), s(\boldsymbol{B}), \boldsymbol{D} \in \mathbb{B}^{N \times M}$ where $M \times N$ is the image size. The elements in $\boldsymbol{D}$ are true wherever there is a difference between the actual view and the expected view, thus indicating an error. To intuitively understand $\boldsymbol{D}$, we need to understand how a camera pixel measures the world. Each pixel, if viewed as ideal, samples incident light, originating from a unique direction. Thus, each pixel covers a unique azimuth- and elevation angle, relative to the camera lens, why each pixel can be thought of as covering a unique frustum of the world. Our method simply predicts if a given frustum, covered by a given pixel, should contain build material or not, and then compares the actual containment of material with the predicted.

Based on $\boldsymbol{D}$, we define an error metric

$$\boldsymbol{E} = N_{\boldsymbol{D}} / N_{\text{total}} \tag{2}$$

Where $N_{\boldsymbol{D}}$ is the number of true pixels in $\boldsymbol{D}$ and N_{total} is the number of foreground pixels in the rendered mask of the complete object.

2.1. Workpiece segmentation

When segmenting the workpiece from a captured image, we utilize the color of the printing material. As our approach is targeted at low-cost consumer printers, the material is expected to be monochrome PLA plastics. The camera captures color images using the Bayer filter technique [6]. The color of each pixel is represented by three intensities, one for each of Red, Green and Blue (RGB). In combination, these three colors can simulate most all human perceivable colors. While good for humans, this color representation is not ideal for algorithmic segmentation of colored objects. Instead, we transform the color space from RGB to Hue, Saturation and Value (HSV) [7]. The HSV space intuitively represents color, with Hue representing the pure color as an angle from $0°$ to $360°$, and Saturation and Value representing the saturation and intensity of the color as values from 0 to 1.

Given a pixel at position $\boldsymbol{x} \in \mathbb{Z}^2$ in the image, with RGB values $r_{\boldsymbol{x}}, g_{\boldsymbol{x}}, b_{\boldsymbol{x}} \in [0,255]$, we first normalize the values:

$$r'_{\boldsymbol{x}} = r_{\boldsymbol{x}} / 255 \tag{3}$$

$$g'_{\boldsymbol{x}} = g_{\boldsymbol{x}} / 255 \tag{4}$$

$$b'_{\boldsymbol{x}} = b_{\boldsymbol{x}} / 255 \tag{5}$$

Then, the maximum intensity, the minimum intensity and their difference are computed:

$$C_{\max} = \max(r'_{\boldsymbol{x}}, g'_{\boldsymbol{x}}, b'_{\boldsymbol{x}}) \tag{6}$$

$$C_{\min} = \min(r'_{\boldsymbol{x}}, g'_{\boldsymbol{x}}, b'_{\boldsymbol{x}}) \tag{7}$$

$$\Delta = C_{\max} - C_{\min} \tag{8}$$

Having those, the HSV representation is computed by:

$$h_{\boldsymbol{x}} = \begin{cases} 0° & \Delta = 0 \\ 60° \cdot \operatorname{mod}\left(\frac{g'_{\boldsymbol{x}} - b'_{\boldsymbol{x}}}{\Delta}, 6\right) & C_{\max} = r'_{\boldsymbol{x}} \\ 60° \cdot \left(\frac{b'_{\boldsymbol{x}} - r'_{\boldsymbol{x}}}{\Delta} + 2\right) & C_{\max} = g'_{\boldsymbol{x}} \\ 60° \cdot \left(\frac{r'_{\boldsymbol{x}} - g'_{\boldsymbol{x}}}{\Delta} + 4\right) & C_{\max} = b'_{\boldsymbol{x}} \end{cases} \tag{9}$$

$$s_{\boldsymbol{x}} = \begin{cases} 0 & C_{\max} = 0 \\ \frac{\Delta}{C_{\max}} & C_{\max} > 0 \end{cases} \tag{10}$$

$$v_{\boldsymbol{x}} = C_{\max} \tag{11}$$

After the captured images are converted to the HSV color space, the PLA plastic is easily segmented by only retaining pixels with a Hue within a range corresponding to that of the material, $H_{\text{t}} = [h_{\min}, h_{\max}]$. In addition, Saturation and Value are thresholded with values T_{S} and T_{V} to remove "dark" pixels, which do not contain much information due to poor illumination. Thus, the value of a pixel at position $\boldsymbol{x}$ in the segmentation mask is computed as follows:

$$\text{s}_{\boldsymbol{x}} = \begin{cases} 1 & h_{\boldsymbol{x}} \in H_{\text{t}}, s_{\boldsymbol{x}} > T_{\text{S}}, v_{\boldsymbol{x}} > T_{\text{V}} \\ 0 & \text{otherwise} \end{cases} \tag{12}$$

This segmentation method implicitly assumes that the workpiece is uniformly illuminated by a diffuse light source and that the workpiece does not share color with any other object inside the printing chamber.

2.2. Segmentation masks versus photorealistic rendering

In principle, it is possible to create a photorealistic rendering of the workpiece. Doing so would allow for detecting a wider range of failure modes than those defined in Section 1. But, as we will describe in this section, it requires detailed knowledge of the radiometric properties of the workpiece material as well as accurate knowledge of the scene geometry to do so.

Three things happen when light crosses from one media into another. Some of the light is transmitted, some is absorbed and some is reflected [8]. We denote the proportion of the light being transmitted, absorbed and reflected as T, A and R, respectively. They sum to 1, as all the energy received by the surface must be transmitted, absorbed or reflected, thus:

$$T + A + R = 1 \tag{13}$$

The transmissivity, T, the absorptivity, A, and the reflectivity, R, are collectively known as radiometric material properties, and are defined as:

$$T = I_{\text{T}} / I_0 \tag{14}$$

$$A = I_{\text{A}} / I_0 \tag{15}$$

$$R = I_{\text{R}} / I_0 \tag{16}$$

where I_0 is the radiant intensity received at the surface of the incident media, I_T is the intensity transmitted through the media, I_A is the intensity absorbed by the media, and I_R is the intensity reflected by the media. In all cases, radiant intensity is defined as watts per steradian $[\text{W/sr}]$.

When rendering the appearance of a given media, T, A and R has to be modelled. The real world scene, in our case the print bed with workpiece and light source, is modelled digitally. This is done by defining lights, objects, materials and rendering "cameras". Different types of lights are available, but in general a light source has intensity, color, direction, and position. The object, or workpiece, is defined as a polygon mesh with a position and orientation. A material is assigned to the object which defines its radiometric properties and therefore its light interactions. The light-material interactions are modelled using angles and distances between the scene elements. A rendering "camera" defines a 2D plane onto which the image of the rendered scene is projected. It has camera parameters, such as focal length and aperture, as well as a position and orientation.

The amount of radiant intensity being absorbed, transmitted and reflected at a given position on the surface of the

workpiece depends on the incoming angle between the surface and the light source and the angle between the surface and the rendering "camera". If the surface has a thickness, i.e. any real world object, light penetrates the surface where it is scattered, with some portion of light exiting at a different location than it entered. To capture this interaction property, as well as T, A, and R, a *Bidirectional Scattering-Surface Reflectance Distribution Function* (BSSRDF) is needed [9,10]. In short, the BSSRDF relates the outgoing radiance at a given surface point to the incoming irradiance received at another point:

$$dL_r(\boldsymbol{x}_r, \boldsymbol{\omega}_r) = S(\boldsymbol{x}_i, \boldsymbol{\omega}_i, \boldsymbol{x}_r, \boldsymbol{\omega}_r) dE_i(\boldsymbol{x}_i, \boldsymbol{\omega}_i) \quad (17)$$

where $\mathrm{E}_i(\boldsymbol{x}_i, \boldsymbol{\omega}_i)$ is the irradiance $[\mathrm{W/m^2}]$ received at a surface point $\boldsymbol{x}_i$ from the direction $\boldsymbol{\omega}_i$, $L_r(\boldsymbol{x}_r, \boldsymbol{\omega}_r)$ is the radiance $[\mathrm{W/sr/m^2}]$ emitted at another surface point $\boldsymbol{x}_r$ in the direction $\boldsymbol{\omega}_r$, and $S(\boldsymbol{x}_i, \boldsymbol{\omega}_i, \boldsymbol{x}_r, \boldsymbol{\omega}_r)$ is the proportion between L_r and E_i, which per definition is the BSSRDF.

A given material have a given BSSRDF which needs to be estimated before that material can be rendered. Generally, the BSSRDF can be an analytic function or a look-up table based on radiance-irradiance measurements of densely sampled perturbations of inward and outward directions. Either way, acquiring the measurements for model fitting is time consuming, requires specialized hardware and is rather difficult to do accurately enough.

In addition to obtaining an accurate radiometric model, a process model, simulating the surface microstructure created by the 3D printer, is required. Finally, the positions of all scene elements, such as lighting, workpiece, camera, and build-plate, would have to be known. The exact required precision depends on the specific parameters of the involved materials.

We assert that the added benefits of photorealistic rendering do not outweigh the difficulties involved, when detecting the defined failure modes. Thus, a simple in-line failure detection system for low-cost printers is better off relying on the much simpler segmentation mask comparison approach outlined previously.

2.3. Perspective projection and the pinhole camera model

To render an image of the workpiece and create its segmentation mask, a model is needed for projecting a volumetric object onto the flat imaging plane formed by the image sensor. First, the workpiece CAD model is tessellated into a polyhedral object. This mesh is composed of a set of K vertices connected by edges, $W = (V, E)$, with each vertex being a homogeneous coordinate in a three dimensional Cartesian coordinate frame, $V = \{\boldsymbol{v}_k \in \mathbb{R}^4\}_{k=1}^{K}$, and each edge being a two-element subsets of V,

$E = \left\{ \{\{a, b\} : a, b \in V, a \neq b\}_{l=1}^{L_k} \right\}_{k=1}^{K}$ where L_k is the number of edges connected to vertex k.

A vertex, $\boldsymbol{v} \in \mathbb{R}^4$, is projected onto the image plane by an affine transformation matrix, $\boldsymbol{P} \in \mathbb{R}^{3\times4}$, thus creating $\boldsymbol{u} \in \mathbb{R}^3$:

$$\boldsymbol{u} = \boldsymbol{P}\boldsymbol{v} \quad (17)$$

with $\boldsymbol{u}$ being a homogeneous point on the two-dimensional plane and $\boldsymbol{P}$ defined as:

$$\boldsymbol{P} = \boldsymbol{A}[\boldsymbol{R}\ \boldsymbol{t}] \quad (18)$$

where $\boldsymbol{t} \in \mathbb{R}^3$ is a three-dimensional translation vector, $\boldsymbol{R} \in \mathbb{R}^{3\times3}$ is a three-dimensional rotation matrix, and $\boldsymbol{A} \in \mathbb{R}^{3\times3}$ is:

$$\boldsymbol{A} = \begin{bmatrix} f & \beta & \Delta x \\ 0 & \alpha f & \Delta y \\ 0 & 0 & 1 \end{bmatrix} \quad (19)$$

where f is the focal length of the camera, $(\Delta x, \Delta y)$ is the image coordinate of the principal point, α is a scaling factor, and β is a shearing factor.

In combination, $\boldsymbol{P}$ defines the perspective projection of a three-dimensional, homogeneous world point onto a two-dimensional, homogeneous image point and is known as the *pinhole camera model* [11]. The matrix $[\boldsymbol{R}\ \boldsymbol{t}]$ defines the transformation from the world coordinate frame and into the cameras coordinate frame. It is known as the *extrinsic camera parameters*. The matrix $\boldsymbol{A}$ defines the transformation from the camera coordinate frame and into the image coordinate frame. It is known as the *intrinsic camera parameters*.

2.4. Camera calibration

The camera parameters need to be estimated beforehand. Ideally, the world coordinate frame coincides with the printer's coordinate frame, such that $[\boldsymbol{R}\ \boldsymbol{t}]$ transforms points from the printer's frame into the camera's frame. We define a new coordinate frame which is spanned by the positions of four corner markers. The markers are superimposed onto the workpiece mesh, such that they are printed together and the workpiece has a known position relative to the markers. This approach gives us a well-defined coordinate frame, which can easily be found relative to both the workpiece and the camera. The markers are illustrated in Figure 2.

The four marks are found from the workpiece segmentation mask defined in equation (12). The method described by [12] is used to extract object contours from the mask. Then, algebraic ellipses are fitted to the contours using [13]. The markers contain three contours: one for each of the internal holes and one for the outer ring. We are only interested in finding the position of the outer ring. Therefore, ellipses which are completely enveloped by another ellipse are removed[1]. The centers of the four remaining ellipses closest to the image corners are used to estimate the extrinsic camera parameters.

Note that the real markers are circles which are perspectively projected onto ellipses in the image plane. Because of this, the ellipse centers will generally not coincide with the actual circle centers. Instead, they will be translated towards the camera, which leads to a small error in the estimation.

The intrinsic camera parameters are found using a set of images captured from different views of a checkerboard and follows the method described by [14].

All computer vision related processing is done using the OpenCV library [15].

2.5 Scene illumination

It is preferable to capture as much of the diffuse component of the light reflected off the workpiece as possible. It is argued in [16] that is done when the angle between the surface and the light source, and the angle between the surface and the observer, are both close to $45°$, while the direction difference between the light and observer is small, thus $\boldsymbol{\omega}_r \approx \boldsymbol{\omega}_i$. Because of this relation, we choose to place the light source as close to the camera as possible, while both are angled approximately $45°$ relative to the build plate. Besides capturing as much diffuse light as possible, this configuration also limits the shadows cast by the workpiece. The setup is shown on Figure 2.

The light source and the camera are cross-polarized. Light with one polarization direction keeps its orientation at specular reflections, but loses the orientation at diffuse reflections. Thus, specular reflections can be removed by having a $90°$ polarization difference between the camera and the light

[1] All permutations of unique pairs of ellipses are tested. The transformation which transforms one of the ellipses to the unit circle is applied to the other ellipse. If the ℓ_2 norm of the most distant point on the transformed ellipse is less than 1 then the point is completely enveloped by the other ellipse.

source. Remaining reflections in the glass build plate were eliminated by adding diffusing black tape.

Figure 2. The experimental camera and illumination setup. Notice the diffused black tape on the build plate which removes reflections.

3. Results

The method described in section 2 was applied to a test print geometry containing the letters "DTU" as shown in figure 2. This geometry is challenging to print with FDM based printers due to unsupported overhangs. Support structure generation was disabled to illustrate the detection of a failing print.

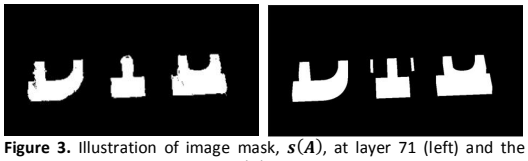

Figure 3. Illustration of image mask, $\boldsymbol{s}(\boldsymbol{A})$, at layer 71 (left) and the corresponding rendered mask, $\boldsymbol{s}(\boldsymbol{B})$ (right).

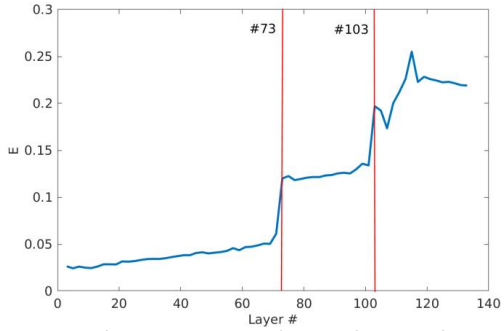

Figure 4. Plot of the error signal as a function of number of printed layers. Print failure occurs in layers 73, and further worsens at layer 103.

An example of the segmented and rendered image masks is shown in Figure 3. Figure 4 shows the evolution of the error measure as defined in Eqn. 2. Clearly, a sudden increase in $\boldsymbol{E}$ occurs before layer 73 and again at layer 103. Figure 5 shows the print shortly before and after print failure is detected. In Figure 6, the situation before and after layer 103 is shown.

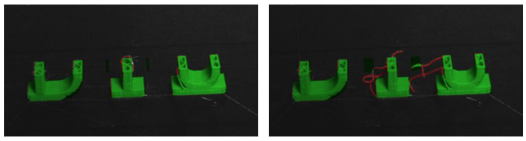

Figure 5. Close-up of the print at layer 71 (left) and layer 73 (right). False colouring was applied such that pixels in $\boldsymbol{s}(\boldsymbol{A})$ are green, pixels in $\boldsymbol{D}$ are coloured red.

It is seen that layer 73 corresponds to the emergence of severe print failure (mainly due to the unsupported serifs of the letter T). In layer 103, a large amount of hanging material is pushed into an area in which no material is expected, thus increasing the value of $\boldsymbol{E}$.

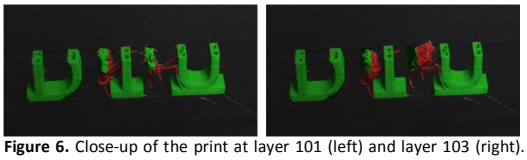

Figure 6. Close-up of the print at layer 101 (left) and layer 103 (right). False colouring was applied such that pixels in $\boldsymbol{s}(\boldsymbol{A})$ are green, pixels in $\boldsymbol{D}$ are coloured red.

4. Conclusion and Discussion

We have demonstrated a complete method for print failure detection by means of computer vision and computer rendering of the expected print geometry. Though the implemented system is a rough prototype, the results show the success of our method, and demonstrate that print failure can be detected early and very clearly using a simple camera system.

The demonstrated method is simple, low-cost, and applicable to all FDM based printers, and will detect failure in most cases of unexpected material deposition, print lifting, etc. A natural extension of the method involves multiple cameras reconstructing the visual hull of the currently printed geometry.

References

[1] Eiríksson ER et al., 2017, "Computer Vision for Additive Manufacturing", *Ph.D. thesis, DTU Compute* **447**

[2] Everton SK et al., 2016, "Review of in-situ process monitoring and in-situ metrology for metal additive manufacturing", *Materials & Design* **95** 431-445.

[3] Tapia G and Elwany A, 2014, "A review on process monitoring and control in metal-based additive manufacturing", *Journal of Manufacturing Science and Engineering* **136.6** 060801.

[4] Baumann F and Roller D, 2016, "Vision based error detection for 3D printing processes", *Int. Conf. on Frontiers of Sensors Technologies* **59** 06003.

[5] Straub J, 2015, "Initial Work on the Characterization of Additive Manufacturing (3D Printing) Using Software Image Analysis", *Machines* **3(2)** 55-71.

[6] Bayer BE, 1976, "Color imaging array", *US Patent 3,971,065*

[7] Smith AR, 1978, "Color gamut transform pairs", *Computer Graphics* **12(3)** 12–19.

[8] Callister WD and Rethwisch DG, 2011, "Materials science and engineering: An introduction", *John Wiley & Sons*, **8**.

[9] Nicodemus FE, Richmond JC, Hsia JJ, Ginsberg IW and Limperis T, 1977, "Geometrical Considerations and Nomenclature for Reflectance", *Technical Report NBS MN-160, National Bureau of Standards*

[10] Jensen HW, Marschner SR, Levoy M, Hanrahan P, 2001, "A Practical Model for Subsurface Light Transport", *Proceedings of ACM SIGGRAPH* 511–518.

[11] Hartley R and Zisserman A, 2003, "Multiple view geometry in computer vision", *Cambridge university press*.

[12] Suzuki S and Abe K, 1985, "Topological Structural Analysis of Digitized Binary Images by Border Following", *CVGIP* **30(1)** 32-46.

[13] Fitzgibbon AW and Fisher RB, 1995, "A Buyer's Guide to Conic Fitting", *Proc.5th British Machine Vision Conference* 513-522.

[14] Zhang Z, 2000, "A Flexible New Technique for Camera Calibration", *IEEE Transactions on Pattern Analysis and Machine Intelligence* **22(11)** 1330-1334.

[16] Bradski G, 2000, "The OpenCV Library", Dr. Dobb's Journal: Software for the Professional Programmer **25(11).**

[15] Nielsen JB, Jensen HW and Ramamoorthi R, 2015, "On Optimal, Minimal BRDF Sampling for Reflectance Acquisition", *ACM Transactions on Graphics* **34(6)**.

CONTRIBUTION B

Scene Reassembly After Multimodal Digitization and Pipeline Evaluation Using Photorealistic Rendering

Journal	Applied Optics
Volumne	56 (27)
Pages	7679-7690
Submission date	May 23, 2017
Publication Date	September 19, 2017
Publisher	OSA Publishing
DOI	10.1364/AO.56.007679

This contribution develops a method for pixel-to-pixel comparison between real images and rendered images of scenes with glass objects. This method allows for quantitatively measuring the realism of a rendering of transparent objects, which can be used to benchmark different rendering techniques. My main contribution to this paper regarded the measurements of the BRDF's of the opaque materials in the scene surrounding the glass objects. In addition, I participated in the writing process, most notably section 2.C.

Scene reassembly after multimodal digitization and pipeline evaluation using photorealistic rendering

JONATHAN DYSSEL STETS[1,†], ALESSANDRO DAL CORSO[1,†], JANNIK BOLL NIELSEN[1], RASMUS AHRENKIEL LYNGBY[1], SEBASTIAN HOPPE NESGAARD JENSEN[1], JAKOB WILM[1], MADS BRIX DOEST[1], CARSTEN GUNDLACH[2], EYTHOR RUNAR EIRIKSSON[1], KNUT CONRADSEN[1], ANDERS BJORHOLM DAHL[1], JAKOB ANDREAS BÆRENTZEN[1], JEPPE REVALL FRISVAD[1,*], AND HENRIK AANÆS[1]

[1] *Department of Applied Mathematics and Computer Science, Technical University of Denmark, Richard Petersens Plads, 2800 Kongens Lyngby, Denmark*
[2] *Department of Physics, Technical University of Denmark, Fysikvej, 2800 Kongens Lyngby, Denmark*
[†] *Joint primary authors*
[*] *Corresponding author: jerf@dtu.dk*

Transparent objects require acquisition modalities that are very different from the ones used for objects with more diffuse reflectance properties. Digitizing a scene where objects must be acquired with different modalities, requires scene reassembly after reconstruction of the object surfaces. This reassembly of a scene that was picked apart for scanning seems unexplored. We contribute with a multimodal digitization pipeline for scenes that require this step of reassembly. Our pipeline includes measurement of bidirectional reflectance distribution functions and high dynamic range imaging of the lighting environment. This enables pixelwise comparison of photographs of the real scene with renderings of the digital version of the scene. Such quantitative evaluation is useful for verifying acquired material appearance and reconstructed surface geometry, which is an important aspect of digital content creation. It is also useful for identifying and improving issues in the different steps of the pipeline. In this work, we use it to improve reconstruction, apply analysis by synthesis to estimate optical properties, and to develop our method for scene reassembly.

OCIS codes: *(150.4232) Multisensor methods; (150.6910) Three-dimensional sensing; (150.1488) Calibration; (160.4760) Optical properties; (290.1483) BSDF, BRDF, and BTDF; (330.1690) Color.*

This is the authors' version of the work. The definitive version is available at https://doi.org/10.1364/AO.56.007679

1. INTRODUCTION

Several research communities work on techniques for optical acquisition of physical objects and their appearance parameters [1–5]. Thus, we are now able to acquire nearly any type of object and perform a computer graphics rendering of nearly any type of scene. The range of applications is broad and includes movie production [2], cultural heritage preservation [3], 3D printing [4], and industrial inspection [5]. A gap left by these multiple endeavors is a coherent scheme for acquiring a scene consisting of several objects that have very different appearance parameters, together with the reassembly of a digital replica of such a scene. Our objective is to fill this gap for the combination of transparent and opaque objects, as many real world scenarios exhibit this combination. An example is a living room, like the one rendered in Fig. 1 (right). We propose a pipeline for acquiring and reassembling digital scenes from this type of heterogeneous real-world scenes. In addition, our pipeline closes the loop by rendering calibrated images of the digital scene that are commensurable with photographs of the original physical scene (see Fig. 1, left). This allows for validation and fine-tuning of appearance parameters. The quantitative evaluation we get from pixelwise comparison of rendered images with photographs is a great improvement with respect to validation of the acquired digital representation of the physical objects.

When addressing the problem of acquiring a heterogeneous scene, there is an infinite variety of scenes and object types to choose from. So, to make our task feasible, we focus on scenes that combine glassware and non-transparent materials, more specifically, white tablecloth and cardboard with a checkerboard pattern. We made these choices as glass requires a different acquisition modality, the tablecloth bidirectional reflectance distribution function (BRDF) is spatially uniform but not necessarily simple, and the cardboard has simple two-color varia-

Fig. 1. To the left, we compare rendered images (top) with photographs (bottom). More views are available in Appendix A. The scenes to the left were digitized using our pipeline and include both glass objects and non-transparent objects (tablecloth and backdrop). To the right, we exemplify the use of our pipeline for virtual product placement using our digitized glass objects, with estimated optical properties and artifact-reduced removal of markers.

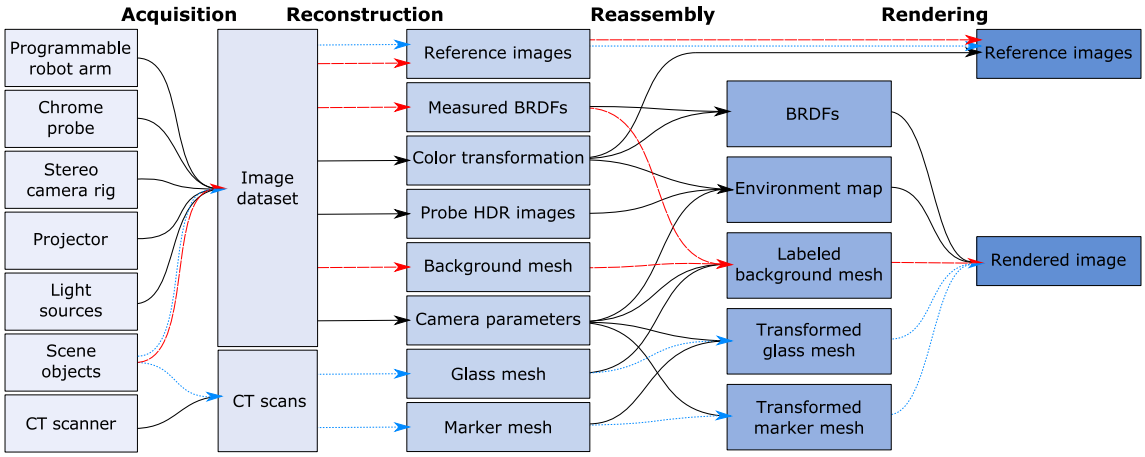

Fig. 2. Overview of our digitization pipeline in four main stages: acquisition, reconstruction, reassembly, and rendering. A video presentation of our pipeline is available in supplementary Visualization 1. Colored arrows show the path through the pipeline of transparent objects (dotted blue) and non-transparent objects (dashed red).

tion. The latter is particularly useful for observing how light refracts through the glass. The chosen case is also of particular interest, since glass is present in many intended applications of optical 3D acquisition. Considering the highly multidisciplinary nature of our work, we have released our dataset (http://eco3d.compute.dtu.dk/pages/transparency). This facilitates further investigation by other researchers of the different steps of our pipeline with the possibility of a quantitative feedback at the end of the process.

A. Related Work and Contributions

Researchers occasionally compare renderings with photographs to provide a qualitative verification of a presented rendering technique. The work by Phong [6], Goral et al. [7], and Takagi et al. [8] are early examples of this trend. A procedure to bring a rendered image close to a photograph was first presented by Meyer et al. [9]. In this work, likeness of images was evaluated perceptually by human observers. Pixelwise comparison of photographs with rendered images is surprisingly uncommon. The few examples we have found are by Rushmeier et al. [10], Karner and Prantl [11], Pattanaik et al. [12], and Jones and Reinhart [13, 14]. These examples build on the rendering framework described by Greenberg et al. [15]. Employing such a framework for more complex scenes is a long and tedious process [16]. The key issue is that a scene specification is expected as an input.

Several problems arise as a result of not having correspondence between the physical and the digital scene. Misalignment due to inaccurate scene and viewing geometry and inaccurate orientation of the lighting environment are some of the essential problems identified in previous work [17, 18]. One way to deal with this problem is to calculate error for image patches when evaluating results [13, 19, 20]. As opposed to this, our digitization pipeline (Fig. 2) provides both reference photographs and correspondingly calibrated scene and viewing geometry so that pixelwise comparison becomes meaningful.

Pixelwise comparison of rendered images with photographs is not only useful for quantifying the photorealism of a rendering in terms of error measurements. We find it particularly useful for improving the digitization pipeline. The fact that our pipeline enables quantitative evaluation led us to more specific contributions in its different steps. These contributions are mostly in the reassembly and are as follows. (a) A cross-modality marker-based placement approach, enabling accurate placement of objects scanned with one modality into scenes scanned with

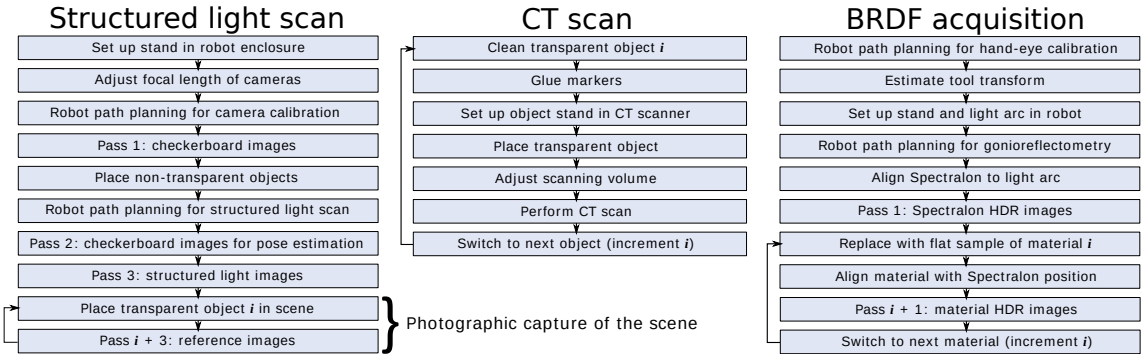

Fig. 3. Our workflow for scanning the geometry of non-transparent objects and collecting reference images (left), for scanning the geometry of transparent objects (middle), and for measuring material reflectance properties (right).

another modality. (b) A soft object deformation technique dealing with surface intersections after object placement, which is critical for scenes containing transparent or translucent objects. (c) A micropolygon labeling approach for assigning BRDFs to acquired geometry. (d) A color calibration scheme enabling use of spectral optical properties for calculating reflectance, transmittance, and absorption. (e) Perspective unwrapping of mirror probe images to improve precision when the environment is not very distant. (f) Use of analysis by synthesis for fine-tuning physics-based optical properties.

Digitization is most often unimodal and tailored toward objects with a specific type of surface reflectance behavior [1]. While unimodal techniques are becoming more versatile [21–23], objects with a transparent material like glass still pose challenging problems. Their reflectance behavior is so different that they require an entirely different modality, such as computed tomography (CT) [24]. The transparent object must then be removed from the scene to be scanned elsewhere. In the meantime, the surrounding scene can be scanned with a more common technique. However, as the transparent object takes most of its appearance from its surroundings, it must be repositioned in the surrounding scene (physically and digitally) if we are to take reference images for comparison with rendered images. The purpose of our scene reassembly is to address this type of issue.

Our digitization technique is multimodal. Currently, such techniques seem to exist only in the context of sensor fusion [25–27]. Here, the goal is to optimize reconstruction by fusing data from different sensor modalities with complementary characteristics. Even so, the different modalities see the same object and thus work for materials with a similar reflectance behavior. The challenge is then mostly in registration of the scans. In their final remarks and suggestions for future work, Weinmann and Klein [1] discuss possible ways of combining multiple techniques tailored to different types of surface reflectance. Our pipeline is a different way to take a step in this direction.

In summary, our work makes it possible to perform multimodal digitization and scene reassembly in such a way that rendered images of the reassembled scene can be quantitatively compared to photographs of the original. This enables us to provide the first empirically founded investigation of the appearance accuracy of objects digitized using a non-optical scanner.

2. DIGITIZATION PIPELINE

We divide our pipeline into four stages: (1) acquisition, (2) reconstruction, (3) reassembly, and (4) rendering. Figure 2 provides an overview. As illustrated, transparent objects (dotted blue arrows) and non-transparent objects (dashed red arrows) take different paths through the pipeline. The acquisition stage includes structured light scanning of non-transparent objects, CT scanning of transparent objects, gonioreflectometric reflectance measurements, and photographic capture of environment, color chart, and scene reference images. Figure 3 provides details of our workflow in these acquisition steps (except the simpler captures of environment and color chart). The second stage includes reconstruction of surface meshes, material BRDFs, and color space. The third stage is reassembly of the digital scene consisting of geometric objects, material appearance properties, and environment map. The fourth and final stage is rendering and comparison with reference images.

Our acquisition stage requires an elaborate hardware setup. We assemble the physical scene in a black light-proof enclosure. This has five LED light tubes for scene lighting, which we capture by high dynamic range (HDR) imaging of a light probe. To acquire non-transparent geometry inside this enclosure, we use a structured light scanner consisting of a toe-in stereo camera rig and a light projector mounted on a robotic arm [28, 29]. We chose a converging camera configuration (toe-in) to increase the overlap of the fields of view so that we get a denser point cloud per stereo view. Together with an LED based illumination arc, we also use this camera rig with exact control for measuring isotropic BRDFs. For transparent objects, we use a CT scanner. In the following subsections, we describe the individual steps of the pipeline with focus on details required for reproducibility and on non-standard techniques that we introduce.

A. Camera Calibration and Settings

The camera system is calibrated using a standard technique [30]. Our calibration board is an 11 by 12 black-and-white checkerboard. For the intrinsic calibration (Pass 1 of Fig. 3, left), we include a large variety of views to estimate good lens distortion coefficients. To facilitate stereo calibration, we also ensure that both cameras have the calibration board fully in view. For extrinsic calibration (Pass 2 of Fig. 3, left), we balance good coverage of the scene and good coverage of the calibration board. Since we cannot change the camera system while collecting data, we

chose a small aperture to ensure that background and projected structured light patterns are always in focus from all views. The full setup is in a dark room environment to eliminate external light, so we use a long shutter time (600 ms) to obtain sufficient exposure. A slight noise component is present in the images, but this is considered negligible. Finally, we use the estimated distortion coefficients to remove distortion from all images in the dataset so that subsequent algorithms may assume a pinhole camera model.

To avoid any compression or manipulation of the images by the camera software, in particular automatic color correction, we read the raw sensor data directly. We use bilinear interpolation to reconstruct RGB images from the raw Bayer pattern images. By doing this, we obtain a consistent RGB color space. Moreover, the raw sensor data is linear and correlates directly with radiometric quantities, which allows for better BRDF and environment map estimation in later stages of our pipeline.

We capture radiometrically relevant parts of our dataset in HDR by stacking multiple exposures [31]. More specifically, we stack 11 exposures at one-stop intervals ranging from 1 to 2048 ms. For the other parts of the dataset, we capture a single image at an exposure time of 600 ms.

B. Surface Reconstruction from Structured Light

We use a standard Gray code structured light approach to generate raw point clouds for a scene [32, 33]. With camera parameters from the calibration, we transform these point clouds into the same world coordinate system.

To reconstruct one connected triangle mesh from the point clouds, we merge them into a single point cloud and perform screened Poisson reconstruction with trimming and an octree depth of nine [34]. This technique requires point normals, so before the merging we generate normals for each point cloud as follows. We resample the point cloud down to 100,000 vertices via Poisson disk sampling [35] and then compute normals via planar fitting to a nearest neighborhood of 500 points ($\sim$16 mm radius). We then reorient all the normals according to the location of one of the cameras and transfer them back onto the original point cloud. This procedure ensures smooth continuous normals, necessary for a good performance of the mesh reconstruction algorithm. As we rely on smoothing, we cannot reconstruct features in the mesh with the same physical size as the alignment error accumulated from structured light and calibration. The aim of the chosen constants was to preserve features by striking a balance between too noisy and too smooth. The operability of the pipeline is however not sensitive to the choice of these constants.

C. Material BRDF Reconstruction

We assume that all non-transparent materials in the scene are opaque and isotropic, so we model their reflectance properties by BRDFs. To acquire a BRDF, we combine traditional canonical gonioreflectometric sampling [36] with a BRDF interpolation (reconstruction) technique [37]. We follow the workflow outlined in Fig. 3 (right). A light arc illuminates material samples from 11 unique inclinations, evenly distributed from 7.5° up to 90° with 7.5° steps. We place a flat material sample at the center of the circle partly traced by the light arc. Using the cameras mounted on the robot, we then measure radiance reflected by the sample across one octant of a sphere. The center of this sphere coincides with that of the light arc, while its radius is slightly larger to avoid collision between the robot and the arc. The robot moves in steps of 7.5° and captures 11 HDR images of the sample per step, one for each light direction. In total, this yields 2,783 HDR images per material. We avoid tangential and zenith viewing directions (90° and 0°, respectively). In the former case, no reflected radiance should be visible, while in the latter the light arc occludes the view of the sample.

The 2,783 observations are too few to faithfully represent the BRDF of a material in a photorealistic rendering. We need an interpolation scheme to fill the entire $(90 \times 90 \times 180)$ Mitsubishi Electric Research Laboratories (MERL) format BRDF look-up table [38]. The reconstruction method by Nielsen et al. [37] is our interpolation scheme. First, we use each of the 100 BRDFs in the MERL-dataset [38] as sample points in a $90 \cdot 90 \cdot 180 = 1{,}458{,}000$ dimensional space. The nonlinear mapping of Nielsen et al. [37] is then applied to each of the samples. The mapped samples are ordered as rows of a matrix $\mathbf{X} \in \mathbb{R}^{m \times d}$ where m is the number of BRDF samples and d is the dimension of the space. The zero-mean matrix is computed as $\mathbf{X} - \bar{\mathbf{x}}$, with $\bar{\mathbf{x}}$ being the sample mean. From this, the singular value decomposition $\mathbf{X} - \bar{\mathbf{x}} = \mathbf{U}\mathbf{\Sigma}\mathbf{V}^T$ is used to compute the eigenvectors and eigenvalues of the covariance matrix of $\mathbf{X} - \bar{\mathbf{x}}$, which are given as the columns of $\mathbf{V}$ and the diagonal elements of $\mathbf{\Sigma}$, respectively. This is effectively a principal component analysis (PCA), where the eigenvectors are the principal components. A matrix composed of the scaled principal components as columns are computed as $\mathbf{Q} = \mathbf{V}\mathbf{\Sigma}$.

Now, the full BRDF can be reconstructed from this principal component space by projection. Let $\mathbf{x}' \in \mathbb{R}^n$ be n BRDF observations measured for a given material. Then, let $\bar{\mathbf{x}}' \in \mathbb{R}^n$ be the mean values and $\mathbf{Q}' \in \mathbb{R}^{n \times k}$ be the scaled eigenvectors corresponding to the direction pairs of those n observations. A vector $\mathbf{c}$ which spans the full space can be constructed by finding the linear combinations of principal components that best approximate the n observations. We do this by solving the linear least-squares optimization problem given by

$$\begin{aligned} \mathbf{c} &= \arg\min_{\mathbf{c}} \|(\mathbf{x}' - \bar{\mathbf{x}})' - \mathbf{Q}'\mathbf{c}\|^2 + \eta\|\mathbf{c}\|^2 \\ &= (\mathbf{Q}'^T\mathbf{Q}' + \eta\mathbf{I})^{-1}\mathbf{Q}'^T(\mathbf{x}' - \bar{\mathbf{x}}'). \end{aligned}$$

Note that by adding a penalty η to the norm of $\mathbf{c}$, this effectively becomes a Tikhonov regularized least squares. Now, the full, mapped BRDF is reconstructed as $\mathbf{x} = \mathbf{Q}\mathbf{c} + \bar{\mathbf{x}}$. The inverse of the nonlinear mapping applied to $\mathbf{X}$ is applied to $\mathbf{x}$ to get the actual, unmapped BRDF of the material. The described approach is applied to every single non-transparent material in the scene in order to obtain models of their reflectance properties.

This approach assumes that the MERL database encompasses the class of materials present in the scene. Effectively, this is a practical compromise between dense, unbiased, canonical BRDF sampling and fast, inferred BRDF sampling. This enables us to obtain high confidence BRDFs in a matter of a few hours.

D. Surface Reconstruction from CT

In our dataset, we have three glass objects: a sphere, a teapot (pot and lid) and a bowl (bowl and lid), for a total of five pieces. All objects have spherical plastic markers glued onto their outer surface. We CT scan each glass piece to obtain X-ray radiographs and use the CT PRO 3D reconstruction software from Nikon Metrology to obtain a volumetric image for each piece. The resolution of the reconstructed volume is up to 1000^3 voxels. Due to beam hardening, high density differences between materials lead to streak artifacts [39], especially around our markers and at the top and bottom of the objects (see Fig. 4). We account for these artifacts in the volumetric segmentation.

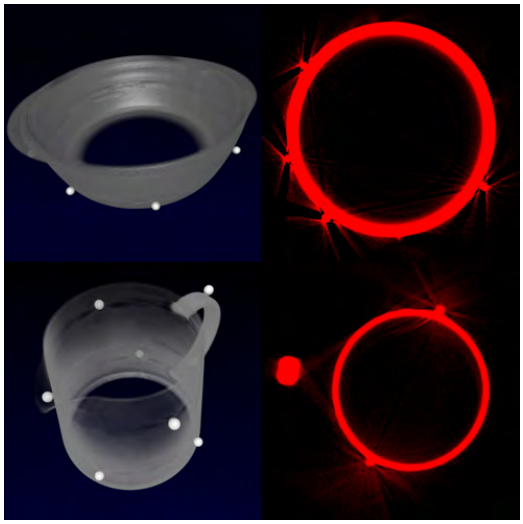

Fig. 4. CT scans of the bowl (top row) and the teapot (bottom row) with markers glued onto them. In the left column, visualized using a 1D transfer function. Note the different density of the markers. In the right column, a slice scaled to display streak artifacts.

From a CT scan, we generate two triangular meshes with vertex normals: one for the glass object and one the plastic markers. Figure 5 provides an overview of our procedure. We start with the markers, which appear as elements of higher density in the scan. We preprocess the scan by clamping all the values under a certain threshold to zero and then create a mesh using dual contouring [40]. Generating the glass mesh is more cumbersome. We also use dual contouring in this case, but because of the streak artifacts (Fig. 4) it is not possible to isolate the glass mesh via a threshold. Instead, we use a lower threshold that only removes noise, then estimate the marker positions, and use these to remove the markers from the glass mesh.

To estimate marker positions, we determine a series of center/radius pairs $(\mathbf{c}_i, r_i)$ by fitting a multi-sphere model to the marker mesh vertices using a tuned random sample consensus (RANSAC) algorithm [41]. We then carve a hole by excluding all the triangles that are inside a sphere with center $\mathbf{c}_i$ and radius $(1+\epsilon)r_i$, where ϵ is usually in the 0.5 to 0.75 range. We store the marker positions $\mathbf{c}_i$ so that we can use them to transform from the local coordinate system of the glass object to the world coordinate system (see Section F).

After removing the markers, the glass meshes still have aliasing artifacts. To deal with this issue, we first decimate the mesh down to 1% of the original vertices via quadric edge collapse. The holes are then easy to close by identifying the edge loops surrounding each hole and filling these with triangles. We then introduce a subdivision-decimation loop with alternating $\sqrt{3}$-subdivision [42] and decimation to 33% of the original vertices. We perform this subdivision-decimation operation four times to obtain a cleaned mesh. The decimation removes unwanted high frequency features from the mesh. Thus, we generate smooth meshes at the cost of some geometric precision. We are again trying to strike a balance between reconstruction error and too much smoothing. In Section 4, we compare our method with a different cleaning procedure that better preserves geometry.

Fig. 5. Reconstruction from CT with stages illustrated using Phong shading (top row) and wireframe shading (bottom row). After estimating the marker mesh (first column) and fitting spheres to the markers, we reconstruct the object mesh (second column). To eliminate noise, we first simplify the mesh (third column) and then close the holes and apply our subdivision-decimation loop to get the final object mesh (fourth column).

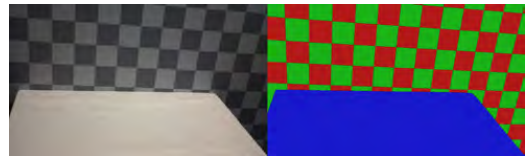

Fig. 6. Labeling of the image to the left results in the label image to the right. Each color in the label image represents a label that we assign a BRDF to. The black edges between labels indicate areas where we apply a nearest neighbor method.

E. Scene Reassembly for Non-Transparent Objects

Two operations are necessary to prepare the background mesh for rendering: labeling and deformation. In the labeling, our objective is to identify BRDFs and label each face of the mesh with a BRDF. Assuming a scene with a small number of known BRDFs, we apply edge detection and watershed on the images of the scene to segment BRDF boundaries. Shadows, specular highlights, and different viewing angles of the scene complicate fully automatic BRDF identification. Our approach gets us most of the way, but we manually correct any residual misclassification. Figure 6 shows a label image produced by our labeling technique.

The label images can be used in multi-view projective texturing of the background mesh. However, we would like to precompute the view and label selection instead of doing it millions and millions of times while rendering. To avoid uv-unwrapping of the mesh for storing precomputed labels, we take an approach inspired by micropolygon rendering [43]. We project each vertex of a face onto the label images of the scene and select the face BRDF according to the image label that most of the face vertices were projected to. If a vertex projects to an unknown label, we resolve it by a nearest neighbor search. Since faces around material boundaries overlap multiple materials,

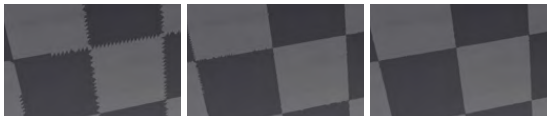

No subdivision One subdivision Two subdivisions

Fig. 7. Subdividing the mesh dissolves unwanted boundary sawtooth artifacts that originate from the BRDF labeling.

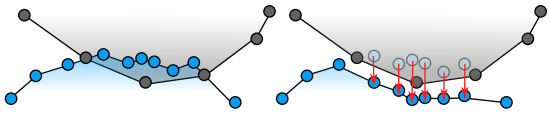

Fig. 8. Deformation of background mesh, where we push the background vertices down to avoid mesh intersection.

we get sawtooth artifacts. We dissolve these by subdividing the mesh until the rendered triangles are smaller than the surface area observed in a pixel, see Fig. 7.

When applying physically based rendering, we observed intersections between background scene and glass meshes. This could be due to small errors in reconstruction and positioning, or perhaps the harder glass objects press down the tablecloth when placed for reference imaging. It causes significant visual artifacts since the rendering exposes all surfaces of a transparent object. To eliminate these artifacts, we accommodate the hard object (glass) by deforming the soft object (tablecloth), see Fig. 8. To deform the soft object, we need a "down" direction in which to push the vertices. We first find contact vertices. These are vertices in each mesh that are close to any vertex of the other mesh. We consider vertices close if the distance between them is less than 7% of the bounding box diagonal of the hard object. Using least squares regression, we fit a contact plane to the contact vertices of the soft object. We set the sign of the contact plane normal so that the upper half-space contains the center of the hard object bounding box. Projection of a contact vertex to the normal of the contact plane then measures the height of the vertex. For each soft object contact vertex $\mathbf{x}$, we find the nearest hard object contact vertices and push $\mathbf{x}$ down below the lowest one of these.

F. Scene Reassembly for Transparent Objects

To reposition the glass objects in the scene, we rigidly transform the meshes reconstructed from CT to the world coordinate system of the background mesh. We obtain this transformation by matching markers in the stereo images with the marker coordinates $\mathbf{c}_i$ computed during reconstruction from CT (see Section D).

To find the markers, we employ a size invariant circle Hough transform [44]. This works well for our dataset, where the markers show high contrast against their surroundings. We match markers in the left and the right images via Sampson distance [45]. Using this technique, markers on the same epipolar line lead to false positives, so we manually inspect the result. We also manually discard detected markers that are visible through the glass, as the refraction would lead to incorrect positioning. Markers in both stereo images with no match are discarded. The result is a set of matched markers in image coordinates as seen in Fig. 9 (bottom left). We then triangulate the matched markers

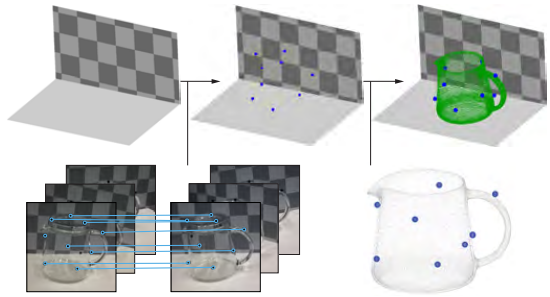

Fig. 9. Repositioning a CT scanned object in the background scene. We identify and match the markers in the stereo image pairs and calculate their corresponding 3D points. Pairing these with marker coordinates from the CT scans, we transform the CT scanned piece of an object into the world coordinate system.

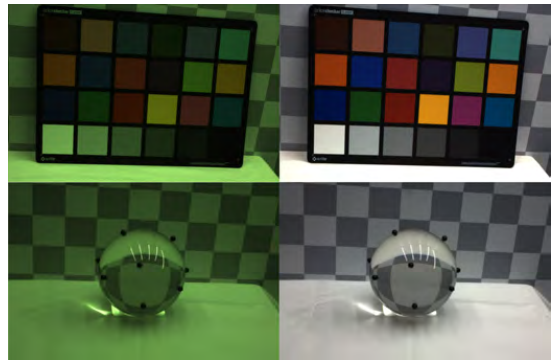

Fig. 10. Color calibration: raw images (left) and color corrected images (right). The camera sensor is particularly sensitive to green.

from the stereo views and gather them in clusters of 3D points. We remove outliers via their distance from the cluster centers, and for each cluster we select the point with the lowest reprojection error. An example of the points and clustering is shown in Fig. 9 (top middle).

We manually pair the 3D marker coordinates from the images with the marker coordinates $\mathbf{c}_i$ from the CT scans. We perform Procrustes analysis [46] on the two point sets, excluding reflection, since we assume a rigid transformation applied to each vertex of the mesh. The bowl and the teapot are composed of multiple pieces. For these objects, we compute the transformation individually for each piece. The result of the object transformed into the scene is shown in Fig. 9 (top right). We found that in order to have low error in the transformation the chosen markers should sample the surface evenly and be visible from most views.

G. Color Calibration

Images are only quantitatively comparable if they live in the same color space. Thus, we must ensure that our radiometry-dependent data, namely reference images, environment map, and BRDFs, are in the same color space. We do this by imaging

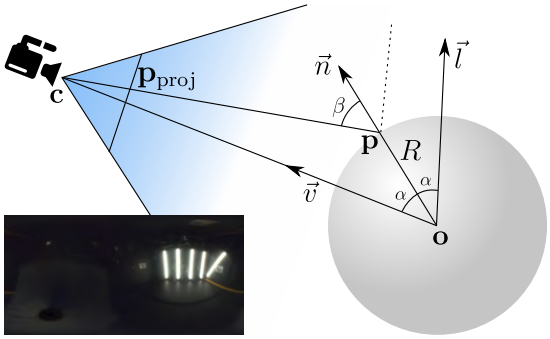

Fig. 11. Unwrapping of a spherical probe. We know the sphere radius R from specification, the camera position $\mathbf{c}$ through calibration, and the sphere center $\mathbf{o}$ by triangulation. Radiance at $\mathbf{p}_{\text{proj}}$ in our image then corresponds to the environment map direction $\vec{l}$. The result for the robot enclosure is in the lower left corner in latitude-longitude panoramic format (here tone-mapped).

a color chart of precisely known colors. More specifically, we use second degree root-polynomial color correction [47] based on a 24 patch ColorChecker Classic from X-Rite. This provides a matrix that transforms from camera RGB to XYZ, where we assume illuminant D50 when specifying the XYZ values of the colorchecker. With the assumption of illuminant D50, we can transform colors to the CIE L*a*b* color space and then compute color difference using the ΔE_{00} metric [48]. We use this to refine our result by minimizing ΔE_{00} using the Broyden-Fletcher-Goldfarb-Shanno (BFGS) algorithm [49]. The result is in Fig. 10. The average color difference is $\Delta E_{00} = 1.97 \pm 1.21$, which is larger than 1 JND (just noticeable difference) [50], but we find it acceptable.

Since we work with glass objects (and chrome, see Section H), we need refractive indices to determine reflectance, transmittance, and absorption properties. Refractive indices can be found per wavelength in tables of research papers. To use such spectral optical properties together with our trichromatic image data, we integrate them to CIE RGB using the CIE RGB color matching functions listed by Stockman and Sharpe [51]. It is important to normalize these functions [52] and to use RGB rather than XYZ [53]. This is because a refractive index is not a color, but rather a quantity that in trichromatic representation should resemble a sparse sampling of the spectrum. Thus, as recommended by other authors [54], we choose CIE RGB as our rendering color space. After transforming our image data from camera RGB to XYZ, we therefore convert them to CIE RGB [55]. As a final step, we apply Bradford chromatic adaptation [50], adapting to the originally assumed illuminant D50, so that renderings and reference images get closer to real life appearance.

H. Environment Lighting

To capture the lighting observed in the reference images, we use a method similar to the mirror probe technique [56]. However, we use a pinhole camera model for probe image unwrapping instead of the standard orthographic model. Our pipeline enables this as we have a calibrated camera and know its position relative to the photographed mirror probe. With the pinhole model, we obtain a more precise estimate of the environment lighting. The environment map is generated from HDR images and stored in latitude-longitude panoramic format [50]. We use a polished grade G100 chrome bearing ball as mirror probe.

An environment map represents an infinite area light and maps a direction to a texture element (a texel). To do unwrapping, we map each texel direction $\vec{l}$ to the corresponding pixel position $\mathbf{p}_{\text{proj}}$ in a light probe image. Given the configuration illustrated in Fig. 11, we have

$$\vec{v} = \frac{\mathbf{c}-\mathbf{o}}{\|\mathbf{c}-\mathbf{o}\|},\ \vec{n} = \frac{\vec{v}+\vec{l}}{\|\vec{v}+\vec{l}\|},\ \mathbf{p} = \mathbf{o} + R\vec{n},\ \mathbf{p}_{\text{proj}} = \mathbf{M}\,[\mathbf{p}^T\ \ 1]^T,$$

where camera matrix $\mathbf{M}$ and camera position $\mathbf{c}$ are available from our calibration. The radius of the sphere R is available from the bearing ball specification, and we find the center of the sphere $\mathbf{o}$ by manually annotating the sphere and then triangulating it. We assume that the distance to the actual light along $\vec{l}$ is equal to the distance between camera and sphere $\|\mathbf{c}-\mathbf{o}\|$. This assumption works well in practice, leading to an error smaller than the uncertainty of $\mathbf{o}$ caused by the triangulation. With the original orthographic camera model, we can reconstruct the lighting for all directions except one ($-\vec{v}$). In our model, we cannot reconstruct the lighting for a set of directions ($\vec{n} \cdot \vec{v} \leq R/\|\mathbf{c}-\mathbf{o}\|$), so we set them to black. Since we do our unwrapping in world space, we can combine contributions from multiple camera views with no need to align them afterwards.

The environment map is color corrected according to Section G, which enables us to correct for the angularly dependent reflectance of chrome. The correction is to divide by Fresnel reflectance, which we compute during unwrapping. As input for Fresnel's equations, we use the angle β between $\mathbf{c}-\mathbf{p}$ and $\vec{n}$ and the complex refractive index of chrome [57] converted from spectrum to CIE RGB. The result is shown in the inset of Fig. 11.

I. Rendering

We render images using progressive unidirectional path tracing [58, 59] implemented in OptiX [60]. The captured HDR environment map is the sole light source in our scene [56]. When rendering non-specular materials, we importance sample the environment map to get direct illumination and use sampling of a cosine-weighted hemisphere to get indirect illumination. From our labeling, we have one BRDF attached to each triangle in our scene. For non-transparent objects, we use our measured BRDFs tabulated in the MERL format [38]. To terminate paths probabilistically, we use Russian roulette based on the bihemispherical reflectance of each measured BRDF. This reflectance is calculated in a preprocessing step using Monte Carlo integration. We deal with transparent objects in the usual way, setting reflectance and transmittance according to Fresnel's equations of reflection and Bouguer's law of exponential attenuation. Given their small surface, we were unable to estimate a BRDF for the markers. Instead, we render them as glass with all refracted rays being absorbed.

3. ANALYSIS BY SYNTHESIS

The ability to render images comparable to photographs enables us to use our pipeline for improving parameter estimates through analysis by synthesis. As an example, we need a scaling factor for our HDR environment map as it measures relative radiance [31]. We estimate this factor by taking ratios of references

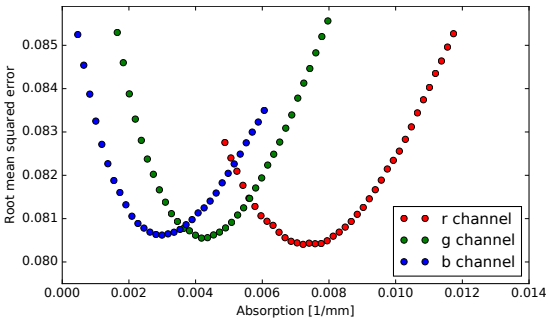

Fig. 12. Analysis by synthesis to estimate absorption of the glass bowl. We run renderings in low resolution and change the absorption in each color channel one at the time. In the case of the bowl, the blue channel is the most sensitive one.

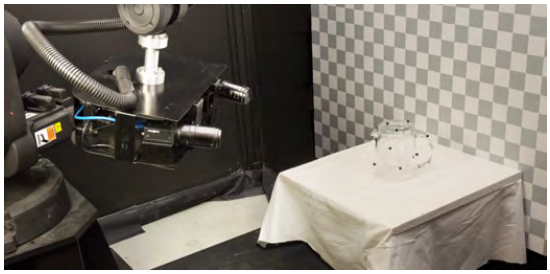

Fig. 13. Scene with checkerboard backdrop, lighting, glass teapot, and stand with table cloth observed by two cameras mounted on a 6-axis industrial robot arm.

and renderings with the background scene alone. Another example is estimating real and imaginary parts of glass refractive indices. As analysis by synthesis is fundamentally ill-posed [61], we take our outset in physics-based initial guesses such as Schott K5 crown glass (sphere and teapot) and soda lime glass (bowl). Spectral refractive indices for these glasses were obtained from an online database (http://refractiveindex.info) and converted to CIE RGB. All parameters were estimated using different views than the ones in our comparisons of renderings with references.

As an example of our analysis by synthesis, we plot the evolution of the root-mean-squared error (RMSE) for different renderings of the glass bowl in Fig. 12. For each rendering, we vary a trichromatic component of the absorption coefficient (which directly relates to the imaginary part of the refractive index). We identify a distinct minimum in the error for each channel, with a slightly larger uncertainty in the red channel. The minimum values in this figure were used in our renderings of the glass bowl. We apply the same analysis to the teapot and the sphere.

Given an initial guess for a parameter, we can employ standard optimization algorithms, defining the RMSE between the reference and the rendering as a cost function to minimize. To reduce rendering times, the evaluation of the cost function can be calculated on a downsampled image or limited to a specific patch of the images. Various general optimization algorithms exist for minimizing expensive cost functions [62].

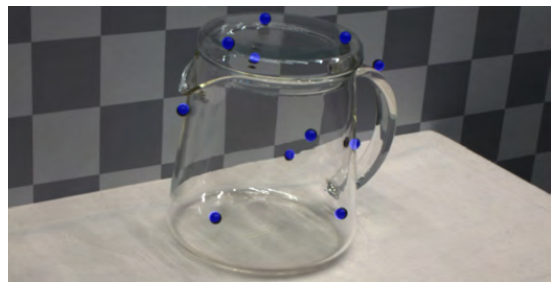

Fig. 14. Markers rendered in blue and added to the reference image to validate marker positions by looking at pixel offsets.

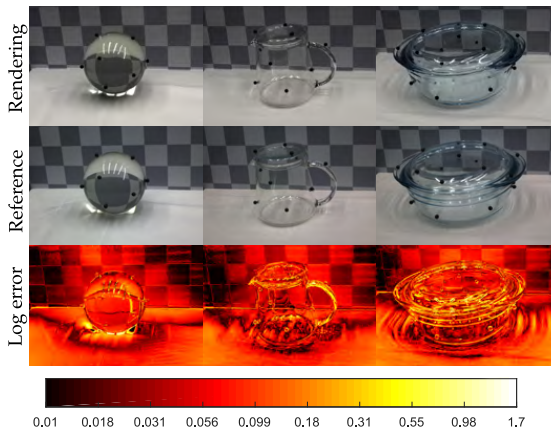

Fig. 15. Pixelwise error for three rendering-reference pairs. Error is the ℓ^2-norm of 32-bit per channel RGB images, visualized using a base 10 logarithmic scale.

4. RESULTS

Our scenes consist of a backdrop, a stand, and a glass object (with markers) placed on the stand. The backdrop is a 30 by 20 white-and-gray checkerboard print on 120 cm by 80 cm semi-matte cardboard and the stand is a tabletop with a white cloth. An example scene is depicted in Fig. 13. We implemented our reconstruction and reassembly procedures as a modular software pipeline and computed all rendered images using our path tracer. As illustrated in Fig. 2 and mentioned in Section G, we color correct both rendered images and reference images to have a meaningful perceptual comparison. Figure 14 compares markers in a reference image with rendered markers to validate our marker positioning. For the teapot, the average distance between the markers from stereo and the transformed markers from CT is 0.43 mm.

Figure 15 presents pixelwise comparisons of reference images and rendered images. The error images allow us to spot subtle differences not easily noticed in a perceptual comparison, such as the slight misalignments in geometry and highlights. As reference photographs were not captured in HDR, we clamp the renderings correspondingly. This means that areas of strong light intensity, such as highlights and intense caustics, appear black in the error images.

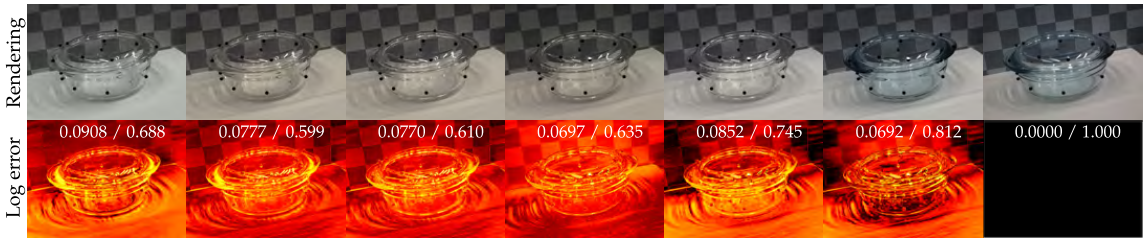

Fig. 16. Qualitative (top) and quantitative (bottom) step-by-step evaluation of our reassembly techniques. The log error images have the same format as in Fig. 15 and the reference photograph is in the rightmost column (g). In each column, we provide root-mean-squared error and structural similarity index (RMSE / SSIM). Both measures attain their best score in our final result (f).

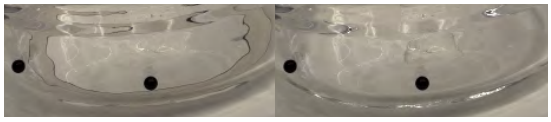

Fig. 17. Zoom-in of Figs. 16 (b) and (c) to emphasize the effect of our background deformation.

Fig. 18. Zoom-in of Fig. 16 (c) and (d) to emphasize the effect of our perspective unwrapping of the environment map.

Figure 16 exemplifies the impact on error images of some of our contributions. In Fig. 16 (a), we only reposition the glass object in the background scene and apply color correction (Sections F and G). This means that we use Lambertian materials (with bihemispherical reflectances from the measured BRDFs), an orthographic unwrapping model of the environment map, and no chrome reflectance correction or analysis by synthesis optimization. We compare to the reference image in Fig. 16 (g), with error images as in Fig. 15. Figure 16 (b) shows the impact of using measured BRDFs (Section C), resulting in a more accurate representation of the folds of the cloth in the background scene (top image) and an overall reduction of the error (bottom image). In Fig. 16 (c), we add deformation of the background mesh (Section E), which ensures that the background mesh does not poke through the glass surface (see a close-up in Fig. 17). Additionally, we can see how this improves the error on the lid of the bowl, because of refraction of light in the glass. The next step, Fig. 16 (d), shows the impact of our modified environment map unwrapping (Section H) against the standard orthographic unwrapping rotated according to our camera parameters. A close-up is available in Fig. 18. Our modified unwrapping provides a better shape and alignment of highlights and caustics. Partially due to the assumption of infinitely distant environment light, some alignment artifacts persist. In Fig 16 (e), we show the

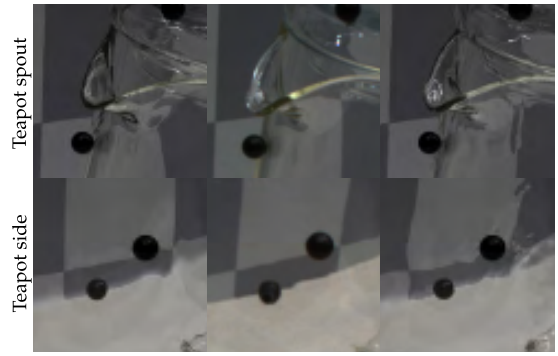

Fig. 19. Trade-off in mesh reconstruction. If we smooth more, we get less distortion in the refractions, but less precision in the mesh geometry. From left to right: Rendering with smoothing, reference image, rendering without smoothing.

effect of correcting for chrome reflectance in our environment map reconstruction. Quantitatively, this changes the distribution of the error (bottom image). On the cloth, the exposure increases, exposing the caustics misalignment. On the backdrop, the error reduces. Interestingly, the structural similarity index (SSIM) improves while the RMSE worsens. Finally, in Fig. 16 (f), we use analysis by synthesis to adjust glass absorption. This improves the glass appearance, but it also leads to slight color changes in other parts of the scene due to indirect light paths. Because of this global influence, the analysis by synthesis introduces slightly too much absorption to compensate for the slightly too bright tablecloth.

As an example of how our pipeline can be used to validate existing algorithms, we investigate the case of glass object reconstruction. In Fig. 19, we compare two different reconstruction methods with focus on two parts of the teapot scene. Smooth reconstruction refers to the procedure described in Section D. The other procedure is to simply decimate the reconstructed mesh to 2.5% of the original vertices and apply Taubin smoothing [63]. This removes the high frequencies of the noise but much noise is still present in the midranges leading to wobbly refractions.

Rendering Reference Log error (as in 15)

Fig. 20. Material transitions: error lines along checker edges and along the boundary between tablecloth and backdrop.

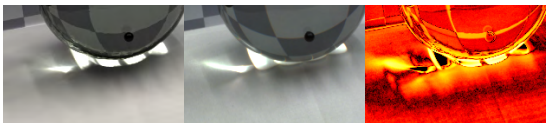

Rendering Reference Log error (as in 15)

Fig. 21. Effect of separating markers from glass (refracted light close to marker) and of not accounting for subsurface scattering (dark areas close to caustics).

Our method in Section D reduces far more noise, but this is at the cost of greater changes to the overall shape. We note that a refractive object with a simple geometry is very hard to reconstruct automatically if fidelity and almost no noise are both required.

5. DISCUSSION

Since our pipeline enables us to compare renderings with photographs, we can identify problems in acquisition, reconstruction, and rendering that would otherwise have been hard to find. Camera calibration issues, for example, reveal themselves as error lines along edges (visible in Fig. 20). Color calibration issues reveal themselves as color shift. Such issues led us to more careful camera calibration procedures and the choice of root-polynomial color correction. Qualitative comparisons revealed artifacts in surface reconstruction, mesh intersections calling for deformation, misplacement of highlights, color shift due to chrome reflectance, and missing absorption in renderings (Figs. 16–19). Quantitative comparisons confirmed improvement due to perspective unwrapping of light probe images and led to analysis by synthesis.

The comparison with reference photographs before and after deformation (Fig. 17) to some extent validates our soft object deformation technique. Further validation would be desirable, but it is difficult to come up with a different experiment. Some kind of soft, durable memory foam with a scannable surface would be required as the soft object would otherwise change shape again once the hard object is removed. Our validation only supports that the cloth appearance (as observed through glass) is represented more faithfully after deformation.

We found analysis by synthesis useful for estimating parameters with an outset in physics-based initial guesses. The results in Fig. 12 show that we can estimate optical properties for a given material and use them in a different setting (right part of Fig. 1). The precision of the estimation varies with the impact of the property on the overall error, and the estimated parameters may compensate for unrelated errors. In this regard, specific scene configurations could be used to favor estimation of a particular parameter.

The most important limitation of our method is that we describe materials as large patches of isotropic BRDFs. In our renderings, this assumptions works well for the checkerboard backdrop but not for the cloth, where we both have subsurface scattering effects and probably anisotropy due to the weave structure of the cloth. Fig. 21 reveals that the rendered image is too dark in areas surrounding caustics. As seen in the light refracted through the sphere in the vicinity of the marker, our processing of the glass object to separate glass from markers causes some imprecision in the geometry. We believe this mainly influences the shape of the caustic. The bleeding of the caustic to areas that are much darker in the rendered images looks like backscattering from the table beneath the cloth. We refer to this as a kind of subsurface scattering.

Another limitation is seen at the transition between non-connected elements. It is visible in the renderings at the boundary between the cloth and the backdrop (see Fig. 20). The problem derives from the fact that the cloth and the backdrop were too close to each other during dataset acquisition. This resulted in the Poisson mesh reconstruction interpreting them as a continuous object instead of two separate ones. The problems around markers (Fig. 21) are also due to transition of materials. The marker removal and whole closing in the glass surface reconstruction interrupts the original shape of the surface. Furthermore, the markers are glued onto the glass surface, and the glue is not considered in the reconstruction and renderings. The marker glue problem is magnified by the glass refraction.

6. CONCLUSION

We have proposed a pipeline for multimodal scene digitization. Our work addresses the entire process from acquisition of the original objects, through reassembly of the digital scene, to accurate modeling of camera and environment. While the pipeline required several non-trivial steps, the benefits are correspondingly great since we can perform pixelwise comparisons between rendered images and photographs of the corresponding physical scene. This means that we have the means to quantitatively assess the accuracy of an acquired model based on comparison with empirical evidence. We believe this kind of quantitative assessment has not previously been possible for transparent objects. In applications like cultural heritage preservation and industrial inspection, where the accuracy of a digitization is important, such comparison with empirical evidence is crucial.

To the best of our knowledge, our work is also the first work to quantify the photorealism of a heterogeneous scene requiring multimodal acquisition.

Our dataset is publicly available so that others can test new techniques for the different steps of the pipeline with quantitative feedback based on photorealistic rendering. The fact that one can use off-the-shelf rendering techniques for improving the different steps of a multimodal digitization pipeline is perhaps the most important benefit of our work. An application of the full pipeline is the virtual product placement in Fig. 1. Another important application is the estimation of radiometric properties through analysis by synthesis. The ability to accurately estimate optical properties through computation rather than measurement, which might require specialized equipment, is likely to greatly simplify the digitization of radiometrically complex objects. In this paper, we estimated absorption and refractive indices of transparent objects, but analysis by synthesis could be equally useful for other materials with non-trivial BRDFs. This is another key benefit of our work that we believe is well worth exploring in the future.

Fig. 22. Comparison of renderings and photographs as in Fig. 1 (left), but with more views.

Funding. Innovation Fund Denmark (IFD) (75-2014-1, 3067-00001B, 5163-00001B, 5163-00003B).

A. APPENDIX

Figure 22.

REFERENCES

1. M. Weinmann and R. Klein, "Advances in geometry and reflectance acquisition (course notes)," in "Proceedings of SIGGRAPH Asia 2015 Courses," (ACM, 2015).
2. P. Debevec, "The light stages and their applications to photoreal digitial actors," in "SIGGRAPH Asia 2012 Technical Briefs," (2012).
3. L. Gomes, O. R. P. Bellon, and L. Silva, "3D reconstruction methods for digital preservation of cultural heritage: A survey," Pattern Recognition Letters **50**, 3–14 (2014).
4. L. Zhang, H. Dong, and A. E. Saddik, "From 3D sensing to printing: A survey," ACM Transactions on Multimedia Computing, Communications, and Applications **12**, 27:1–27:23 (2016).
5. J. B. Nielsen, E. R. Eiriksson, R. L. Kristensen, J. Wilm, J. R. Frisvad, K. Conradsen, and H. Aanæs, "Quality assurance based on descriptive and parsimonious appearance models," in "Workshop on Material Appearance Modeling (MAM 2015)," (The Eurographics Association, 2015), pp. 21–24.
6. B. T. Phong, "Illumination for computer generated pictures," Communications of the ACM **18**, 311–317 (1975).
7. C. M. Goral, K. E. Torrance, D. P. Greenberg, and B. Battaile, "Modeling the interaction of light between diffuse surfaces," Computer Graphics (Proceedings of SIGGRAPH 84) **18**, 213–222 (1984).
8. A. Takagi, H. Takaoka, T. Oshima, and Y. Ogata, "Accurate rendering technique based on colorimetric conception," Computer Graphics (Proceedings of SIGGRAPH 90) **24**, 263–272 (1990).
9. G. W. Meyer, H. E. Rushmeier, M. F. Cohen, D. P. Greenberg, and K. E. Torrance, "An experimental evaluation of computer graphics imagery," ACM Transactions on Graphics **5**, 30–50 (1986).
10. H. Rushmeier, G. Ward, C. Piatko, P. Sanders, and B. Rust, "Comparing real and synthetic images: Some ideas about metrics," in "Rendering Techniques '95 (Proceedings of EGWR 1995)," (Springer, 1995), pp. 82–91.
11. K. F. Karner and M. Prantl, "A concept for evaluating the accuracy of computer generated images," in "Proceedings of Spring Conference on Computer Graphics (SCCG 1996)," (1996).
12. S. N. Pattanaik, J. A. Ferwerda, K. E. Torrance, and D. P. Greenberg, "Validation of global illumination solutions through CCD camera measurements," in "Proceedings of Color Imaging Conference (CIC 1997)," (1997), pp. 250–253.
13. N. L. Jones and C. F. Reinhart, "Parallel multiple-bounce irradiance caching," Computer Graphics Forum (Proceedings of EGSR 2016) **35**, 57–66 (2016).
14. N. L. Jones and C. F. Reinhart, "Experimental validation of ray tracing as a means of image-based visual discomfort prediction," Building and Environment **113**, 131–150 (2017).
15. D. P. Greenberg, K. E. Torrance, P. Shirley, J. Arvo, J. A.Ferwerda, S. Pattanaik, E. Lafortune, B. Walter, S.-C. Foo, and B. Trumbore, "A framework for realistic image synthesis," in "Proceedings of SIGGRAPH 97," (ACM/Addison-Wesley, 1997), pp. 477–494.
16. F. Drago and K. Myszkowski, "Validation proposal for global illumination and rendering techniques," Computers & Graphics **25**, 511–518 (2001).
17. C. Ulbricht, A. Wilkie, and W. Purgathofer, "Verification of physically based rendering algorithms," Computer Graphics Forum **25**, 237–255 (2006).
18. J. Meseth, G. Müller, R. Klein, F. Röder, and M. Arnold, "Verification of rendering quality from measured BTFs," in "Proceedings of Applied Perception in Graphics and Visualization (APGV 2006)," (ACM, 2006), pp. 127–134.
19. A. I. Ruppertsberg and M. Bloj, "Rendering complex scenes for psychophysics using RADIANCE: How accurate can you get?" Journal of the Optical Society of America A **23**, 759–768 (2006).
20. A. Dal Corso, J. R. Frisvad, T. K. Kjeldsen, and J. A. Bærentzen, "Interactive appearance prediction for cloudy beverages," in "Workshop on Material Appearance Modeling (MAM 2016)," (The Eurographics Association, 2016), pp. 1–4.
21. B. Tunwattanapong, G. Fyffe, P. Graham, J. Busch, X. Yu, A. Ghosh, and P. Debevec, "Acquiring reflectance and shape from continuous spherical harmonic illumination," ACM Transactions on Graphics (Proceedings of SIGGRAPH 2013) **32**, 109:1–109:11 (2013).
22. T. Nöll, J. Köhler, G. Reis, and D. Stricker, "Fully automatic, omnidirectional acquisition of geometry and appearance in the context of cultural heritage preservation," Journal on Computing and Cultural Heritage **8**, Article 2 (2015).
23. H. Wu, Z. Wang, and K. Zhou, "Simultaneous localization and appearance estimation with a consumer RGB-D camera," IEEE Transactions on Visualization and Computer Graphics **22**, 2012–2023 (2016).
24. I. Ihrke, K. N. Kutulakos, H. P. A. Lensch, M. Magnor, and W. Heidrich, "Transparent and specular object reconstruction," Computer Graphics Forum **29**, 2400–2426 (2010).
25. A. Kolb, J. Zhu, and R. Yang, "Sensor fusion," in "Digital Representation of the Real World," M. A. Magnor, O. Grau, O. Sorkine-Hornung, and C. Theobalt, eds. (CRC Press, 2015), chap. 9, pp. 133–150.
26. V. Bhateja, H. Patel, A. Krishn, A. Sahu, and A. Lay-Ekuakille, "Multimodal medical image sensor fusion framework using cascade of wavelet and contourlet transform domains," IEEE Sensors Journal **15**, 6783–6790 (2015).
27. A. Pamart, O. Guillon, J.-M. Vallet, and L. De Luca, "Toward a multimodal photogrammetric acquisition and processing methodology for monitoring conservation and restoration studies," in "Eurographics Workshop on Graphics and Cultural Heritage," (The Eurographics Association, 2016), pp. 207–210.
28. H. Aanæs and A. B. Dahl, "Accuracy in robot generated image data sets," in "Proceedings of SCIA 2015," , vol. 9127 of *Lecture Notes in Computer Science* (Springer, 2015), pp. 472–479.
29. H. Aanæs, R. R. Jensen, G. Vogiatzis, E. Tola, and A. B. Dahl, "Large-scale data for multiple-view stereopsis," International Journal of Computer Vision **120**, 153–168 (2016).
30. Z. Zhang, "A flexible new technique for camera calibration," IEEE Transactions on Pattern Analysis and Machine Intelligence **22**, 1330–1334 (2000).
31. P. E. Debevec and J. Malik, "Recovering high dynamic range radiance maps from photographs," in "Proceedings of SIGGRAPH 97," (ACM/Addison-Wesley, 1997), pp. 369–378.
32. J. L. Posdamer and M. Altschuler, "Surface measurement by space-encoded projected beam systems," Computer Graphics and Image Processing **18**, 1–17 (1982).
33. J. Geng, "Structured-light 3D surface imaging: a tutorial," Advances in

Optics and Photonics **3**, 128–160 (2011).
34. M. Kazhdan and H. Hoppe, "Screened Poisson surface reconstruction," ACM Transactions on Graphics **32**, 29:1–29:13 (2013).
35. M. Corsini, P. Cignoni, and R. Scopigno, "Efficient and flexible sampling with blue noise properties of triangular meshes," IEEE Transactions on Visualization and Computer Graphics **18**, 914–924 (2012).
36. J. F. Murray-Coleman and A. M. Smith, "The automated measurement of BRDFs and their application to luminaire modeling," Journal of the Illuminating Engineering Society **19**, 87–99 (1990).
37. J. B. Nielsen, H. W. Jensen, and R. Ramamoorthi, "On optimal, minimal BRDF sampling for reflectance acquisition," ACM Transactions on Graphics (Proceedings of SIGGRAPH Asia 2015) **34**, 186:1–186:11 (2015).
38. W. Matusik, H. Pfister, M. Brand, and L. McMillan, "A data-driven reflectance model," ACM Transactions on Graphics (Proceedings of SIGGRAPH 2003) **22**, 759–769 (2003).
39. J. F. Barrett and N. Keat, "Artifacts in CT: Recognition and avoidance," RadioGraphics **24**, 1679–1691 (2004).
40. T. Ju, F. Losasso, S. Schaefer, and J. Warren, "Dual contouring of Hermite data," ACM Transactions Graphics (Proceedings of SIGGRAPH 2002) **21**, 339–346 (2002).
41. M. A. Fischler and R. C. Bolles, "Random sample consensus: A paradigm for model fitting with applications to image analysis and automated cartography," Communications of the ACM **24**, 381–395 (1981).
42. L. Kobbelt, "$\sqrt{3}$-subdivision," in "Proceedings of SIGGRAPH 2000," (ACM/Addison-Wesley, 2000), pp. 103–112.
43. R. L. Cook, "The Reyes image rendering architecture," Computer Graphics (Proceedings of SIGGRAPH 87) **21**, 95–102 (1987).
44. T. Atherton and D. Kerbyson, "Size invariant circle detection," Image and Vision Computing **17**, 795 – 803 (1999).
45. P. D. Sampson, "Fitting conic sections to "very scattered" data: An iterative refinement of the Bookstein algorithm," Computer Graphics and Image Processing **18**, 97–108 (1982).
46. J. C. Gower, "Generalized Procrustes analysis," Psychometrika **40**, 33–51 (1975).
47. G. D. Finlayson, M. Mackiewicz, and A. Hurlbert, "Color correction using root-polynomial regression," IEEE Transactions on Image Processing **24**, 1460–1470 (2015).
48. G. Sharma, W. Wu, and E. N. Dalal, "The CIEDE2000 color-difference formula: Implementation notes, supplementary test data, and mathematical observations," Color Research & Application **30**, 21–30 (2005).
49. J. Nocedal and S. J. Wright, *Numerical Optimization* (Springer, 2006), 2nd ed.
50. E. Reinhard, G. Ward, S. Pattanaik, P. Debevec, W. Heidrich, and K. Myszkowski, *High Dynamic Range Imaging: Acquisition, Display and Image-Based Lighting* (Morgan Kaufmann/Elsevier, 2010), 2nd ed.
51. A. Stockman and L. T. Sharpe, "The spectral sensitivities of the middle- and long-wavelength-sensitive cones derived from measurements in observers of known genotype," Vision Research **40**, 1711–1737 (2000).
52. J. R. Frisvad, N. J. Christensen, and H. W. Jensen, "Computing the scattering properties of participating media using Lorenz-Mie theory," ACM Transactions on Graphics (Proceedings of SIGGRAPH 2007) **26**, 60:1–60:10 (2007).
53. C. Ulbricht and A. Wilkie, "A problem with the use of XYZ colour space for photorealistic rendering computations," in "Proceedings of Colour in Graphics, Imaging, and Vision (CGIV 2006)," (2006), pp. 435–437.
54. J. Meng, F. Simon, J. Hanika, and C. Dachsbacher, "Physically meaningful rendering using tristimulus colours," Computer Graphics Forum (Proceedings of EGSR 2015) **34**, 31–40 (2015).
55. H. S. Fairman, M. H. Brill, and H. Hemmendinger, "How the CIE 1931 color-matching functions were derived from Wright-Guild data," Color Research & Application **22**, 11–23 (1997).
56. P. Debevec, "Rendering synthetic objects into real scenes: Bridging traditional and image-based graphics with global illumination and high dynamic range photography," in "Proceedings of SIGGRAPH 98," (ACM, 1998), pp. 189–198.
57. A. D. Rakić, A. B. Djurišić, J. M. Elazar, and M. L. Majewski, "Optical properties of metallic films for vertical-cavity optoelectronic devices," Applied Optics **37**, 5271–5283 (1998).
58. J. T. Kajiya, "The rendering equation," Computer Graphics (Proceedings of SIGGRAPH 86) **20**, 143–150 (1986).
59. M. Pharr, W. Jakob, and G. Humphreys, *Physically Based Rendering: From Theory to Implementation* (Morgan Kaufmann/Elsevier, 2017), 3rd ed.
60. S. G. Parker, J. Bigler, A. Dietrich, H. Friedrich, J. Hoberock, D. Luebke, D. McAllister, M. McGuire, K. Morley, A. Robison, and M. Stich, "OptiX: A general purpose ray tracing engine," ACM Transactions on Graphics (Proceedings of SIGGRAPH 2010) **29**, 66:1–66:13 (2010).
61. M. Hejrati and D. Ramanan, "Analysis by synthesis: 3D object recognition by object reconstruction," in "Proceedings of IEEE Conference on Computer Vision and Pattern Recognition (CVPR 2014)," (2014), pp. 2449–2456.
62. D. R. Jones, M. Schonlau, and W. J. Welch, "Efficient global optimization of expensive black-box functions," Journal of Global Optimization **13**, 455–492 (1998).
63. G. Taubin, "A signal processing approach to fair surface design," in "Proceedings of SIGGRAPH 95," (ACM Press, 1995), pp. 351–358.

CONTRIBUTION C

Quality Assurance Based on Descriptive and Parsimonious Appearance Models

---

Conference	MAM2015: Eurographics Workshop on Material Appearance Modeling: Issues and Acquisition
Organizer	EUROGRAPHICS
Venue	Darmstadt, GE
Submission date	May 31, 2015
Presentation Date	June 23, 2015
DOI	10.2312/mam.20151199

This contribution suggest ways in which BRDF models might be used for non-rendering tasks, particularly for quality control. My primary contribution to this paper was writing Section 3.3.

Material Appearance Modeling Workshop (2015), pp. 1–4
Holly Rushmeier and Reinhard Klein (Editors)

Quality Assurance Based on Descriptive and Parsimonious Appearance Models

J. B. Nielsen, E. R. Eiriksson, R. L. Kristensen, J. Wilm, J. R. Frisvad, K. Conradsen, H. Aanæs

Technical University of Denmark

Abstract

In this positional paper, we discuss the potential benefits of using appearance models in additive manufacturing, metal casting, wind turbine blade production, and 3D content acquisition. Current state of the art in acquisition and rendering of appearance cannot easily be used for quality assurance in these areas. The common denominator is the need for descriptive and parsimonious appearance models. By 'parsimonious' we mean with few parameters *so that a model is useful both for fast acquisition, robust fitting, and fast rendering of appearance. The word 'descriptive' refers to the fact that a model should represent the main features of the acquired appearance data. The solution we propose is to reduce the degrees of freedom by greater use of multivariate statistics.*

Categories and Subject Descriptors (according to ACM CCS): I.4.1 [Image Processing and Computer Vision]: Digitization and Image Capture—Reflectance

1. Introduction

Much work has gone into formulating radiometric models of surface reflectance for believable photorealistic rendering of material appearance. This has led to a number of physically plausible models with intuitively meaningful parameters that are appropriate for direct manipulation [MHH*12]. In this positional paper, we discuss the use of appearance models in a different context, namely in quality assurance of physical and digital products. We argue that this area of application requires models with few parameters, or parsimonious models. Through our example use cases, we further argue that there is a significant need for such parsimonious models, and that effort should be put into their development.

The need for parsimonious radiometric models manifests itself when we need to estimate the radiometric properties of surfaces in practice, e.g. when doing industrial inspection to ensure that the products have the specified visual properties, or when we would like to acquire photorealistic models from images. In such cases, the number of measurements is limited, maybe 5 to 20 per surface patch. This should be seen in light of the number of measurements needed to reliably estimate a general bidirectional reflectance distribution function (BRDF). A BRDF is modeled by a 4D manifold and is typically measured using a spherical gantry (a gonioreflectometer). This means that a very large number of measurements is required, which in many cases is practically infeasible.

According to the philosophy associated with Occam's razor, the formulation of descriptive and parsimonious models will also force us to better model and understand the underlying radiometric phenomena. Thus, in the end, our models should hopefully lead to physically plausible models with few intuitively meaningful parameters as is needed for the more classical applications of appearance models. We believe that it is possible to make large advances in this direction, meaning that the task of formulating parsimonious models does not seem to be a frugal one.

2. Relating to existing models

Previous work has shown that the classical empirically and physically based computer graphics reflectance models cannot fit all measured reflectance data well [NDM05]. This has led to a quest for models that provide a better fit [BSH12, LKYU12]. The cost of a better fit is an increase in the number of model parameters, and the simplest model (the Phong model [Pho75]) already has two parameters per color band and one parameter to describe the material glossiness. As such, the simplest model requires at least seven measurements although ideally many more to robustly fit measured reflectance data. In applications of real-time reflectance acquisition, this quickly becomes infeasible.

The fitting of most parametric models is far from triv-

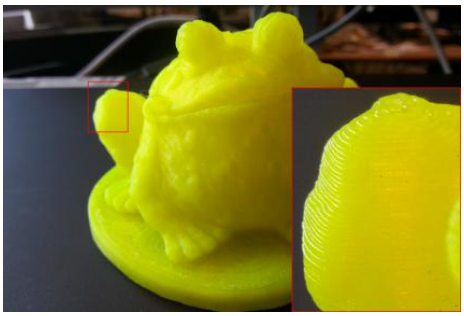

Figure 1: *Frog printed out of Polylactic acid (PLA) plastic using a Fused Deposition Modeling (FDM) printer.*

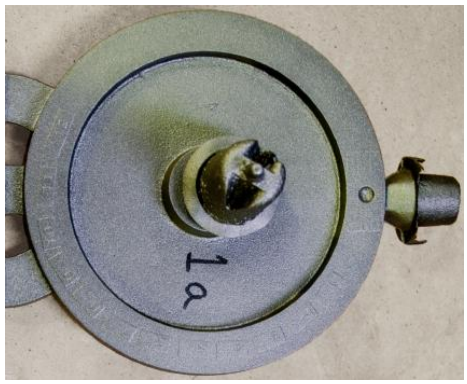

Figure 2: *Example of iron casting [VSRT15], where the mould has introduced a surface roughness affecting the visual appearance of the product. Image is courtesy of Nikolaj Kjelgaard Vedel-Smith.*

ial. Major challenges include determining what optimizers to use and what objective functions they should minimize. For the latter, various suggestions have been proposed including L_1 minimization [NFCA14] and log-transformation with cosine-weighting of observed data [NDM05]. To address the issues of non-linear model fitting, alternative approaches have been proposed where reflectance is modeled by linear combinations of basis functions. Suggestions to basis functions include spherical harmonics [WAT92], wavelets [SS95], and densely sampled reference reflectances [MPBM03]. The advantage here is that fitting models to observations becomes extremely easy as this corresponds to solving a linear system of equations. The challenge however, which is an unsolved problem, is identifying a *sparse* set of basis functions that model a wide variety of material appearances well. We need, as a community, to work on this.

3. Relevant Cases

To argue relevance, we now describe four cases where we have identified that the current radiometric models or acquisition methods simply do not suffice. The cases are (1) additive 3D printing, where the 3D microstructures caused by the printing process cannot be modeled well by standard reflectance models; (2) real-time monitoring of reflectance in metal production; (3) estimation of surface reflectance on massive objects (wind turbine blades); and (4) reflectance models to be used with 3D scanners to allow simultaneous acquisition of geometry and appearance. These are all problems that cannot be solved by conventional methods.

3.1. Additive Manufacturing

For the past decade, additive manufacturing (3D printing) has been an accepted production method. Today, it is possible to manufacture products in multiple materials ranging from soft polymers to metals [WC13]. A rapidly growing market of internet printing services is emerging (shapeways.com and i.materialise.com, for example) where users can upload their own 3D models for printing. Fast and realistic material rendering is of great interest to these types of services, allowing users to previsualize the printed outcome of their models prior to committing to purchase. However, accurately obtaining these radiometric models is a challenge. The layer-like nature of the printing process yields surface artifacts, the most prominent known as the 'staircase effect' which drastically alters material appearance for some materials. Visually, we observe this as a local anisotropy, often correlated with the surface curvature, see Figure 1. Thus the printing process itself must be considered when producing an accurate model of the printed appearance.

Radiometric model acquisition also has an application in the quality assurance aspect of additive manufacturing. So far, most effort has been placed on in-line geometric verification of parts [HNRP14, PH14] and color verification [EPA15]. These optical systems capture each and every layer during the print in order to verify its correctness. Combinations of such systems along with rapid radiometric acquisition could prove beneficial as slight deviations from the material optical properties could indicate failure due to e.g. overheating (color change) or structural collapses (surface normal orientation). In essence, we need to verify the quality of 3D prints, but practical constraints limit the number of measurements that it is possible to acquire.

3.2. Metal Casting

Metal casting is still an actively used production method. Casting allows for the creation of seamless and rigid structures in various materials. However, post machining of said

Figure 3: *Wind turbine blade right after molding.*

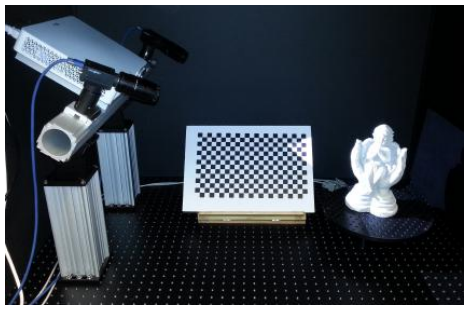

Figure 4: *Structured Light system scanning a statue.*

objects is in many cases required due to the rough surface texture resulting from the casting process, see Figure 2. Measurements of surface roughness parameters are useful for industry and academia in order to optimize the casting procedure as it is related to the overall cast quality. Obtaining surface roughness parameters from optical reflectance is thus of great interest and is an active field of research [NTH13]. As in the case of additive manufacturing, we see a scenario where practical constraints limit the feasible number of measurements, thus creating a demand for accurate parsimonious reflectance models that enable robust fitting.

3.3. Wind Turbine Blades

One of the most important steps in quality inspection of wind turbine blades is to find transverse folds in their longitudinal fiberglass mats. The longitudinal mats run all the way from the root of the blade to the tip and provide the blade with the bulk of its rigidity and strength. Multiple layers of longitudinal mats are needed to provide the necessary strength, and the load must be evenly distributed across the layers. If one layer has a fold, that layer will be tightened harder than the rest of the layers, thus carrying more load when the blade is being operated. Over time, this increased load will wear the fold-layer down to the point where it snaps and thereby compromises the entire structure of the blade. Usually, this sudden release of tension creates a force on the remaining layers so that these also snap. The result is a broken blade.

Before painting, wind turbine blades are translucent due to their composition of transparent epoxy resin and fiberglass (see Figure 3). A fold on a fiberglass mat will create a bulge beneath the surface which alters the optical properties of the material. Currently, specially trained quality engineers shine powerful light parallel to the surface and look for changes in the reflections. An accurate automated measure of surface BRDFs could increase the efficiency and accuracy of the quality assurance by transforming the fold inspection from a qualitative process into a quantitative process.

3.4. Creating 3D Content

Optical 3D scanners are actively used throughout various fields such as archaeology, biology, production, entertainment, medicine, and art. All aiming to capture high resolution 3D models in a relatively short amount of time. However, in order to produce realistic and applicable digitization of scanned objects, their radiometric properties must also be determined. Many commercial systems provide the ability to capture surface textures in order to provide more aesthetically pleasing models, but are often limited to assuming Lambertian behaviour or at most a simple parametric model, such as Phong [Pho75] or Ward [War92]. As indicated in Section 2, these models fail to fit the reflectance properties of many real-world materials. Trouble is that we cannot improve the fit by increasing the number of model parameters as we need to acquire reflectance properties at speeds comparable to the 3D scanning process. This underlines the need for descriptive and parsimonious appearance models.

An interesting property of structured light (SL) scanners is the fixed angle between observer (camera) and lightsource (SL projector). This is illustrated in Figure 4. Using only existing components of such a setup thus poses a constraint on the observable regions in the BRDF domain. Likewise, the geometry also dictates illumination and view directions relative to the surface normal. Hence, again we see a practical limitation on the available observations, which causes a demand for parsimonious models that enable robust fitting.

4. Discussion

From the above, it is evident that there are number of relevant cases where today's methods do not suffice. We believe that the problems in the mentioned cases can be solved, but that they require us to approach material appearance modeling from a new angle. Specifically, we believe that data analysis and multivariate statistics should be involved more than we see it today, and also that we should introduce stronger priors on the data. Such tools are necessary to considerably

reduce the degrees of freedom in the problems. A solution of this kind will greatly contribute to streamlining and automating the entire production pipeline, which is an essential part of agile product development.

Conclusively, we would like to reiterate that descriptive and parsimonious reflectance models seem indispensable if we are to use material appearance models in the context of quality assurance of printed, molded, and digitized products.

References

[BSH12] BAGHER M. M., SOLER C., HOLZSCHUCH N.: Accurate fitting of measured reflectances using a Shifted Gamma micro-facet distribution. *Computer Graphics Forum (Proceedings of EGSR 2012) 31*, 4 (June 2012), 1509–1518. 1

[EPA15] EIRIKSSON E., PEDERSEN D., AANAES H.: Predicting color output of additive manufactured parts. In *Proc. ASPE Spring Topical Meeting on Achieving Precision Tolerances in Additive Manufacturing (26-29 April 2015, Raleigh, North Carolina, USA)* (2015), pp. 95–99. 2

[HNRP14] HANSEN H., NIELSEN J., RASMUSSEN J., PEDERSEN D.: Performance verification of 3d printers. In *Proc. ASPE Spring Topical Meeting on Dimensional Accuracy and Surface Finish in Additive Manufacturing (13-16 April 2014, Berkeley, CA, USA) pp* (2014), pp. 104–107. 2

[LKYU12] LÖW J., KRONANDER J., YNNERMAN A., UNGER J.: BRDF models for accurate and efficient rendering of glossy surfaces. *ACM Transactions on Graphics 31*, 1 (January 2012), 9:1–9:14. 1

[MHH*12] MCAULEY S., HILL S., HOFFMAN N., GOTANDA Y., SMITS B., BURLEY B., MARTINEZ A.: Practical physically based shading in film and game production. In *ACM SIGGRAPH 2012 Courses* (2012), no. 10. 1

[MPBM03] MATUSIK W., PFISTER H., BRAND M., MCMILLAN L.: Efficient isotropic BRDF measurement. In *Rendering Techniques (Proceedings of EGSR 2003)* (June 2003), pp. 241–247. 2

[NDM05] NGAN A., DURAND F., MATUSIK W.: Experimental analysis of BRDF models. In *Rendering Techniques (Proceedings of EGSR 2005)* (2005), pp. 117–126. 1, 2

[NFCA14] NIELSEN J. B., FRISVAD J. R., CONRADSEN K., AANÆS H.: Addressing grazing angle reflections in phong models. In *SIGGRAPH Asia 2014 Posters* (2014), ACM, p. 43. 2

[NTH13] NWAOGU U. C., TIEDJE N. S., HANSEN H. N.: A non-contact 3d method to characterize the surface roughness of castings. *Journal of Materials Processing Technology 213*, 1 (2013), 59–68. 3

[PH14] PEDERSEN D., HANSEN H.: Comparability of the performance of in-line computer vision for geometrical verification of parts, produced by additive manufacturing. In *Proc. ASPE Spring Topical Meeting on Dimensional Accuracy and Surface Finish in Additive Manufacturing (13-16 April 2014, Berkeley, CA, USA) pp* (2014), pp. 179–183. 2

[Pho75] PHONG B. T.: Illumination for computer generated pictures. *Communications of the ACM 18*, 6 (1975), 311–317. 1, 3

[SS95] SCHRÖDER P., SWELDENS W.: Spherical wavelets: Efficiently representing functions on the sphere. In *Proceedings of the 22nd annual conference on Computer graphics and interactive techniques* (1995), ACM, pp. 161–172. 2

[VSRT15] VEDEL-SMITH N. K., RASMUSSEN J., TIEDJE N. S.: Thermal distortion of disc-shaped ductile iron castings in vertically parted moulds. *Journal of Materials Processing Technology* (2015), 262–271. 2

[War92] WARD G. J.: Measuring and modeling anisotropic reflection. In *SIGGRAPH 92* (1992), pp. 265–272. 3

[WAT92] WESTIN S. H., ARVO J. R., TORRANCE K. E.: Predicting reflectance functions from complex surfaces. *Computer Graphics (Proceedings of ACM SIGGRAPH 92) 26*, 2 (July 1992), 255–264. 2

[WC13] WOHLERS T., CAFFREY T.: Additive manufacturing and 3d printing state of the industry annual worldwide progress report. 2014. *Wohlers Associates* (2013). 2

CONTRIBUTION D

Using an Industrial Robot Arm for Measuring BRDFs

Technical Report DTU Compute Technical Report 2018-07
Published in DTU Orbit

This contribution describes a system for measuring bidirectional reflectance distribution functions (BRDFs), known as a gonioreflectometer, of flat material samples. The system is composed of an industrial 6-axis robot, a calibrated camera and a flat Spectralon ® diffuse reflectance standard. The results of this work was applied directly in Contribution B, and was used internally during the study in Contribution E, but has not previously been described in detail, why it is presented here as a technical report. My primary contribution to this work was leading the development of the robotic system, together with Jannik Boll Matthiassen, and leading the writing of the report. I developed the unbiased reconstruction method, but had no share in the biased reconstruction method.

Using an Industrial Robot Arm for Measuring BRDFs

Rasmus Ahrenkiel Lyngby, Jannik Boll Matthiassen, Jeppe Revall Frisvad,
Anders Bjorholm Dahl, Henrik Aanæs
Department of Applied Mathematics and Computer Science, Technical University of Denmark
Richard Petersens Plads, Building 321, 2800 Kgs. Lyngby, Denmark
raly@dtu.dk

Abstract

The measurement of a bidirectional reflectance distribution function (BRDF) requires a purpose-built instrument. This technical report ease this requirement by presenting a relative method for measuring a BRDF using a multipurpose robotic arm. Our focus is on the alignment of the system to perform accurate camera positioning and orientation. We use a six degrees of freedom robotic arm to move a camera on a hemisphere surrounding a flat material sample. Point-like light sources, fixed on a quarter circle arc, sequentially illuminate the sample from different directions. The resulting images are used to reconstruct the material BRDF. We limit ourselves to tristimulus (RGB) isotropic BRDF acquisition.

1. Introduction

A gonioreflectometer is a device for measuring reflectance distribution functions [1]–[3]. Such an instrument is usually an expensive, purpose-built machine that does only one job. While gonioreflectometers have important applications in computer graphics and computer vision, purchasing one is a substantial investment. To pursue scientific discoveries within these areas while limiting the amount of cash tied up in specialized equipment, we propose to use a multipurpose robot arm as a gonioreflectometer. This is a technical report, which documents the work that was done to develop our robot-based gonioreflectometer. We focus on describing what was done, and details the technical principles.

Many six-axis industrial robots, including the one used, has a low absolute position precision. They do, however, have a very high repeatability. We utilize this feature in our acquisition, by measuring angles between camera and light directions relative to a 3D artifact using pose estimation. We avoid measuring the exact distances between camera and surface, and between surface and light source, and the light source irradiance, and the absolute camera intensity response, by normalizing our observed pixel intensities using Spectralon ®; which is an almost perfectly diffuse (Lambertian) material.

2. Previous Work

Several precise, robot-based gonioreflectometers exist today [4]–[8]. Hünerhoff, Grusemann, and Höpe [4] presents a gonioreflectometer with a five-axis robot for holding the sample, a homogeneous sphere radiator for providing the irradiance, mounted on a ring-shaped rotation stage, and a monochromator for measuring the radiance. The system relies on calibrated irradiance and is generally comprised of more purposely build components than our setup. A five-axis robot for sample holding was also used by Baribeau, Neil, and Côté [5], and others use a six-axis robot for the same task [6], [8]., These systems use a ring-shaped rotation stage for holding either a collimated light source or a spectroradiometer. Commonly, previous robot-based gonioreflectometer relies on a relatively large amount of very specialized hardware. Our gonioreflectometer is designed to use as much commercially available hardware as possible and to employ nonobstructive components that can easily be removed such that the robot can also be used for other tasks. Therefore we constructed a simple light arc which can easily be removed from the robot. Moreover, we do not rely on calibrated light sources or cameras.

3. Instrumentation

In our experiments, we use a six-axis ABB IRB 1600 10/1.45 industrial robot. It is capable of carrying a payload of 10 kg and has a repeatability of 50 μm. This means that we are guaranteed that the sensors will always arrive at the same poses[1] within 50 μm. Fig. 1 shows the robot in the experimental setup. It has been painted black to avoid unwanted reflections, giving us a more controlled radiometric

[1] https://library.e.abb.com/public/3b0491a94bd700a248257c71004ef393/PR10282EN_R8.pdf

environment. The camera we use is a Point Grey Grasshopper3 9.1MP RGB camera.

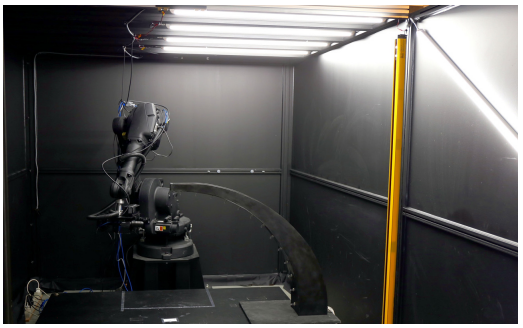

Figure 1: Robotic arm holding a camera in a lightproof enclosure.

As seen in Fig. 1, our setup is completely surrounded by an enclosure that is painted black. This shields our setup from any illumination from the surroundings and prevents most internal reflections from disrupting our experiments. However, a completely dark environment is not of much interest when acquiring optical data. We built an arch shaped light source covering 90° vertical angle with an array of light sources placed 7.5° apart, see Fig. 2. This gives control over the direction of lighting relative to the material sample. As a whole, this setup provides us with control over sensor pose and lighting conditions.

4. BRDF Acquisition

The BRDF characterizes material appearance by describing the changes in the reflectance of a surface for varying view and illumination directions. Generally, the BRDF is a four-dimensional quantity, depending on incident and outgoing directions of view and illumination, but for many materials this can be reduced to three dimensions under the common assumption of isotropic reflectance, meaning that there is no preferred orientation of the material, as in brushed metals or some fabrics, for example. Irradiance represents the radiant flux falling onto a surface, and is defined by

$$E = \frac{d\Phi}{dA}\,, \tag{1}$$

where Φ is radiant flux and A is the area of the illuminated surface. The irradiance is in differential form to define it as the amount of flux in the limit where the illuminated area goes to zero. Likewise, the light emitted from, or reflected off, a surface in a direction is given by the radiance, which is defined by

$$L = \frac{d\Phi}{dA_{\mathrm{proj}} d\omega}\,, \tag{2}$$

Figure 2: Light arch with the camera system visible to the left, measuring the BRDF of an aluminum laptop.

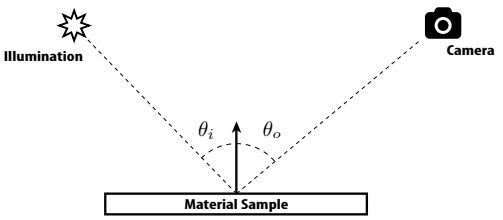

Figure 3: Illustration of incoming and outgoing rays of light at a point on a surface. The BRDF is defined by the ratio of outgoing to incoming light.

where A_{proj} is the illuminated area projected along the viewing direction and ω is the solid angle of the emitted ray. The BRDF is defined as the ratio between reflected radiance and irradiance, again in differential form to define it in the limit where only one direction of incidence is considered. This is illustrated in Fig. 3.

Formally, the BRDF is defined by [9]

$$f_r(\theta_i, \phi_i; \theta_o, \phi_o) = \frac{dL_o(\theta_o, \phi_o)}{dE(\theta_i, \phi_i)}\,, \tag{3}$$

where θ_i, ϕ_i denote the direction of incoming light in spherical coordinates, θ_o, ϕ_o denote the direction of outgoing

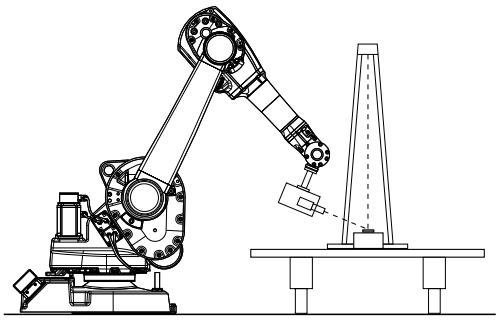

Figure 4: Illustration of the surface reflectance measuring system. It contains the robot, the light arc, a table, a sample stand, and the sample, which is illustrated by the gray box.

light in spherical coordinates, L_o is the reflected/outgoing radiance, and E is the irradiance of the sample. The BRDF obeys Helmholtz reciprocity, which means that the incoming and outgoing directions can be flipped without changing the ratio, thus $f_r(\theta_i, \phi_i; \theta_o, \phi_o) = f_r(\theta_o, \phi_o; \theta_i, \phi_i)$.

In principle, it is easy to measure the BRDF using a gonioreflectometer, by observing a flat material sample under all possible view and illumination combinations. Unfortunately, dense sampling of BRDFs requires many samples to accurately capture the appearance of a material, which is a comprehensive task to perform, even with an automated robot.

4.1. Dense Isotropic Capture

By equipping a robotic arm with a camera, and combining this setup with an arc-formed point-light array, we can semi-densely sample light reflections off a flat material sample for various configurations of incoming and outgoing light directions. See Fig. 4 for an illustration of the measurement setup.

The basic idea is to move the camera around a sample which is placed under the light arc, while capturing the sample reflectance under each of the light sources, thus sampling all combinations of incoming and outgoing light rays. Remembering that the BRDF obeys Helmholtz reciprocity, we actually sample both configurations of light and camera positions in one go. In addition, we limit ourselves to isotropic BRDFs, which is why a rotation around the surface normal of the incoming and outgoing ray does not change the BRDF. Thus, we can simply keep the light arc at a fixed position and only move the camera around, hereby sampling the entire isotropic BRDF.

The factors limiting how densely we can sample surface reflectance are the spacing between the light-sources in the arc and the resolution of the Cartesian space in which the robot moves. The robot has a non-uniform grid of reachable positions, but, in general, the spacing between two reachable positions is sub-millimeter. The light arc is constructed with a fixed set of bulbs with a spacing of 7.5° and has a radius of 1000 mm. Thus, the resolution of the robot is orders of magnitude higher than that of the light arc. However, we have assessed that a bulb spacing of 7.5° provides a good compromise between sample rate and measurement time, thus providing a semi-dense sampling within a reasonable time frame.

The light sources in the arc must be as close to point sources as possible. In theory, with only one light source on, this will ensure that each infinitesimal point on the sample surface will receive only a single, incoming ray of light. In effect, we can measure the reflectance of a single ray at an infinitesimal point by narrowing the camera's field of view to a fraction of a degree, such that it observes only a single outgoing ray at a time. That can be done by combining a long focal length and image cropping. However, in practice, it is impossible to move the camera around the sample, while keeping a narrow field of view aligned exactly with an infinitesimal surface point. Thus, a broader field of view is used, and the mean value of reflected light, within the field of view, is used as an estimate of the point radiance. In addition, the lights are not perfect point sources, as they also have a spatial extend. Thus, they would have to be placed infinitely far away to act as true point sources. This is not feasible and therefore we have compromised by choosing a sample-to-light distance which is at least three times longer than the camera-to-sample distance.

The camera is moved around the sample point on a hemisphere. The robot's arm-length resulted in an optimal hemisphere radius of 350 mm. The camera is oriented such that it always points toward the sphere center. An isotropic BRDF is mirror symmetric around the vertical plane of the light arc. Put in another way, the light reflected at the right-hand side of the arc is identical to that reflected at the left-hand side. Thus, the first half of the hemisphere from azimuth 0° to 180° is identical to the other half going from 180° to 360°. The camera path is defined in spherical coordinates with a resolution of 7.5° in both azimuth and elevation. Thus, the Cartesian equivalent of a given spherical camera position is calculated as follows:

$$x_{ij} = x_0 + r \sin\theta_i \cos\phi_j \quad (4)$$

$$y_{ij} = y_0 + r \sin\theta_i \sin\phi_j \quad (5)$$

$$z_{ij} = z_0 + r \cos\theta_i \,, \quad (6)$$

where θ_i is the inclination of sample row i, ϕ_j is the inclination of sample column j. The position (x_0, y_0, z_0) is the center of the sphere. The orientation of the camera is

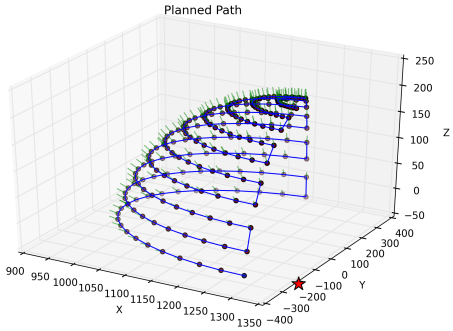

Figure 5: Illustration of the camera's trajectory, given in the robot's coordinate frame. The star indicates the sphere center, the purple dots indicates sample positions, and the green lines indicates the camera orientation. Note that the plotted trajectory "hovers" above the sample plane which is why the star does not appear to be aligned with the sphere center, even though it is. We do not sample elevations of 0° as they cause no reflection. Thus, the first row is located at an elevation of 7.5°. The trajectory's center is located roughly -100 mm down the y-axis because the sample was not placed exactly infront of the robot. This was done for practical reasons, in an efford to avoid kinematic singularities, which was a problem.

calculated as follows:

$$\beta_{ij} = \frac{\pi}{2} + \theta_i \quad (7)$$

$$\gamma_{ij} = \phi_j \,, \quad (8)$$

where β_{ij} is the camera pitch and γ_{ij} is the camera yaw. The Cartesian coordinates and orientations for each sample point are calculated and stored in a matrix, which at run time is fed one-by-one to the robot in order to move it, and thus the camera, around. In practice, the orientation of the camera is converted to quaternion representation to comply with the robot controller. The camera trajectory with sample positions are illustrated in Fig. 5.

Note that the orientation of the robots coordinate system has to be taken into account. In practice, points lying on the robots x-axis corresponds to an azimuth of 0°. In order to operate the robot within its working area, we had to position the arc along the robots y-axis. Consequently, our coordinate system is rotated by 90°. This is illustrated in Fig. 6.

Instead of calibrating our light source intensities precisely, we measure the BRDFs in a relative way which uses Spectralon®. Spectralon is patented and manufactured by Labsphere. It is a material which has $> 99\%$ diffuse reflectance. Its reflection is thus very Lambertian, meaning

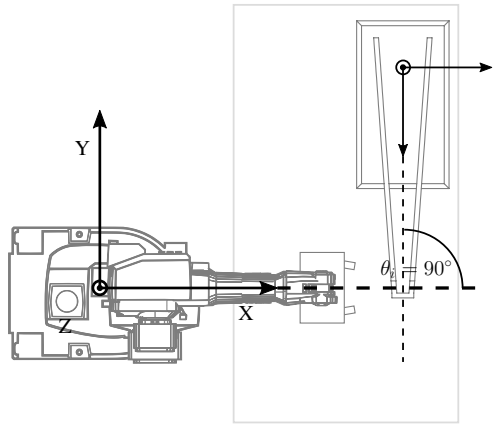

Figure 6: Illustration of the robot coordinate system and the relative position of the light arc. The intersection between the two stippled lines indicates the sphere path center where the sample is placed. The azimuth of the incoming light is $\theta_i = 90^\circ$.

that the relationship between radiance and irradiance is approximately given by $L^{(\mathrm{L})} = \mathbf{n}^T \mathbf{l} E$ where $\mathbf{n}$ and $\mathbf{l}$ are the surface normal and the unit-length incoming light direction, respectively. Note that the outgoing direction is not a part of the relationship, i.e. the radiance is identical for all view directions. Spectralon uniformly spreads the incoming flux at a point over the hemisphere of that point, with very little loss, meaning that the radiance integrated over the hemisphere is approximately equal to the incoming irradiance. This allows us to use Spectralon as a reference to which a given material sample can be compared. We can measure the BRDF for a given pair of incoming and outgoing directions for a given material by calculating the ratio between the reflected intensity of the material and the reflected intensity of Spectralon for the same directions. This is defined by

$$f_r(\theta_i, \theta_o, \phi_o) = \frac{I^{(M)}(\theta_i, \theta_o, \phi_o)}{\pi\, I^{(S)}(\theta_i, \theta_o, \phi_o)} \,, \quad (9)$$

where $I^{(M)}$ is the intensity of the material and $I^{(S)}$ is the intensity of Spectralon. Note that this is a relative measure and therefore the intensities measurement unit is irrelevant. It could be flux, but it could as well be pixel intensity in $[0, 1]$ or in $[0, 255]$.

The above constitutes all the components needed for constructing a BRDF measurement system. The work flow is defined in Table 1 and the process is illustrated in Fig. 7.

The robot is guided in its own reference frame, with ori-

Table 1: Work flow to measure a BRDF

Step		Time	Notes
1	Tool transform	1[h]	In practice, the tool transform only has to be estimated once. However, as the tools changes with temperature, humidity, and wear and tear, it is a good idea to re-estimate it regularly.
2	Alignment of Spectralon to arc	5[min]	The surface of the Spectralon sample has to be carefully aligned with the center of the semicircle formed by the light arc.
3	Spectralon measurement	3[h]	As with the tool transform, this process can be omitted. However, it should be conducted at least once for every new measurement day.
4	Alignment of material to arc	5[min]	Replace the spectralon sample with the material sample. Make sure the surface of the material align exactly with the surface of the Spectralon.
5	Material measurement	3[h]	
6	BRDF calculation	5[min]	Use Equation 9 to calculate the BRDF of the material.
Total		7[h]:15[min]	
Additional samples		3[h]:10[min]	

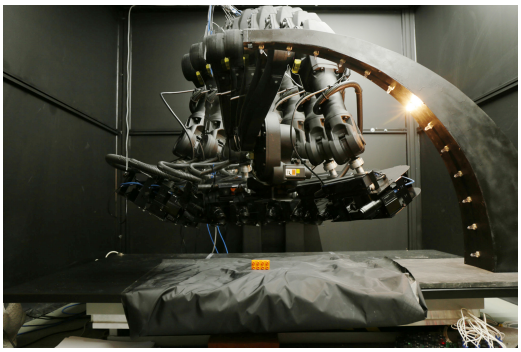

Figure 7: Illustration of the measurement process for a single light source. The image is composed of a sequence of images as the robot sweeps across one row of the path sphere.

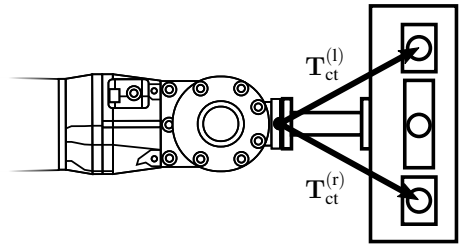

Figure 8: Illustration of the tool-camera transformation. A stereo camera rig with a projector in the middle is mounted on the robot for structured light scanning of geometry. $\boldsymbol{T}_{\text{ct}}^{\text{l}}$ and $\boldsymbol{T}_{\text{ct}}^{\text{r}}$ is the transformation from the end effector to the camera, for the left and right camera, respectively. We only mention one of the two cameras in the main text, as we only use one for our BRDF measurements.

gin at the robot base, by specifying positions of its end-effector. It is, however, easier to specify the camera's position and pose directly. This requires that the spatial transform from end-effector to camera is known. The transformation has to be known fairly precise, as it is desired to keep the camera orientated as close as possible to the same infinitesimal surface point. We deal with this issue in the following section.

5. Hand-Eye Calibration

The position of the robot's end-effector is defined relative to a standard tool. For BRDF measurement, it is more practical to position the robot cameras at specific locations, relative to a sample. We thus need to accurately determine the six degrees of freedom (DoF) transformations between the robot's standard tool and the camera. Having these transformations, the position of the camera within the robot's coordinate system can be determined by

$$\boldsymbol{P}_{\text{c}} = \boldsymbol{P}_{\text{rt}}\boldsymbol{T}_{\text{ct}}\,, \tag{10}$$

where $\boldsymbol{T}_{\text{ct}}$ is the robot tool to camera transformation, $\boldsymbol{P}_{\text{rt}}$ is the six DoF standard tool position, and $\boldsymbol{P}_{\text{c}}$ is the resulting six DoF camera position. This transformation is illustrated in Fig 8.

We estimate the transformation $\boldsymbol{T}_{\text{ct}}$ using hand-eye calibration, which is based on a set of relative camera and

tool motions. Specifically, the solution $\boldsymbol{X}$ to the system $\boldsymbol{AX} = \boldsymbol{XB}$ is found, where $\boldsymbol{A}$ represents the relative motions of the camera, $\boldsymbol{B}$ represents the corresponding relative motions of the tool, and $\boldsymbol{X}$ is the transformation between the camera and the tool. Several algorithms exists to solve this problem. We use the one by Liang and Mao [10]. We start by finding a closed-form solution to the rotation part of the transformation. This is done using a Kronecker product and singular value decomposition (SVD). A least-squares optimization is then performed to find the optimal rotation, using the rotation from SVD as an initial guess. In the end, the translation is found using a least-squares optimization based on the optimal rotation. This procedure combines the performance of the closed-form solutions with the accuracy and noise invariance of the least-squares solutions, thus providing a good estimate of the transformation in a short amount of time.

To practically solve this transformation, a checkerboard is positioned in the working area. Then, 20 images of the checkerboard are captured from different locations with the camera. For each position, the position of the robot tool, with respect to the robots base, is recorded along with the position of the camera, with respect to the checkerboard, obtained through camera calibration [11]. The 20 positions are found by manually jogging the robot tool such that the positions spans the hemisphere above the checkerboard, all six degrees of freedom of the robot are varied, and the entire checkerboard is within the cameras field of view. The checkerboard's saddle points must be easily identifiable in all images, which is why the viewing angle of the checkerboard can not be too steep. The process is illustrated in Fig. 9.

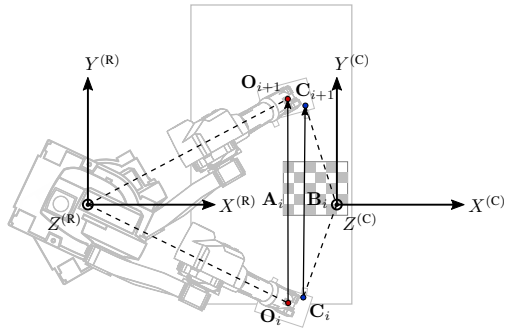

Figure 9: Illustration of the hand-eye calibration process for two robot/camera positions. The robot's and the checkerboard's coordinate systems are marked. The red dots represent the position of the robot relative to its coordinate system, and the blue dot represents the camera's position relative to the checkerboard. The pair of relative translations are calculated based on the positions. Multiple of these transformation-pairs are needed to do the calibration.

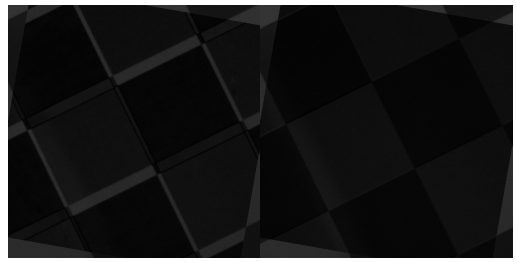

(a) (b)

Figure 10: Difference image (cost function E_{R}) between an orthogonal image acquired by the camera and the same image with a camera roll of around the optical axis of 90° and a counter-rotation of the image of 90°. Minimizing this error ensures that the offset of the tool is accurate. Before refinement is to the left and after refinement is to the right.

5.1. Photometric Optimization

Although the hand-eye calibration gives a good estimate of the tool transformation of the camera, we wish to refine this further, through optimization, to ensure that the uncertainty in camera position is as close as possible to be within the size of a pixel. To do this, we use an error measure, E_{R}, ensuring that the offset of the camera tool relative to the robot is correct. The error is measured by having the camera look orthogonally at a surface, and then rolling it 90° while counter-rotating the captured image 90°. If the estimated optical axis (roll-axis) is aligned with the true optical axis of the camera, the image-rotation should counter the camera-rotation and cause the exact same image. Differences between the two images thus correspond to either rotational or translational errors, relative to the robot. The error, E_{R}, is thus the sum of pixel differences between the two images, which are illustrated in Fig. 10.

We use the BFGS algorithm [12] to minimize E_R by optimizing combined rotation and translation of the camera, which is six dimensions in total. Fig. 10b shows the result of this minimization, and we observe that the tool transformations have indeed improved considerably. This refinement is particularly important, as we wish to position a camera at a very precise angle relative to a material sample.

5.2. Pose Estimation

As previously noted, the robot has a repeatability of 50 μm, but the uncertainty of its actual position is much

Figure 11: 3D artefact used for pose estimation. The position of the centers of the ceramic spheres are known with a low uncertaunty. Their material makes them relatively easy to segment in images.

larger. A relatively precise measurement of the camera pose is needed in order to assign the measured intensity ratios to the correct angles. Therefore, we constructed the 3D artefact shown in Fig. 11 for pose estimation of the camera positions. The artefact is first manually aligned with the light arc. Then, the camera trajectory is traversed, while capturing an image of the artefact at each sample position. An initial guess of the sphere centers are annotated manually in the image captured at the first position. Then, a least-squares optimization minimizes the error between the back-projection of the spheres, onto the image plane, and the segmented spheres, by tweaking the estimated camera pose, relative to the artefact. As the relative transformation between two positions on the planned trajectory can be roughly estimated, the estimated sphere centers can be projected into subsequent images, and used as an initial guess. Finally, the absolute camera pose for all positions, relative to the pose at the first position, can be computed from the poses estimated relative to the artefact.

The poses of the arc lights were brought into the same frame of reference, by use of a mirror. By observing the light bulbs through a mirror, at positions from the sample trajectory with now known poses, with the stereo camera setup, the pose of each light bulb could be estimated through triangulation.

Pose estimation was found to increase the quality of the BRDF measurements significantly. Better highlights were observed, due to the increased angle precision. Note that the sample itself was not pose estimated. The artifact and our sample was positioned on the same surface, and therefore the general orientation of the surface impacted the artifact and specimen in the same way. Only the absolute height of the sample surface remained unknown, but it was found that a manual alignment of the height was precise enough.

6. Representation and Sample Interpolation

A common format for storing BRDFs is the MERL binary format [13]. Data is stored in a non-linear voxel-grid using the 3D Rusinkiewicz parametrization $(\theta_h, \theta_d, \phi_d)$ [14], allowing a fine data-resolution around specular highlights. Most BRDF tools and physically based renderers support this format and it is therefore a convenient way of representing the measured BRDFs.

Although our BRDFs consists of hundreds to thousands of samples, they are still somewhat sparse compared to the MERL cubes' $90 \times 90 \times 180 \approx 1.5 \cdot 10^6$ values. To convert the observations to this much finer resolution format, we thus impose two different strategies: an unbiased and a biased approach.

In the unbiased interpolation strategy, all values in the MERL cube are obtained through 1-Nearest-Neighbour (1NN) interpolation. Euclidian distances in the MERL cube are not necessarily meaningful because the cube spans a 4D angular domain. Instead, we perform the 1NN search in a 6D Euclidean space formed by concatenating the normalized 3D direction vectors toward light and camera. We keep the light direction vector on the semicircle through the zenith of the hemisphere and place it in the first three dimensions of the 6D space (the azimuthal angle between first and second vector should not be greater than $180°$). The camera direction vector is placed in the other three dimensions. From the 1NN interpolation, the MERL cube is filled by copying the nearest measurements to their neighboring voxels, without introducing any new values. Thus, the resulting MERL cube accurately reflects the raw measurements, and can thus be used to visualize the data. The cost is that the information is very discrete and does not utilize the full potential of the MERL representation. Thus, this interpolation is only used for visualization of the measurements, and not as actual BRDFs. It should also be noted that by applying nearest neighbor interpolation, the property of energy conversion is likely to be violated as $\int\int f_\mathrm{r}(\theta_\mathrm{i}, \theta_\mathrm{o}, \phi_\mathrm{o})\,\mathrm{d}\theta_\mathrm{o}\mathrm{d}\phi_\mathrm{o}$ may become greater than 1.

In the biased interpolation strategy, we use the principal component based method of Nielsen et al. [15] to reconstruct the missing information in the MERL cube, using a prior learned from the MERL dataset itself [13]. This method creates a smooth and continuous interpolation of the MERL volume, with high quality highlights.

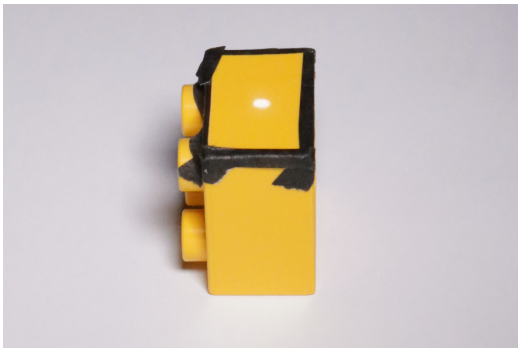

Figure 12: Photo of a yellow toy brick made from ABS polymer. A point light source is positioned directly opposite of the camera. Two diffuse light sources, positioned above and below the camera, illuminates the brick from the front. The specular highlight, imposed by the point light source, is clearly visible on the top surface. Note that it is slightly blurred due to the size of the aperture and the resulting point spread function. Black tape was added to remove glares from the edges.

7. Results

A yellow toy brick made from acrylonitrile butadiene styrene (ABS) polymer, shown in Fig. 12, is used here to illustrate the capability of our robot gonioreflectometer. The measured BRDF is illustrated in Fig. 13.

8. Discussion

Fig. 13a shows the unbiased interpolation, which was used exclusively to visualize the raw data. The left hemisphere is a mirroring of the right. The dark areas in the visualization, seen below the specular highlight, originates from an impossible camera position, i.e. the camera can not be located in the same position as the light source. The measurements look consistent, with no apparent discontinuities, other than the specular highlight. The biased interpolation is shown rendered on a sphere in Fig. 13b and on a dragon in Fig. 13c. This reconstruction method struggles to correctly represent the specular highlight, as indicated by the dark spot exactly in the middle of the specular highlight in Fig.13b. This might indicate that the highlight should be sampled more densely [15]. It could also stem from a bias in the MERL dataset. Other materials, with less defined highlights, were much better reconstructed.

An actual quantification of the gonioreflectometer was not done. In future work, this could be done through measurements of a material with known BRDF. This can be made by having one, or preferably more, materials measured by a calibrated, and well known, gonioreflectometer, and then compare those measurements to ours. The reconstruction error was also not quantified. Future work can investigate this error by leaving out measurements at certain positions from the reconstruction, and then compare corresponding predicted values from the reconstruction with these measured values.

From measurements of other materials, it was found that the relative intensity method might fail for materials which completely absorbs all wavelengths inside either of the red, green or blue color channel. In this situation, the measured intensity of $I^{(M)}$ in Equ. 9 drops below the camera's noise floor, for the respective channel, which results in a noisy BRDF. Further, when the Spectralon was observed at gracing angles, the reflected intensity had a tendency to drop below the noise floor, especially for the blue channel. This led the denominator in Equ. 9 tending to zero, as $I^{(S)}$ constituted mostly noise. The same effect was observed for some of the measured materials, which meant that also $I^{(M)}$ would be mostly noise. Thus, noise was divided by noise, which resulted in an undefined behavior. The effect was seen as a purple tint in the BRDF at gracing angles, such as the rim of the rendered spheres. The purple color was due to the blue channel being more susceptible to noise, which is properly linked to the quantum efficiency of the blue channel being slightly lower than that of the red and green channels. However, for most of our test materials, this turned out not to be a problem, but should be seen more as a warning which applies to certain types and colors of materials. To address this in future work, more powerful light sources or more sensitive cameras may be utilized.

References

[1] W. Erb, "Computer-controlled gonioreflectometer for the measurement of spectral reflection characteristics," *Applied optics*, vol. 19, no. 22, pp. 3789–3794, 1980.

[2] H. Li, S.-C. Foo, K. E. Torrance, and S. H. Westin, "Automated three-axis gonioreflectometer for computer graphics applications," *Optical Engineering*, vol. 45, no. 4, p. 043 605, 2006.

[3] C. Schwartz, R. Sarlette, M. Weinmann, and R. Klein, "Dome ii: A parallelized btf acquisition system.," in *Material Appearance Modeling*, 2013, pp. 25–31.

[4] D. Hünerhoff, U. Grusemann, and A. Höpe, "New robot-based gonioreflectometer for measuring spectral diffuse reflection," *Metrologia*, vol. 43, no. 2, S11, 2006.

[5] R. Baribeau, W. S. Neil, and É. Côté, "Development of a robot-based gonioreflectometer for spectral BRDF measurement," *Journal of Modern Optics*, vol. 56, no. 13, pp. 1497–1503, 2009.

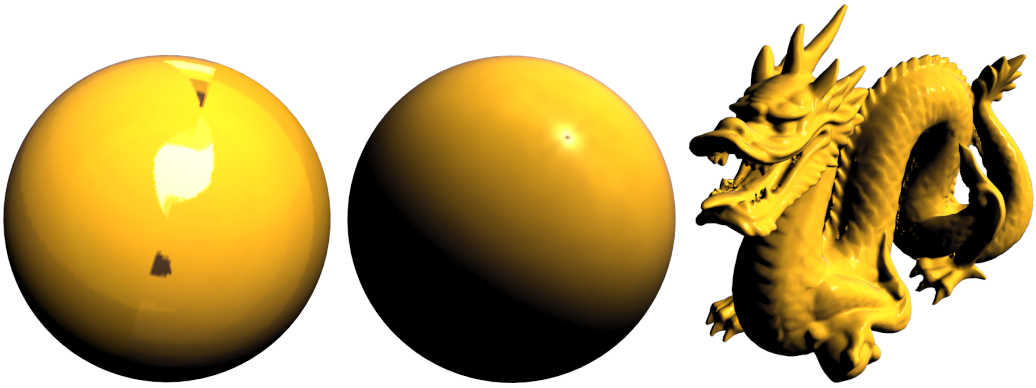

(a) (b) (c)

Figure 13: Visualization of the BRDF measured from the toy brick shown in Fig. 12. From left to right: the unbiased interpolation BRDF rendered on a sphere, the biased interpolation BRDF rendered on a sphere, and the biased interpolation rendered on a dragon.

[6] A. M. Rabal, A. Ferrero, J. Campos, J. L. Fontecha, A. Pons, A. Rubiño, and A. Corróns, "Automatic gonio-spectrophotometer for the absolute measurement of the spectral brdf at in-and out-of-plane and retroreflection geometries," *Metrologia*, vol. 49, no. 3, p. 213, 2012.

[7] A. Höpe, T. Atamas, D. Hünerhoff, S. Teichert, and K.-O. Hauer, "ARGon^3: ''3D appearance robot-based gonioreflectometer" at PTB," *Review of Scientific Instruments*, vol. 83, no. 4, p. 045 102, 2012.

[8] G. Obein, J. Audenaert, G. Ged, and F. B. Leloup, "Metrological issues related to BRDF measurements around the specular direction in the particular case of glossy surfaces," in *Measuring, Modeling, and Reproducing Material Appearance 2015*, International Society for Optics and Photonics, vol. 9398, 2015, p. 93980D.

[9] F. E. Nicodemus, J. C. Richmond, J. J. Hsia, I. W. Ginsberg, and T. Limperis, *Geometric Considerations and Nomenclature for Reflectance (NBS Monograph 160)*. National Bureau of Standards (US), 1977.

[10] R.-h. Liang and J.-f. Mao, "Hand-eye calibration with a new linear decomposition algorithm," *Journal of Zhejiang University SCIENCE A*, vol. 9, no. 10, pp. 1363–1368, 2008.

[11] Z. Zhang, "A flexible new technique for camera calibration," *IEEE Transactions on Pattern Analysis and Machine Intelligence*, vol. 22, no. 11, pp. 1330–1334, Nov. 2000.

[12] J. Nocedal and S. J. Wright, *Numerical Optimization*, second. Springer, 2006.

[13] W. Matusik, H. Pfister, M. Brand, and L. McMillan, "A data-driven reflectance model," *ACM Transactions on Graphics (Proceedings of SIGGRAPH 2003)*, vol. 22, no. 3, pp. 759–769, Jul. 2003.

[14] S. Rusinkiewicz, "A new change of variables for efficient BRDF representation," in *Eurographics Rendering Workshop*, 1998, pp. 11–22.

[15] J. B. Nielsen, H. Jensen, and R. Ramamoorthi, "On optimal, minimal BRDF sampling for reflectance acquisition," *ACM Transactions on Graphics (TOG)*, vol. 34, no. 6, 2015.

CONTRIBUTION E

A Variational Study on BRDF Reconstruction in a Structured Light Scanner

---

Conference	International Conference on Computer Vision Workshops (ICCVW)
Organizer	IEEE
Venue	Venice, IT
Submission date	July 31, 2017
Presentation Date	October 23, 2017
DOI	10.1109/ICCVW.2017.25

This contribution investigates the relation between various parameters in a structured light 3D scanner system and their influence on BRDFs reconstructed using data from this system. My primary contribution to this paper was writing parts of the text, most notable Section 2, and participating in discussions regarding the planning and execution of the experiments.

2017 IEEE International Conference on Computer Vision Workshops

A Variational Study on BRDF Reconstruction in a Structured Light Scanner

Jannik Boll Nielsen, Jonathan Dyssel Stets, Rasmus Ahrenkiel Lyngby,
Henrik Aanæs, Anders Bjorholm Dahl, Jeppe Revall Frisvad
Technical University of Denmark
http://eco3d.compute.dtu.dk/

Abstract

Time-efficient acquisition of reflectance behavior together with surface geometry is a challenging problem. In this study, we investigate the impact of system parameter uncertainties when incorporating a data-driven BRDF reconstruction approach into the standard pipeline of a structured light scanning system. The parameters investigated include geometric detail of scanned objects; vertex positions and normals; and position and intensity of light sources. To have full control of uncertainties, experiments are carried out in a simulated environment, mimicking an actual structured light scanning setup. Results show that while uncertainties in vertex positions and normals have a high impact on the quality of reconstructed BRDFs, object geometry and light source properties have very little influence on the reconstructed BRDFs. With this analysis, practitioners now have insight in the tolerances required for accurate BRDF acquisition to work.

1. Introduction

The topic of accurate appearance capture and digitization is gaining attention in areas like the movie and gaming industries [9], preservation of cultural heritage [6], and quality assurance in production [18]. These applications demand automatic and fast systems that can acquire full and accurate appearance, including both radiometry and geometry. In combination, these two components define appearance, and numerous methods have been proposed for their acquisition. Capturing high quality geometric models of real world objects is today a well-addressed problem with many good solutions. Different technologies exist such as structured light (SL) scanners, multi-view stereo, or time-of-flight, each having their own advantages and disadvantages. With respect to radiometric properties, techniques such as goniometric setups, curved mirror configurations, and light domes can be used for accurately estimating bidirectional reflectance distribution functions (BRDFs) of simple, often flat, geometries. However, robust approaches for jointly estimating radiometry and geometry are few and often require advanced and expensive setups or produce low quality results.

In this paper we investigate how a SL scanner, designed for high quality geometry acquisition, can be modified with few adjustments to also capture reflectance samples. Thus, the scanner can also sample the BRDF of a scanned object and reconstruct it using state of the art BRDF reconstruction methods. Using this system as an offset, we investigate the influence on BRDF estimation caused by various system uncertainties. The uncertainties investigated include: geometric complexity of the scanned object, vertex position and normal, and light source position and intensity. Our aim is to gain insight into how BRDF reconstruction is affected by various error sources and uncertainties. As a main result, we provide a lookup table for system designers, telling them the system specifications required for correctly estimating BRDFs in a given material/geometry configuration. In order to ensure full control of all uncertainties, the experiment is designed as a simulation of an SL scanner system. The simulation is based on real world parameters from an actual SL scanning system, as well as real measured BRDFs from the MERL database [17].

Although this study focuses on an SL scanning system, we believe that the proposed modification, as well as the insights into the influence of error sources, applies to most 3D scanning systems where an image-forming sensor and a light source is present. Likewise, while we apply the BRDF reconstruction framework of Nielsen et al. [20], we expect other BRDF modeling frameworks with strong priors to be applicable as well.

2. Related Work

A multitude of techniques exist for acquiring shape and appearance [30]. Most techniques are time consuming or require highly specialized equipment. In the following, we relate our work to instrumental setups that are similar to the one we propose. Our setup is a structured light 3D scanner setup with two cameras, a projector light source, and a turntable. An additional LED source is added to our setup.

2473-9944/17 $31.00 © 2017 IEEE
DOI 10.1109/ICCVW.2017.25

An example of early work investigating the acquisition of shape and reflectance properties using images is that of Ikeuchi and Sato [11]. They fit the Torrance-Sparrow BRDF model [28] to samples obtained from a range image and a brightness image. To investigate the convergence of their method to true values (robustness), they do a simulation study based on rendered images with different noise levels applied. This enables them to draw important conclusions with respect to the sensitivity and range of applicability of their method. Unfortunately, it seems that such simulation studies are very uncommon in subsequent work in this area. To fill this gap, we present a simulation study of this kind for our more contemporary acquisition technique.

The idea of a camera, a light source, and a turntable for joint acquisition of shape and appearance (surface geometry and BRDF) was pioneered by Lu and Little [15]. They use a collimated source and estimate the BRDF for (near) zero half-angle by finding the points of maximum intensity and tracking them as the object turns around its axis. After this, they acquire the surface geometry using a shape from shading approach. Their approach requires assumption of a smooth object and a uniform BRDF across the object surface. The instrument we consider is similar in complexity, but based on a structured light setup with a projector light source and two cameras (stereo). We also flip the procedure and acquire shape using structured light, and then we estimate a full isotropic BRDF.

It is interesting to note that Lu and Little [15] try perturbations of depth and rotation axis to investigate robustness of their technique. In addition, they indicate that experiments on synthetic images to perform a more in-depth investigation would be appropriate. Nevertheless, we are unable to find such an investigation in the work following that of Lu and Little. Our goal is thus to provide one.

Based on robot arm sample rotation and a structured light range scanner, Sato and Ikeuchi [24] extend their earlier (range and brightness image) technique to include scan of the full geometry of an object and estimation of its spatially varying reflectance properties. The reflectance properties are, however, parameters in an analytic BRDF model and no BRDF ground truth is available for validation. Marschner et al. [16] propose a similar technique, but based on a handheld camera and the Lafortune BRDF model [13]. Employing a more conventional structured light 3D scanner (or a computed tomography scanner) to obtain surface geometry, Lensch et al. [14] extend the technique to acquire Lafortune model parameters for spatially varying BRDFs.

Krzesłowski et al. [12] present a structured light scanner with added LED sources for integrated acquisition of BRDF and surface geometry. However, they fit their sampled BRDF data to the Blinn-Phong model [2, 22], which only provides a good BRDF fit for a limited range of materials [19]. The structured light scan provides a sparse sampling of the BRDF per sample point in the scanned surface geometry. The Blinn-Phong model is fitted to this sparse set of BRDF samples. The acquisition approach we investigate is similar, but we do a simulation study to identify the impact of different potential error sources. We limit our study to an object with just one BRDF across the object surface, and we use the BRDF model of Nielsen et al. [20].

Using a beam splitter to have coaxial camera and projector light source, Holroyd et al. [10] develop a gonioreflectometer which can also acquire the surface geometry using structured light. While this technique delivers high quality acquisitions, it is not a time-efficient approach like a structured light setup. Sitnik et al. [27] propose a faster integrated measurement system with a single image sensor. Here, a multi-spectral camera is combined with a projector and a grid of 16 broadband light sources to capture both the 3D geometry and multi-spectral light intensity information. In another complex setup, Tunwattanapong et al. [29] propose a rotating light arc providing spherical harmonic illumination used together with five cameras to reconstruct reflectance maps. The geometry is then reconstructed using multi-view stereo based on the diffuse and specular reflectance maps. Finally, Schwartz et al. [25] propose a system, based on SL and HDR imaging, for measuring bidirectional texure functions (BTFs) using a light dome composed of 188 LEDs, four projectors, eleven cameras and a rotation stage. The complexity of these instrumental setups is significantly higher than the SL setup that we propose.

3. Implementation

In this study, the BRDF estimation process revolves around a structured light scanning system like the one illustrated in figure 1. The system is composed of two cameras used for triangulation, a projector for projecting an encoding pattern, a rotation stage for rotating a sample, and a scene light. The principles behind the approach should be applicable to any 3D scanning system comprised of components including an image-forming sensor and a light source. In the following subsections, the modified SL capturing pipeline is outlined along with the reconstruction method. The implementation of the modifications required for a structured light scanning system to estimate BRDFs is fairly straightforward in practice, however, to ensure full control of all variables in the study, as well as avoiding unforeseen noise sources, the reflectance acquisition part of the pipeline is here simulated. Below, the details of this simulation process will also be covered.

3.1. Capture Pipeline

The principles behind estimating a BRDF in the SL pipeline are based on the assumption that the BRDF can be observed under a sufficient number of view/light configurations. We need enough to confidently fit a model to the ob-

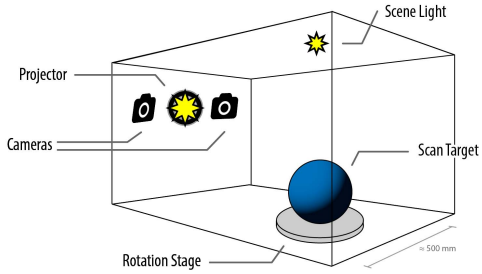

Figure 1: Structured light scanning system consisting of two cameras used for triangulation, a projector for projecting an encoded pattern, a rotation stage for rotating the sample, and a scene light.

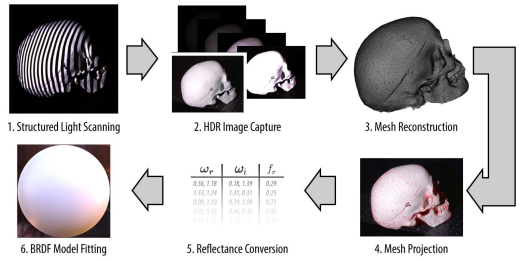

Figure 2: Geometry and BRDF capture pipeline in a structured light scanning system.

servations. Enough configurations are obtained in scenarios where a scanned object, with a sufficiently varying surface geometry, consists of a homogeneous material and is rotated during the capturing process. Any point on the surface will thus be observed under different view/light configurations, and with a sufficiently large number of points with unique surface normals, a sufficiently large number of BRDF samples can be acquired for reconstruction.

Clearly, the full four-dimensional space spanned by the BRDF will not be covered by these observations, let alone due to the fixed baseline between light source (projector) and observer (cameras), which corresponds to a fixed difference angle (θ_d) in the Rusinkiewicz parametrization [23]. Even in a better posed scenario as figure 1, where an additional scene light is present, the BRDF space is still very sparsely sampled. Nonetheless, a sufficient number of observations can in fact be acquired through this process if we use a strong prior when fitting a BRDF model.

The SL scanning pipeline involves projecting an encoding pattern onto the target object and triangulating the encoded pixels seen by the camera(s). This is sometimes followed by a rotation of the sample, after which the scanning is repeated. The modification to the standard SL scanning pipeline is simple and consists only in capturing a high dynamic range (HDR) image of the sample. This is done before the sample is rotated (or removed) using the triangulation camera(s) and a fully lit projector. If a scene light is present, as it is here, an additional HDR image is captured under its illumination. With the captured HDR images, it is possible in post-processing to reproject the captured vertices onto these and acquire a radiance value. With knowledge of vertex normal, camera position, light source position, and light source intensity, this radiance value may be converted into a BRDF sample, defined by

$$f_r\left(\boldsymbol{\omega}_i, \boldsymbol{\omega}_r\right) = \frac{dL_r\left(\boldsymbol{\omega}_r\right)}{dE_i\left(\boldsymbol{\omega}_i\right)}, \tag{1}$$

which is the ratio between the radiance reflected off a surface in a specific direction and the irradiance hitting a surface from another specific direction.

The overall capturing pipeline is depicted in figure 2. The pipeline consists of:

1. Structured light scanning
2. HDR image capture
3. Mesh reconstruction
4. Mesh projection onto HDR images
5. Per vertex HDR intensity to reflectance conversion
6. BRDF model fitting

In step 1, a traditional 3D scanning is carried out, in this case using structured light. Before altering anything in the scene in any way, e.g. by rotating or removing the sample, an HDR image is captured in step 2 using the multiple exposure approach of Debevec et al. [3]. This ensures a floating point precision image conforming with the scanned geometry and camera calibration of the SL scanner. The acquisition part is followed by post processing, initialized with a meshing in step 3 of the acquired point cloud. As will later become apparent, a mesh is required for filtering purposes. In step 4, the mesh is projected onto the HDR images, assigning every vertex with an HDR intensity. All vertex intensities are in step 5 converted to reflectance values based on scene geometry, and finally in step 6 a BRDF model is fitted to the observed BRDF samples.

3.1.1 Structured Light Scanner

In order to provide a thorough description of our method, we briefly outline our SL scanning strategy. Please note that this is by no means a complete description. For specific details, we refer to the work of others [8, 33, 4].

SL scanning is a form of stereo vision. Essentially, stereo vision is the process of reconstructing the 3D shape of an object by using a set of cameras as protractors. The pixel positions, and thereby the incident angles, of a given 3D

point are found in the camera images. From knowing the mutual transformations between the cameras, the 3D position of the point can be computed based on trigonometry. The key difficulty is finding corresponding points in the images. SL based techniques seek to lower the complexity of this correspondence problem by projecting a known pattern onto the reconstruction object. There are a plethora of encoding strategies available [5], but they all seek to assign unique ID numbers to pixels based on their distance from the projector. These ID numbers are then used to determine pixel correspondences, and from that compute the depth of the surface under the pixels.

Based on the conclusions made by Eiríksson et al. [4], we have selected a scanner system composed of two cameras and one projector which uses the phase shifting (PS) encoding strategy [7]. In short, the projector projects a series of spatially distributed gray-scale sinusoidal patterns onto the target surface. Each pattern has a given frequency and phase shift. We use three frequencies with up to 32 phase shifts per frequency for a total of 64 patterns.

3.1.2 Vertex Reflectance Assignment

From the calibration of the SL scanning system, the intrinsics and extrinsics have been determined. Commonly these are described by a pinhole camera model with a projection matrix $\boldsymbol{P}$ given as:

$$\boldsymbol{P} = \boldsymbol{K}\left[\boldsymbol{R}\ \boldsymbol{t}\right], \tag{2}$$

with $\boldsymbol{R}$ and $\boldsymbol{t}$ being the rotation and translation of the camera respectively, and $\boldsymbol{K}$ being the intrinsic parameters of the camera [34]. With this, any 3D point in homogeneous coordinates, $\boldsymbol{q}$, may be projected onto the cameras 2D image plane by:

$$\hat{\boldsymbol{q}} = \boldsymbol{P}\boldsymbol{q}. \tag{3}$$

Thus, any vertex from a scanned object may be reprojected onto its corresponding HDR image and have a specific radiance RGB value assigned to it. By calibration with e.g. Spectralon, the light intensity at the sample can be predetermined, and often this intensity can be assumed constant over the physical span of the sample. With this prior knowledge, and correcting with the cosine between light and vertex normal, the vertex radiance value may be converted into a BRDF value:

$$f_r = \frac{\texttt{HDR}(\boldsymbol{P}\boldsymbol{v}_{\texttt{position}})}{(\boldsymbol{\omega}_i \cdot \boldsymbol{v}_{\texttt{normal}})\ I}, \tag{4}$$

where $\texttt{HDR}(\hat{\boldsymbol{q}})$ is the HDR radiance value at position $\hat{\boldsymbol{q}}$, $\boldsymbol{v}$ is the vertex, $\boldsymbol{\omega}_i$ is the normalized light direction, and I is the predetermined light intensity at the position of the scanned sample.

Note that some vertices may be projected into shadow regions in the HDR image. In order to avoid this, two tests are employed. First, all vertices with a normal facing away from the camera or light are removed, this is the case when $\boldsymbol{\omega}_{r/i} \cdot \boldsymbol{v}_{\texttt{normal}} <= 0$. This test filters most invalid observations away, but in scenarios where self-shadowing may occur, a shadow map calculation is also applied [31]. This, however, requires that the scanned object has been converted into a 3D mesh, which in itself may introduce artifacts if care is not taken.

3.1.3 Data-Driven BRDF Reconstruction

The challenge of fitting a reflectance model to the sparse number of BRDF samples calls for a model with a strong prior. In this study, the data-driven BRDF reconstruction framework of Nielsen et al. [20, 32] is chosen for this purpose, as it is known to work well for problems where only very few BRDF samples are available. The model is based on the MERL database [17] of isotropic BRDFs spanning a wide range of common materials. Using a log-relative mapping of reflectance values, projections in principal component space allows inferring missing observations from existing ones. Effectively the model reconstructs a MERL format BRDF, i.e. a $90 \times 90 \times 180$ bin tabulated isotropic BRDF, from any number of input observations provided. The biggest limitation of this approach is that it requires the measured material to lie within the convex hull spanned by the MERL database. If this is met, under ideal lighting conditions, as little as two images are sufficient to faithfully reproduce a material.

3.2. Simulation of Pipeline

In order to maintain full control of all uncertainties in this fairly complex acquisition pipeline, a simulated pipeline is used to produce realistic HDR images, conforming with a true SL system. We do this by initially picking a ground truth mesh and ground truth measured BRDF from the MERL database. Using these, combined with the true SL system projection matrices, light source positions, and rotation stage positions, an OpenGL renderer is used to produce a series of HDR renderings of the chosen geometry and BRDF as it would have been seen by the SL system. An example of such renderings is shown in figure 3, where 3 different meshes with the "blue-rubber" BRDF applied have been rendered as would be seen by the SL scanning system (although cropped here). With this, the ground truth appearance behind every HDR image is available, allowing for a quantitative evaluation of reconstruction.

3.2.1 Dataset Generation

Four different types of materials and three different types of geometries were chosen to generate the evaluated dataset. Material-wise, four different levels of specularity were chosen, all in different colors, covering the span of material

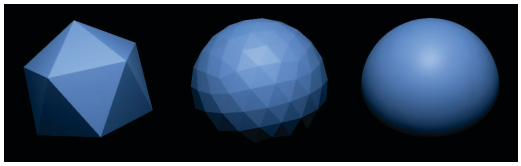

Figure 3: Icospheres with 3 different tessellation levels: 1, 3 and 5. For the highest tesselation level vertex normals have been smoothed.

behavior that would be expected in the real world. The materials are "blue-rubber", "green-metallic-paint", "purple-plastic", and "specular-black-phenolic", with the first having very soft highlights and the last being highly specular (renderings are available in the lower left corner of figures 5–8). As the data-driven BRDF reconstruction model is also based on the MERL database, these four materials were excluded in the model-training. Geometry-wise three different geometries were chosen, spanning the amount of geometric detail that can be expected from real world objects. The geometries are based on an icosphere with increasing tesselation levels and are shown in figure 3. This is motivated by the fact that a sphere naturally covers all possible surface normals, while a plane only covers a single. Thus, the closer the geometry is to a sphere, the more ideal are the BRDF reconstruction conditions from a geometry point of view. Each of the three meshes has been subdivided to consist of roughly 15000 vertices and are scaled to have a diameter of 100 mm in the simulator.

We generate a dataset of HDR images using the materials and geometries described above. Both the scene-light and projector are used as light sources and both cameras are used for observing, see figure 1. In addition, the sample is rotated in 10 steps from $0°$ to $180°$. This gives $n_{\texttt{conf}} = n_{\texttt{rot}} \times n_{\texttt{lights}} \times n_{\texttt{cameras}} = 10 \times 2 \times 2 = 40$ HDR images per material/geometry configuration and $n_{\texttt{total}} = n_{\texttt{conf}} \times n_{\texttt{materials}} \times = n_{\texttt{geometries}} = 40 \times 4 \times 3 = 480$ HDR images in total.

3.2.2 Noise Addition

There are a range of elements in the pipeline depicted in figure 2 that affect the accuracy of the BRDF observations acquired. Any uncertainties in these will obviously cause uncertainties in the BRDF model-fitting. To gain insight into this, four types of uncertainties are investigated:

Vertex position. The precision of the SL system will determine the geometric noise present in a 3D scan. Clearly, as the vertices are projected onto HDR images, any error in position will cause a wrong assignment of radiance value.

Vertex normal. Commonly, surface normals are not a direct product of the 3D acquisition procedure but are estimated afterwards, e.g. based on the spatial distribution of neighboring vertices. This makes the estimation prone to errors, and any wrong orientation of normals will directly influence the reflectance estimate.

Light position. While camera positions are very precisely calibrated, the light position is oftentimes significantly more difficult to determine. The position affects the light direction and thus also the reflectance estimate.

Light intensity. Finally, precise knowledge of the light intensity at any given 3D point in the SL system is not easily obtained. As the light intensity is used to compute the fraction of light reflected off the material surface, it too directly influences the reflectance estimate.

As the evaluated dataset is simulated, the exact system parameters are known. This allows for, prior to processing the data, manually adding a controlled amount of noise to any of the above components. To apply noise in our experiments, we use a normal distribution (Gaussian noise) with the given position or normal as mean and σ is standard deviation. For normals, the noise only applies to the polar angle. To add noise in the case of light intensity, we multiply the intensity by a normal distribution with unit mean and $\sigma/100$ as standard deviation (percentage noise).

3.2.3 Evaluation

Evaluating the quality of an estimated BRDF compared to the ground truth is not trivial and is indeed a research field in itself. In these experiments, both qualitative and quantitative measures are presented:

In-plane reflectance profiles. For qualitative evaluation, $45°$ in-plane reflectance profiles of estimated and ground truth BRDFs are presented. These plots visualize the general shape of the specular highlight as well as parts of the grazing angle behaviour.

Ray-traced sphere renderings. Another qualitative evaluation is using a physically based renderer [21]. Here the BRDFs can be visualized under realistic environment lighting conditions, giving the viewer an impression of how the material would look in the real world. The material examples shown in figures 5–8 are rendered this way.

Tone mapped color difference. Rendered images, using the approach above, of the ground truth and reconstructed BRDFs are compared using the CIEDE2000 color difference perception measure. The HDR images are first scaled to the visible range using Reinhard tonemapping, and gamma correction ($\gamma = 2.2$) at F-stop 0 is applied [1]. The images are then converted to the CIE 1976 L*a*b* color space, and the CIEDE2000 color difference formula [26] (with $[k_L\ k_C\ k_H] = [1\ 1\ 1]$) is used to calculate the color difference ΔE_{00}. The average of all pixel differences is calculated and used as a perceptual similarity measure between

	blue-rubber	green-metallic-paint	purple-paint	specular-black-phenolic
Icosphere 1	0.77 ± 1.02	2.77 ± 2.93	1.56 ± 1.96	1.07 ± 1.13
Icosphere 3	0.37 ± 0.78	2.60 ± 3.11	0.82 ± 1.01	2.50 ± 3.14
Icosphere 5	0.41 ± 0.67	3.00 ± 3.23	0.55 ± 0.75	1.43 ± 1.92
Icosphere 5*	0.52 ± 0.96	5.19 ± 5.20	1.58 ± 1.55	2.29 ± 1.63

Table 1: Errors for increasing geometric detail (icosphere tesselation level). Errors are measured as the average ΔE_{00} color difference between tone mapped renderings of ground truth BRDF and reconstruction. Icosphere 1,3,5 are reconstructions using two light sources, while 5^* are reconstructions using only the projector as light source.

images, and the standard deviation represents the certainty of this number.

4. Results

We report results for BRDF estimation under various noise influences. This includes an evaluation of BRDF estimation performance under three different geometry complexities, followed by an evaluation of performance under influence of uncertainties with respect to vertex position, vertex normal, light source position, and light source intensity. Due to page limitations, some comparisons of in-plane reflectance profiles and renderings have been omitted. A summary of comparisons are reported in tables 1 and 2.

4.1. Geometry Dependency

In order to evaluate how much geometric complexity affects the quality of an estimated BRDF, estimations were carried out on the simulated icospheres with tesselation levels 1, 3 and 5, depicted in figure 3. The estimates were computed under ideal conditions, i.e. no noise added to any of the system components listed in section 3.2.2. In figure 4, quantitative comparisons of the material "purple-paint" are presented in the form of in-plane reflectance profiles and renderings. It may be seen that as geometric detail increases, the quality of reconstruction improves, however the improvement is surprisingly small. In table 1, the results for all four materials are listed, using the ΔE_{00} color-difference measure between ground truth rendering and reconstructed rendering. To the convenience of system designers, errors using icosphere level 5 combined with only the projector as light source is also presented in the bottom row of table 1.

To provide as ideal conditions as possible for the noise simulations, the icosphere level 5 geometry will be used in the following evaluations. For all evaluations, 30 repetitions were carried out to estimate mean and standard deviation of reconstruction. Quantitative comparisons for all materials,

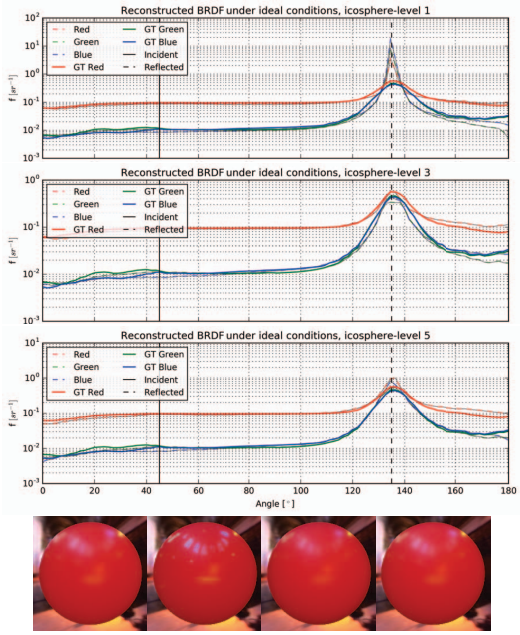

Figure 4: Ideal reconstructions of "purple-paint" material, using icosphere tesselation levels $\{1, 3, 5\}$, shown as $45°$ in-plane profiles. Solid lines indicate ground truth BRDF RGB channels, dashed lines are the reconstructed BRDF RGB channels. Bottom row shows renderings of reference BRDF (left) and reconstructions for the respective icosphere levels.

under various error influences are reported in table 2 using the ΔE_{00} error measure.

4.2. Influence of Vertex Position Noise

Errors in triangulation during the SL scanning procedure directly affect the precision of vertex positions. Commonly, but depending on material, SL scanners have a very high precision in the order of microns [4]. To investigate the sensitivity to vertex positions, all vertices are affected by three relatively large levels of noise prior to projection onto HDR images. The noise is added as a normally distributed noise on the xyz-components of each vertex with standard deviations of $\sigma \in \{1, 3, 5\}$mm. In figure 5, the qualitative evaluations for material "blue-rubber" are presented. As is apparent, grazing angle behavior is greatly affected by vertex uncertainties. This is most likely caused by the fact that even small uncertainties may at grazing angles project a vertex onto the black background, rather than the target sample. Likewise, for very specular materials as "specular-black-phenolic", vertices may miss the very narrow highlight causing errors in estimating the specular reflection.

		blue-rubber	green-metallic-paint	purple-paint	specular-black-phenolic
Ideal		0.41 ± 0.67	3.00 ± 3.23	0.55 ± 0.75	1.43 ± 1.92
Vertex	1mm	0.66 ± 1.15	3.03 ± 3.44	0.91 ± 1.56	2.27 ± 3.37
	3mm	2.50 ± 2.82	3.11 ± 4.17	2.11 ± 3.16	3.41 ± 5.15
	5mm	4.16 ± 4.08	3.24 ± 4.77	3.59 ± 4.32	4.22 ± 5.76
Normal	5°	0.42 ± 0.63	3.00 ± 3.20	0.68 ± 1.03	3.15 ± 5.66
	10°	0.67 ± 0.98	3.08 ± 3.17	0.99 ± 1.70	3.72 ± 6.92
	30°	1.81 ± 2.11	4.70 ± 5.08	2.27 ± 3.27	5.24 ± 8.31
Light Pos.	10mm	0.51 ± 0.72	3.01 ± 3.26	0.62 ± 0.84	2.17 ± 3.32
	25mm	0.73 ± 0.89	2.68 ± 3.03	1.02 ± 1.16	3.05 ± 5.03
	50mm	1.77 ± 1.92	3.14 ± 3.51	1.91 ± 2.27	3.74 ± 6.08
Light Int.	5%	0.64 ± 0.79	3.01 ± 3.29	0.66 ± 0.78	1.90 ± 2.80
	10%	1.00 ± 1.15	3.05 ± 3.38	0.96 ± 0.99	1.98 ± 2.81
	20%	1.75 ± 1.75	3.40 ± 3.74	1.86 ± 2.10	2.27 ± 2.80

Table 2: Errors for different types of noise introduced to the structured light scanner system. Errors are measured as the average ΔE_{00} color difference between tone mapped renderings of ground truth BRDF and reconstruction.

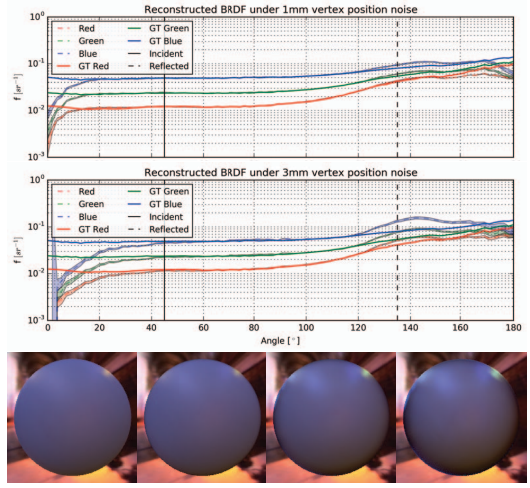

Figure 5: BRDF reconstructions of "blue-rubber" material, for increasing noise added to vertex positions, shown as 45° in-plane profiles. We add Gaussian noise with a standard deviation of $\{1, 3, 5\}$mm. BRDF RGB channels are plotted with solid lines as ground truth and dashed lines as the mean reconstruction. Shaded regions indicate limits for ± 2 standard deviations. Bottom row shows renderings of reference BRDF (left) and mean reconstructions for the respective noise levels. Statistics are based on 30 evaluations.

4.3. Influence of Vertex Normal Noise

As surface normals are often derived from the mesh, they often suffer from large uncertainty. This directly affects the frame of reference in which the BRDF is estimated. To simulate such uncertainties, all normals in the mesh are tilted in a random direction away from the true normal by a normally distributed angle. Three different standard deviations are reported here: $\sigma \in \{5^\circ, 10^\circ, 30^\circ\}$. In figure 6, qualitative evaluations are presented for "purple-paint". Although specular highlights are somewhat affected, it is noteworthy how large an amount of noise we can add to the normals while still obtaining a decent recovery of the material.

4.4. Influence of Light Source Position Noise

As mentioned in section 3.2.2, it may be difficult to determine the precise position of light sources in the SL system. To simulate such uncertainties, normally distributed noise is added to the xyz-components of the light positions (projector and scene-light) with standard deviations of $\sigma \in \{10, 25, 50\}$ mm. In figure 7, the influence of this error is shown for the "green-metallic-paint" material. Surprisingly, even for the relatively large amounts of noise applied here, reconstructions remain very close to the results under ideal conditions as well as the ground truth.

4.5. Influence of Light Source Intensity Noise

Finally, noise applied to the intensity of the light sources (projector and scene light) is applied. Here, the noise is modeled as a normally distributed percentage with a mean of 100%. The standard deviation of the noises applied are $\sigma \in \{5, 10, 20\}\%$. Figure 8 shows the results for the material "specular-black-phenolic". Here, the strong prior of the BRDF reconstruction model almost fully handles the uncertainties in intensity although this property is very tightly coupled to reflectance.

4.6. Summary

Table 2 summarizes the BRDF errors caused by introducing the noise types listed above using the ΔE_{00} error measure. We observe that, not surprisingly, accuracy of vertex positions has a great impact on the quality of the recovered material. Recall that the object size is 100 mm, only a few percent error are enough to throw the BRDF estimate off. On the contrary, variations in surface normals are less influencing than we would have expected, requiring especially for soft materials a lot of noise before throwing the BRDF recovery off. Finally positions and intensities of light sources are seen to have a surprisingly small impact on BRDF reconstructions.

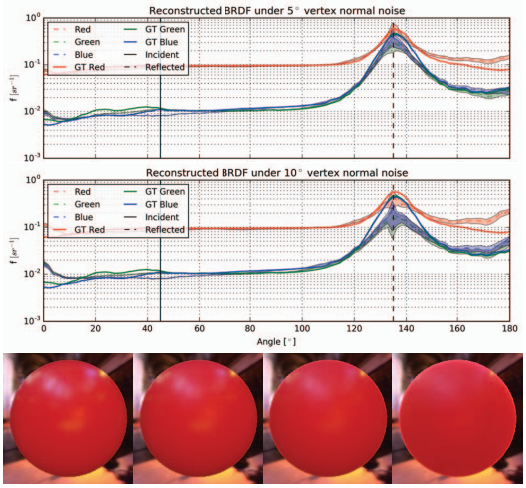

Figure 6: BRDF reconstructions of "purple-paint" material, for increasing noise added to vertex normals, shown as $45°$ in-plane profiles. We add Gaussian noise with a standard deviation of $\{5°, 10°, 30°\}$.

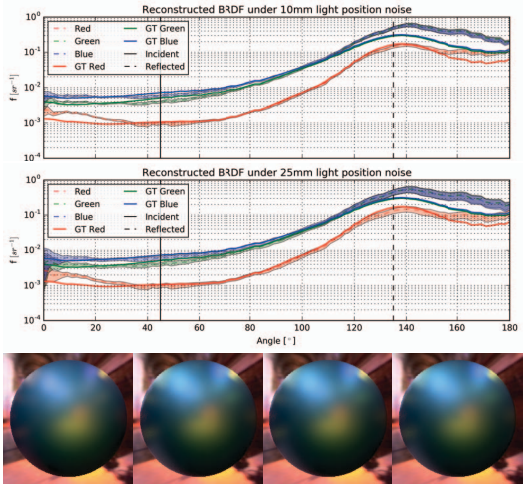

Figure 7: BRDF reconstructions of "green-metallic-paint" material, for increasing noise added to the two light source positions, shown as $45°$ in-plane profiles. We add Gaussian noise with a standard deviation of $\{10, 25, 50\}$mm.

5. Discussion and Conclusion

We investigated how a structured light 3D scanning system can be modified with minimal effort to also estimate

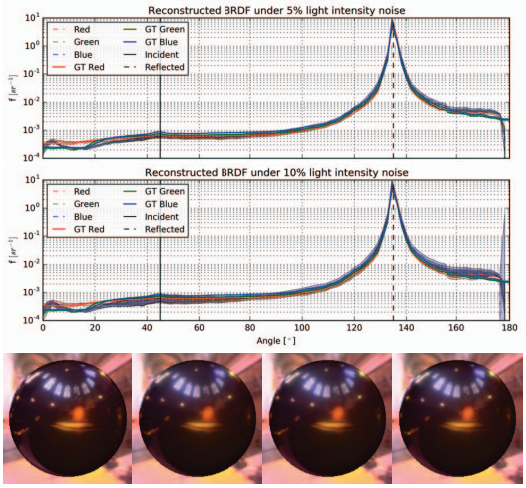

Figure 8: BRDF reconstructions of "specular-black-phenolic" material, for increasing noise added to the two light source intensities, shown as $45°$ in-plane profiles. We add Gaussian noise with a standard deviation of $\{5\%, 10\%, 20\%\}$.

BRDFs. Results indicate that high quality reflectance recovery is in fact possible in such a setup. We carried out a variational study in a simulated environment to investigate how a range of uncertainties in system parameters affect the quality of the estimated reflectance properties. The goal of this study is to provide system designers with a lookup table of system parameter uncertainties required to recover a given material at a given quality-level. This is needed in the design phase of future systems for full appearance acquisition. Tables 1 and 2 provide this information and demonstrate that even under the poor gonioreflectometric conditions provided by a SL system, very high quality reflectance may be recovered. An interesting insight gained here is that uncertainties in surface normals in fact have a smaller impact on the quality of estimated BRDFs than one might have expected. Likewise, uncertainties in illumination properties, including position and intensity, have little influence on the recovered reflectance.

Although the experiments carried out here are only simulated, we believe that they reflect well what can be expected from real world measurements. It has not been the intention with this paper to cover the physical implementation of this pipeline as well as the performance of the approach in real-world scenarios. Nonetheless, the images presented in figure 2 do in fact originate from an actual implementation of the system, demonstrating that it also works in practice. It is our intention to elaborate on these results in the future.

References

[1] F. Banterle, A. Artusi, K. Debattista, and A. Chalmers. *Advanced High Dynamic Range Imaging: Theory and Practice*. AK Peters (CRC Press), Natick, MA, USA, 2011.

[2] J. F. Blinn. Models of light reflections for computer synthesized pictures. *Proceedings of ACM SIGGRAPH 77*, 11(2):192–198, July 1977.

[3] P. E. Debevec and J. Malik. Recovering high dynamic range radiance maps from photographs. In *Proceedings of SIGGRAPH 97*, pages 369–378. ACM/Addison-Wesley, 1997.

[4] E. R. Eiríksson, J. Wilm, D. B. Pedersen, and H. Aanæs. Precision and accuracy parameters in structured light 3-D scanning. *International Archives of the Photogrammetry, Remote Sensing and Spatial Information Sciences*, XL-5/W8:7–15, 2016.

[5] J. Geng. Structured-light 3d surface imaging: a tutorial. *Advances in Optics and Photonics*, 3(2):128–160, 2011.

[6] L. Gomes, O. R. P. Bellon, and L. Silva. 3D reconstruction methods for digital preservation of cultural heritage: A survey. *Pattern Recognition Letters*, 50:3–14, December 2014.

[7] M. Halioua and H.-C. Liu. Optical three-dimensional sensing by phase measuring profilometry. *Optics and Lasers in Engineering*, 11(3):185–215, 1989.

[8] R. I. Hartley and A. Zisserman. *Multiple View Geometry in Computer Vision*. Cambridge University Press, second edition, 2004.

[9] S. Hill, S. McAuley, A. Conty, M. Drobot, E. Heitz, C. Hery, C. Kulla, J. Lanz, J. Ling, N. Walster, F. Xie, A. Micciulla, and R. Villemin. Physically based shading in theory and practice. In *ACM SIGGRAPH 2017 Courses*, July 2017.

[10] M. Holroyd, J. Lawrence, and T. Zickler. A coaxial optical scanner for synchronous acquisition of 3d geometry and surface reflectance. *ACM Transactions on Graphics (Proceedings of SIGGRAPH 2010)*, 29(4):99:1–99:12, July 2010.

[11] K. Ikeuchi and K. Sato. Determining reflectance properties of an object using range and brightness images. *IEEE Transactions on Pattern Analysis and Machine Intelligence*, 13(11):1139–1153, November 1991.

[12] J. Krzesłowski, R. Sitnik, and G. Mączkowski. Integrated three-dimensional shape and reflection properties measurement system. *Applied optics*, 50(4):532–541, February 2011.

[13] E. P. Lafortune, S.-C. Foo, K. E. Torrance, and D. P. Greenberg. Non-linear approximation of reflectance functions. In *Proceedings of SIGGRAPH 1997*, pages 117–126. ACM/Addison-Wesley, 1997.

[14] H. Lensch, J. Kautz, M. Goesele, W. Heidrich, and H.-P. Seidel. Image-based reconstruction of spatial appearance and geometric detail. *ACM Transactions on Graphics*, 22(2):234–257, April 2003.

[15] J. Lu and J. Little. Reflectance function estimation and shape recovery from image sequence of a rotating object. In *Proceedings of International Conference on Computer Vision (ICCV 1995)*, pages 80–86. IEEE, 1995.

[16] S. R. Marschner, S. H. Westin, E. P. Lafortune, K. E. Torrance, and D. P. Greenberg. Image-based BRDF measurement including human skin. In *Rendering Techniques 1999*, pages 131–144. Springer, 1999.

[17] W. Matusik, H. Pfister, M. Brand, and L. McMillan. A data-driven reflectance model. *ACM Transactions on Graphics (Proceedings of SIGGRAPH 2003)*, 22(3):759–769, 2003.

[18] J. B. Nielsen, E. R. Eiríksson, R. L. Kristensen, J. Wilm, J. R. Frisvad, K. Conradsen, and H. Aanæs. Quality assurance based on descriptive and parsimonious appearance models. In *Workshop on Material Appearance Modeling (MAM 2015)*, pages 21–24. The Eurographics Association, June 2015.

[19] J. B. Nielsen, J. R. Frisvad, K. Conradsen, and H. Aanæs. Addressing grazing angle reflections in Phong models. In *SIGGRAPH Asia 2014 Posters*, page 43. ACM, 2014.

[20] J. B. Nielsen, H. W. Jensen, and R. Ramamoorthi. On optimal, minimal BRDF sampling for reflectance acquisition. *ACM Transactions on Graphics (Proceedings of SIGGRAPH Asia 2015)*, 34(6):186:1–186:11, November 2015.

[21] M. Pharr, W. Jakob, and G. Humphreys. *Physically Based Rendering: From Theory to Implementation*. Morgan Kaufmann, third edition, 2016.

[22] B. T. Phong. Illumination for computer generated pictures. *Communications of the ACM*, 18(6):311–317, June 1975.

[23] S. Rusinkiewicz. A new change of variables for efficient BRDF representation. In *Rendering Techniques '98 (Proceedings of EGWR 1998)*, pages 11–22, 1998.

[24] Y. Sato, M. D. Wheeler, and K. Ikeuchi. Object shape and reflectance modeling from observation. In *Proceedings of SIGGRAPH 1997*, pages 379–387. ACM/Addison-Wesley, 1997.

[25] C. Schwartz, R. Sarlette, M. Weinmann, and R. Klein. DOME II: A parallelized BTF acquisition system. In *Workshop on Material Appearance Modeling (MAM 2013)*, pages 25–31. The Eurographics Association, June 2013.

[26] G. Sharma, W. Wu, and E. N. Dalal. The CIEDE2000 color-difference formula: Implementation notes, supplementary test data, and mathematical observations. *Color Research & Application*, 30(1):21–30, 2005.

[27] R. Sitnik, J. KrzesŁ, M. Grzegorz, et al. Archiving shape and appearance of cultural heritage objects using structured light projection and multispectral imaging. *Optical Engineering*, 51(2):021115–1, 2012.

[28] K. E. Torrance and E. M. Sparrow. Theory for off-specular reflection from roughened surfaces. *Journal of the Optical Society of America*, 57(9):1105–1114, September 1967.

[29] B. Tunwattanapong, G. Fyffe, P. Graham, J. Busch, X. Yu, A. Ghosh, and P. Debevec. Acquiring reflectance and shape from continuous spherical harmonic illumination. *ACM Transactions on graphics (Proceedings of SIGGRAPH 2013)*, 32(4):109, 2013.

[30] M. Weinmann and R. Klein. Advances in geometry and reflectance acquisition (course notes). In *Proceedings of SIGGRAPH Asia 2015 Courses*. ACM, November 2015.

[31] L. Williams. Casting curved shadows on curved surfaces. *Computer Graphics (Proceedings of SIGGRAPH 78)*, 12(3):270–274, August 1978.

[32] Z. Xu, J. B. Nielsen, J. Yu, H. W. Jensen, and R. Ramamoorthi. Minimal BRDF sampling for two-shot near-field reflectance acquisition. *ACM Transactions on Graphics (Proceedings of SIGGRAPH Asia 2016)*, 35(6):188:1–188:12, November 2016.

[33] S. Zhang and P. S. Huang. Novel method for structured light system calibration. *Optical Engineering*, 45(8):083601–083601, 2006.

[34] Z. Zhang. A flexible new technique for camera calibration. *IEEE Transactions on Pattern Analysis and Machine Intelligence*, 22(11):1330–1334, 2000.

CONTRIBUTION F

Make Geometry Inspection of Wind Turbine Blades Great Again with Robots

---

Technical Report DTU Compute Technical Report 2018-07
Published in DTU Orbit

This technical report describes the control algorithm used to plan the motions of the developed autonomous inspection system. The system design and simulation was done in close cooperation with FORCE Technology, who also stood for the construction and assembly. I developed the control algorithm, based on the cited references, complete with motor and robot interfaces, scanner operation and data handling. In addition, there is, as always, a vast set of functions which sits under the hood and make everything work in the real world. This includes handling of emergency stop, with the ability to resume an aborted scan sequence, noise removal from the acquired point clouds, and general health and sensibility checks.

Make Geometry Inspection of Wind Turbine Blades Great Again with Robots

Rasmus Ahrenkiel Lyngby, Anders Bjorholm Dahl
Department of Applied Mathematics and Computer Science, Technical University of Denmark
Richard Petersens Plads, Building 321, 2800 Kgs. Lyngby, Denmark
raly@dtu.dk

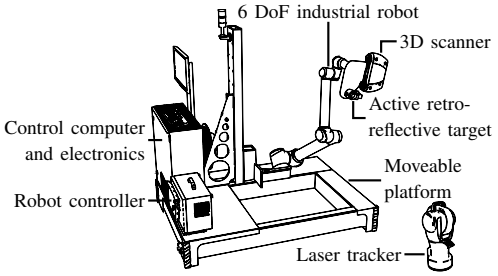

Figure 1: Annotated drawing of the inspection system.

Abstract

This technical report presents one way of adaptive motion planning for a robotic inspection system. The robot system features a pivoting locomotion platform and a six degrees of freedom industrial robot arm. It carries a 3D scanner with which it inspects the outer geometry of wind turbine blades. The acquired 3D geometry is used in a feedback loop to plan the following motions. This avoids the need for a digital blade model, and allows the inspection system to automatically adapt to the inspected geometry.

1. Introduction

The scanner system introduced by Lyngby, Aanæs, Nielsen, *et al.* [1] is able to autonomously inspect the outer geometry of wind turbine blades. This technical report presents the control loop used to plan the motions of the aforementioned robotic inspection system. Figure 1 shows an overview of the robotic inspection system. The system has proved able to scan the outermost 20 meters, which are the most crucial, of a 55 meter long blade within 1.5 hours, which is significantly faster than the current manually-based inspection methods.

In a talk given by Dr. H Friedmann, Woelfel Engineering GmbH, on July 11, 2018 at the European Workshop for Structural Health Monitoring, he assessed that about 80% of blade failures, which happen during the blade's operational life time, can be traced back to defects which was introduced during production. Errors in the blade's outer geometry, which leads to a retarded power output and a shortened life expectancy, can be introduced at multiple stages during production. Quality inspection of the geometry is therefore important. Today, geometrical inspections are often done manually. While the current inspection methods have adequate sensitivity, the time needed to complete them does not scale well with blade length. For modern blades, the inspection process has become too time consuming, and therefore expensive.

The proposed blade scanner system resembles the one presented by [2], but with a novel, freely driving platform and control algorithm. Their system relied on a linear drive unit to move the robot, and the robot's path was hard coded from the blades design model. Note that our system is patent pending. The robot moves the scanner over the surface such that it can measure the needed geometry. The platform, in turn, moves the robot to extend its working envelope, such that it encapsulates the entire blade length. Only the front most part of the blade profile, known as the leading edge, is to be measured. This paper describes the algorithm used to plan the robot path. As the robot is stationary during acquisition, the algorithm can be seen as solving a next best view problem.

Looking more broadly, several robot based 3D scanner systems, with accompanying path planning algorithms, have been described previously. Many of these papers either focuses on following curved geometry or on optimal sampling of curved geometry, often aided by a CAD model. [3] presented a path planning algorithm for smoothly moving a laser line 3D scanner, mounted on a stationary 6 DoF industrial robot arm, around curved geometry. Their system was targeted at reverse engineering, and able to scan small objects that could fit into the cylindrical work envelope which had a height of 650 mm and a radius of 250

mm. Their path planning algorithm used a representation of geometry which was based on intersecting planes. Another laser based robot system was presented by [4] with a control algorithm for *next best view* planning. Their algorithm modeled the unknown geometry of an unknown workpiece, and used this model to compute the next best view position and angle. This system relies on meshed geometry, and was also for small objects. A system for measuring small and relatively flat industrial components was presented by [5]. They also employed a 6 DoF robot arm with a laser based 3D scanner. They planned overlapping consecutive scan paths by mapping acquired 3D measurements to a 2D plane, which simplified the next best view problem as it could be solved in the plane and then mapped back into 3D. While this small overview of previous work is by no means complete, it gives an indication of the general tendencies within the field of path planning for robotic 3D scanning.

The proposed scanner system's drive platform has two drive wheels, one on each side, which sits at the front of the machine. Two freely spinning follow-wheels sits at the rear end. A Festo electric motor drives each of the drive wheels. The platform is moved by controlling the motors speed and direction of rotation. A Universal Robots UR10 sits on top of the platform. It is mounted on a plate which can be moved up and down manually in order to adjust the robot's base height. The robot's position is moved by issuing a pose, consisting of a position and orientation in 3D space, to it, together with a motion interpolation type. The robot carries the payload, which is a light based 3D scanner from Automated Precision Inc. (API) and a six degrees of freedom (DoF) active tracking probe, also from API. The scanner covers an area of roughly 300 mm by 300 mm at a distance of 300 mm per scan. When measuring a flat surface, it returns roughly 1.2 million 3D points per scan. The probe is tracked by a laser tracker, also from API, which gives an accurate six Dof position for each acquired 3D scan. These positions are, however, not used by the control algorithm presented here. They are only used for subsequently stitching together all the acquired scans to make one, combined scan of the blade geometry.

First, the algorithm itself is presented, and the a small number of examples are shown, together with a brief discussion.

2. Control System

We would like to move the scanner on a trajectory which follows curves on the blade surface. Figure 2 illustrates the trajectory. From simulations of the system done in Robcad, it was found that the robot can reach over two consecutive curves for every platform position. The scanner has a shutter-time of 2.7 seconds, why it has to be held stable during acquisition. Therefore, the robot "trajectory" is specified as a sequence of discrete robot poses. The robot tool is set such that it corresponds to the scanners coordinate frame, why the terms "robot position" and "scanner position" are used interchangeably. When a round of acquisition is finished, that is two curves, the platform has to move forward along the blade such that the robot can reach the following two curves. The just finished round of measured point clouds are used to compute the movement of the platform and the sequence of robot positions, for the subsequent round of measurements. Thus, every motion event consists of first a platform movement and secondly a series of robot movements. Fig. 3 illustrates the control loop.

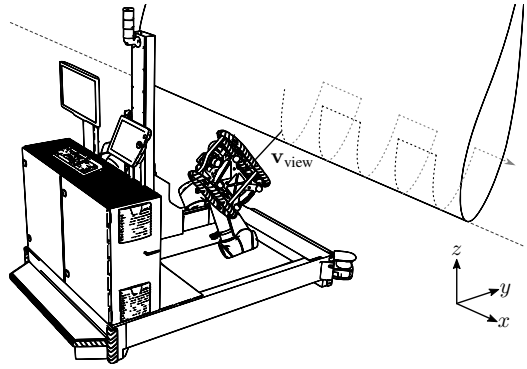

Figure 2: Drawing of the trajectory followed by the scanner over the surface. The annotated coordinate frame does not coincide with any actual coordinate frame, but simply shows the orientation of the platforms coordinate frame.

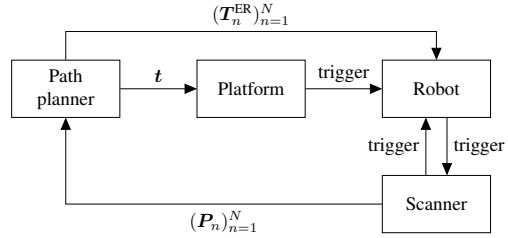

Figure 3: Flowchart overview of the control loop. $\boldsymbol{T}_n^{\text{ER}}$ are transformations from the robot's base to its tool, and $\boldsymbol{P}_n$ are acquired point clouds. "Trigger" signifies that a trigger signal is send once a process finishes.

For the sake of simplicity, we describe the control loop while being in process. This means, that a sequence of previous point clouds are available. Say that N point clouds were returned by acquisition round t, and that we now wants to compute the relative platform position and the sequence

of N robot poses, consisting of position and orientation, for acquisition round $t+1$. Let P be the sequence of N point clouds returned from round t. Each element of P is a point cloud represented as a matrix belonging to $\mathbb{R}^{M_n \times 3}$, where n is the point cloud's number in the sequence, and M_n is the number of individual points in point cloud n. In the following derivations, it is implicit that we are talking about acquisition round t, and as such, subscript t is omitted.

2.1. Combining the Point Clouds

After acquisition, the point clouds are located in the scanner's local coordinate frame. They are combined into one point cloud by transforming them into the platform's coordinate frame. Using the respective robot position belonging to each point cloud, together with the calibrated scanner to target, target to end-effector, and robot to platform transformations, the sequence of point clouds can be transformed into the platform's coordinate frame. The sequence of transformations, from the scanner to the platform, is given by

$$T = \left(\boldsymbol{T}^{\text{RP}}\boldsymbol{T}_n^{\text{ER}}\boldsymbol{T}^{\text{AE}}\boldsymbol{T}^{\text{SA}}\right)_{n=1}^{N}, \tag{1}$$

where $\boldsymbol{T}_n^{\text{ER}}$ is the n'th robot position, represented as a transformation from the robot's tool to its base. Figure 4 illustrates the transformations between the different components reference frames. Let n be such that $X(n)$ yields the n'th element of sequence X. The point clouds are transformed and combined into one, big cloud by

$$P' = \left(P(n) \cdot T(n)^{\text{T}}\right)_{n=1}^{N} \tag{2}$$

$$\boldsymbol{P} = \begin{bmatrix} P'(1) \\ P'(2) \\ \vdots \\ P'(N) \end{bmatrix}, \tag{3}$$

where $\cdot$ is the inner product between two matrices, $T(n)^{\text{T}}$ is the transpose of matrix $T(n)$, and $\boldsymbol{P} \in \mathbb{R}^{(M_1+M_2+\cdots+M_N)\times 3}$ is the combined point cloud, located in the platforms coordinate frame.

2.2. Computing the Platform Position

The platform follows the direction of the blade's leading edge, while maintaining a close alignment of the direction of its x-axis and the leading edge direction. The leading edge is facing down towards the floor during inspection. Therefore, the leading edge can be detected by intersecting the point cloud with a number of yz-planes, project the closest points onto the planes, and then find the point with the lowest z-coordinate in each of the planes. These lowest points will lay on the leading edge, why fitting a line through them provides a good estimate of the leading edge.

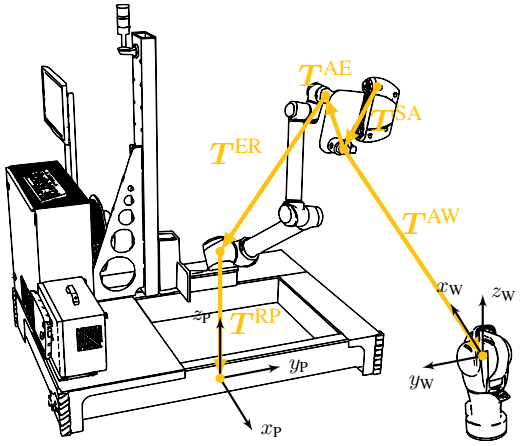

Figure 4: Transformations between the reference frames. The yellow arrows illustrate the transformations, while the black arrows annotates the world coordinate frame, defined by the tracker, and the platform's local coordinate frame. Note that the global coordinate frame is used only for the final stitching together of all the acquired point clouds, when forming the final blade model. Only the platforms local coordinate frame is used by the control algorithm.

The blade is longitudinally aligned with the platform's x-axis. The intersecting planes are therefore chosen such that they are spanned by the y-axis and z-axis, and have normal vectors $\boldsymbol{n} = [1,0,0]^{\text{T}}$. A total of K planes are used.The mean position of the point cloud is found as

$$\boldsymbol{\mu} = \frac{1}{M}\sum_{i=0}^{M-1}\boldsymbol{p}_i\,, \tag{4}$$

where $M = \sum_{n=1}^{N} M_n$ is the total number of rows, i.e. points, in $\boldsymbol{P}$, and $\boldsymbol{p}_i$ is the i'th row of $\boldsymbol{P}$. The range spanned by the point cloud along the x-axis is found as

$$x_{\text{begin}} = \min_i p_{i0} \tag{5}$$

$$x_{\text{end}} = \max_i p_{i0} \tag{6}$$

$$x_{\text{range}} = x_{\text{end}} - x_{\text{begin}}\,, \tag{7}$$

where p_{i0} is the first column of the i'th row, which corresponds to the x-coordinate, and is thus a scalar.

Here, we define a plane as a homogeneous transformation, $\boldsymbol{H} \in \mathbb{R}^{4\times 4}$, which describes a pose consisting of a position and an orientation. This definition allows us to project a homogeneous point, $\boldsymbol{p}$, into the planes coordinate frame by $\boldsymbol{p}' = \boldsymbol{H}\boldsymbol{p}$, and then get the points distance from the plane directly from its projected z-coordinate, $\boldsymbol{p}'_2$.

The transformation for each of the K intersecting planes, $\boldsymbol{H}_n \; \forall \; n = 1, \cdots, K$, are computed as

$$\boldsymbol{R} = \begin{bmatrix} 0 & 1 & 0 \\ 0 & 0 & 1 \\ 1 & 0 & 0 \end{bmatrix} \tag{8}$$

$$\boldsymbol{t}_n = \boldsymbol{\mu} - \begin{bmatrix} \left(\frac{1}{2} - \frac{n}{K}\right) x_{\text{range}} \\ 0 \\ 0 \end{bmatrix} \tag{9}$$

$$\boldsymbol{H}_n = \begin{bmatrix} & \boldsymbol{R} & & \boldsymbol{t}_i n \\ 0 & 0 & 0 & 1 \end{bmatrix} \quad \forall \; n = 1, \cdots, K \,, \tag{10}$$

where $\boldsymbol{R} \in \mathbb{R}^{3\times3}$ is a rotation matrix and $\boldsymbol{t}_n \in \mathbb{R}^3$ is the translation vector for the n'th plane. The point cloud is transformed into the coordinate frame of each of the planes, but only the points which are located within a distance threshold, d, are retained and projected flat onto the planes:

$$\boldsymbol{P}'_n = \begin{bmatrix} \boldsymbol{P} & \mathbf{1} \end{bmatrix} \boldsymbol{H}_n^{\mathrm{T}} \tag{11}$$

$$\boldsymbol{Q}'_n = \left[\boldsymbol{p}'_{n,i[0\;1]} \mid -d \leq p'_{n,i2} \leq d \right]_{i=1}^{M} \,, \tag{12}$$

where $\mathbf{1}$ is the 1-vector, where all elements are 1, and has the same number of elements as there are rows in $\boldsymbol{P}'$. The 2D vector $\boldsymbol{p}'_{n,i[0\;1]}$ is the x- and y-coordinate of row i of $\boldsymbol{P}'_n$, and $p'_{n,i2}$ is its z-coordinate. $\boldsymbol{Q}'_n$ is the matrix composed of the x-axis and y-axis columns of all rows of $\boldsymbol{P}'_n$, which have a z-axis coordinate within the threshold d. Thus, $\boldsymbol{Q}'_n$ contains the points projected onto plane number n.

Now, as the y-axis of the planes coordinate frames corresponds to the z-axis of the platform's coordinate frame, the point with the lowest y-coordinate in each plane, denoted as $\boldsymbol{q}'_{n,\text{min}}$, is found,

$$\hat{i}_n = \arg\min_i q'_{n,i1} \tag{13}$$

$$\boldsymbol{q}'_{n,\text{min}} = \boldsymbol{q}'_{n,\hat{i}_n} \quad \forall \; n = 1, \cdots, K \,, \tag{14}$$

and then projected back into the platform's coordinate frame. The K back-projected lowest points are then assembled into a matrix, $\boldsymbol{Q}_{\text{min}}$,

$$\boldsymbol{q}_{n,\text{min}} = \boldsymbol{H}_n^{-1} \begin{bmatrix} \boldsymbol{q}'_{n,\text{min}} \\ 0 \\ 1 \end{bmatrix} \quad \forall \; n = 1, \cdots, K \tag{15}$$

$$\boldsymbol{Q}_{\text{min}} = \left[\boldsymbol{q}_{n,\text{min}}^{\mathrm{T}} \right]_{n=1}^{K} \,. \tag{16}$$

A straight line is fitted to the minimum points through the singular value decomposition (SVD),

$$\boldsymbol{\mu}_{\text{min}} = \frac{1}{K} \sum_{n=1}^{K} \boldsymbol{q}_{n,\text{min}} \tag{17}$$

$$\boldsymbol{U}, \boldsymbol{\Sigma}, \boldsymbol{V}^{\mathrm{T}} = \text{SVD}\left(\boldsymbol{Q}_{\text{min}} - \boldsymbol{\mu}_{\text{min}}\right) \tag{18}$$

$$\boldsymbol{v}_{\text{le}} = \boldsymbol{V}_0 \,, \tag{19}$$

where $\boldsymbol{v}_{\text{le}}$ is a unit vector pointing in the direction of largest variance, which is in the direction of the leading edge. Thus, this vector indicates the direction of the leading edge, in the platform coordinate frame. Note that it has to be flipped if it is oriented towards the negative x-axis.

The platform moves linearly along the $\boldsymbol{v}_{\text{le}}$ vector. As the leading edge direction is re-estimated after each round of measurements, the platform's relative motion makes it follow the leading edge in small, linear steps. The relative destination is computed from the direction vector, $\boldsymbol{v}_{\text{le}}$. A parameter, Δ_{platform}, is specified, which defines the displacement between consecutive platform positions. Thus, the displacement vector is given simply by $\boldsymbol{v}_{\text{le}}\Delta_{\text{platform}}$. This model assumes that the leading edge forms a straight line, when observed locally, over a short distance. It was considered to use a polynomial model, but this did not provide any significant improvements in the platforms ability to follow the leading edge.

The platform is moved in two steps. First, its bearing is adjusted to align with the leading edge direction, by pivoting around the center between the drive wheels. Then, the platform drives straight ahead for Δ_{platform} meters. This method is simple, but it ensures that the platform's x-axis is well aligned with the leading edge. Differential steering was considered, where the platform would have been steered by continuously varying the speed of the wheels when driving forward. However, as the leading edge tracks a relatively simple, bend curve, which is locally well approximated by a line, it was deemed unnecessary to use differential steering.

2.3. Computing the Robot Positions

After the platform has finished moving to the next position, the robot is put into action. We want the scanner to be moved over a smooth curve on the blades surface, where its position is determined based on an arc-length distance on that curve. A distance of 0 should be located right at the leading edge, with positive distances being located on the blades far side, relative to the robot base, and negative distances being located on the blades near side. This allows us to specify acquisition positions which directly follows the course of the surface. The scanner is orientated relative to the surface normal, preferably with some slant to avoid direct reflections into the cameras. The optimal standoff distance is given by the scanner's focusing point and its depth of focus.

The goal is to compute the set of robot positions which positions the scanner where we would like it to be, relative to the surface. It was chosen to use a planar trajectory which is orthogonal to the leading edge direction. A plane projection similar to Equ. 10 is used to collapse the point

cloud onto a plane. The plane is positioned such that it includes the point cloud's mean, and is oriented orthogonal to the leading edge vector, $\boldsymbol{v}_{\text{le}}$,

$$\boldsymbol{e}_0 = \begin{bmatrix} 0 & 1 & 0 \end{bmatrix}^{\text{T}} \tag{20}$$

$$\boldsymbol{e}_{\text{y}} = \boldsymbol{v}_{\text{le}} \times \boldsymbol{e}_0 \tag{21}$$

$$\boldsymbol{e}_{\text{x}} = \boldsymbol{e}_{\text{y}} \times \boldsymbol{v}_{\text{le}} \tag{22}$$

$$\boldsymbol{R} = \begin{bmatrix} \boldsymbol{e}_{\text{x}} & \boldsymbol{e}_{\text{y}} & \boldsymbol{v}_{\text{le}} \end{bmatrix}^{\text{T}} \tag{23}$$

$$\boldsymbol{H} = \begin{bmatrix} & \boldsymbol{R} & & \boldsymbol{\mu} \\ 0 & 0 & 0 & 1 \end{bmatrix}, \tag{24}$$

where $\times$ denotes the cross-product, and μ is defined by Equ. 4. As seen, $\boldsymbol{R}$ is selected such that the plane's x-axis points in the same general direction as the platform's y-axis. The y-axis is computed using the cross-product to ensure that the assigned coordinate frame obeys the right-hand rule. The point cloud is then collapsed onto the plane following Equ. 12,

$$\boldsymbol{P}' = \begin{bmatrix} \boldsymbol{P} & \boldsymbol{1} \end{bmatrix} \boldsymbol{H}^{\text{T}} \tag{25}$$

$$\boldsymbol{Q}' = \left[\boldsymbol{p}'_{i[0\ 1]} \mid -d \leq p'_{i2} \leq d \right]_{i=1}^{M}. \tag{26}$$

The convex hull algorithm [6] is used to simplify the projected points in $\boldsymbol{Q}'$. This weed out internal points, and sorts the remaining points consecutively, such that points who are neighbors in space are also neighbors in the underlying data structure. This basically corresponds to reducing the thickness of the projected surface to a single point. Let $\boldsymbol{Q}'_{\text{sorted}} \in \mathbb{R}^{M_{\text{sorted}} \times 2}$ be the M_{sorted} remaining, sorted points.

We wish to have a parametric representation, $f : \mathbb{R} \mapsto \mathbb{R}^3$, of the curve traced out by the points in $\boldsymbol{S}'_{\text{sorted}}$, such that a point on the curve can be sampled as $f(s) = [x(s)\ y(s)]^{\text{T}}$, where s is the arc length, in meters, from the leading edge, and each of $x(s)$ and $y(s)$ is a function which yields the x and y coordinate, respectively, of the point situated s meters from the leading edge. A model based on the arc-length parametric spline curve presented by Wang, Kearney, and Atkinson [7] was selected. In its original form, this algorithm yields a parametric cubic spline interpolation based on curve arc-length. The presented technique estimates the parametric curve efficiently and is suitable for real time applications, as demonstrated by Chu, Lee, and Sunwoo [8]. However, as the sorted points in our application still lies relatively close together, the spline model is too flexible. It tends to overfit the data, and yield a curve which "ripples" as it tries to intersect every point. Therefore, we exchange the spline model with a polynomial model, which asserts a stronger bias on the smoothness of the geometry. The details of the resulting algorithm are presented below.

The arc lengths of the points in $\boldsymbol{Q}'_{\text{sorted}}$ are not known *a priori*, why we start with a polynomial model of the form

$$f(r) = \begin{bmatrix} \sum_{i=0}^{C_{\text{x}}} a_i r^i \\ \sum_{i=0}^{C_{\text{y}}} b_i r^i \end{bmatrix}, \tag{27}$$

where $r \in [0, 1]$ specifies the position on the polynomial. A consecutive equidistant r-value is assigned to each point in $\boldsymbol{Q}'_{\text{sorted}}$, such that the first point has the value $r_1 = 1/M_{\text{sorted}}$, the second point has the value $r_2 = 2/M_{\text{sorted}}$, and so on. The values are combined in the vector $\boldsymbol{r} = [1/M_{\text{sorted}}\ 2/M_{\text{sorted}}\ \cdots\ M_{\text{sorted}}/M_{\text{sorted}}]^{\text{T}}$. The model coefficients, $a_0, \cdots, a_{C_{\text{x}}}$ and $b_0, \cdots, b_{C_{\text{y}}}$, are estimated by minimizing the least squares problem

$$\begin{bmatrix} \boldsymbol{a}_{\text{r}} & \boldsymbol{b}_{\text{r}} \end{bmatrix} = \underset{\boldsymbol{a},\boldsymbol{b}}{\arg\min} \left\| f(\boldsymbol{r}|\boldsymbol{a}, \boldsymbol{b}) - \boldsymbol{Q}'_{\text{sorted}} \right\|^2. \tag{28}$$

The target points are not evenly spread, why the resulting parameterization based on r can no be used directly as an expression of distance, but it can, however, be used to generate another polynomial parameterization, which is indeed based on arc-lengths.

From $f(r)$, the total arc length, L, of the curve can be computed through integration. Then, $M_{\text{spread}} + 1$ equally spaced points can be spread along the curve, one point per $\hat{l} = L/M_{\text{spread}}$ meters. Finally, a new polynomial model, which is now parameterizeds by arc length, s, can be fitted to the equally spaced points.

The arc length, in meters, between two r-values of the parameterization is given by

$$\ell(r_{\text{begin}}, r_{\text{end}}) = \int_{r_{\text{begin}}}^{r_{\text{end}}} \left\| \frac{\text{d}}{\text{d}r} f(r) \right\| \text{d}r \tag{29}$$

$$= \int_{r_{\text{begin}}}^{r_{\text{end}}} \left\| \begin{bmatrix} \sum_{i=1}^{C_{\text{x}}} a_i i r^{i-1} \\ \sum_{i=1}^{C_{\text{y}}} b_i i r^{i-1} \end{bmatrix} \right\| \text{d}r \tag{30}$$

$$= \int_{r_{\text{begin}}}^{r_{\text{end}}} \sqrt{\left(\sum_{i=1}^{C_{\text{x}}} a_i i r^{i-1} \right)^2 + \left(\sum_{i=1}^{C_{\text{y}}} b_i i r^{i-1} \right)^2} \text{d}r \tag{31}$$

The arc length between points i and $i+1$ is then given by $l_i = \ell(r_i, r_{i+1}) = \ell\left(\frac{i}{M_{\text{sorted}}}, \frac{i+1}{M_{\text{sorted}}} \right)$, why the total arc length of the curve is $L = \sum_{i=1}^{M_{\text{sorted}}-1} l_i$.

Now, $M_{\text{spread}} + 1$ points are distributed equally on the curve, one point for every $\hat{l}$ meters, so that there is a point

at arc lengths $0, \hat{l}, 2\hat{l}, 3\hat{l}, \cdots, L$. To do so, we need the r-values which correspond to these lengths. Let $\hat{r}_i$ be the sought after r-value of the i'th equally spaced point, which must be placed at arc length $i\hat{l}$. First, the possible r-interval is narrowed down by finding the two consecutive original points, with know r-values, which flanks the desired point on the curve. Say that these are original point number j and original point number $j+1$. Then, it is given that

$$\sum_{k=0}^{j} l_k \leq i\hat{l} < \sum_{k=0}^{j+1} l_k \,, \tag{32}$$

and therefore $\hat{r}_i$ must be such that the following equality holds

$$\ell(r_j, \hat{r}_i) + \sum_{k=0}^{j} l_k = i\hat{l} \tag{33}$$

$$\implies \qquad \ell(r_j, \hat{r}_i) = i\hat{l} - \sum_{k=0}^{j} l_k \,. \tag{34}$$

Using this equality, $\hat{r}_i$ can be found through the bisection method, which essentially determines $\hat{r}_i$ by optimization. Start from the current bounds of the solution, which are $r_{\text{lower}} = r_j$ and $r_{\text{upper}} = r_{j+1}$, and compute the arc length at the middle between the two bounds, i.e. $r_{\text{middle}} = r_{\text{lower}} + (r_{\text{upper}} - r_{\text{lower}}/2$. Evaluate the arc length at the middle by $s_{\text{middle}} = \ell(r_j, r_{\text{middle}})$. If $s_{\text{middle}} > i\hat{l} - \sum_{k=0}^{j} l_k$, then update the lower bound such that $r_{\text{lower}} \leftarrow r_{\text{middle}}$. Else, update the upper bound such that $r_{\text{upper}} \leftarrow r_{\text{middle}}$. Continue this bisection until s_{middle} converges. The corresponding r_{middle} is then equal to the desired $\hat{r}_i$. This procedure is used to get $\hat{r}_i$ for all $i = 0, \cdots, M_{\text{spread}}$, which are combined into the vector $\hat{\boldsymbol{r}} = [\hat{r}_0 \; \hat{r}_1 \; \hat{r}_2 \; \cdots \; \hat{r}_{M_{\text{spread}}}]^{\text{T}}$.

Using $\hat{\boldsymbol{r}}$, the positions of the $M_{\text{spread}} + 1$ equally spaced points can be sampled from $f(r)$ by

$$\boldsymbol{S} = f(\hat{\boldsymbol{r}})^{\text{T}} \,, \tag{35}$$

where $\boldsymbol{S} \in \mathbb{R}^{M_{\text{spread}} \times 2}$ is the matrix which contains the equally spaced points positions as rows. The points corresponding arc-lengths are given by the vector $\hat{\boldsymbol{s}} = [0 \; \hat{l} \; 2\hat{l} \; \cdots \; L]^{\text{T}}$. We would like the position of the leading edge to correspond to an arc length of 0. The leading edge point is found from $\boldsymbol{Q}'_{\text{sorted}}$, Equ. 26, using an approach similar to Equ. 13, $\hat{i} = \arg\min_i q'_{\text{sorted},i1}$. The leading edge's r-value is then $r_{\text{le}} = r_{\hat{i}}$. The corresponding arc-length, s_{le} is found using the bisect method. The arc-lengths in $\hat{\boldsymbol{s}}$ are then shifted by s_{le} to create the final arc-length vector, thus $\boldsymbol{s} = \hat{\boldsymbol{s}} - s_{\text{le}}$.

The arc-length parameterization is defined similarly to the definition of $f(r)$ in Equ. 27, but parameterized on arc-length, s, instead of r-value, thus $f(s)$. Its coefficients are obtained from the optimization

$$\begin{bmatrix} \boldsymbol{a}_{\text{s}} & \boldsymbol{b}_{\text{s}} \end{bmatrix} = \underset{\boldsymbol{a},\boldsymbol{b}}{\arg\min} \left\| f(\boldsymbol{s}|\boldsymbol{a},\boldsymbol{b}) - \boldsymbol{S} \right\|^2 . \tag{36}$$

The robot's acquisition positions are computed from a vector of specified arc-lengths, $\boldsymbol{s}_{\text{acq}} \in \mathbb{R}^N$, where N is the number of acquisition positions per curve. The planar positions on the curve are computed as $\boldsymbol{Q}'_{\text{acq}} = f(\boldsymbol{s}_{\text{acq}}|\boldsymbol{a}_{\text{s}}, \boldsymbol{b}_{\text{s}})$, and projected back into the platforms coordinate frame by $\boldsymbol{Q}_{\text{acq}} = \begin{bmatrix} \boldsymbol{Q}'_{\text{acq}} & \boldsymbol{0} & \boldsymbol{1} \end{bmatrix} \boldsymbol{H}^{-1\,\text{T}}$, where $\boldsymbol{0}$ is the 0-vector.

The orientations, which corresponds to the positions, are computed such that they corresponds to the curve's normal vectors. For position number n, at arc-length s_n, the tangent vector is

$$\boldsymbol{t}'_n = \left. \frac{\mathrm{d}}{\mathrm{d}s} f(s) \right|_{s=s_n} \Bigg/ \left\| \left. \frac{\mathrm{d}}{\mathrm{d}s} f(s) \right|_{s=s_n} \right\| . \tag{37}$$

The vector is rotated 90° in the plane, $\boldsymbol{n}'_n = \boldsymbol{R}_{90^\circ} \boldsymbol{t}_n$, and then flipped if it does not point towards the surface's internals. This vector represents the robot's direction vector. It is projected back into the platforms coordinate frame, using the same transformation as described above for $\boldsymbol{Q}'_{\text{acq}}$. A tilt, in the leading edge direction, can be added to counteract that light emitted by the scanner reflects off of the surface and directly back into the scanner. The final direction vector is $\boldsymbol{n}_n$.

The robot also has to be given a roll in order to fully specify its orientation. Here, it was chosen to specify the complete orientation through a full coordinate frame. We want the z-axis of the robot's tool, i.e. the scanner, to point in the reverse direction of the surface normal, thus in the directions of $\boldsymbol{n}_n$, and the y-axis to be aligned with the leading edge vector, $\boldsymbol{v}_{\text{le}}$. The x-axis is set such that the right hand rule applies. The full orientation for position n is thus

$$\boldsymbol{R}_n = \begin{bmatrix} \boldsymbol{v}_{\text{le}} \times \boldsymbol{n}_n \\ \boldsymbol{v}_{\text{le}} \\ \boldsymbol{n}_n \end{bmatrix} \; \forall \; n = 0, \cdots, N_{\text{acq}} - 1 \,. \tag{38}$$

As stated previously, the robot can reach two curves from each platform position. Therefore, the robot trajectory, defined by the above positions and transformations, is traversed twice. First, the robot moves in the positive direction of the platform's y-axis, towards the far side of the blade as seen from the platform. Then it steps a defined distance, Δ_{robot} meters, to the side along the leading edge in the positive x-axis direction. Finally, it returns to the platform by traversing the trajectory backwards in the negative direction of the y-axis. The side-step is given by $\boldsymbol{v}_\Delta = \Delta_{\text{robot}} \boldsymbol{v}_{\text{le}}$. The sequence of poses for the forward traversal is then

$$U_{\text{forward}} = \left(\begin{bmatrix} \boldsymbol{R}_n & & \boldsymbol{q}_{\text{acq},n} - \frac{1}{2}\boldsymbol{v}_\Delta \\ 0 \quad 0 \quad 0 & & 1 \end{bmatrix} \right)_{n=0}^{N_{\text{acq}}-1} , \tag{39}$$

and the pose sequence of the returning traversal is

$$U_{\text{backward}} = \left(\begin{bmatrix} \boldsymbol{R}_n & \boldsymbol{q}_{\text{acq},n} + \frac{1}{2}\boldsymbol{v}_\Delta \\ 0 \quad 0 \quad 0 & 1 \end{bmatrix} \right)_{n=N_{\text{acq}}-1}^{0}. \tag{40}$$

Observe that the blade's general direction is taken into account, as we slide the acquisition positions in the leading edge direction, but it does not consider the change in the blade profile's size as we move away from the mean. However, this was found not to be a problem, as the rate of change is so small, that the surface did not fell outside the scanner's focus depth. If it had been an issue, the point cloud could have easily been sliced by two planes instead of one. A completely separate curve could then have been computed for each plane, but this would have doubled the algorithms processing time, and thus prolonged the inspection time.

The platform moves before the robot, and this movement changes the robot's orientation and position relative to the blade. We counteract this by transforming U_{forward} and U_{backward} accordingly. Finally, the poses in the two sequences are transformed into the robots coordinate frame by applying $\left(\boldsymbol{T}^{\text{RP}}\right)^{-1}$ to each of them. This concludes computing the robot positions for acquisition round $t+1$.

3. Experiment and Results

The outermost 20 meters of a 55 meter long wind turbine blade was scanned to evaluate the control loop. Figure 5 shows the system as it finishes the scanning session. The parameters were set as follows during the experiment:

$$K = 10 \tag{41}$$

$$\Delta_{\text{platform}} = 0.42\,[\text{m}] \tag{42}$$

$$\Delta_{\text{robot}} = 0.21\,[\text{m}] \tag{43}$$

$$\boldsymbol{s}_{\text{acq}} = \begin{bmatrix} -0.245 \\ -0.1 \\ -0.02 \\ 0.02 \\ 0.1 \\ 0.245 \end{bmatrix} [\text{m}] \tag{44}$$

$$C_{\text{xr}} = C_{\text{yr}} = 15 \tag{45}$$

$$C_{\text{xs}} = C_{\text{ys}} = 9 \tag{46}$$

By setting the platform move distance to the double of the robot's sideways move distance, all point clouds get approximately the same overlap in the leading edge direction. The arc-lengths of the acquisition positions define the center positions of the scanners field of view, why the actual, returned point clouds extends past the arc-lengths of the beginning and end point. The degree of the r polynomials and the degree of the s polynomials were set to 15 and 9, respectively, as this was found to yield a better curve fit than using the same degree for both the r and s polynomials.

Figure 5: Photograph of the inspection system during the final acquisition rounds of a scan session. The outermost 20 meters of the blade's length was covered.

Fig. 6 shows the fitting of the initial polynomial to each of the x and y coordinates of the 9'th acquisition round. Fig. 7 shows the curve fit to the acquired point cloud from the 1'st acquisition round, together with the robot positions in the projection plane. Fig. 8 shows the curve to the point cloud from the 9'th round, and Fig. 9 shows the curve fit to the point cloud from the 15'th round. Note that the slant of the leading edge plane is difficult to see in the figures, but the transverse plane which crosses the point clouds to the left is actually a plane viewed almost edge on.

4. Discussion

From Fig. 7 and Fig. 8, we see that the model fits the measured points rather well, and that the surface normals (black arrows) also follows the surface orientation nicely. It is also seen, that the direction of the direction of the leading edge is found rather well. From these plots, it would seem like the leading edge direction could be detected directly from a Principal Component Analysis (PCA) of the point cloud. This was tried, and this method turned out to capture the leading edge's orientation in the x and y axis rather good, though with less precision than the presented method, but the direction in the z axis was often way off.

Fig. 9 showcase an example of a bad fit. The curve does not stretch to include the leading edge, and the to lower most acquisition positions, and their corresponding orientations, are off. This could pose a problem, but in all events where

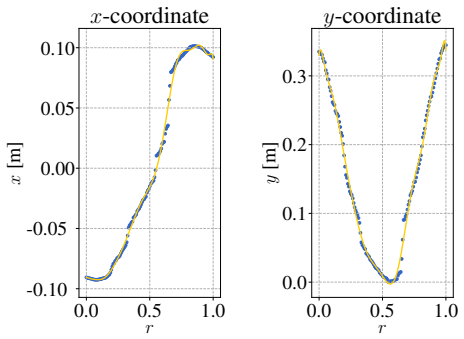

Figure 6: Plot of the x and y coordinates of the points projected onto the projection plane, after sorting, and the initial polynomial models. The left plot is the x coordinate with respect to r and the right plot is the y coordinate with respect to r.

this behavior was observed, the surface was still well within the scanners depth of focus. It is believed that the model is rather sensitive to noise in the points at the beginning or end of the curve. As seen on the figure, the curve ripples slightly at the end of the curve, to the right. We think that this wobble makes it impossible for the curve to get back to include the leading edge, due to its limited degree of freedom. It was experimented with using a higher polynomial degree, but this introduced more small ripple effects, where the model would start to over-fit. This resulted in a curve which was closer to the points, but with fluctuating surface normals.

References

[1] R. A. Lyngby, H. Aanæs, E. Nielsen, and A. B. Dahl, "Autonomous surface inspection of wind turbine blades for quality assurance in production," in *9th European workshop on structural health monitoring*, 2018.

[2] Y. Petryna, A. Künzel, and M. Kannenberg, "Fault detection and state evaluation of rotor blades," in *EWSHM-7th European Workshop on Structural Health Monitoring*, 2014.

[3] S. Larsson and J. A. Kjellander, "Path planning for laser scanning with an industrial robot," *Robotics and autonomous systems*, vol. 56, no. 7, pp. 615–624, 2008.

[4] S. Kriegel, C. Rink, T. Bodenmüller, and M. Suppa, "Efficient next-best-scan planning for autonomous 3d surface reconstruction of unknown objects," *Journal of Real-Time Image Processing*, vol. 10, no. 4, pp. 611–631, 2015.

[5] N. D. M. Phan, Y. Quinsat, S. Lavernhe, and C. Lartigue, "Scanner path planning with the control of overlap for part inspection with an industrial robot," *The International Journal of Advanced Manufacturing Technology*, pp. 1–15, 2018.

[6] C. B. Barber, D. P. Dobkin, and H. Huhdanpaa, "The quickhull algorithm for convex hulls," *ACM Transactions on Mathematical Software (TOMS)*, vol. 22, no. 4, pp. 469–483, 1996.

[7] H. Wang, J. Kearney, and K. Atkinson, "Arc-length parameterized spline curves for real-time simulation," in *Proc. 5th International Conference on Curves and Surfaces*, 2002, pp. 387–396.

[8] K. Chu, M. Lee, and M. Sunwoo, "Local path planning for off-road autonomous driving with avoidance of static obstacles," *IEEE Transactions on Intelligent Transportation Systems*, vol. 13, no. 4, pp. 1599–1616, 2012.

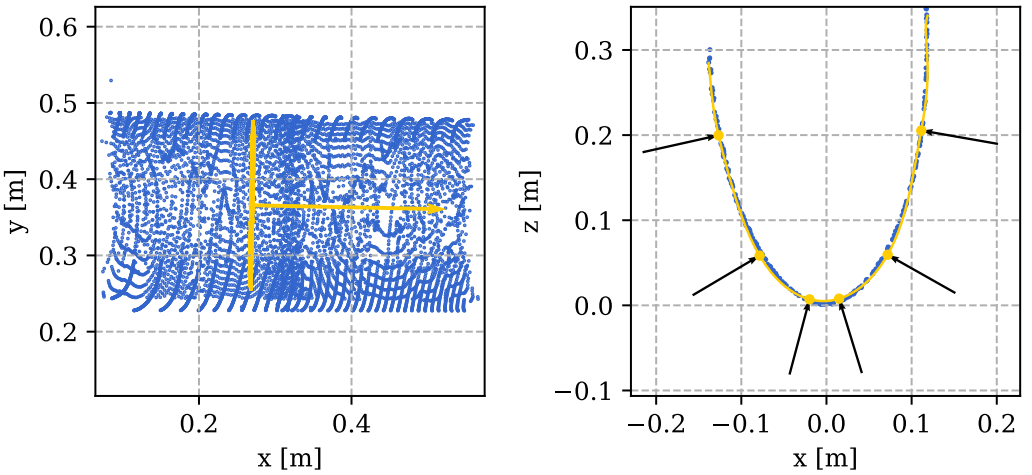

Figure 7: Plot of a planned robot trajectory from acquisition round 1 in the plane. The left plot shows 0.05% of the individual points in the combined point cloud, as seen from above, with the projection plane and leading edge direction shown in yellow. Note that the actual plane extends infinitely. The right plot shows the fitted curve and planned scan poses on the projection plane. Here, 2% of the sorted points, which are used as the target for the fitted curve, are shown.

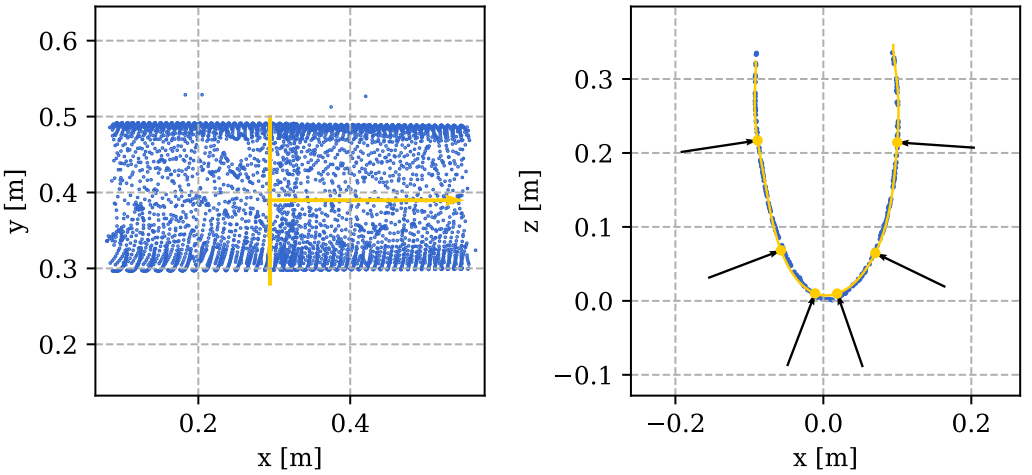

Figure 8: Plot of a planned robot trajectory from acquisition round 9. Refer to Fig. 7 for a general explanation of the figure. It can be seen from the combined point cloud, that the blade is narrower in this position, as compared to the measurements from round 1.

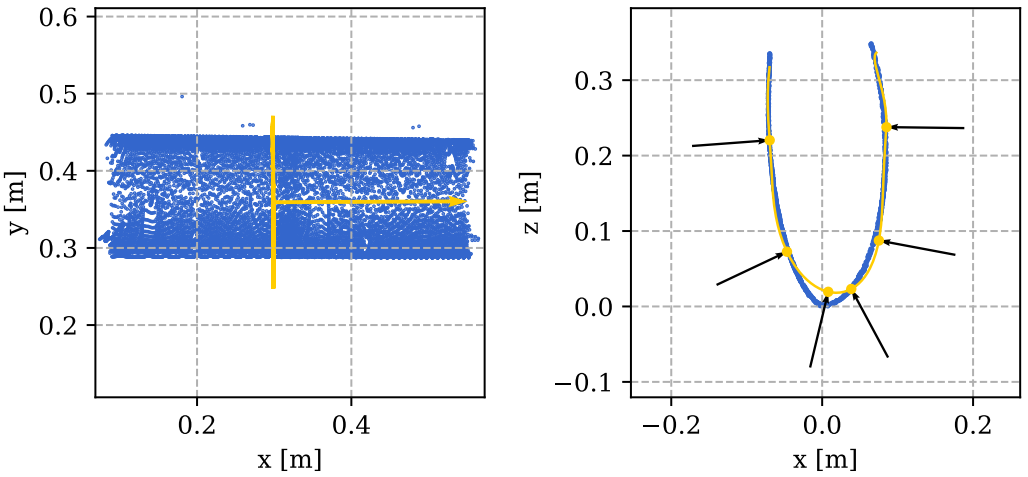

Figure 9: Plot of a planned robot trajectory from acquisition round 15. Refer to Fig. 7 for a general explanation of the figure. As seen in the right plot, the fitted curve failes to properly align with the target points. This behaviour was observed in situations where noise or mis-alignment would cause either the beginning or end of the curve to wobble. The wobble can be seen here near the end of the curve to the right.

CONTRIBUTION G

Visual Inspection Arrangement

Patent application	18171466.8
File date	May 9, 2018
Publication date	November 9, 2019

This patent application was submitted to the European Patent Office and relates to the autonomy and locomotion of the blade scanner system. The application was filed and awaits publishing and scrutinizing by the patent office.

Description

Visual inspection arrangement

The invention describes a visual inspection arrangement, and a method of performing a visual inspection of an object.

In keeping with advances in the field of renewable energies, larger wind turbines are being designed and constructed, with rated power output in the region of several megawatts. Generally, this is made possible by the use of longer rotor blades that turn an outer rotor of a permanent magnet generator. Rotor blade lengths in excess of 50 m are no longer the exception. To achieve a resilient but also relatively light structure, a wind turbine rotor blade is generally moulded in a composite layup procedure. The established geometry of a rotor blade comprises an essentially circular root end for mounting to the hub, and a gradually tapering airfoil shape over the remaining length of the blade, terminating in a narrow and flat tip end.

Defects in the rotor blade can be introduced at various stages during the blade manufacturing process, and can significantly detract from the wind turbine performance and from the rotor blade lifetime. For example, irregularities at the surface can lead to erosion and increased drag. Therefore, it is very important to inspect the quality of the blade's surface before it leaves the production site, such that any significant errors can be traced to their origin in the production process so that the cause of the problem can be eliminated.

The size of a defect can go from macro (with a size of 1 metre or more) to micro (with a size of only a few micrometres), and it is difficult to provide a testing procedure that is capable of detecting all kinds of defect to the same level of accuracy. There are various prior art testing methods, each of which is generally suited to

detecting defects within a certain size range. For example, a gauge template can be used to detect deviations from the design geometry, i.e. macro-scale defects, following Taylor's measurement principle. However, this approach can be problematic owing to the complex shape of modern rotor blades. To counteract an undesirable bending of a long rotor blade during operation, the rotor blade usually does not have a straight longitudinal or chordwise axis, and instead the chordwise axis may follow a gentle curve. The airfoil part of the blade therefore "twists" to a certain extent about the chordwise axis. It is important that the shape of the finished rotor blade meets any such design requirement.

A visual inspection using a flashlight is carried out in order to detect small-scale defects such as small cracks or pits in the outer surface of the rotor blade. However, this kind of inspection technique is time-consuming and requires trained personnel, since small-scale defects can be difficult to detect.

Another technique makes use of a manually operated, laser-based coordinate measuring machine (CMM). In such an approach, a stationary laser tracker is used to track and continuously measure the position of a probe that is moved over the blade surface by an operator. This creates a set of profile curves which are sampled sparsely over the surface. Another laser-based system is based on stationary Lidar and does not require a probe to measure the profile curves. In these measurement procedures, the laser system must be repositioned and re-calibrated multiple times in order to cover the entire length of the blade. This makes the acquisition process slow and therefore also expensive. Furthermore, these methods result in profile curves that are separated by relatively large distances, so that they are not suitable for detecting small-scale defects and micro-defects. The need to re-position the laser system may be avoided by deploying a rail-mounted laser system. However, the rails must generally be fixed to the ground and therefore greatly

limit the flexibility of the system. Within the constraints of a rail-based system, it is generally not possible to cover the entire surface of a curved rotor blade. Furthermore, since the rails are a permanent fixture, any rotor blade to be tested must be moved to that location, further adding to the overall cost of manufacture.

It is therefore an object of the invention to provide an improved way of inspecting a wind turbine rotor blade.

This object is achieved by the visual inspection arrangement of claim 1, and by the method of claim 12 of performing a visual inspection of an object.

According to the invention, the visual inspection arrangement comprises an imaging assembly, and a robot assembly realised to move in an unconstrained manner – i.e. freely - alongside an object being subject to visual inspection. In the context of the invention, the term "unconstrained" is to be understood to mean that the robot assembly is not constrained by fixed elements such as rails or tracks, but can move freely and in any direction relative to the object being inspected. The robot assembly comprises a robot arm with an end effector to which the imaging assembly is mounted. The robot assembly is realised to direct the imaging assembly at the object. The visual inspection arrangement further comprises a drive arrangement realised to effect a displacement of the robot assembly; a positioning system configured to track the position of the imaging assembly relative to the object; and a controller configured to control the drive arrangement. The controller generates control signals for the drive arrangement, and these control signals are preferably generated on the basis of the measured geometry of the object. The geometry of the object is determined using data collected by the imaging assembly and also using data provided by the positioning system. The controller is therefore configured to control the drive

arrangement on the basis of the tracked position of the imaging assembly and the geometry of the object.

The imaging assembly may be assumed to be held by the robot arm end effector in such a way that an imaging device of the imaging assembly can be pointed at the surface of the object undergoing inspection. A robot arm can be realised so that its end effector can be moved with six degrees of freedom. The end effector can be moved relative to mutually orthogonal X, Y and Z axes in a local reference frame in three-dimensional space. Its orientation can comprise roll, pitch and yaw about those X, Y and Z axes. The position of the end effector and therefore also the imaging assembly can therefore be expressed using three components of translation (the XYZ position) and three components of rotation (the RxRyRz position), giving a total of six degrees of freedom. The three components of translation can be described as forward/back (along a local X axis), left/right (along a local Y axis) and up/down (along a local Z axis). The three components of rotation can be described as roll (about the local X axis), yaw (about the local Y axis) and pitch (about the local Z axis). Roll, pitch and yaw can be determined using any suitable arrangement of sensors, for example a sensor arrangement of the robot assembly that is used to track the RxRyRz position of the end effector. These six degrees of freedom can be achieved by constructing the robot arm with an appropriate arrangement of joints and actuators, as will be known to the skilled person. Such robot arms are known in the field of automated precision manufacturing, for example. A desired level of precision can be achieved by realising the robot arm so that its motion is smooth and controlled. In the context of the invention, the position of the imaging assembly relative to the object shall be understood to comprise a complete or unique XYZ and RxRyRz position definition in that local reference frame.

An advantage of the inventive visual inspection arrangement is that it is not constrained in any way, unlike the known

prior art systems that use a system of rails to support an imaging assembly. Furthermore, the visual inspection arrangement can perform a complete visual inspection of an object without any user intervention, unlike in some known prior art systems that require relocation of an imaging assembly from one side of the object to the other. An advantage of the inventive visual inspection arrangement is that the drive arrangement effects a displacement of the robot assembly on the basis of the determined position of the imaging assembly, without any need for manual intervention. In other words, information regarding the position of the imaging assembly relative to the object undergoing inspection is used as a basis to determine the future position of the imaging assembly. The inventive visual inspection arrangement may therefore be regarded as a self-driving or autonomous visual inspection arrangement. Another advantage is that the inventive visual inspection arrangement does not require any alterations to the production facility. All that may be required is a relatively flat floor. If the underside of the object is also to be inspected, the visual inspection arrangement should also be given unobstructed passage below the object. The autonomous nature of the inventive visual inspection arrangement can therefore lead to a significant reduction in the overall manufacturing costs.

According to the invention, the method of performing a visual inspection of an object uses an embodiment of the inventive visual inspection arrangement. The method comprises the steps of moving the robot assembly to a working position and then scanning the surface portion of the object accessible from within the work envelope of the robot assembly at that working position (step S1), while tracking the position of the imaging assembly; computing the next working position for the robot assembly (step S2) on the basis of the just scanned surface portion and/or the tracked position of the imaging assembly; effecting a displacement of the robot assembly to that working position (step S3); and repeating steps S1 – S3 to scan the area of interest. The "area of interest" might be

the entire surface area of the object or only a portion of the object's surface. The term "work envelope" is known from the field of robotics and refers in this case to the volume defined by the reaching space of the robot arm. The size of the work envelope will depend on the length of the robot arm, the number and type of joints in the robot arm, etc.

An advantage of the inventive method is that it can be easily implemented in any production facility. As mentioned above, there is no need to make any alterations to the production facility, or to provide a dedicated area in which to carry out the inventive method. All that is required is a relatively flat floor, and preferably also sufficient clearance underneath the object. The inventive method provides a way of performing a quick and thorough visual inspection of an area of interest without any user intervention, since there is no need to manually relocate elements of the visual inspection arrangement at any stage during the procedure.

The invention also describes a computer program product comprising a computer program that is directly loadable into a memory of the control unit of an embodiment of the visual inspection arrangement, and which comprises program elements for performing steps of the inventive method when the computer program is executed by the control unit of the visual inspection arrangement.

Particularly advantageous embodiments and features of the invention are given by the dependent claims, as revealed in the following description. Features of different claim categories may be combined as appropriate to give further embodiments not described herein.

The inventive visual inspection arrangement can be used to perform a visual inspection of any kind of object. Because of its flexibility and adaptability, the inventive visual inspection arrangement is particularly suited to the visual inspection of objects with irregular or complex surfaces. In

the following, without restricting the invention in any way, it may be assumed that the object undergoing visual inspection is the rotor blade of a wind turbine. A wind turbine rotor blade can be very long (lengths in excess of 50 m are no longer the exception) and generally comprises several differently shaped regions. Typically, a wind turbine rotor blade commences at an essentially cylindrical root end which transitions to an airfoil shape that extends over most of the blade length and terminates in a thin and narrow tip. The cylindrical root end can be up to several metres in length. The longest chord of the airfoil portion of the rotor blade is generally found in the transition region, and the chord decreases steadily in the direction of the tip. The blade thickness also decreases steadily in the direction of the tip. For reasons of energy efficiency, acoustic optimisation, etc., the rotor blade of a large wind turbine will also generally be shaped to exhibit some degree of flex or twist. The overall shape of a wind turbine rotor blade is therefore complex. However, as mentioned above, it is necessary to completely and thoroughly examine the rotor blade in order to detect defects and also to determine whether the measured geometry of the rotor blade matches the intended geometry. Such a complete and thorough inspection can be carried out in a quick and efficient manner using the inventive method.

In a particularly preferred embodiment of the invention, the positioning system comprises a stationary laser tracker arranged in the vicinity of the object, and one or more retro-reflective targets. For example, the laser tracker can be mounted on a suitably stable support that can be placed near the rotor blade tip end in such a way that it can "see" a retro-reflective target at all times. A retro-reflective target can be realised as a passive or active retro-reflector, for example. A passive retro-reflective target simply reflects the laser beam. If passive retro-reflectors are used as targets, it is necessary to track several targets, and the laser tracker must shift between targets.

Following each shift, the laser tracker must locate the next target, so that the procedure is relatively time-consuming. Therefore, in a preferred embodiment of the invention, the retro-reflective target is an active target carried by the end effector. An active retro-reflective target also includes electronics and/or sensors that can provide RxRyRz information, for example. In such a preferred embodiment, the imaging assembly and the active target are both carried by the end effector and therefore move as one entity. In a calibration step, the position of the imaging assembly can be determined relative to the active target.

Preferably, the laser tracker is configured to generate position data describing the XYZ position of the imaging assembly in a local reference frame, and the active target is configured to generate position data describing the RxRyRz position of the imaging assembly in the local reference frame. In one embodiment, the laser tracker comprises a laser source for generating a laser beam, and the laser source is rotatable within a relatively large range. The laser tracker is realised to aim the laser beam in the direction of the active target and receives the reflected laser beam, from which it can compute the XYZ position of the active target. From this information and the calibration data, it is possible to compute the XYZ position of the imaging assembly.

Being mounted on the end effector, the active target is movable in six degrees of freedom. Preferably, the active target is equipped with a sensor assembly such as an angular encoder arrangement so that it can determine its RxRyRz orientation. From this information, it is possible to compute the RxRyRz position of the imaging assembly. On the basis of the XYZ position information and RxRyRz position information, the control unit can track the movements of the imaging assembly and compute a next position for the imaging assembly, as well as any appropriate control signals for one or more actuators of the visual inspection arrangement in order to move the imaging assembly to the next position. With

such a laser-based positioning system, an unobstructed view between the active target and the laser tracker is only required in a relatively narrow field.

As explained above, the laser tracker can "follow" or track the active target. In a preferred embodiment of the invention, the laser tracker is realised to compute the position of the active target in spherical coordinates. To this end, the distance r to the active target is calculated based on the time it takes for the light to hit the active target and return to the laser tracker, and the elevation angle θ and azimuth angle φ are measured (for example using data provided by angular encoders mounted on mechanical axes of the moveable laser source). The spherical coordinates can be converted to Cartesian coordinates by the equations

$$X = r \sin\theta \cos\varphi$$

$$Y = r \sin\theta \sin\varphi$$

$$Z = r \cos\theta$$

to obtain the XYZ position of the active target (and therefore also the XYZ position of the imaging assembly). The $R_X R_Y R_Z$ position of the active target (and therefore also the $R_X R_Y R_Z$ position of the imaging assembly) can be computed using information from motion sensors arranged in a housing of the active target, for example, or from sensors mounted on the end effector or elsewhere on the robot assembly.

In a further preferred embodiment of the invention, elements of the visual inspection arrangement can communication in a wireless manner. For example, the active target and laser tracker can be equipped with a means to communicate over a wireless local area network. In such an embodiment, the active target can send RxRyRz position information to the laser tracker, and the laser tracker can transmit the complete XYZ and RxRyRz position information of the imaging assembly to the control unit, which can use this information

to generate control signals for one or more actuators in order to move the imaging assembly to its next position.

Any suitable kind of imaging assembly may be used to scan the surface of the object under inspection. In a preferred embodiment of the invention, the imaging assembly may be realised as a geometrical measurement device such as an area-sampling 3D scanner. Examples of such devices are a structured light scanner, a moving laser scanner, a time-of-flight scanner, etc. The imaging assembly may be realised to generate photographic images or contour images of the object's surface. Alternatively, image data collected by such a device may be a point cloud. The image data returned by the imaging assembly is processed by a controller and used in a feedback loop to autonomously plan and control the future movement of the platform. For example, the controller or control unit may analyse the images to determine whether a surface region of the object has been sufficiently covered before moving on to the next surface region. Neighbouring and/or overlapping images can be "stitched" using any suitable stitching technique as will be known to the skilled person.

Stitching of neighbouring scans ("sub-scans") is generally performing by aligning measured points of neighbouring scans. The sub-scans are ordered in the common reference frame using the tracked position of the imaging assembly, i.e. using the XYZ and RxRyRz position information provided by the positioning system. Since the local geometry of wind turbine blades is very monotonous (i.e. there is little change), prior art techniques of visual inspection have difficulty in unambiguously identifying the correct alignment positions for two neighbouring scans. The inventive visual inspection arrangement with its positioning system as described above can accurately track the position of the imaging assembly relative to the object being inspected, thereby providing all necessary information for accurate and rapid image stitching, since the relative positions of neighbouring scans can be

accurately established. The positioning system therefore provides precise information that can be used to stitch the sub-scans together to a much higher level of accuracy than would otherwise be possible using only the scan data.

In a preferred embodiment of the invention, the alignment of neighbouring scans is enhanced by a suitable algorithm, for example an iterative closest point (ICP) algorithm. Preferably, the uncertainty of the position should be lower than half of the minimum point-to-point distance. This distance is scanner dependant, and as such is not a limiting property of the system. For example, this distance can be in the order of 200 µm.

The robot arm could be arranged on a body with "robot legs" so that it can "walk" alongside the object undergoing visual inspection. However, in a more straightforward and economical realisation, the robot assembly comprises a mobile base frame realised to support the robot arm and to move in an entirely unconstrained manner alongside the object being subject to visual inspection. The mobile base frame can be realised as a horizontal or flat frame close to floor level, equipped with wheel pairs so that it can move along the ground.

In one preferred embodiment of the invention, the mobile base frame is equipped with two wheel pairs, and the drive arrangement comprises an electric motor assembly to drive one of these wheel pairs. The other two wheels can be non-driven wheels or follow-wheels. In an alternative embodiment, a mobile base frame of a holonomic robot assembly can be equipped with omniwheels. Any of these embodiments ensures that the mobile base frame can move forward and back, and also from side to side. Since the mobile base frame carries the robot arm, it already contributes two degrees of freedom to the robot arm end effector.

As mentioned above, a wind turbine rotor blade can be very large. When supported on a factory floor, the upper surface of the rotor blade may be several metres above floor level.

The required vertical movement range may be obtained by choosing a suitably long robot arm, i.e. a robot arm with two or more suitably long sections. Such a robot arm can reach to the necessary height, but will have a corresponding large work envelope and may be cumbersome to manipulate. Furthermore, it can be difficult for such a robot arm to reach underneath the rotor blade. Therefore, to obtain a desired vertical movement range, the inventive visual inspection arrangement preferably comprises a vertical elevator support mounted on the mobile base frame, and a mounting interface of the robot arm is secured to a vertical elevator or platform mounted to the vertical elevator support. In this way, the mobile base frame contributes three degrees of freedom to the robot arm end effector. The vertical elevator support can be realised as a linear drive, with a motor that can be controlled to effect a desired vertical displacement of the platform (and therefore also the robot arm). In this way, a satisfactory work envelope can be obtained for a compact robot arm constructed from favourably short sections. The drive arrangement shall be understood to also comprise any motor(s) or actuator(s) of the vertical elevator support.

As indicated above, it may also be desirable or necessary to inspect the underside or under surface of the object. To this end, the imaging assembly must be manoeuvred in some way underneath the object. One way of doing this would be to use long robot arm sections, as indicated above, and to move the mobile base frame sufficiently far back from the object so that the long arm sections can be manipulated to move them under the object. However, this realisation can be unstable as well as being expensive to realise. Therefore, in a preferred embodiment of the invention, the mobile base frame is constructed to have an aperture that can accommodate at least a portion of the robot arm. In this way, an elbow of the robot arm can be lowered to almost floor level and can sweep closely over the floor. This manoeuvrability of the robot arm allows the end-effector of the robot to move

underneath the object. One way of achieving such an aperture might be to construct the mobile base frame as an open rectangular frame, or as a C-shaped frame, so that an elbow of the robot arm can be lowered into the aperture or empty space formed by the frame.

Any suitable kind of positioning system can be used as an alternative to the laser-based system described above. For example, an existing indoor positioning system might be used. In such an embodiment, a tracking device can be mounted on the end effector, and can be any device that is able to communicate with one or more anchor nodes or satellites arranged about the object undergoing inspection. For example, anchor nodes can be realised as wireless access points, and the tracker can communicate with these anchor nodes so that, by triangulation, the position of the imaging assembly in the reference frame can be unambiguously established.

The skilled person will be familiar with the various possibilities and may consider the use of any of several available wireless, acoustic or optical positioning systems. In most indoor positioning system, a minimum of four "satellites" may be attached to the ceiling, and the tracking device is a suitable transmitter mounted on the imaging assembly. In a wireless system, the transmitter emits a radio signal which is received by the satellites, and the time delays between the signals can be used to compute the position of the imaging assembly. In an audio positioning system, the principle is the same, but the tracking device emits an audio signal instead of radio. The XYZ position information can be obtained from just one transmitter, but at least three transmitters are needed to establish a local reference frame and thereby the orientation or rotation information $R_X R_Y R_Z$. In these satellite-based realisations, a disadvantage is that the satellites are generally permanently installed (on the ceiling), placing a constraint on the location of the visual inspection arrangement and necessitating permanent alterations to the production

environment. In addition, the satellites must be evenly distributed around the object being inspected in order to avoid large uncertainties arising during extrapolation, and the space between transmitter and satellites must be free of any obstruction. If the satellites are moved for any reason, recalibration of the visual inspection arrangement is necessary.

Preferably, the inventive visual inspection arrangement is realised for the visual inspection of a large wind turbine rotor blade. To this end, the robot assembly is preferably realised as a multiple-jointed robot arm, and is mounted to a mobile base frame that preferably has a weight of at least 250 kg, more preferably 500 kg to support the robot arm. Preferably the mobile base frame has a footprint of at least 2.5 m^2, more preferably at least 3 m^2. When the mobile base frame is realised as a flat and low structure, its large footprint does not in any way restrict the motion of the robot arm.

To initiate a scan procedure, the robot assembly is placed in a suitable initial working position, for example any position from which the robot arm can direct the imaging assembly at the surface of the object in order to generate a useful image. With the robot assembly at this initial position, the controller actuates the robot arm to move the imaging assembly (step S1) while scanning the surface that is accessible from within the work envelope of the robot assembly at that working position. Preferably therefore, this step S1 comprises the steps of positioning the imaging assembly in a sampling position to direct it at the object (step S1.1), generating image data for that sampling position (step S1.2) and then moving the imaging assembly to a subsequent sampling position S1.3. These steps are repeated to scan the surface portion that is accessible from within that work envelope. The "sampling position" shall be understood to be the uniquely defined position of the imaging assembly in the local reference frame. A sampling position

can be defined as a set of coordinates in the reference frame, for example. A subsequent sampling position will result in the position and/or orientation of the imaging assembly being offset in one or more directions. Preferably, the density of the sampling positions is adapted to the shape of the object's surface. For example, sampling positions may be spaced close together when the shape of the object is complex or irregular, and may be spaced further apart when the shape of the object is relatively flat or only slightly curved.

The data generated at each scan position therefore comprises image information as well as position information provided by the tracker.

After complete coverage of the surface accessible from within a specific work envelope, the next working position for the robot assembly is computed in step S2. The next working position can be defined as one or more sets of coordinates in the reference frame, for example. Alternatively, the next working position can be formulated as a set of relative displacements (e.g. move x cm along X-axis, move y mm along Y-axis, etc.). Preferably, the next working position defines the next position of the mobile base frame and also the next position of the imaging assembly. On the basis of this information, the control unit generates control commands for the various elements of the drive arrangement in order to effect the corresponding displacement of the robot assembly to the next working position (step S3).

Steps S1 – S3 are repeated until the entire area of interest has been scanned.

Depending on the depth-of-field of the scanner, the visual inspection could be carried out in a two-tier approach, i.e. scanning at a first distance from the blade to map its geometry and to determine whether the blade has the correct overall shape, and then scanning from a second distance

(closer to the surface) to detect small-scale surface defects.

Other objects and features of the present invention will become apparent from the following detailed descriptions considered in conjunction with the accompanying drawings. It is to be understood, however, that the drawings are designed solely for the purposes of illustration and not as a definition of the limits of the invention.

Fig 1 shows a side view of an embodiment of the inventive visual inspection arrangement;
Fig 2 shows a plan view of the visual inspection arrangement shown in Fig 1;
Fig 3 shows a side view of the visual inspection arrangement shown in Fig 1 and Fig 2;
Fig 4 shows a further side view of an embodiment of the inventive visual inspection arrangement;
Fig 5 is a flowchart showing the steps in an exemplary embodiment of the inventive method;
Fig 6 shows a computation unit of an embodiment of the inventive visual inspection arrangement;
Fig 7 is a schematic representation of a drive arrangement for an embodiment of the inventive visual inspection arrangement;
Fig 8 shows elements of a positioning system used in an embodiment of the inventive visual inspection arrangement.

In the diagrams, like numbers refer to like objects throughout. Objects in the diagrams are not necessarily drawn to scale.

Fig 1 shows a side view of an embodiment of the inventive visual inspection arrangement 1, and Fig 2 shows a plan view of the setup. The diagrams show a robot assembly 10 supported on a platform 103P of a vertical elevator support 103, which in turn is mounted on a mobile base frame 102. The robot assembly 10 is shown relative to the airfoil portion of a wind turbine rotor blade 2, which is held in position so that

the trailing edge is pointing upward, and the leading edge faces the floor. As indicated in the diagrams, the rotor blade is supported so that there is some clearance between the leading edge and floor level to permit a visual inspection of the leading edge.

The image scanner 11 may be any suitable type of scanner. Preferably, the image scanner 11 is an area-sampling 3D scanner with a suitably fine resolution, for example at least 250 µm between points (25 points per square mm), and an uncertainty which is less than one third of the minimum point-to-point distance, in this case maximum 83.3 µm. This resolution and precision is sufficient to detect very small structures such as the height of the transition from the blade's outer surface to a protective layer applied about the leading edge.

The image scanner 11 can therefore be used to detect small-scale surface defects and also to map the overall geometrical shape of the blade. Of course, a higher resolution can be achieved by using a camera with a higher resolution or a smaller field of view. In this way, it is possible to measure structures that have a size in the region of only 100 µm.

The mobile base frame 102 is equipped with two wheel pairs. A control unit 14 supported by the mobile base frame 102 is configured to control a drive unit or actuator that turns one wheel pair 12W1, and the other wheel pair simply follows. The robot assembly 10 comprises a robot arm 100 that has a number of jointed sections, and which terminates in an end effector 101 that holds an image scanner 11. In this exemplary embodiment, the robot arm 10 is realised to displace the end effector 101 along its local X, Y and Z axes, and to rotate the end effector 101 about these axes, so that the end effector 101 (and therefore also the image scanner 11) has six degrees of freedom. These degrees of freedom are obtained by constructing the robot assembly 100 using suitable actuators. The control unit 14 is configured to control the

actuators of the robot arm 100 and end effector 101. Translation movement of the end effector 101 in X, Y and Z axes can also be achieved by the driven wheel pair 12W1 of the mobile base frame 102 and the vertically moveable platform 103P. These components of the visual inspection arrangement 1 can be used for a "rough" positioning of the end effector 101, and the actuators of the robot assembly 100 are then controlled to achieve a "fine" positioning of the end effector 101. The control unit 14 therefore always knows the XYZ position and the $R_X R_Y R_Z$ position of the end effector 101 and imaging assembly 11.

As mentioned above, the surface of the rotor blade 2 can be locally monotonous, so that there does not appear to be any difference between adjacent images of the surface. However, the images must be stitched to a sufficiently accurate degree in order to determine the overall shape of the rotor blade. This is done by using a positioning system to continually determine the position of the imaging assembly 11 relative to the rotor blade 2 within a reference frame. There are various types of positioning system that may be used for this purpose. In this exemplary embodiment, a laser-based positioning system is used, and a laser tracker 130 (shown in Fig 2) is positioned near the tip of the blade 2. An active retro-reflective target 131 is mounted onto the image scanner 11 so that the active target 131 and image scanner 11 move as one entity. The laser tracker 130 emits a laser beam B that is reflected by the active retro-reflective target. The laser tracker 130 is configured to continually measure the distance to the target 131. Initially, the position of the imaging assembly 11 relative to the active target 130 is known from a previous calibration procedure. The stationary laser tracker 130 remains in place for the duration of the inspection procedure. The features of this type of positioning system will be known to the skilled person. The assembly comprising the image sensor, gyroscope and laser tracker can be an off-the-shelf device such as the vProbe from Automated Precision Inc., as will be known to the skilled person.

Fig 2 shows the airfoil portion of the wind turbine rotor blade 2, the laser tracker 130 arranged near the tip end of the blade 2, and the retro-reflective active target 131. The mobile base frame 102 has been moved sufficiently close to the side of the rotor blade 2, using the driven wheel pair 12W1, so that the robot assembly 100 can then be actuated to collect images of the rotor blade surface area in an image region R. The laser tracker 130 emits a laser beam B that is reflected by the active target 131, so that the XYZ position of the imaging assembly 11 can be determined. Using a sensor arrangement configured to track the $R_XR_YR_Z$ rotation of the imaging assembly 11, the $R_XR_YR_Z$ position of the imaging assembly 11 can be determined. Using this information 13_XYZ, 13_ $R_XR_YR_Z$, the control unit 14 controls any actuators of the robot assembly 100 so that the end effector 101 moves the imaging assembly 11 until it has captured (preferably overlapping) images of all sub-regions R within the accessible region R_{env}. As explained above, the images are stitched using a suitable stitching algorithm that is fed with image data 11_D as well as position data 13_XYZ, 13_$R_XR_YR_Z$ of the imaging assembly 11.

Fig 3 shows a side view of the assembly described in Fig 1 and Fig 2 above. In this embodiment, the robot assembly 10 is realised so that the platform 103P (to which the robot arm 100 is mounted) can also be tilted from side to side, thereby also contributing to the rotation component of the imaging assembly 11. As mentioned above, the platform 103P can be raised and lowered, in this case along a vertical spindle axis 1030, thereby contributing to the translational Z-axis displacement of the imaging assembly 11. The control unit 14 is configured to control any actuator(s) used to achieve these displacements and to record the relevant position data.

Fig 4 illustrates an alternative embodiment of the inventive visual inspection arrangement 1. Here, the positioning system 13 makes use of an indoor positioning system, with a number of stationary ceiling-mounted targets 132 and a means of

communicating with these in a wireless manner in order to determine the XYZ position of the imaging assembly. As explained above, the RxRyRz position of the imaging assembly can be determined by evaluating information provided by sensors of the robot assembly, for example transducers, gyroscopes, charge-coupled devices etc.

The robot assembly 10 is being used to inspect a rotor blade 2 over a specific length L_{scan} of its airfoil portion. This is the region of most interest, since most of the lift is generated in this blade region and defects present over this length L_{scan} are most critical to the performance of the rotor blade 2. Any reference to the "complete object" or "entire object" scanned by the visual inspection arrangement 1 shall be understood to refer to the region of interest that is scanned, since any other part of the object may be considered to be irrelevant. Here, the "entire object" is the outer end of the rotor blade, i.e. the airfoil tip portion of the blade.

The diagram indicates a support 4 for the rotor blade 2 near the root end of the blade 2. The root end is unimportant aerodynamically and need not be scanned. The scan sequence can commence on one side of the rotor blade 2 close to the support 4, proceeding along the rotor blade 2 and around the tip end, back to the support 4 on the other side. In this way, the entire region of interest (the airfoil portion over length L_{scan}) can be imaged in a single uninterrupted scan sequence.

Alternatively, if the blade must be supported at some point along the region of interest, the visual inspection arrangement 1 can be equipped with a laser range scanner which informs the control unit 14 when the distance to the support drops below a threshold, and the mobile base frame 102 can then be manually moved around the obstacle (or automatically if the location and dimensions of the obstacle are known), so that the scan sequence may resume.

Fig 5 is a flowchart showing the steps in an exemplary embodiment of the inventive method. To perform a visual inspection of an object such as a wind turbine rotor blade or any large, complex object, a robot assembly of the inventive visual inspection arrangement is moved in step S0 to an initial working position, and the positioning system is activated. In step S1 the accessible surface portion of the object is scanned, i.e. the imaging assembly captures image data of the surface that is visible to the imaging assembly from within the current work envelope of the robot assembly. The positioning system is continually tracking the position of the active target, which essentially provides the position in space of the imaging assembly through careful calibration. This step S1 comprises several sub-steps, which may be summarized as follows: the imaging assembly is arranged in step S1.1 in a scan position, and the imaging assembly is directed at the surface of the object. In step S1.2, image data is acquired or captured at that scan position. In step S1.3, the next scan position for the imaging assembly is computed on the basis of the position data being continually provided by the positioning system. In step S1.4, the imaging assembly is moved to that next scan position. These steps S1.1 to S1.4 are repeated as often as necessary to scan the surface portion that is accessible from within the current work envelope of the robot assembly. Here, the decision whether or not steps S1.1 to S1.4 should be repeated is made in step SD1.

In step S2, the next working position for the robot assembly is computed on the basis of the position data being provided by the positioning system. In step S3, the robot assembly is moved to that next working position. These steps S1 to S3 are repeated as often as necessary in order to scan the entire surface of the object. The decision whether or not steps S1 to S3 should be repeated is made in step SD2. When the complete object has been imaged, the method terminates.

The aim of the imaging procedure is to completely map the surface of the object. Depending on the imaging assembly used, the result of the imaging procedure may be a virtual 3D image of the object. This can be achieved by stitching the image data to obtain an image of the complete object. Image stitching can be done at any appropriate stage, for example following step S1.4, preceding step S2, etc.

By using an imaging assembly with a suitably high resolution and precision, surface defects as small as a few micrometres may be visible in the final computed shape, and any departure from the intended geometry of the object may be detected to an accuracy of a few micrometres. Since the visual inspection arrangement can result in a 3D image of the entire object, macro-defects can also be accurately detected. This is illustrated in Fig 6, which shows a computation unit 15 that computes images on the basis of the image data 11_D captured by the imaging assembly and position data 13_D provided by the tracker, and stitches the images to generate a geometrical model M_{real} of the entire object. To assess the quality of the manufacturing process, the computed shape M_{real} of the manufactured object is compared to the intended shape M_{plan} of the object. Deviations from the intended shape M_{plan} are detected in an analysis unit 16. The analysis unit 16 can also examine the computed shape M_{real} of the manufactured object to detect any surface defects, as explained above. Information regarding the locations and dimensions of defects or manufacturing faults may be provided in the form of a suitable output 160.

Fig 7 illustrates a drive arrangement 12 for an embodiment of the inventive visual inspection arrangement 1. Here, a control signal computation unit 120 receives position data P_{next} specifying the next position of the image scanner 11. For example, after completely scanning the accessible surface from one working position, the control unit may want to move the image scanner 10 cm to the left and 20 cm downwards. Depending on the current position and orientation of the end

effector and the current position of the mobile base frame, which may be assumed to be known to the drive arrangement 12, the control signal generator 120 can then generate suitable control signals for any actuators 100A of the robot arm and/or for any actuators 101A of the end effector and/or for any actuators 102A of the mobile base frame and/or for any actuators 103A of the vertical support. A suitable combination of such control signals can displace the end effector in the desired manner as made possible by its six degrees of freedom.

Fig 8 illustrates the operating principle of the preferred positioning system 13. The diagram shows a laser tracker 130 and an active target 131. The robot assembly is not shown, but may be assumed to be present, with its end effector arranged to hold an imaging assembly 11. Here, the imaging assembly 11 comprises two cameras 110 and a projector 111, and these are mounted to a holding frame 104 which may be assumed to be secured to the end effector of the robot arm, so that the imaging assembly 11 and the active target 131 can be moved as one entity. From a calibration step, the position of the imaging assembly 11 is known relative to the active target 131. The laser tracker 130 aims a laser beam B in the direction of the active target 131. The laser source is moveable within a relatively large range, and the active target 131 is also movable in six degrees of freedom as explained above. Here, the laser tracker 130 is mounted on a suitably stable support that can be placed near the rotor blade tip end in such a way that it can "see" the active target 131 at all times. The laser tracker 130 emits a laser beam B in the direction of the active target 131 and receives the reflected laser beam, from which it can compute the XYZ position of the active target 131. The laser tracker 130 sends XYZ position information 13_XYZ to the control unit (not shown). The active target 131 is equipped with a sensor assembly so that it can determine its RxRyRz orientation, and sends the RxRyRz position information 13_RxRyRz to the control unit (the skilled person will be familiar with the

types of sensor assemblies that can be used for this purpose). On the basis of this data, the control unit can track the movements of the imaging assembly 11 and can compute a next position for the imaging assembly 11, and can generate control signals for any actuators in order to move the imaging assembly 11 to the next position. Although the present invention has been disclosed in the form of preferred embodiments and variations thereon, it will be understood that numerous additional modifications and variations could be made thereto without departing from the scope of the invention. For example, a robot with at least three degrees of freedom could be used instead of one with six degrees of freedom. The remaining degrees of freedom would then be covered by the moveable base frame, but with greater requirements on the precision of its movement as a consequence. In a laser-based positioning system, multiple active targets might be implemented if the geometry of the inspected object is too complex to keep the aperture of a single active target aligned with the laser tracker throughout the inspection process.

In addition to visually inspecting an object, it would be possible to perform non-destructive testing by arranging a suitable probe on the end effector of the robot assembly. For example, an ultrasound probe could be included as part of the imaging assembly in order to detect sub-surface faults such as delaminations.

For the sake of clarity, it is to be understood that the use of "a" or "an" throughout this application does not exclude a plurality, and "comprising" does not exclude other steps or elements.

Claims

1. A visual inspection arrangement (1) comprising
- a robot assembly (10) realised to move in an unconstrained manner relative to an object (2) being subject to visual inspection, which robot assembly (10) comprises a robot arm (100) with an end effector (101) realised to direct an imaging assembly (11) at the object (2);
- a drive arrangement (12) realised to effect a displacement of the robot assembly (10);
- a positioning system (13) configured to track the position (13_XYZ, 13_RxRyRz) of the imaging assembly (11) relative to the object (2); and
- a control unit (14) configured to control the drive arrangement (12) on the basis of the tracked position of the imaging assembly (11).

2. A visual inspection arrangement according to claim 1, wherein the robot assembly (10) comprises a mobile base frame (102) realised to support the robot arm (10) and to move in an unconstrained manner relative to the object (2) undergoing visual inspection.

3. A visual inspection arrangement according to claim 1 or claim 2, wherein the positioning system (13) is a laser-based positioning system.

4. A visual inspection arrangement according to claim 3, wherein the positioning system (13) comprises a stationary laser tracker (130) arranged in the vicinity of the object (2), and an active retro-reflective target (131) carried by the end effector (101).

5. A visual inspection arrangement according to claim 4, wherein the laser tracker (130) is configured to generate position data (13_XYZ) describing the XYZ position of the imaging assembly (11) in a local reference frame, and the active target (131) is configured to generate position data

(13_RxRyRz) describing the RxRyRz position of the imaging assembly (11) in the local reference frame.

6. A visual inspection arrangement according to any of the preceding claims, realised such that the end-effector (101) of the robot arm (100) has six degrees of freedom and wherein the positioning system (13) is realised to track the motion of the imaging assembly (11) accordingly.

7. A visual inspection arrangement according to any of the preceding claims, wherein the mobile base frame (102) is equipped with two wheel pairs (12W1, 12W2), and wherein the drive arrangement (12) comprises a motor arranged to drive a wheel pair (12W1).

8. A visual inspection arrangement according to any of the preceding claims, comprising a vertical support (103) mounted on the mobile base frame (102), and wherein the robot arm (100) is secured to a platform (103P) carried by the vertical support (103).

9. A visual inspection arrangement according to any of the preceding claims, wherein the drive arrangement (12) comprises a vertical displacement means (1030) realised to effect a vertical displacement of the platform (103P).

10. A visual inspection arrangement according to any of the preceding claims, wherein the mobile base frame (102) comprises an aperture (102A) dimensioned to allow the robot arm (10) to extend to floor level.

11. A visual inspection arrangement according to any of the preceding claims, wherein the imaging assembly (11) comprises an area-sampling 3D scanner realised as any of: a moving laser scanner, a time-of-flight scanner, a structured light scanner.

12. A method of performing a visual inspection of an object (2) using a visual inspection arrangement (1) according to any of claims 1 to 11, comprising the steps of

S0) moving the robot assembly (10) to an initial working position and activating the positioning system (13);

S1) scanning the surface portion (S) of the object (2) accessible from within the work envelope of the robot assembly (10) at its working position;

S2) computing the next working position for the robot assembly (10) on the basis of position data (13D) provided by the positioning system (13);

S3) effecting a displacement of the robot assembly (10) to that next working position; and

repeating steps S1 to S3 to scan the area of interest of the object (2).

13. A method according to claim 12, wherein step S1 comprises the steps of

S1.1) positioning the imaging assembly (11) in a scan position and directing the imaging assembly (11) at the surface of the object (2);

S1.2) acquiring image data (11_D) for that scan position;

S1.3) computing the next scan position for the imaging assembly (11) on the basis of position data (13_D) provided by the positioning system (13);

S1.4) effecting a displacement of the imaging assembly (11) to that next scan position; and

repeating steps S1.1 to S1.4 to scan the surface portion (S) of the object (2) accessible from within the work envelope of the robot assembly (10) at that working position.

14. A method according to claim 12 or claim 13, wherein image data (11_D) acquired in the scan positions are combined in an image stitching step to obtain an image model (M_{real}) of the entire object (2).

15. A computer program product comprising a computer program that is directly loadable into a memory of the control unit of a visual inspection arrangement (1) and which comprises program elements for performing steps of the method according to any of claims 11 to 14 when the computer program is

executed by the control unit (14) of the visual inspection arrangement (1).

Abstract

Visual inspection arrangement

The invention describes a visual inspection arrangement (1) comprising a robot assembly (10) realised to move in an unconstrained manner relative to an object (2) being subject to visual inspection, which robot assembly (10) comprises a robot arm (100) with an end effector (101) realised to direct an imaging assembly (11) at the object (2); a drive arrangement (12) realised to effect a displacement of the robot assembly (10); a positioning system (13) configured to track the position (13_XYZ, 13_RxRyRz) of the imaging assembly (11) relative to the object (2); and a control unit (14) configured to control the drive arrangement (12) on the basis of the tracked position of the imaging assembly (11). The invention further describes a method of performing a visual inspection of an object (2).

Figure 1

FIG 1

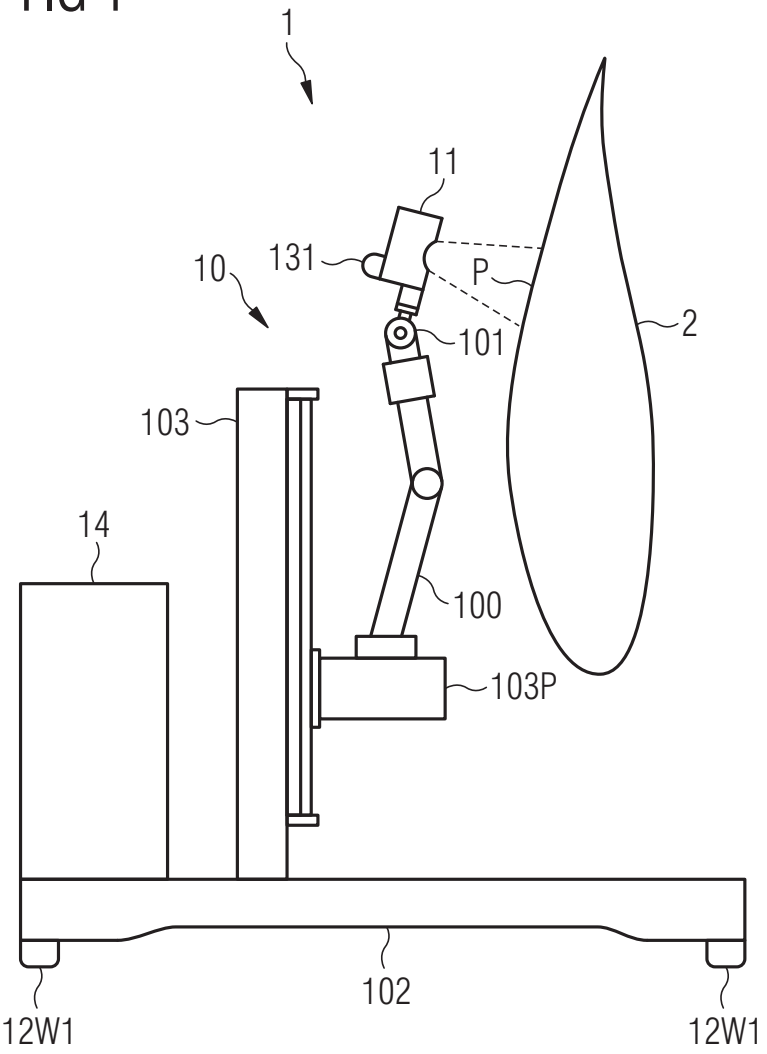

FIG 2

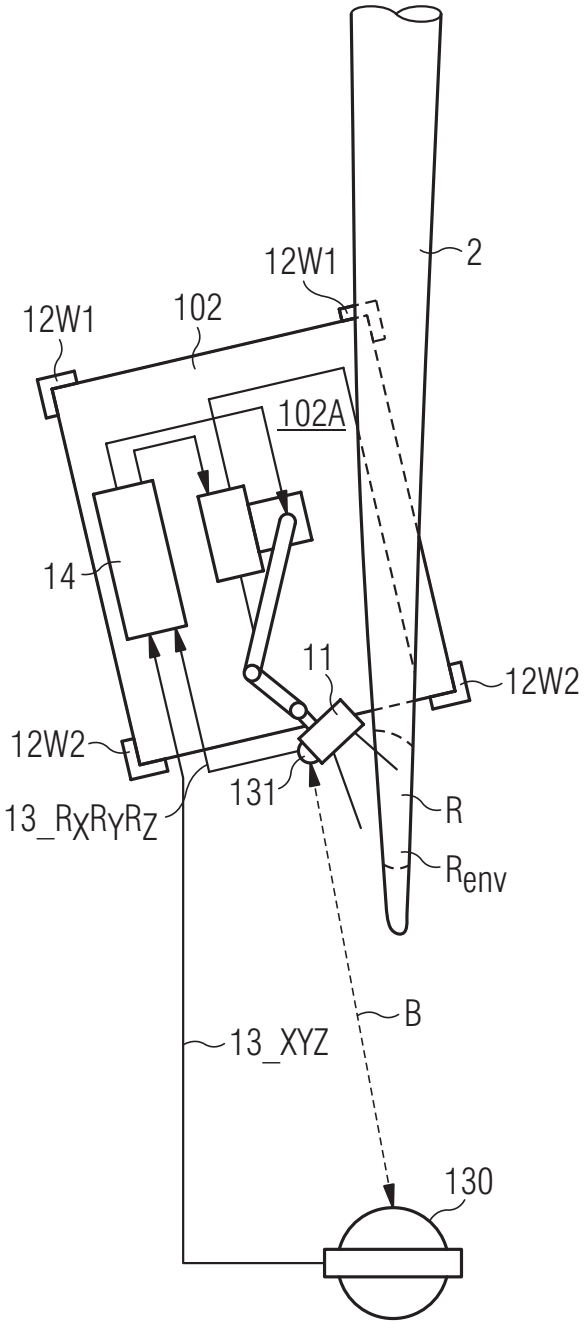
12W1
2
12W1
102
102A
14
11
12W2
12W2
131
13_RXRYRZ
R
Renv
B
13_XYZ
130

FIG 3

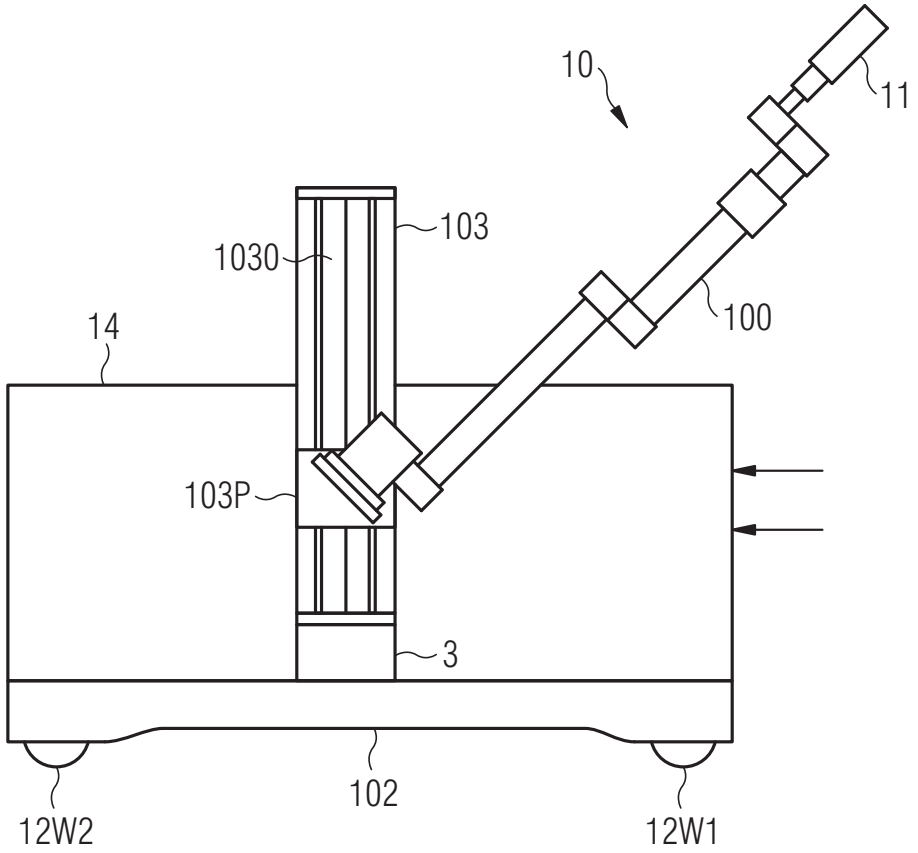

FIG 4

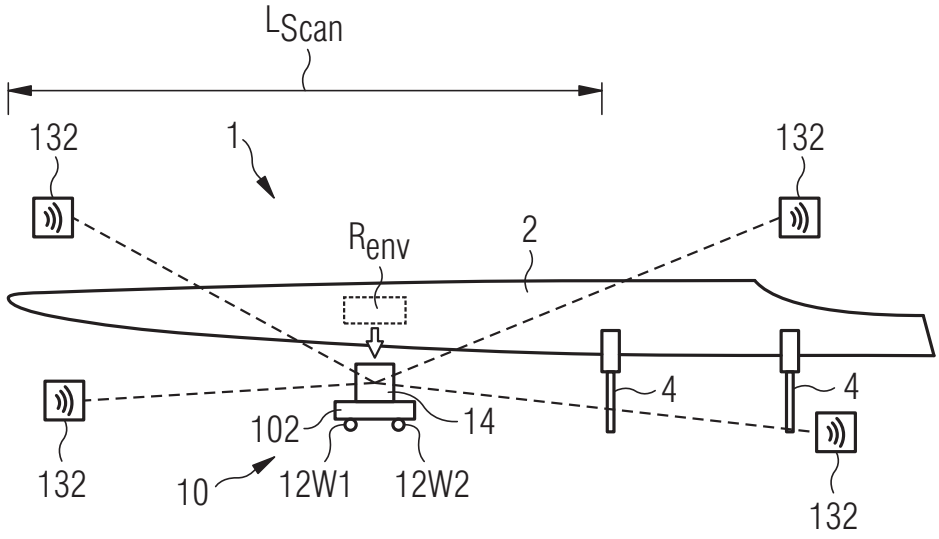

FIG 5

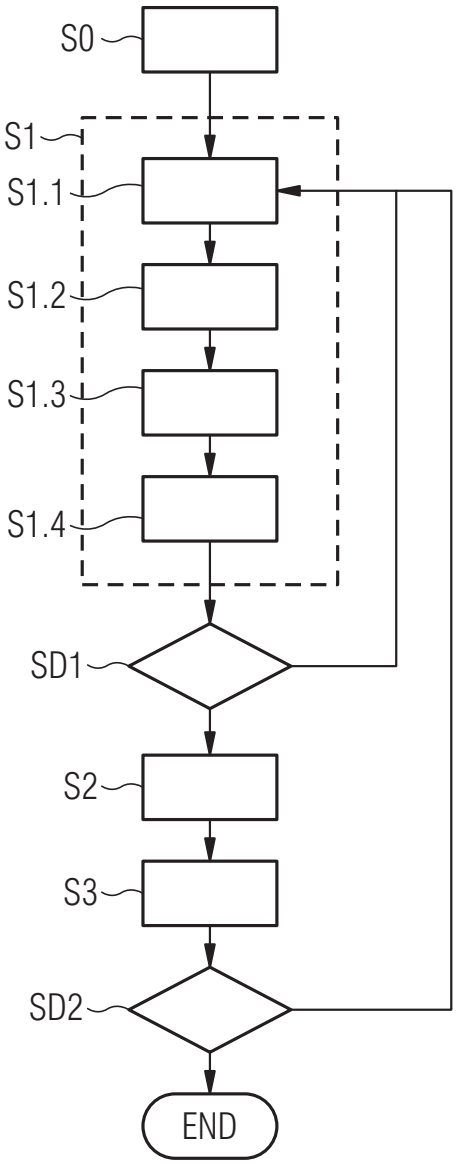

FIG 6

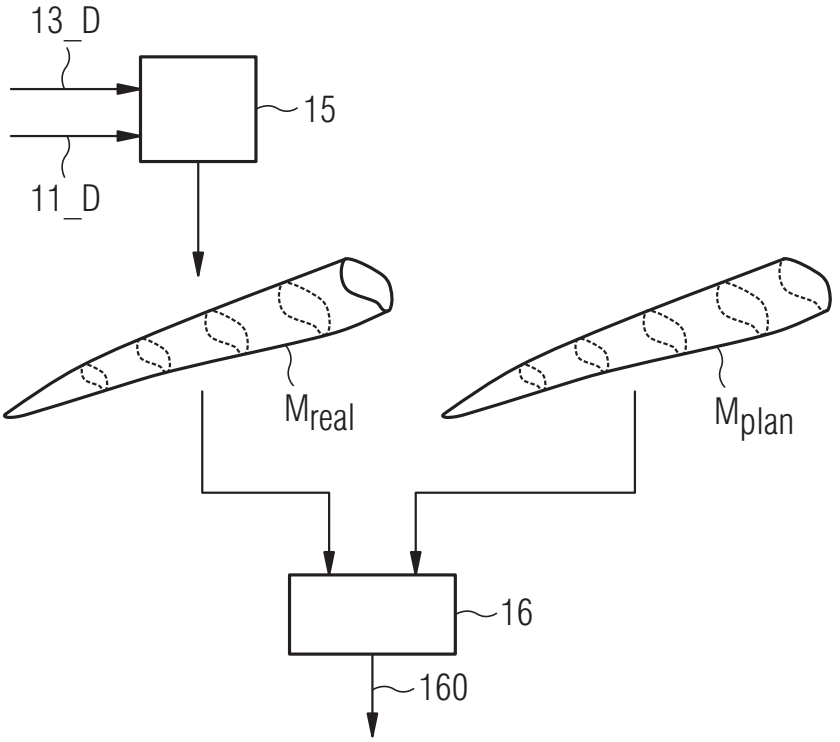

FIG 7

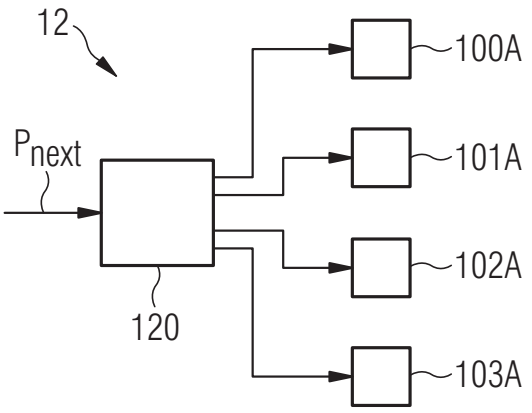

FIG 8

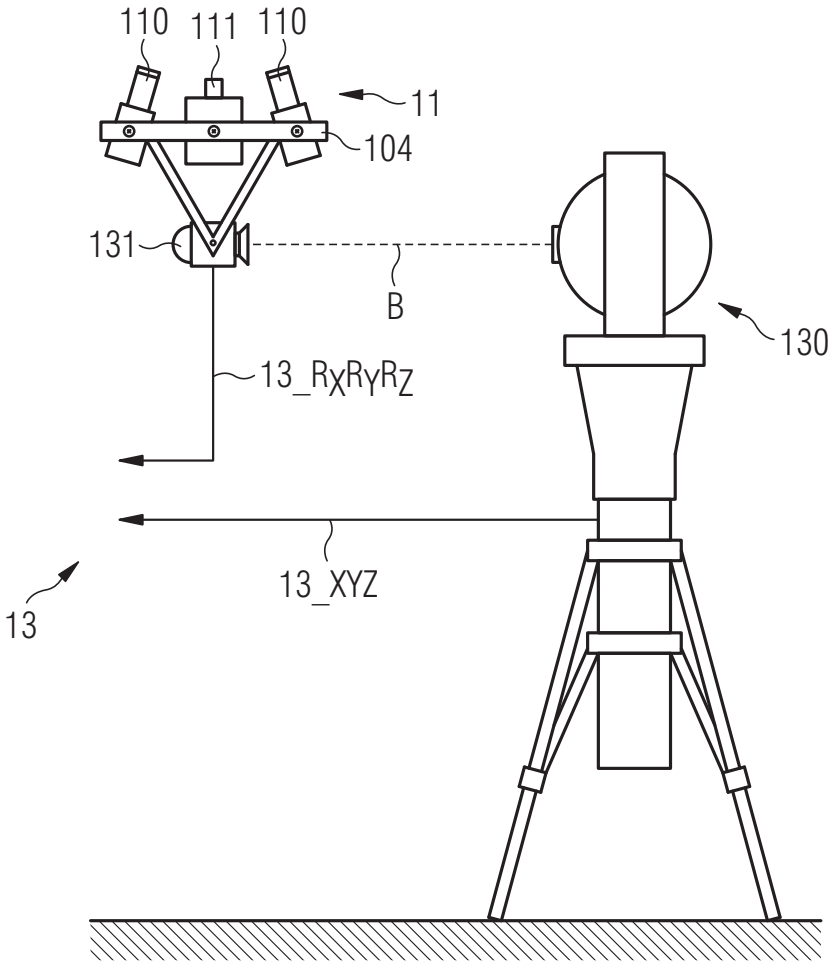

CONTRIBUTION H

Snags on Surfaces: Detecting Geometrical Defects on Wind Turbine Blades

Technical Report DTU Compute Technical Report 2018-07
Published in DTU Orbit

This technical report presents two methods for how defects might be found from 3D point clouds, which originates from the blade measurement system. The methods are merely proof-of-concepts, and as such, the report only showcase the feasibility of using 3D scans for detecting defects. Further work would be needed to scale these methods into algorithms which could actually be implemented in a blade production pipeline.

Snags on Surfaces: Detecting Geometrical Defects on Wind Turbine Blades

Rasmus Ahrenkiel Lyngby, Anders Bjorholm Dahl
Department of Applied Mathematics and Computer Science, Technical University of Denmark
Richard Petersens Plads, Building 321, 2800 Kgs. Lyngby, Denmark
raly@dtu.dk

Abstract

This technical report presents two approaches for detection defects on the outer geometry of wind turbine blades, from measured 3D point clouds. Focus is on the technical aspect of the methods, Results are presented together with ideas for future work, but a general account fo previous work is not given.

1. Introduction

We introduced an autonomous scanner system, for inspecting the outer geometry of wind turbine blades, in [1]. This technical report presents two proof-of-concepts for detecting geometrical surface defects, from the point clouds acquired with the scanner. One for estimating the size of the transition between the base paint and the leading edge protective paint, and one for comparing the measured point clouds against the blade's digital geometry model. Other kinds of defect detection could be imagined, why this report should not be seen as a full coverage of the possibilities, but merely an initial demonstration of what the acquired data could be used for. This report focus on the data's technical possibilities without positioning the presented methods in relation to prior art. Note, however, that the general approaches are not as such novel. The novelty lies in the the application.

The report starts by describing the two methods and the obtained results, and then reflects over future work which would have to be done to use the methods for quality assurance in an actual manufacturing pipeline.

2. Paint Transitions

A workpiece, which simulates the leading edge, including the transition between base paint and LEP, is 3D scanned with the SeeMaLab scanner [2]. Fig. 1 shows a photograph of the workpiece. By using a emulating workpiece, and not the real blade, we can directly document the results without worrying about revealing proprietary information.

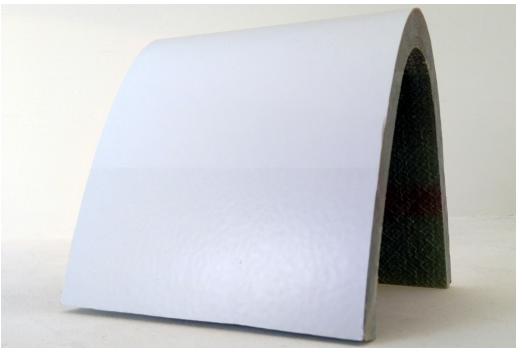

Figure 1: Photograph of the workpiece.

Figure 2: Rendering of the point cloud cut-out of the workpiece. The transition between the base paint and leading edge protection is slightly visible close to the center of the image.

Further, we can also have the piece manufactured such that there is a good amount of variance in the the LEP transition. With the workpiece's small size, it would also be relatively easy to compare the results reported here against those obtained via other techniques. Such a comparison is not presented here. The laboratory grade SeeMaLab scanner was used because this study was done as a proof-of-concept, before the actual blade scanner had been constructed.

Using MeshLab[1] [3], the leading edge on one side of workpiece is cut out. Fig. 2 shows the resulting cut-out point cloud. The cut-out is aligned to its principal components, using the SVD, and the surface normal is estimated for each vertex from their 10 nearest neighbor vertices,

[1] Version 1.3.3.

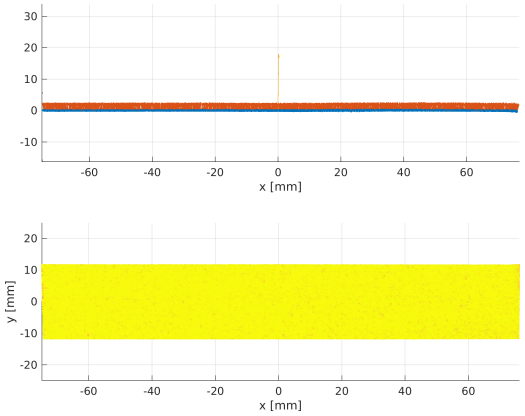

Figure 3: The cut out point cloud aligned to its two principal axes, and the mean surface normal vector. The top plot displays the point cloud from the side (colored blue). Some of the normal vectors are shown in orange, and the mean normal is shown as a long vector in the center. The bottom plot shows the point cloud with colors indicating the angle between the normals of the points and the mean normal. Yellow corresponds to a small angle and orange corresponds to a large angle.

again using the SVD. The resulting normal vectors, along with the mean normal direction, is shown in Fig. 3.

Seeing the cut-out from the side, as shown at the top in Fig. 4, there is a variance in the height, partly due to actual surface height differences, and partly due to noise. The bottom plot in Fig. 4 shows the cut-out, seen from above, overlaid with a 2D grid. All vertices, which fall into a given cell in the grid, are pooled together by computing their mean distance to the best-fit plane. This sub-sampling approach transforms the point cloud into a height map, and mean-filter the heights. A cell size of 0.5 mm by 0.5 mm is used. The SeeMaLab scanner has a higher spatial resolution than the blade scanner, but the sub-sampling brings the resolution of the height map below that of the blade scanner. Figure 5 shows the resulting height map. The map display some discontinuities, why it is further filtered by a 5 by 5 Gaussian kernel with a variance of 1.

First, the depth map is numerically differentiated in order to detect the exact position of the LEP slope. This is done for each column of cells in the height map. When seen in isolation, each of these columns corresponds to a discrete 2D signal. The signals are numerically differentiated through convolution with a Sobel kernel. The position of the slope formed by the LEP transition can then be found as the maximum of the differentiation. The resulting positions are showed on Fig.6.

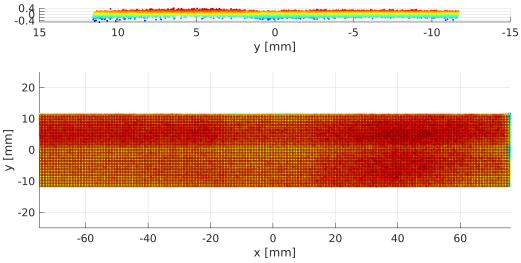

Figure 4: The top plot shows the point cloud, as seen edge one from the side. It is not a completely flat plane due to noise. The transition can be glimpsed to the left of 0 on the x-axis. The bottom plot shows a small region overlayed with the sampling grid. The color coding reflects the points distances to the best fit plane.

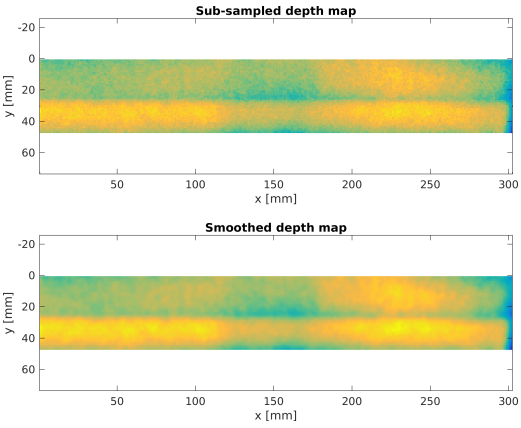

Figure 5: The resulting height map from the grid sampling, before and after Gaussian filtering.

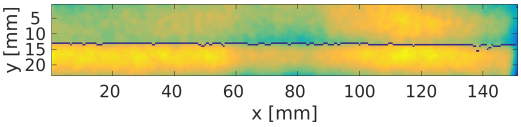

Figure 6: The detected leading edge protection transition marked with dark blue.

For each of the columns in the height map, the position where the slope flattens, i.e. its derivative approaches 0, is found before and after the transition, and labeled $p^{(n)}_{\text{begin}}$ and $p^{(n)}_{\text{end}}$, respectively, for column number n. Then, a second order polynomial is fitted to all the samples located behind the beginning of the slope, $p^{(n)}_{\text{begin}}$, and likewise a second or-

der polynomial is fitted to all the samples located ahead of the slope's end, $p_{\text{end}}^{(n)}$. This is done to cope with the general non-linear shape of the surface.

The tangents of the two polynomials are calculated right at $p_{\text{begin}}^{(n)}$ and $p_{\text{end}}^{(n)}$, respectively. The surface normal is estimated for the lower polynomial at $p_{\text{begin}}^{(n)}$, by rotating the tangent 90°. The intersection of this normal and the tangent of the upper polynomial is computed. The height is then calculated as the linear distance from the slope's beginning point, $p_{\text{begin}}^{(n)}$, to the intersection, and the width is calculated as the distance between the intersection point and the slope's ending point, $p_{\text{end}}^{(n)}$. An example of a fitting is shown on Fig. 7.

2.1. Results and Discussion

The slope height and width are calculated at all positions along the LEP transition, and the results are showed in Fig. 8. Fig. 9 shows the ratio between the slope's width and its height. Usually, geometric tolerances on the LEP transition is defined by this ratio.

Based on the previously shown height map, Fig. 5, and the physical feel of the workpiece, the slope heights shown to the left in Fig. 8 seem reasonable. There was no LEP applied at the very right edge of the workpiece, and this is well reflected by the measurements. It is strongly believed, that a ratio plot, similar to the one in Fig. 9, could be generated from the point clouds obtained via the blade scanner, and thus used directly as a quality assurance tool. The tolerance zone can be easily plotted as a horizontal line across the plot, which would make it easy to spot positions which was outside the tolerance zone.

3. Profile Shape

The tolerance specification is defined based on the CAD model, as a surface profile which is not related to a datum [4]. The tolerance zone defines a maximum permissible deviation between the digital model and the physical surface, and generally varies over the surface. This report is not concerned with the specific size of the tolerance zone, but provides a simple proof of concept for estimating the deviation between the blade model and 3D measurements of the physical blade. In an actual application of detecting deviations from the digital model, the physical blade's elastic deformations, influenced by gravity, would have to be taken into account. This is described in more detail under "Future work" in Sec. 4.

The smooth blade model is shown in Fig. 10. From studying the model in FreeCAD[2], it seems that the surface contains some small geometric defects, as seen in Fig. 10b and Fig. 10c. The defects might be an artifact of the rendering process, such as the tessellation needed for drawing the surface with graphics hardware, but this is unclear. With smooth surface representations, what you see is not necessarily what you get.

Fig. 11 shows a rendering of the triangle mesh which results from a tessellation of the smooth surface. This representation is needed for measuring deviations using CloudCompare[3]. The mesh is made with the standard procedure of FreeCAD's mesh-workbench, in a way which ensures a maximum deviation of 50 μm from the smooth surface. Some degenerate triangles and tessellation artifacts are visible. From manual inspection and comparison between the smooth model and the mesh, rendered in FreeCAD and MeshLab respectively, it was not directly possible to retrieve the aforementioned abnormalities. This does, however, not fully guarantee that some artifacts are carried over, and this possibility should be kept in mind when judging the comparison between measurements and the model mesh.

For the proof of concept documented here, one set of measured point clouds resulting from two acquisition curves, one forward and one backward, is used. They approximately cover 0.5 meters of the blade's length, and are acquired roughly 10 meters from the tip. The influence from elastic deformations are expected to be insignificant over such a small length, at this position. The point clouds are transformed into the common coordinate frame defined by the laser tracker, and manually aligned to the mesh model. Then, CloudCompare's iterative closest point (ICP) implementation is used to fine tune the registration [5]. A close-up of the fit, seen from below, is shown in Fig. 12.

The deviations between the point clouds vertices and the mesh are computed with CloudCompare's Cloud-to-Mesh Distance tool. This operation color-codes the point clouds relative to their deviation from the mesh. For a given point, the distance is computed as the smallest possible distance between that point and the triangles in the mesh.

3.1. Results and Discussion

The color coded point clouds resulting from the deviation computation is shown in Fig. 13, Fig. 14 and Fig. 15. The colored bands, which extends all the way from the left side to the right side, is most likely due to uncertainties in the registration. It could be, that a better fit could have been obtained further down the blade, but the standard ICP algorithm only considers nearest neighbors between the point clouds and the mesh, why it easily gets stuck in a local minimum. This is especially likely due to the homogeneity of the geometry, when seen locally. Therefore, instead of looking at the absolute deviations, we are interested in vertical changes in the deviation.

[2] Version 0.17.13509.

[3] Version 2.10.alpha.

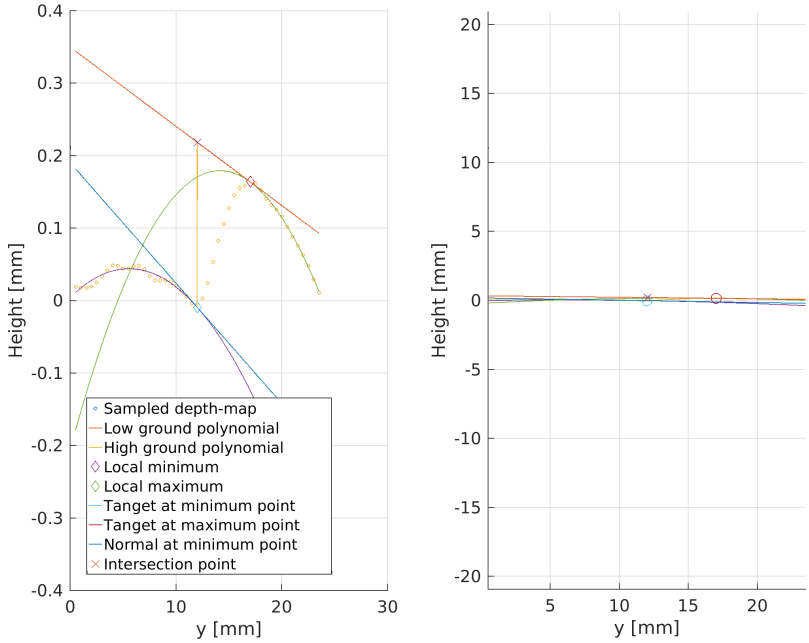

Figure 7: Plot of polynomials fitted to the surface before the transition, and to the surface after the transition, for column number 101 of the height map in Fig. 6, corresponding to a position 50.5 mm from the edge of the workpiece. The left side shows a skewed version, where the units on the axis does not have the same scale. The right side shows the same plot, but with the same units on the axis. Note that right angles does not look right in the left plot, due to the different axis units, but that it is impossible to see anything in the right plot. The slope height is measured along the normal, and here it is calculated to 0.22 mm. The width is measured along the upper tangent, and here it is calculated to 5 mm.

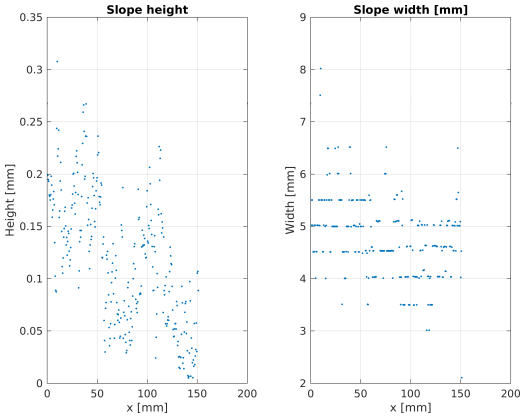

Figure 8: Plots of the measured slope height and width.

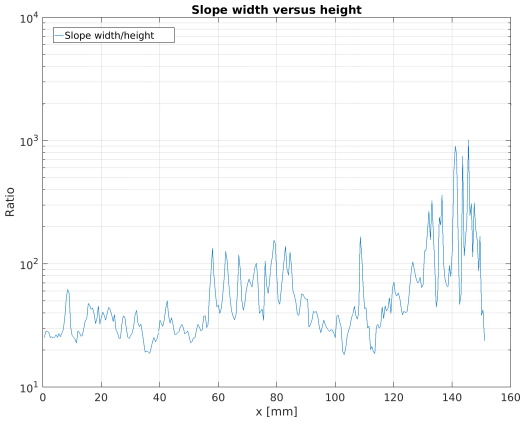

Figure 9: Plots of the measured slope height versus the measured slopw width, over the length of the cut-out.

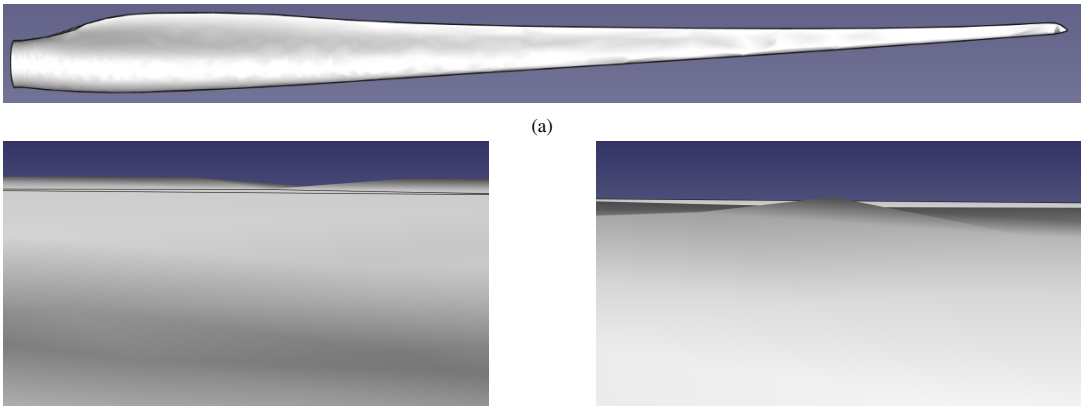

(a)

(b) (c)

Figure 10: Rendering of the blade CAD model. The rendered non-uniform rational b-spline surface is shown in (a). When looking closely at the surface, it seems like it is somewhat degenerate, as illustrated in (b) and (c). Rendered with FreeCAD.

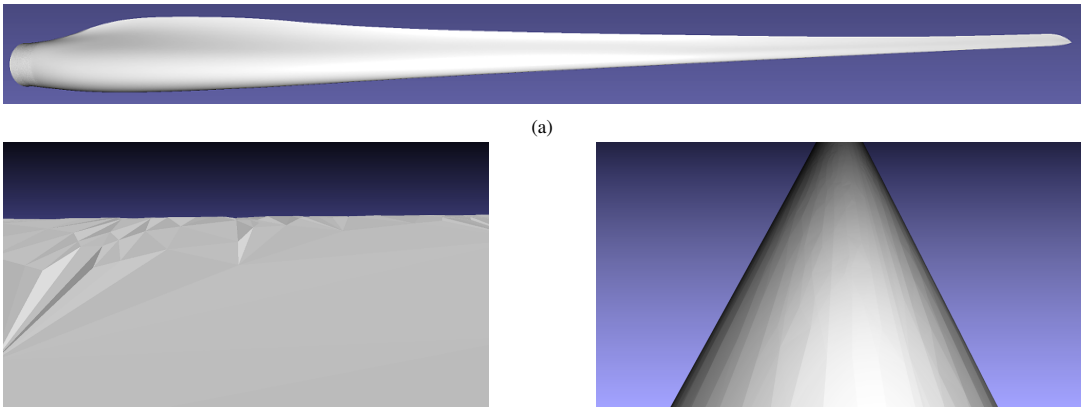

(a)

(b) (c)

Figure 11: Rendering of the mesh tesselated from the smooth surface representation shown in Fig. 10a. The maximum deviation from the original surface, at any point on the mesh, is 50 μm. In addition to the artefacts present in the original smooth representation, the resulting mesh also contains discrete artefact stemming from the tesselation procedure, as seen in (a) and (a). Rendered with MeshLab.

Vertical changes are seen close to the center in Fig. 13. There is a region which is slightly bluer than the surrounding green region. This indicates that the region is placed lower than it surroundings, and thus is a depression, or valley, in the surface. The depression is also slightly visible near the center at the top-most edge in Fig. 14.

A discrete transition can be seen near the top center of Fig. 15. This comes from the overlap between the point clouds coming from each of the two acquisition curves. It indicates, that some form of post-acquisition fine-registration of the point clouds should be performed. A method such as the one presented by Rusu, Blodow, and Beetz [6] could be used. Other than that, an elongated protuberance is visible at the bottom left, which has a slightly more orange hue than the surrounding yellow region. It is also visible at the bottom right of Fig. 14.

Figure 12: Best fit position of the point clouds, seen from below, against the black silhouette of the blade mesh. Rendered with CloudCompare.

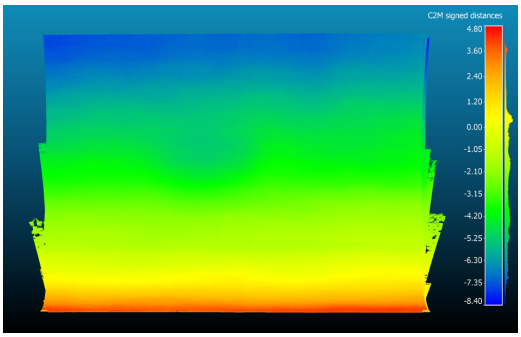

Figure 13: Point clouds with vertices colored relative to their deviations from the model mesh, seen from the left hand side. All values are in mm. The width is 480 mm. Rendered with CloudCompare.

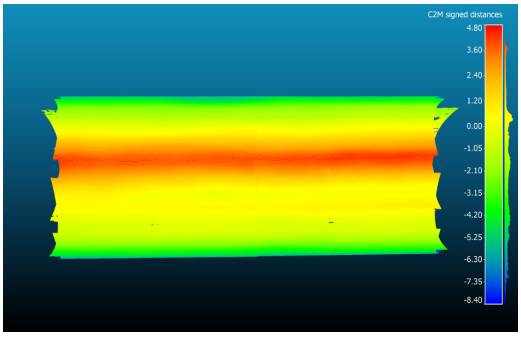

Figure 14: Same as Fig. 13, but seen from below.

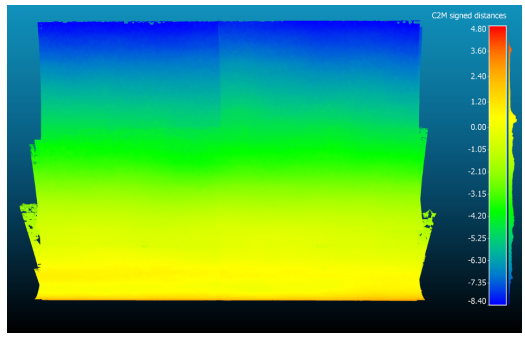

Figure 15: Same as Fig. 13, but seen from the right hand side.

4. Future Work

The LEP transition was detected in Sec. 2, but not validation of the results were presented. This requires measurements from another, calibrated, measurement system. Further, it should be verified that the transition can also be measured from the point clouds acquired with the blade scanner. Finally, a method for automatic segmentation of the region, which contains the LEP transition, should be developed. The most simple procedure would be to specify a mapping between longitudinal position, relative to the blades length, and nominal arc length distances of where the transition is located.

The blade's elastic deformation should be considered when aligning the full data-set, which is about 20 m long, to the blade mesh, as done in Sec. 3. It was also seen, that the registration influences the measured deviations. A registration approach which considers both local and global

shape would possibly provide better alignment. One approach could be to slice the point cloud into thin slices with a thickness determined by the required deviation resolution, i.e. 1 mm. The slices could then be registered to the blade model through an approach which, in addition to the translational difference, allowed some rotational deviation between consecutive slices. Distanced could be measured by projecting points directly onto the smooth blade model, instead of the tessellated mesh, which would remove a potential error source. Defect detection could be automated either by specifying a tolerance zone of maximum permissible deviation, or by numerically differentiate the deviation map and setting a tolerance on the maximum permissible shape change. It was seen, that uncertainties in the poses, returned by the laser system, results in slight deviations between overlapping point clouds. Post-acquisition fine alignment should be performed, which optimizes the fit between all overlapping point clouds simultaneously. This approach could utilize 3D geometry features, possibly combined with the blade model.

5. Conclusion

This technical report presented a proof-of-concept of geometrical defect detection in 3D point clouds, acquired by scanning the surface of wind turbine blades. It documented results from two defect detection methods. The first method did not require a blade model, and measured the slope from the base paint layer up to the leading edge protection. The second method was model based, and measured geometric deviations between the point clouds and a best fit blade model. It was found, that both methods are feasible, but that further developments are needed before they can be implemented in actual quality assurance.

References

[1] R. A. Lyngby, H. Aanæs, E. Nielsen, and A. B. Dahl, "Autonomous surface inspection of wind turbine blades for quality assurance in production," in *9th European workshop on structural health monitoring*, 2018.

[2] E. R. Eiríksson, J. Wilm, D. B. Pedersen, and H. Aanæs, "Precision and accuracy parameters in structured light 3-d scanning," *The International Archives of Photogrammetry, Remote Sensing and Spatial Information Sciences*, vol. 40, p. 7, 2016.

[3] P. Cignoni, M. Callieri, M. Corsini, M. Dellepiane, F. Ganovelli, and G. Ranzuglia, "Meshlab: An open-source mesh processing tool.," in *Eurographics Italian chapter conference*, vol. 2008, 2008, pp. 129–136.

[4] ISO 1101:2017, "Geometrical product specifications (GPS) – Geometrical tolerancing – Tolerances of form, orientation, location and run-out," International Organization for Standardization, Geneva, Switzerland, Standard, 2017.

[5] P. J. Besl and N. D. McKay, "Method for registration of 3-d shapes," in *Sensor Fusion IV: Control Paradigms and Data Structures*, International Society for Optics and Photonics, vol. 1611, 1992, pp. 586–607.

[6] R. B. Rusu, N. Blodow, and M. Beetz, "Fast point feature histograms (fpfh) for 3d registration," in *Robotics and Automation, 2009. ICRA'09. IEEE International Conference on*, Citeseer, 2009, pp. 3212–3217.

CONTRIBUTION I

Autonomous Surface Inspection of Wind Turbine Blades for Quality Assurance in Production

---

Conference	9th European Workshop on Structural Health Monitoring
Organizer	BINDT
Venue	Hilton Manchester Deansgate, Manchester, UK
Submission date	May 02, 2018
Presentation Date	July 11, 2018
DOI	N/A

This contribution presents the developed blade scanner system with a focus on manufacturer requirements. The paper serves as an initial publication of the scanner system. The measuring performance is assessed through VDI/VDE guideline 2634, and thus focus on the RapidScan's ability to measure spheres and planes. Being first author, my primary contribution to this paper was development of the scanner system, conducting the experiments, writing the text, and presenting the work during the conference.

9th European Workshop on Structural Health Monitoring
July 10-13, 2018, Manchester, United Kingdom

Autonomous surface inspection of wind turbine blades for quality assurance in production

Rasmus A Lyngby[1], Henrik Aanæs[1], Ewa Nielsen[2] and Anders B Dahl[1]
1 DTU Compute, Technical University of Denmark, Denmark, raly@dtu.dk
2 Siemens Gamesa Renewable Energy, Denmark, ewa.nielsen@siemens.com

Abstract

This paper defines a method, and associated automated system, for production inline inspection of the surface geometry of wind turbine blades which can be plugged directly into existing production facilities without changing the setup. During current production, turbine blades are manually inspected, and this system aims at automating this process. Various geometrical defects can occur in the surface during production and these defects can lead to shortened life times and lowered power output of the turbine. Automating the inspection process requires a method which is at least as sensitive as the currently used manual process while significantly lowering the time consumption. It is shown that the proposed method is fast and has the potential to deliver the high precision and resolution needed to resolve both small and large scale surface defects.

1. Introduction

Wind turbine blades are usually made by infusion moulding where multiple layers of fiberglass or carbon fibre are infused with epoxy resin to create a strong, flexible mesh. This method has numerous advantages (1), but is vulnerable to several failure modes, such as wear on the moulds, erroneous packing of the fiberglass, sliding of the fiberglass, post-moulding treatments such as sanding, plastering and painting etc. Each of these failure modes can impact a blade's final surface geometry, transforming it away from the intended, optimized design with reduced lifetime and power generation as a result. Surface quality inspection is used to ensure that blade specifications are complied with and to identify the causes for defects and to eliminate these causes.

Generally, defects occur on two spatial scales. The first are submillimetre which originates from the various surface treatments that the blade undergoes. Examples are pinholes, cracks, steps etc., all of which can hinder laminar air flow and create damaging surface erosion. The second scale is decametric with defects being introduced during the moulding process and seen as deviations in the surface trajectory relative to its design, causing suboptimal lift. Both types of defects are most devastating if positioned on the blades leading edge, why this part of the surface is in focus. In current production, these defects are detected through manual inspection.

This paper investigates a method for in-line, autonomous surface quality inspection of wind turbine blades. The method has the potential to significantly reduce inspection cost and time, while even further enhancing the already good accuracy and precision of currently used, manually based surface inspection processes. In addition, it can create a highly detailed virtual copy of the blade surface, which can be used in an Industry 4.0

setting (2) for simulations, documentation, planning, etc. The two main contributions of this paper are as follows:

1. Development of method to automate wind turbine blade surface digitalization and inspection.
2. Investigation of the measurement uncertainty of this method.

The inspection method materializes as a robotic system composed of a measurement system which is moved over the blade surface by a locomotion system to survey the entire leading edge. This system is illustrated in Figure 1.

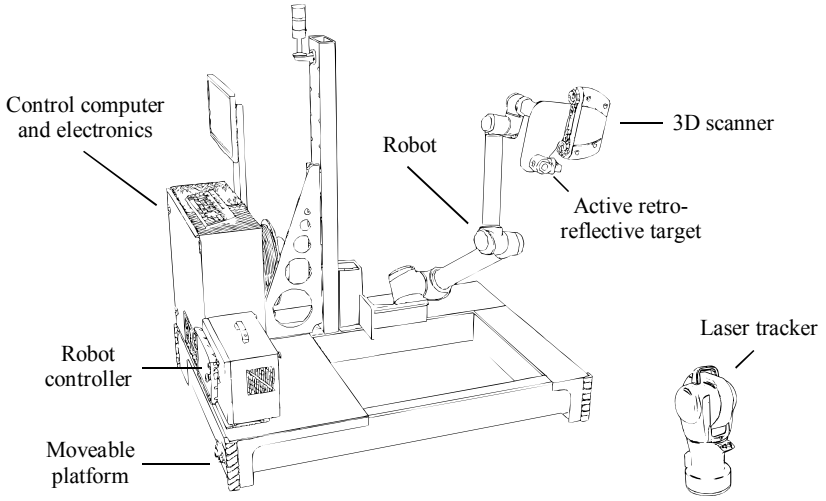

Figure 1. Sketch of the inspection system.

According to the ISO 2859 series, quality inspection is composed of two steps, namely: 1) conducting measurements and 2) decide upon conformity with specification. This paper focuses on the measuring step, although a novel idea for comparing measurements and 3D CAD model is also presented.

Schubel (3) showed that fully automating the wind turbine blade production line can significantly reduce manufacturing costs. The automated inspection method proposed here is designed to be operational within current production environments without any alterations, allowing for gradual automation. Albeit easing integration and flexibility, this restriction introduces several design challenges. An industrial wind turbine blade is a slender object with lengths currently up to 88.4 meters. When moving through the production line, a blade is placed in a two-wheeled carriage. There is no fixed transformation between the carriage and the blade coordinate frames, or between the carriage and the production floor, why an automated system has to plan its inspection path online in order to adapt to the position of the surface.

2. Previous work

Large scale geometrical metrology has been an active area of research for many years (4) with significant developments in measurement methods and applications (5,6). This section outlines the contributions which influenced the choices taken when designing the inspection method.

A general overview of current large scale metrology measurement methods was presented by (7). It was concluded that conventional tactile CMMs are generally only applicable for objects with ranges lower than 10 [m] and that target based photogrammetry is faster than tracking based laser systems and retains comparable measurement accuracy when demonstrated on a 25 [m] long train wagon.

A coherent laser radar system was used to measure the geometry of a composite ship hull by (8). It was found that coherent laser radar outperformed laser tracking and time-of-flight scanning. The 215 [m^2] surface of the ship hull was scanned with a resolution of 10 [mm] and an accuracy of 0.5 [mm] in 30.5 hours. The process required that the laser radar was moved several times, why spheres were mounted on the hull for aligning the measurements.

Several relevant contributions have been made in the wind power domain. In (9) a Microsoft Kinect mounted on an industrial robot was used to inspect a down-scaled version of a turbine hub. It was demonstrated that the CAD model can be used to plan the robot motion based on a set of Critical-To-Quality parameters and that these parameters could be measured from the 3D scan data.
A system composed of several laser trackers was used in (11) to sample blade profile curves which were then aligned to the CAD model to do in-field inspection of installed wind turbine blades.
To the extent of our knowledge, the first idea for a practical, autonomous, inline quality inspection system for surface geometry on industrial sized wind turbine blades was presented by (12). The system is composed of a linear drive stage and two 2D laser line scanners, one mounted on either side. The linear drive is placed beneath the blade which is suspended from the root end. The system was, however, only demonstrated on a small blade with a length of 2 meters, and it is thus unknown how the system would perform on a large blade.

An inspection system composed of a linear drive stage, an industrial 6 Degree-of-Freedom (DoF) robot arm, a structured light 3D scanner and a laser tracker was proposed by (13). In addition to discuss the various difficulties of registering measurements with the CAD model, the paper successfully demonstrates that such a system can provide accurate and dense measurements of blades with a length of up to 12 [m]. Blades were mounted in a special fixture and the scan path pre-programmed offline.

Coherent laser radar was used to inspect blade surface geometry in (14) and (15). The papers describe the measurement strategy, but focus on the measurement analysis and registration. Like (8), their method requires that the laser system is moved several times to cover a 60 [m] blade. The method is not demonstrated on a full blade.

3. Method for autonomous blade surface inspection

The measurement system presented here is composed of a high-resolution, structured light based 3D scanner and a local positioning system. The locomotion system is composed of a six-axis industrial robot mounted and a moveable platform, and this design is described in the following.

3.1 Requirements

Manufactures impose several soft requirements for blade surface inspection. They are denoted soft requirements as they are closer to guidelines than actual hard, numerical requirements. These are established through interviews with manufactures, form the basis for the system design, and are highlighted in Table 1.

Table 1. Requirements imposed on inspection method

Requirement	Description
Sensitivity	The sensitivity must be high enough to detect discrete defects with a spatial distribution covering only a few hundred micrometres.
Range	The measurement range must be large enough to cover defects with a spatial extend from a few hundred micrometres up to a few meters.
Speed	The number of consumed operator hours per blade must be lower when compared against current methods.
Deployment	The method must be easily deployable in the current production environment and flexible enough to be conducted at various sites around the factory.
Cost	Procurement and running costs must be low enough to yield a positive business model.
Safety	The health of operators and co-workers must not be put at risk by the method.

3.2 The measurement system

Several technologies for measuring the blade surface are available. Inspired by (13), a Structured Light (SL) based 3D scanner was selected, which projects a 2D pattern onto the surface which is then distorted by the surface's curvature. This distortion is sampled by one or more camera(s). The 3D structure of the surface can be reconstructed digitally as a point cloud from the image(s). This method excels by its high resolution, relative low uncertainty and high data rates, but is limited by the optical properties of the surface and the field of view and focus distance of the cameras. Many other 3D scanning technologies exist, each with its own pros and cons, but it was found that they require significantly longer time to achieve the same resolution as SL scanners (16). The scanner must have the following properties:

- A resolution and precision which is high enough to resolve the small scale defects.
- An optical system which makes it operational in the light conditions present at the production floor.
- A reconstruction time that is significantly short, preferably less than five seconds.

The RapidScan from Automated Precision Inc. (API) was chosen as it delivers a good compromise between cost and performance. It uses invisible near infrared light which is not emitted by energy saving overhead lights, why they will not interfere with the projected pattern. A pilot study proved that the paint used for turbine blades does not pose problems as it has a nice high albedo and low scattering. Note that this would not have been the case if the blade were to be scanned before painting, as the composite material observes strong scattering properties. From its specifications, the RapidScan has a measurement area of 300 by 300 [mm] at a distance of 350 [mm], with a point spacing of 200 [µm] and a point uncertainty of 50 [µm].

3.2.1 Scanner tracking

As indicated above, the SL scanner covers only a small fraction of the entire blade surface per scan, why it must be moved across the surface. See Figure 2 for an illustration. As the scanner moves, its position has to be tracked in a global coordinate frame such that consecutive scans can be transformed into that same reference frame. This is necessary as it is difficult to accurately register neighbouring scans to each other using post-processing alignment strategies, such as ICP (17), because the blade surface is very monotonous.

Again, several different technologies are available for tracking, but a laser tracker with an active target was selected. This combination can provide 6 DoF positions with an uncertainty below half the minimum point-to-point distance of the scans. The laser tracker and active target delivers high data rates, with positions many times per second. From trials, it is known that this combination is significantly faster than measuring four passive targets and then assign a coordinate frame to the measurements, as done in (13).

It was found that a combination of API's vProbe active target and their OmniTrack II laser tracker provided a good compromise between price and performance. The vProbe is closely aligned with the internal coordinate frame of the scanner in order to adhere to the Abbe principle. The combined measurement system is sketched in Figure 3.

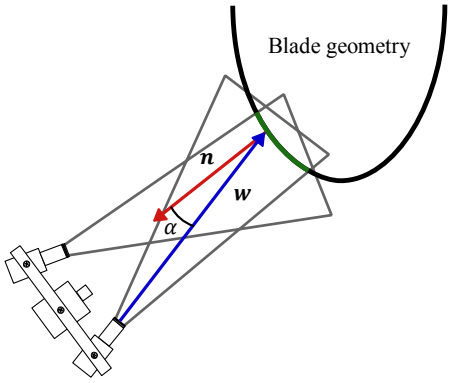

Figure 2. Illustration of the area covered by the scanner (green) based on the frustums of the two cameras (grey). The angle between the scanner view *w* (blue) and the surface normal *n* (red) should be small to increase precision, but $\alpha > 0$ to avoid specular highlights.

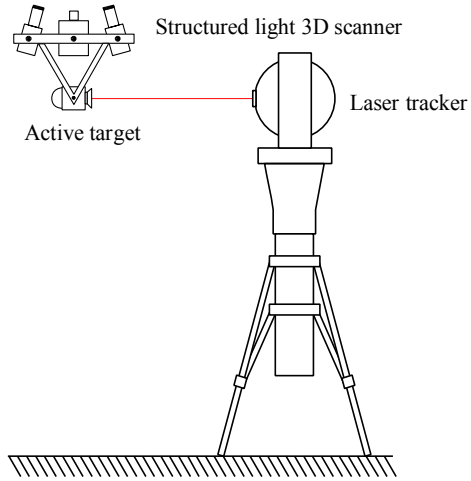

Figure 3. Sketch of the measurement system.

3.3 The locomotion system

A six axis industrial robot arm was chosen for carrying the scanner. The versatility of the robot makes it a good platform for moving the scanner around the leading edge and track the course of the surface. By mounting the robot on a moveable platform, the working envelope of the system is greatly increased, allowing it to survey the entire leading edge.

Health and safety are major concerns for manufactures. Because of that, a collaborative robot (cobot) was selected. Of the various available options, the Universal Robots UR10 fits nicely with the specifications. It is relatively cheap, adheres to ISO standard 15066 about collaborative robots, has an Ethernet interface for computer communication and control, digital interfaces for low level PLC communication, and it has a fairly large working envelope.

3.4 System calibration

The system contains six local coordinate frames, with a chain of five rigid transformations combining them. Starting from the bottom, $\boldsymbol{T}_{\mathbf{fr}}$ transforms coordinates from the moving platform, or frame, to the robot base. $\boldsymbol{T}_{\mathbf{rt}}$ transforms from the robot base to the robot tool centre point (TCP). $\boldsymbol{T}_{\mathbf{ts}}$ transforms from the TCP to the scanner. $\boldsymbol{T}_{\mathbf{sp}}$ transforms from the scanner to the tracking probe. $\boldsymbol{T}_{\mathbf{pg}}$ transforms from the tracking probe to the global coordinate frame defined by laser tracker. The transformations are illustrated in Figure 4. All of the transformations have to be known in order to control the robot and transform the measurements into the same reference frame.

$\boldsymbol{T}_{\mathbf{rt}}$ is given as the robots position in its own coordinate frame and $\boldsymbol{T}_{\mathbf{pg}}$ is given as the measured six DoF position of the tracking probe using the laser tracker. The remainder transformations, $\boldsymbol{T}_{\mathbf{fr}}$, $\boldsymbol{T}_{\mathbf{ts}}$ and $\boldsymbol{T}_{\mathbf{sp}}$, must be obtained through calibration.

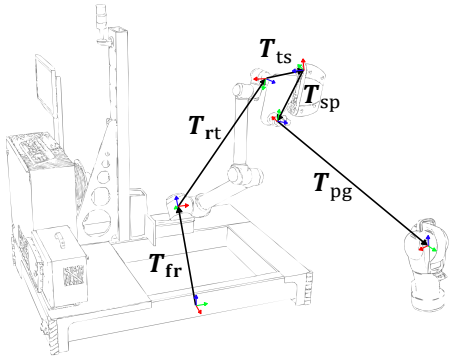

Figure 4. Illustration of coordinate frames and their transformation chain.

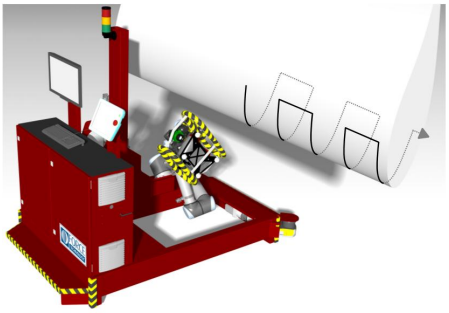

Figure 5. Illustration of the trajectory of the scan path followed by the scanner over the surface. The scanner is off-set from the surface by its focus distance.

$\boldsymbol{T}_{\mathbf{fr}}$ is estimated from the CAD design model of the inspection system. $\boldsymbol{T}_{\mathbf{ts}}$ is computed using the hand-eye calibration from (18). To calibrate $\boldsymbol{T}_{\mathbf{sp}}$, a set of four Spherical Mounted Reflectors (SMR) are mounted in sockets on the scanner whose positions in

the scanner coordinate frame is calibrated by the manufacturer. From measurements of the positions of the four SMRs and the probe, $\boldsymbol{T}_{\mathbf{sp}}$ can be computed using least squares optimization.

3.5 Control of the surveying process

The scanner tracks out a U-shaped trajectory over the blade surface, going forth and back to cover the leading edge. This trajectory is illustrated on Figure 5. The robot makes six stops on every U-curve to sample the surface. The API scanner captures the necessary data in two seconds and the 3D point cloud is reconstructed while the robot moves to the next sample position. The robot can reach two U-curves from one position and then the platform has to be moved. The two U-curves will yield a total of 12 point clouds which are used to plan the next sample positions on the following two U-curves, and the movement of the platform. The 12 point clouds are projected into the coordinate frame defined by the moveable platform, combined, and sliced by a transverse plane through the middle. Points located up to 5 [cm] away on both side of the plane are projected onto the plane, and a 2D polynomial path is fitted to these points. The method presented here is based on (19), but replaces spline curves with polynomials to enforce a stronger prior on the surface trajectory. Six points are sampled from the polynomial path based on their arc-length from the leading edge. There should be more sampled points in areas where the surface curvature is big compared to areas where the curvature is small. The six points are then back-projected into the 3D coordinate frame and copied for a total of 12 points. The first point set copy is slided backwards to cover the first U-curve and the second is slided forwards to cover the second U-curve. The process is illustrated on Figure 6.

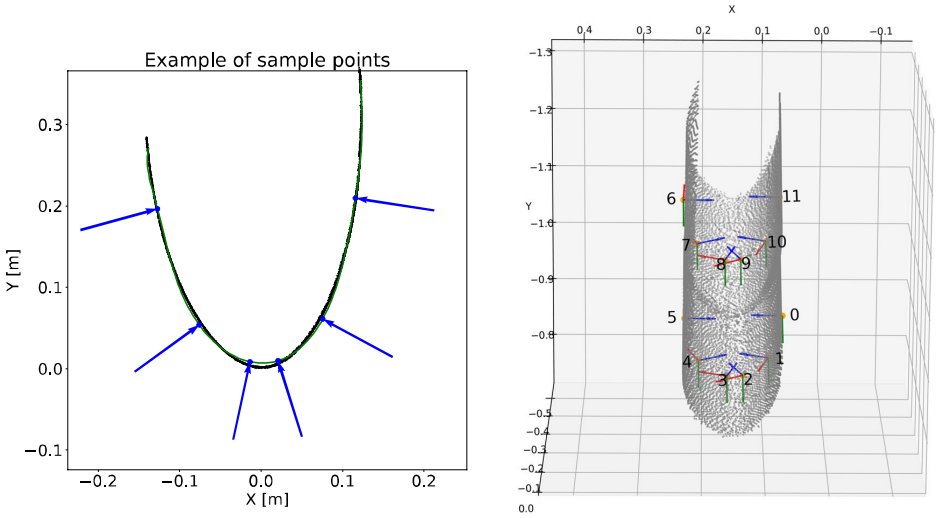

(a) **(b)**

Figure 6. Illustration of the sample point planning. The sampled 3D point clouds from the previous sample positions are sliced by a transverse plane and a polynomial path is fitted to the points projected onto this 2D space (a). The green line shows the model and the blue points and arrows indicate the computed sample positions. The positions are projected back into the 3D space, copied, and moved both backwards and forward along the longitudinal direction (b).

4. Measuring performance of the method

In order to assess the measurement performance, the guidelines in VDI/VDE 2634 was used, which is based on a calibration artefact, and not the measurement of the turbine blade. It specifies probing error, sphere-spacing error and flatness which, in combination, hint about the measurement uncertainty of the 3D scanner. Traceability is established through the use of a 200 [mm] long ball-bar standard with 25 [mm] diameter spheres and a 200 [mm] by 50 [mm] flatness standard, both which were calibrated and certified by Ingeniería Y Servicios De Metrología Tridimensional Sl (ISM3D). The ball-bar was used to estimate both the probing and sphere-spacing error. More details on the standards and the general procedure can be found in (20). The inspection system was positioned roughly 5 meters from the laser tracker. The ball bar and flatness plane was measured in the required positions relative to the scanners frustum by moving the scanner with the robot. The measurements, transformed into the global reference frame, are shown on Figure 7.

(a) **(b)**

Figure 7. 3D point clouds from measurements of ball bar (a) and reference standards (b). Each individual measurement has been assigned a distinct color.

During analysis, it was noticed that the scanner struggled to accurately reconstruct the spheres near the rim where the angle between the view direction and surface normal approached 90º. An example is shown in Figure 8.a. As the guideline operates with maximum values, these points dominate the error measures. Thus, it was deemed necessary to remove them. The distribution of centre-to-point distances, over all measured spheres, is depicted in Figure 8.c. By fitting a Gaussian distribution and setting a threshold at four standard deviations, it was possible to remove the points. Ten randomly selected spheres were visually inspected in order to verify that the correct points were removed. In addition, the 0.3% points which contributed the largest error was removed as is allowed by the guideline. The results are presented in Table 2. The variables in the table are as follows: P_F is the form probing error, P_S is size probing error, SD is sphere-spacing error and F is flatness measurement error. Results from the unfiltered measurements are denoted “Original” and results from the filtered measurements are denoted “Filtered”.

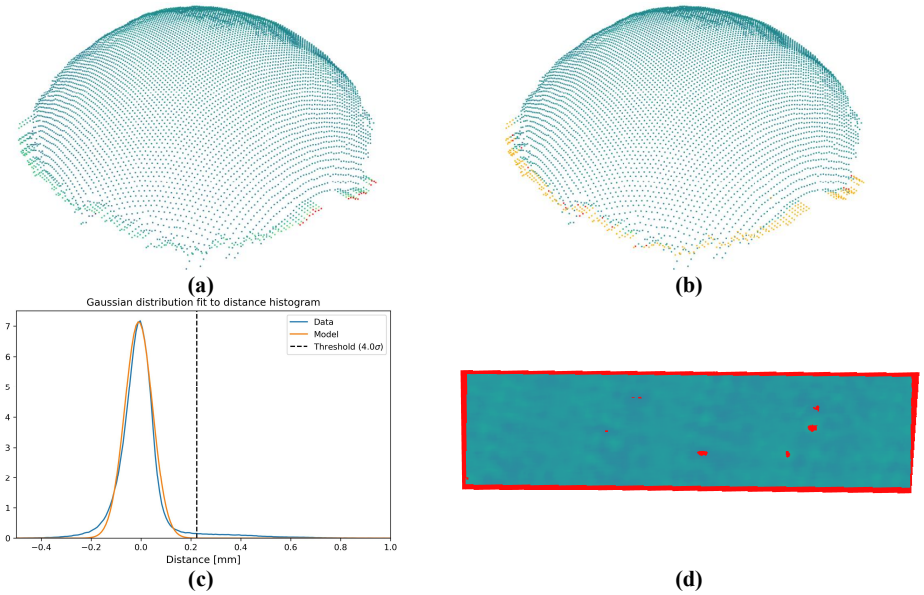

Figure 8. Examples of point clouds from reference standard measurements. Red points are extremum points which are omitted as per VDI/VDE 2634. (a) shows one sphere from the ball bar with fictional points protruding from the rim. (b) shows the same sphere but with the erroneous points detected and highlighted in orange. The colouring of both point clouds illustrates the normalized distance from the sphere's centre to the points. (c) shows the distribution of point-to-centre distances among all spheres. (d) shows the flatness plane with points coloured by their distance over the fitted plane. This is also a point cloud, but sampled so densely that it looks solid.

Table 2. Results of the calculated error parameters in [mm]

	Mean	**Std.**	**Min.**	**Max.**
P_F original	1.248	0.301	0.694	2.069
P_F filtered	0.585	0.115	0.391	0.983
P_S original	0.814	0.444	0.221	1.827
P_S filtered	0.373	0.309	-0.309	1.401
SD original	0.399	0.162	-0.032	0.855
SD filtered	0.245	0.142	-0.204	0.680
F	0.173	0.029	0.115	0.233

Filtering of the ball bar point cloud significantly improved the associated error measures, but as the guideline specifically concerns maximum values, the measurement uncertainty of the system should be the 1.4 [mm] obtained from the proofing error, P_S. However, based on the low mean values and low standard deviations, it is believed that some noise points still linger in the measurements of the ball bar. It is assessed that the actual measurement uncertainty is lower than $\mathbf{0.7}$ [mm], but a more thorough investigation is needed to definitively establish the uncertainty.

An example of a measured blade section is showed on Figure 9. The example section is four meters long and composed of 70 individual point clouds for a total of roughly 45 million individual points. The inspection system has successfully been tested on blade

sections of up to 19 meters in length, which was scanned in 1 hour and 15 minutes, with the scanners shutter time being the bottleneck.

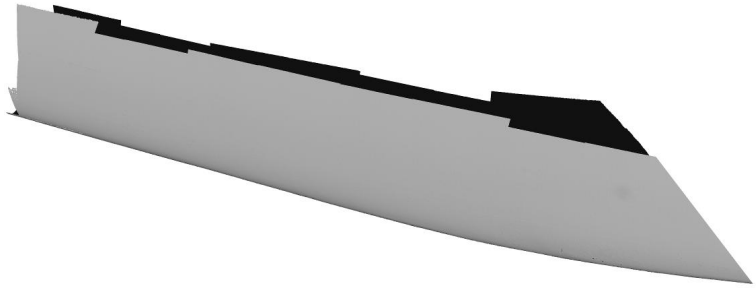

Figure 9. Example of a measured blade section. Note that this is not the surface has not been reconstructed, but that it is sampled so densely that it looks like a surface. This section is approximately three meters long.

5. Idea for automatic detection of surface defects

As detailed by the previous work, in particular (13), the flexibility of the material combined with the size of the blades pose a significant challenge when registering the point clouds to the blade CAD model. Previous work indicates that registration through finite element modelling is difficult due to production tolerances and the properties of the composite material. Instead, it seems that it would be easier to achieve the required accuracy through a local method.

It is proposed to take the local fitting to limit. A plane would be aligned to the second and third principal components of the point cloud and slided down the first principal component. For each slide, a small volume of nearest points around the plane would be cut out and registered separately to the blade CAD model, but regulated in a bundle adjustment setting (21) which allows only a certain, small deviation between overlapping scans. In this way, the low frequency changes attributed to gravitationally induced deformations would be handled through the registration, while still retaining the possibility to detect higher frequency surface changes stemming from defects.

6. Conclusions

This paper developed an autonomous inspection system for wind turbine blade surfaces. It was found that a combination of a structured light 3D scanner and a laser tracker with an active target formed a good measurement system, and that the range of this system could be extended by an industrial robot mounted on a moveable platform. It was shown that the system is fast and achieves low measurement uncertainty on the investigated calibration artefact, though more thorough uncertainty investigations are needed. The results documented here and the experiences with the system show a great potential of the system in practical blade manufacturing. Future work will focus on fully automating the blade inspection by further investigating the measurement uncertainty and developing automatic registration and comparison between measurements and model. Hereby, the current manual process can be completely replaced.

Acknowledgements

The authors would like to acknowledge the kindness and helpfulness demonstrated by the employees at Siemens Gamesa's production facility in Aalborg, Denmark. This paper would not have been possible without them.

References and footnotes

1. M Jureczko, M Pawlak and A Mężyk, "Optimisation of wind turbine blades", Journal of Materials Processing Technology 167 (2-3), pp 463-471, 2005.
2. M Hermann, T Pentek and B Otto, "Design Principles for Industrie 4.0 Scenarios", 49th Hawaii International Conference on System Sciences (HICSS), pp. 3928-3937, 2016.
3. P Schubel, "Cost modelling in polymer composite applications: Case study Analysis of existing and automated manufacturing processes for a large wind turbine blade", Composites Part B: Engineering 43 (3), pp 953-960, 2012.
4. WT Estler, KL Edmundson, GN Peggs and DH Parker, "Large-scale metrology–an update", CIRP Annals-Manufacturing Technology 51(2), pp 587-609, 2002.
5. GN Pegg, PG Maropoulos, EB Hughes, AB Forbes, S Robson, M Ziebart and B Muralikrishnan, "Recent developments in large-scale dimensional metrology", Proceedings of the Institution of Mechanical Engineers, Part B: Journal of Engineering Manufacture 223 (6), pp 571-595, 2009.
6. RH Schmitt, M Peterek, E Morse, W Knapp, M Galetto, F Härtig, G Goch, B Hughes, A Forbes and WT Estler, "Advances in large-scale metrology–review and future trends", CIRP Annals 65 (2), pp 643-665, 2016.
7. W Cuypers, N Van Gestel, A Voet, JP Kruth, J Mingneau and P Bleys, "Optical measurement techniques for mobile and large-scale dimensional metrology", Optics and Lasers in Engineering 47 (3-4), pp 292-300, 2009.
8. SD Hand, DB Ober, BA Bond and EA Devine, "Dimensional measurement of a composite ship hull using coherent laser radar yielding submillimeter results", Journal of ship production 20 (4), pp 232-239, 2004.
9. E Secco, C Deters, HA Wurdemann, HK Lam and K Althoefer, "An Integrated Method for the Geometric Inspection of Wind Turbine Hubs with Industrial Robot", Journal of Intelligent Computing 7 (1), pp 1-7, 2016.
10. D Vučina, M Ćurković and T Novković, "Classification of 3D shape deviation using feature recognition operating on parameterization control points", Computers in industry 65 (6), pp 1018-1031, 2014.
11. M Grosse-Schwiep, J Piechel and T Luhmann, "Measurement of rotor blade deformations of wind energy converters with laser scanners", Journal of Physics: Conference Series 524 (1), pp 012067, 2014.
12. HL Fu, KC Fan, YJ Huang and MK Hu, "Innovative optical scanning technique and device for three-dimensional full-scale measurement of wind-turbine blades", Optical Engineering 53 (12), pp 122411, 2014.
13. Y Petryna, A Künzel and M Kannenberg, "Fault Detection and State Evaluation of Rotor Blades", 7th European Workshop on Structural Health Monitoring, 2014.
14. J Talbot, Q Wang, N Brady and R Holden, "Offshore wind turbine blades measurement using Coherent Laser Radar", Measurement 79, pp 53-65, 2016.

15. A Summers, Q Wang, N Brady and R Holden, “Investigating the measurement of offshore wind turbine blades using coherent laser radar”, Robotics and Computer-Integrated Manufacturing 41, pp 43-52, 2016.
16. L De Chiffre, HN Hansen, JL Andreasen, E Savio and S Carmignato, “Geometrical metrology and machine testing”, DTU Mekanik, 2015.
17. PJ Besl and ND McKay, “Method for registration of 3-D shapes”, Sensor Fusion IV: Control Paradigms and Data Structures 1611, pp. 586-607, 1992.
18. RH Liang and JF Mao, “Hand-eye calibration with a new linear decomposition algorithm”, Journal of Zhejiang University-SCIENCE A 9 (10), pp 1363-1368, 2008.
19. H Wang, J Kearney, and K Atkinson, “Arc-length parameterized spline curves for real-time simulation”, Proc. 5th International Conference on Curves and Surfaces, pp 387-396, 2002.
20. ER Eiríksson, J Wilm, DB Pedersen, H Aanæs, “Precision and accuracy parameters in structured light 3-D scanning”, The International Archives of Photogrammetry, Remote Sensing and Spatial Information Sciences 40, pp 7, 2016.
21. K Ni, D Steedly and F Dellaert, “Out-of-core bundle adjustment for large-scale 3d reconstruction”, IEEE 11th International Conference on Computer Vision (ICCV), pp. 1-8, 2007.

CONTRIBUTION J

Development and Metrological Validation of a New Automated Scanner System for Freeform Measurements on Wind Turbine Blades in the Production

Journal	Precision Engineering
Volumne	In Press
Pages	In Press
Submission date	August 1, 2018
Publication Date	In Press
Publisher	Elsevier
DOI	10.1016/j.precisioneng.2018.12.006

This contribution provides a more detailed description of the scanner system, which compliments the one in Contribution I, and meticulously documents the uncertainty of the blade measurements. My main contribution to this paper was constructing the scanner system, executing and assisting in the data acquisition, and writing the majority of the paper.

Development and Metrological Validation of a New Automated Scanner System for Freeform Measurements on Wind Turbine Blades in the Production

Rasmus Ahrenkiel Lyngby[a,b,*], Ewa Nielsen[b], Leonardo De Chiffre[c], Henrik Aanæs[a], Anders Bjorholm Dahl[a]

[a] *Department of Applied Mathematics and Computer Science, the Technical University of Denmark, Richard Petersens Plads, Building 324, 2800 Kgs. Lyngby, DK*
[b] *Siemens Gamesa Renewable Energy, Assensvej 11, 9220 Aalborg Øst, DK*
[c] *Department of Mechanical Engineering, the Technical University of Denmark, Nils Koppels Allé, Building 404, 2800 Kgs. Lyngby, DK*

Abstract

Geometrical defects on the surface of wind turbine blades can severely degrade the blade during operation and lead to reduced lift, which in turn reduces the power output of the turbine. This paper presents an automated surface geometry inspection system, which is designed based on manufacturing requirements. Estimating the measurement uncertainty and establishing traceability is difficult for huge, freeform objects. An approach based on the Modular Freeform Gauge (MFG) method is presented and used to estimate the measurement uncertainty of the system. An expanded measurement uncertainty of 665 μm ($k = 2$) was established for the system and verified by measurements on a 55 meter long blade.

Keywords: 3D measurement, Freeform surface metrology, Large object metrology, Wind turbine blade, Modular Freeform Gauge, ISO 15530-3

1. Introduction

Surface defects on a wind turbine blade can significantly lower the blade's lift and thus the power output of the turbine [1]. This paper presents a method for creating a dense 3D model of a wind turbine blade's surface, which can be used for surface quality inspection during production. Moreover, such a surface model is a step towards creating a digital blade twin. This is a prerequisite for efficient, modern manufacturing [2] and quality control [3]. Our proposed scanner system is illustrated in Figure 1.

*Corresponding author. Tel.: +45 4525 3407
Email address: raly@dtu.dk (Rasmus Ahrenkiel Lyngby)
URL: www.dtu.dk (Rasmus Ahrenkiel Lyngby)

This paper considers the following measurement task: Conduct dense freeform measurements of a wind turbine blades leading edge for the outermost one third of its length.

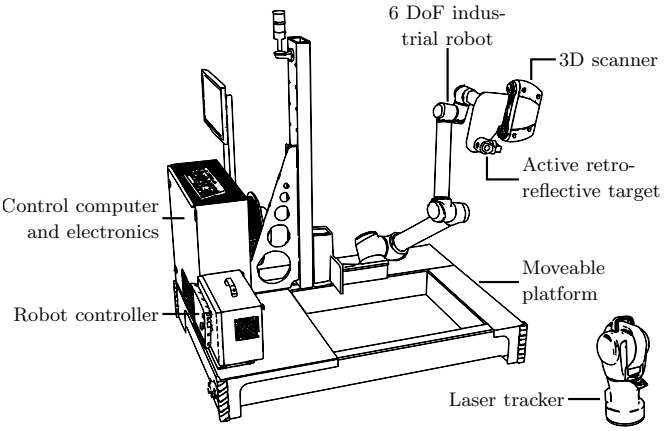

Figure 1: Drawing of the proposed scanner system. A structured light based 3D scanner captures sub-scans of the wind turbine blade surface while a laser based six Degrees-of-Freedom (DoF) positioning system records the positions of the individual sub-scans.

1.1. Wind turbine blade manufacturing and geometrical quality control

The outer geometry of a wind turbine blade is carefully designed so that the shape of its airfoil optimizes lift while reducing drag within the designated wind speed range. Every step in the production from packing of fiberglass into the mold to final surface treatment can potentially introduce surface defects. The aproximately cylindrical shaped part of the blade, which hits the wind first, is called the leading edge. The leading edge is the most critical zone of the airfoil because it "carves" the air. The maximum lift on the blade is attained when the airflow around the airfoil is laminar. Small-scale defects, such as pinholes, cracks or steps, can cause prematurely breakage of laminar flow in the boundary layer around the airfoil, which causes increased drag and can lead to damaging surface erosion [4, 5]. When the blade is turning, the tangential velocity of a point on the blade's surface is proportional to the distance from that point to the turbine's hub. For current blades, the velocity at which surface related defects become significant is attained from about two thirds of the blades length and onward. For a 75 meter long blade, this corresponds to the last 25 meters towards its tip.

Today, manufactures rely on trained experts and manual labor to measure the blade's surface and detect defects. While this method provides decent sensitivity, it is rather slow, relatively expensive and does in many circumstances not provide quantitative measurements.

Previous research has made significant contributions towards developing an accurate and fine grained quantitative measurement method for measuring huge freeform components, which is suitable for automation [6, 7]. However, it seems that none of these methods have been demonstrated to work on life-sized offshore wind turbine blades. Thus, such a method has to be developed and demonstrated.

The lack of established standards related to huge freeform components has resulted in poor documentation of their measurement uncertainties. This paper presents an automated method for measuring the leading edge geometry, which surpasses manual inspection in speed and quantifiability, while retaining good sensitivity. Traceability, as defined in the International Vocabulary of Metrology (VIM) [8] and following the Guide to the Expression of Uncertainty in Measurement (GUM) [9], is established by an approach based on a combination of the Procedure for Uncertainty Management (PUMA) method, described in ISO 14253-2 [10], the modular free form gauge (MFG) method [11], which is based on the substitution method defined in ISO 15530-3 [12], and reverse engineering [13].

2. The new scanner system

Modern blades for offshore turbines are huge and flexible structures with the biggest currently extending past 80 meters in length. The blade surface is double curved but with a much higher curvature in the transverse direction than in the longitudinal direction. These two properties makes it a subject of large scale, freeform metrology as described by Savio et al. [14]. Peggs et al. [15], Franceschini et al. [16] and Schmitt et al. [17] agree that large scale metrology continues to pose challenges, especially with regards to standards and uncertainty estimation, but that a recent increase in interest and research has made it more readily available. The difficulties often arise due to the size of the measurement volume and workpiece deformation under the influence of gravity, combined with the required measurement precision .

Several investigations towards dense geometry measurements of wind turbine blades have recently been made. Fu et al. [18] used two sled-mounted laser line scanners to measure surface deformations on a small household blade. Petryna et al. [19] measured a small industrial blade with a system composed of a structured light based 3D scanner, an industrial robot and a linear drive stage. Shmueli et al. [20] employed photogrammetry to measure local deformations in the trailing edge of wind turbine blades. Talbot et al. [21] measured a blade-like artifact using coherent laser radar. While all of these contributions provided valuable insight, none of them produced a scanner system which had the resolution, speed and flexibility required by modern blade manufacturing. The scanner system presented in this paper is based on the lessons learned from

the studies outlined above, but with a greater focus on manufacturer requirements.

Current offshore blades rotate with tip speeds around 300 km/h. At that speed, the smallest significant geometrical defects has a spatial extent of about 200 μm. This sets a base target for the distance between neighboring measurement points and their associated measurement uncertainty. Laser based scanner systems are highly accurate but require a relatively long time to densely measure large scale structures [6] and would likely require more than a full shift (8 hours) to measure the full leading edge on a blade. Due to the production frequency and takt times, a maximum inspection time of a quarter of a shift (two hours) seems to be the upper limit allowed by manufacturers. Structured light based scanners can achieve uncertainties down to about 100 μm while covering a 300×300 mm area with a point density of 25 points per mm^2 (equivalent to a point-to-point distance of 200 μm) or better [22]. This type of scanner has to be moved many times in order to measure the entire surface. The maximum permissible reconstruction time per sub-scan can be computed by:

$$t_{\mathrm{mpr}} = \frac{(t_{\mathrm{mpm}} - t_{\mathrm{set}})A_{\mathrm{m}}(1-Q)}{A_{\mathrm{s}}} - t_{\mathrm{han}} \tag{1}$$

where t_{mpm} is the maximum permissible measurement time, t_{set} is the initial setup time, A_{m} is the measurement area covered by each sub-scan, Q is the overlap ratio between neighboring sub-scans, A_{s} is the area of the critical part of the blade surface and t_{han} is the time it takes to handle and move the scanner between locations.

The advantages of commercially available standard components, over custom build ones, are support, scalability and cost. Therefore, standard components were used as much as possible.

When selecting the best suited 3D scanner, the most important factors are speed, precision, resolution, robustness and price. To select the best one, a benchmark of current commercially available 3D scanners were performed and the RapidScan from Automated Precision Inc. (API) was chosen. It employs an unstructured light pattern [23], where two cameras capture images of a random dot pattern which is projected onto the surface. The acquisition takes roughly 2.7 seconds to finish and the subsequent reconstruction of 3D points takes about 2.3 seconds. The point-to-point spacing ranges from 220 μm nearest to the scanner and up to 350 μm furthest away in its depth of field. The depth of field extends from 245 mm to 400 mm. With about 1,100,000 points per scan at best, it covers an area of roughly 300×300 mm. The use of infrared light makes the scanner very robust against ambient illumination, as long as that lighting is constant during pattern projection, which avoids the need for screening away lights sources present in the production environment. Finally, it is reasonably priced compared to competing industrial scanners.

To measure the blade, the scanner system must be moved around the blade in all directions [19]. Due to the length of the blade, it is not possible to scan it from one position. Using a rail system is inconvenient because it limits the flexibility of the system, and instead a self-driving platform was chosen that can easily be set up at any factory floor.

The self-driving platform is constructed from hollow steel sections. It has a footprint of 1.7×1.2 meters and a height over the floor of just 200 mm. This relatively flat footprint, combined with a total assembly weight of more than 600 kg, makes it a very stable platform, which effectively dampens vibrations induced by the robot. In addition, its low profile makes it ideal for crawling under the blade, even in positions with low clearance between the leading edge and the floor. The robot is mounted at an angle of 45° relative to the platform such that its primary region of singularities are tilted backwards away from the measuring region. A rectangular hole placed right below the robot's base allows the elbow joint to sweep closely over the floor, which further enhances its ability to navigate in tight spaces.

A Universal Robots UR10 industrial robot with six Degree of Freedom (DoF) is used due to its low weight, adequate carrying capacity, easy control and low cost. Further, it can be made ISO 15066 [24] compliant, which means that it can be operated as a collaborative robot that does not need a safety cage. This is in line with the manufacture requirement of minimizing changes to the current production environment. The robot moves the 3D scanner in a series of U-shaped trajectories around the leading edge with a number of stops to allow the scanner to measure. The trajectory is illustrated in Figure 2. Whenever the robot reaches the end of its work envelope, the platform moves forward in the direction of the leading edge and then the robot continues on its trajectory.

The system's control loop moves the robot and platform based solely on the measured surface geometry and a set of predefined parameters. A global positioning and tracking system is therefore not required for controlling the scan sequence. However, each sub-scan has to be transformed into a global reference frame with a precision which is on par with the scanner precision. The OmniTrack II laser tracker and vProbe active target from API was selected over the others that were benchmarked. The vProbe reflects the tracker's laser beam, such that the tracker can measure x, y and z positions, but it also uses an in-build camera sensor to observe the incident angles of the beam, into the reflector, which it uses to compute its pitch and yaw orientation. The roll is provided by a gyroscope. In combination, this system measures six DoF positions. Other trackers often rely on a 3D artifact, which has to be pose estimated through observations made with a camera, in order to measure orientation. Available camera resolutions seem to limit the range of such system below that which is needed. Using an active target, such as the vProbe, six DoF positions can be obtained without the need of measuring four distinct passive targets, known as spherical mounted reflectors (SMRs).From its certificate, the positional uncertainty of the vProbe is $3D^U = (30 + 5L)$ μm (L in m). Assuming $k = 2$, this corresponds to an uncertainty of 65 μm at $L = 20$ m. The combined OmniTrack

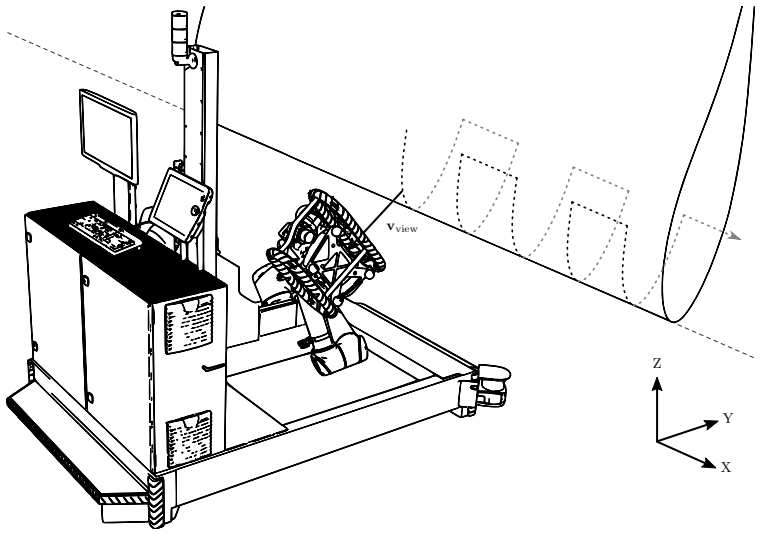

Figure 2: Illustration of the trajectory which is covered by the scanner on the blade surface through movements of the robot and platform. The vector $\mathbf{v}_{\text{view}}$ indicates the scanner's position relative to the surface and is aimed at a length $||\mathbf{v}_{\text{view}}|| \approx 300$ mm.

II and vProbe positioning system has a maximum range of 80 meters. Occlusions between the laser tracker and the scanner is avoided by placing the laser tracker in front of the scanner system, near the blade tip. The probe is rigidly mounted close to the scanner. In this setup, the tracker defines the common global reference frame.

In theory, the tracking could have been done by dead reckoning. Each robot movement is governed by a relative transformation $\mathbf{T}_{i,i+1}$ which moves it from position i to position $i+1$. A sub-scan at position i could be transformed into a global reference frame, defined by the initial robot position, by the combined transformation $\mathbf{T}_i = \mathbf{T}_{1,2}^{-1}\mathbf{T}_{2,1}^{-1}\cdots\mathbf{T}_{i-1,i}^{-1}$. However, dead reckoning accumulates small errors, which relatively quickly leads to a significant positioning uncertainty. Other means of tracking, such as the Nikon iGPS radio based system, was also considered, but they generally either required mounting fixed "satellites" around the measurement area or could not deliver the required precision.

A photograph of the scanner system in action is shown in Figure 3.

2.1. Controlling the scan sequence

Before describing the control loop, it is necessary to have an estimate of how much time is available for each sub-scan. Manufactures are keen on limiting inspection times as much as possible, but they generally seem content if the

Figure 3: Photograph of the scanner system in action. The 3D scanner is encapsulated in a black and yellow striped protective cage and the robot is covered by a tight fabric tube to protect its joints and motors from dust. The laser tracker with its green "on"-LED, standing 20 meters away, can be glimpsed in the middle towards the photo's right edge.

geometrical inspection can be conducted within two hours. As explained previously, only the outer third of the blade is inspected, which amounts to 25 m for an off-shore blade. In a realistic setting, it would probably be enough to measure 0.5 m up on both sides of the leading edge. Some overlap between sub-scans is preferable, and 20% of the scan width could be a reasonably number. Given that 20 minutes are needed for setting up the measurement system, Equation 1 gives a maximum permissible sub-scan and movement time of 17.3 s. The scanner takes 2.7 seconds to acquire the necessary images and then 2.3 seconds to reconstruct 3D surface points from the images. The reconstruction can take place while the scanner moves, which leaves $17.3 - 2.7 = 14.6$ seconds for movement. This example, which uses realistic values, gives an idea of how much time can be spend on moving the scanner. While it might be feasible to manually move the scanner, there are multiple benefits gained by automating the process. Schubel [25] showed that automation, in general, reduces blade manufacturing costs. The movement can be completed significantly faster by automating the scan sequence, which can reduce the total inspection time significantly, with cost savings in return.

The control loop is designed such that it does not rely on any kind of CAD model. It only requires specifying certain parameters such as the number of sub-scans per U-curve, length of the U-curve and overlap between scans from neighboring U-curves. Avoiding a dependency of CAD model eases the usability of the system when different kinds of blade types have to be inspected. Moreover, a pre-computed path would somehow have to be aligned to the physical

blade, which is difficult due to the gravity induced blade deformation mentioned previously. Instead of using pre-computed robot positions, the scanner system computes the positions as it goes. It plans its next movement based on the just acquired surface scans, why no direct alignment between measurements and design model is necessary.

A block diagram of the control loop is illustrated in Figure 4. The path planner sends a translation vector, $\mathbf{t}$, to the platform and a sequence of N acquisition positions, $(\mathbf{T}_i)_{i=1}^N$, to the robot. The platform adjust its bearing and then drives along the translation vector. When finished, it triggers the robot which then begins moving on its sequence. For every position, $\mathbf{T}_i$, the robot stops and trigger the scanner which measures the surface. Once the scanner finishes its acquisition, it triggers the robot which moves to the next position in the sequence. When the last position is reached, the scanner sends the N resulting scans, $(\mathbf{P}_i)_{i=1}^N$, back to the path planner, which then uses them to compute the next sequence of acquisition positions. The loop stops once the blade tip has been scanned.

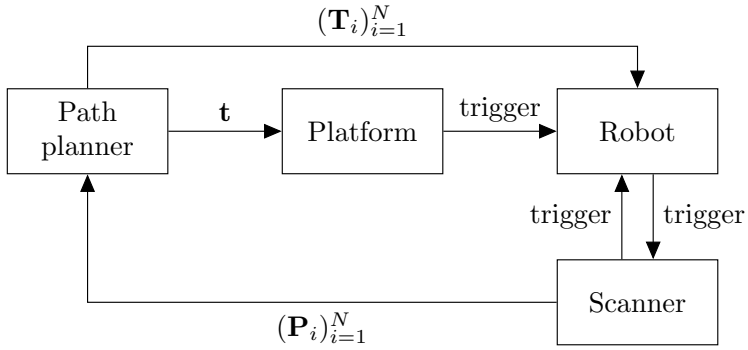

Figure 4: Illustration of the scanner system's control loop. $\mathbf{t} \in \mathbb{R}^2$ is a translation vector in the 2D plane constituted by the floor. $(\mathbf{T}_i)_{i=1}^N$ is a sequence of N six DoF robot poses, with $\mathbf{T}_i \in \mathbb{R}^{4\times4}\ \forall\ i$. $(\mathbf{P}_i)_{i=1}^N$ is a sequence of N resulting point clouds corresponding to the N robot positions.

3. Traceability

Traceability for measurements obtained with the scanner system is established through a comparison with freeform measurements using a tactile coordinate measuring machine (CMM). We propose a method which is based on the MFG method [11] derived from the substitution method described in ISO 15530-3 [12]. The approach follows the general guidelines in the GUM [9, 10], but is specifically tailored to the blade measurement task. In the following,

notation follows the GUM, where type A standard uncertainties are estimated from sampled distributions, and type B are given from *a priori* distributions. The designed traceability chain for the blade measurements, acquired by the scanner system, is illustrated in Figure 5.

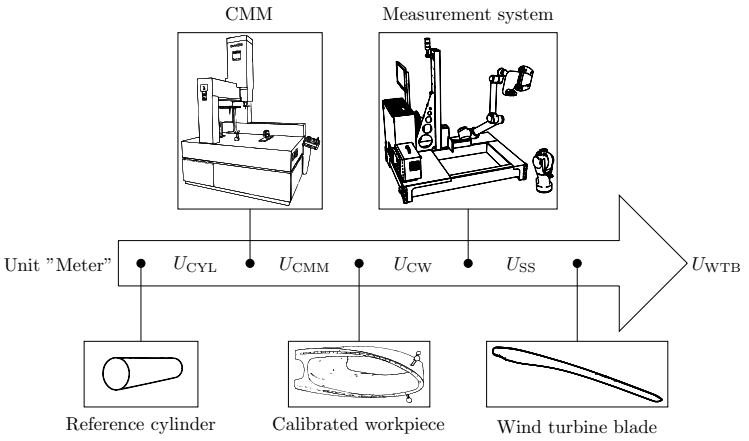

Figure 5: Illustration of the traceability chain. Symbols refer to the text.

This paper gives particular care to the leading edge, which has the most crucial impact on a blade's aerodynamic performance. It can be well approximated by a 100 mm cylinder for blades with a length between 40 and 80 meters. If the low curvature regions surrounding the leading edge were to be measured as well, a cylinder with a diameter of 1200 mm would be needed. This is illustrated in Figure 6. As we focus exclusively on the leading edge, we only need one 100 mm cylinder as our MFG.

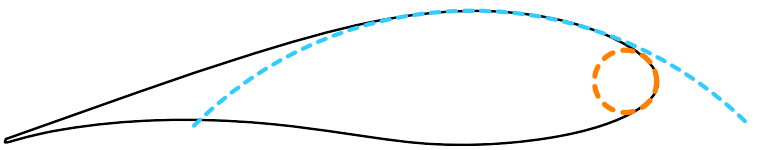

Figure 6: Profile view of the cylinders needed to approximate a 55 meter wind turbine blade by an MFG. The dashed orange circle illustrates a cylinder with a 100 mm diameter. The dashed blue circle arc illustrates part of a cylinder with a 1,200 mm diameter. The black curve illustrates the leading edge together with the top and bottom sides of the blade profile.

It is not necessary to calibrate the MFG configuration because the MFG consists of only one object. Following Savio and De Chiffre [11], the uncertainty contributions of the cylinder's local deviation are illustrated in Table 1.

Here, U_{CYL} is the uncertainty assigned to local deviations of its radius, which is defined as the distance between the "calibrated" CAD model and a point measured on the cylinder's surface in the direction of the surface normal [11]. In our application, the *"calibrated" CAD model* is a mathematical cylinder with a diameter that is equal to the real cylinder's calibrated diameter, as stated in its calibration certificate [26]. The uncertainty of the cylinder's radius is represented by u_{rCYL}. It is equal to half of the uncertainty of the diameter from the certificate, because the form error from the cylinder certificate is given with respect to diameter instead of radius [11, 26].

The uncertainty stemming from the assessment of the cylinder's form error is given by u_{fCYL}. It is defined as half of the uncertainty of the form error from the certificate [11]. Even though the MFG's contributions to the final uncertainty of the blade measurements is expected to be small, they are included following [11] for completeness.

The MFG cylinder is used to calibrate the CMM. An expanded measurement uncertainty can be assigned to the CMM when used for freeform measurements, labeled U_{CMM}, from a combination of repeated profile measurements of the cylinder, u_{repCYL}, the cylinder's calibration, u_{CYL}, and a contribution coming from thermal effects, u_{eCYL}. The contribution from thermal effects are added if the repeated measurements are not conducted at 20°C. This is illustrated in Table 2, which gives an estimate of the CMM's measurement uncertainty when measuring our kind of freeform object.

Traceability is propagated from the reference cylinder, through the CMM, to the calibrated workpiece following the substitution method [12]. It is not possible to measure an entire blade in the CMM due to the blade's size and the limited reach of the CMM. Therefore, we use a smaller workpiece as substitute, which contains the leading edge and fits within the CMM. We fabricate such a workpiece by cutting out a section from an actual blade. The piece was chosen such, that the diameter of the half-cylinder formed by its leading edge is within 25 mm of the diameter of the MFG, as required by ISO 15530-3:2011 [12]. The geometry of the leading edge is relatively uniform when seen over the inspection blade region. It is thus within the 10% geometrical deviation allowed by ISO 15530-3:2011 [12].

The workpiece is calibrated through a series of repeated profile measurements, given by u_{repCW}. The CMM's measurement uncertainty, u_{CMM}, and environmental effects, u_{eCW}, are added separately. The resulting expanded uncertainty is labeled U_{CW}, and it is defined in Table 3. This procedure overestimates the measurement uncertainty, as the uncertainty of the CMM is implicitly being counted twice. The CMM's measurement uncertainty is expressed both in the repeated measurements of the cylinder and in the repeated measurements of the calibrated workpiece. However, including both uncertainties in the uncertainty estimation ensures an unbroken traceability chain. In this way, the CMM's measurement uncertainty acts as a lower bound on the uncertainty of the calibrated workpiece. The CMM's uncertainty is anticipated to be small, relative to the uncertainty contributed by the calibrated workpiece, and there-

fore the double counting is negligible. Thus, this procedure merely ensures the concept of traceability, and is deemed necessary for having an unbroken chain, but does not affect the final measurement uncertainty estimate much.

The uncertainty of the calibrated workpiece is transferred to the scanner system through repeated scans of the workpiece with the system. A series of repeated measurements with different distances to the laser tracker is acquired in order to investigate the relation between this distance and the measurement uncertainty. The uncertainty is labeled U_{SS} and defined in Table 4. As the scanner system's measurements of the workpiece take place in the production environment and the CMM measurements take place in a laboratory, the workpiece forms a link between the laboratory acquired measurements and the production acquired measurements.

Finally, the uncertainty of the blade measurements is assumed to be equal to the measurement uncertainty of the optical scanner system, provided that the repeatability of measurements on the blade is on the same order of magnitude as that obtained from measurements on the calibrated workpiece. This will be verified by measurements. The overall uncertainty of wind turbine blade (WTB) measurements is

$$U_{\mathrm{WTB}} = U_{\mathrm{SS}} \tag{2}$$

$$= k\sqrt{u_{\mathrm{rCYL}}^2 + u_{\mathrm{fCYL}}^2 + u_{\mathrm{repCYL}}^2 + u_{\mathrm{eCYL}}^2 + u_{\mathrm{repCW}}^2 + u_{\mathrm{eCW}}^2 + u_{\mathrm{repSS}}^2 + u_{\mathrm{eSS}}^2} \tag{3}$$

We can expect that the CMM and laser tracker are well within the manufacturer specifications in terms of length measurement performance and much below the CW and WTB repeatability value. An upper bound value could be added, having a uniform distribution and limits corresponding to the largest distance measured on the CMM (for CW) and the laser tracker (for WTB). As documented by the data, the final uncertainty assessment will not change, being dominated by repeatability.

Table 1: Uncertainty contributions on the MFG cylinder (CYL) (adapted from [11]).

Uncertainty Component	Symbol	Type	Estimation
Uncertainty of radius	u_{rCYL}	B	Half of diameter uncertainty from certificate
Uncertainty of form	u_{fCYL}	B	Half of form uncertainty from certificate
$U_{\mathrm{CYL}} = k\sqrt{u_{\mathrm{rCYL}}^2 + u_{\mathrm{fCYL}}^2}$			

Table 2: Uncertainty budget for CMM measurements on MFG cylinder (CYL).

Uncertainty Component	Symbol	Type	Estimation
Calibration uncertainty of MFG cylinder	u_{CYL}	B	From Table 1
Repeatability	u_{repCYL}	A	Repeated CMM measurements on MFG cylinder
Temperature	u_{eCYL}	B	U-shaped distribution
$U_{\mathrm{CMM}} = k\sqrt{u_{\mathrm{CYL}}^2 + u_{\mathrm{repCYL}}^2 + u_{\mathrm{eCYL}}^2}$			

Table 3: Uncertainty budget for CMM measurements on calibrated workpiece (CW).

Uncertainty Component	Symbol	Type	Estimation
Uncertainty of CMM measurements	u_{CMM}	B	From Table 2
Repeatability	u_{repCW}	A	Repeated CMM measurements on CW
Temperature	u_{eCW}	B	U-shaped distribution
$U_{\mathrm{CW}} = k\sqrt{u_{\mathrm{CMM}}^2 + u_{\mathrm{repCW}}^2 + u_{\mathrm{eCW}}^2}$			

Table 4: Uncertainty budget for measurements with the optical scanner system (SS) on calibrated workpiece (CW).

Uncertainty Component	Symbol	Type	Estimation
Uncertainty of CMM measurements on CW	u_{CW}	B	From Table 3
Repeatability	u_{repSS}	A	Repeated SS measurements on CW
Temperature	u_{eSS}	B	U-shaped distribution
$U_{\mathrm{SS}} = k\sqrt{u_{\mathrm{CW}}^2 + u_{\mathrm{repSS}}^2 + u_{\mathrm{eSS}}^2}$			

4. Experimental investigation

The measurements needed for estimating the uncertainties were acquired in four distinct sessions. The calibration of the MFG cylinder is described by Savio [26]. The MFG was used to calibrate the CMM. Then, the CMM was used to calibrate the workpiece. The workpiece was measured by the scanner system in a way which best simulated the actual blade measurement process. Finally, an actual blade was measured with the scanner system and used to assign a final measurement uncertainty to the freeform measurements of the blade.

4.1. Experimental setup

A Zeiss OMC 850 tactile CMM, with a Maximum Permissible Error in space of $\mathrm{MPE}_{U3} = (3 + L/250)$ μm (L in mm) and a probe force of 0.2 N, was used for all CMM measurements. It was operated through the Zeiss Calypso software. The stylus system was chosen such that the tip was able to reach points well underneath the downwards facing side of the cylinder. This was achieved by selecting a 180 mm long stylus with a 8 mm diameter ruby sphere. The CMM was placed in a temperature controlled room where the temperature is $21 \pm 1°$C.

The used MFG was a 360 mm long steel test cylinder with a calibrated diameter of 100.0112 mm with an expanded measurement uncertainty of 0.4 μm ($k = 2$) and a 1.0 μm cylindricity calibrated with an expanded measurement uncertainty of 0.5 μm ($k = 2$) [26]. Here, k is the coverage factor, as defined by the GUM, which is multiplied onto the standard uncertainty. A coverage factor of 2 implies that all values within two times the standard deviation from the mean is retained inside the expanded uncertainty, which corresponds to roughly 95% of all possible values.

The leading edge workpiece was fabricated by cutting a 600×750 mm section out of the leading edge of a real blade. Four 25.4 mm reference spheres were mounted on the workpiece near the leading edge to be used for alignment in the CMM as well as scanner.

4.2. Calibration of CMM

The cylinder was placed in the CMM and supported by two V-blocks as shown in Figure 7. After having fixed the cylinder to the CMM's table, the setup was allowed to acclimatize. The stylus system was qualified using a reference sphere placed next to the cylinder. The cylinder was aligned through a plane measured on its top and a point defined as the center of a circle traced around the middle of the cylinder.

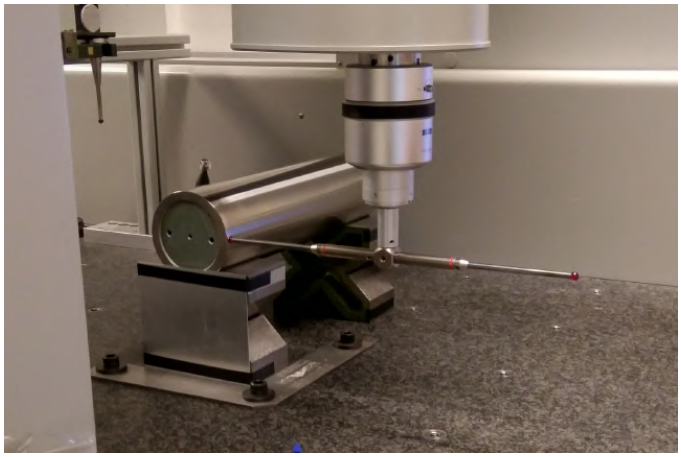

Figure 7: Photograph of the CMM measuring process of the reference MFG cylinder showing the probe near the cylinder's top.

Five profile curves were programmed using the cylinder's CAD model, as seen in Figure 8, with each of the profiles repeated five times. The profiles spanned 180° of a circle arc and were placed at 90 mm, 135 mm, 180 mm, 225 mm and 270 mm from the cylinder's top. 52 measuring points were evenly distributed on each of the profile curves. The measurements were conducted as individual point measurements in free-form mode, which allowed the CMM to save the 3D coordinates of the measured points. Due to a period of exceptionally warm weather in Denmark, the temperature control struggled immensely, why the temperature varied between 24.0°C and 25.1°C during the measurements. A systematic correction for temperature was applied to the measurements.

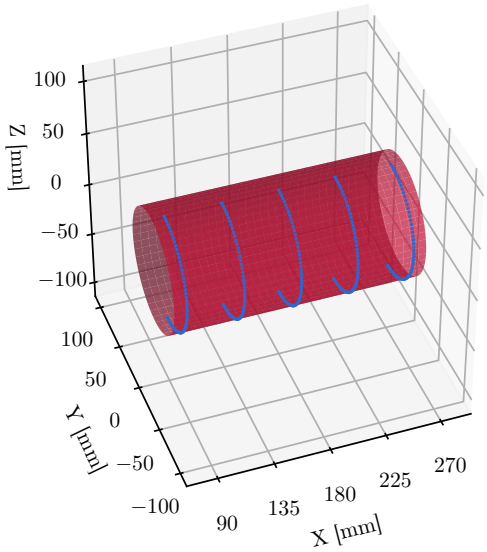

Figure 8: Plot of the measuring points on the profile curves together with a section of the cylinder CAD model.

The standard deviation of the repeated measurements was estimated by fitting a mathematical cylinder to the measurements. The signed distance between each of the measured points and the surface of the mathematical cylinder was computed using Calypso. The standard deviation of these distances was used to estimate the measurement uncertainty u_{repCYL} in Table 2.

4.3. Calibration of calibrated workpiece

The workpiece was mounted in the CMM such that the leading edge was nearly parallel to the CMM's Y-axis at approximately the same location as the cylinder. Three rods with spherical ends provided a stable nest for the workpiece, preventing it from tilting. The rods also lifted the workpiece up over the CMM's measurement table, which allowed the stylus to reach around the leading edge and measure points on a curve starting underneath the bottom of the workpiece and extending up on its top. A beam was mounted through the workpiece in the transverse direction and used to fix it to the table. Through expert assessment, it was sought to fasten the workpiece tight enough to withstand the force of the CMM stylus, but not so tight that it would deform. The arrangement is shown in Figure 9. The black and white circular stickers, seen on the figure, were added for a separate investigation with a commercial scanner,

not reported here. The stickers were placed such that they did not interfere with the CMM measurements.

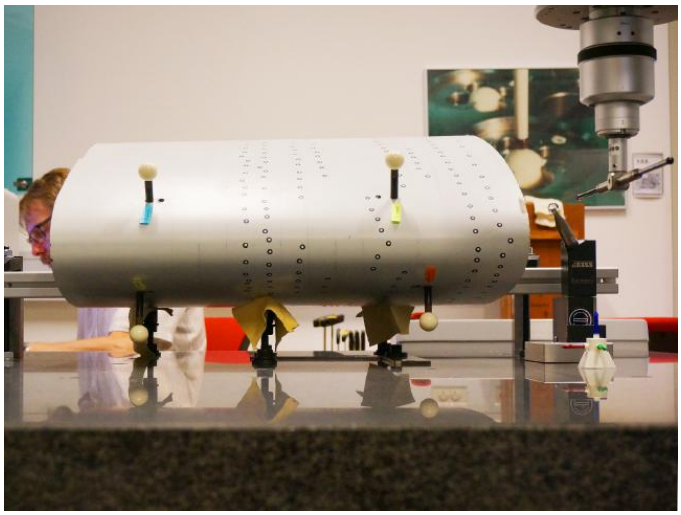

Figure 9: Photograph of the calibrated workpiece mounted in the CMM. The black and white stickers were used for a separate investigation, which is not reported here.

The workpiece was measured through a set of perpendicular curves. The curves were planned by manually measuring the start and end point of each curve with the CMM and then let the CMM automatically trace out the rest of the curve by "feeling its way forward". It did so by moving in circles in the direction from the start point towards the end point. Whenever it hit the surface, it measured the position and started a new circular motion. This process was repeated until the end point was within a threshold distance of 15 mm. A circle radius of 15 mm was chosen, which resulted in 36 points on each curve. The curves were placed with a spacing of 40 mm. The length of the workpiece would have allowed for 14 curves had it not been for the four spheres which shadowed three curves, thus yielding a total of 11 curves.

After mounting and planning, the workpiece was cleaned and allowed to acclimatize. The stylus system was qualified as done before the cylinder measurements. Five points were measured on each of the two top spheres and then six points on one of the bottom spheres. The bottom sphere was difficult to reach and thus six points were needed to measure it properly. Three mathematical spheres where fitted to the measurements and the positions of their centers were used to form a reference plane. The CMM then executed the measurement program which consisted of five repetitions of the $36 \cdot 11 = 396$ semi-automatically defined points.

The temperature varied between 23.5°C and 25°C during the measurements. Fiberglas and epoxy composites have a Coefficient of Thermal Expansion (CTE) of $\alpha_{\mathrm{t}} = 54.8 + 0.163T$ μm/°C/m in the direction running across the fibers, and $\alpha_{\mathrm{l}} = 14.8 + 0.039T$ μm/°C/m in the direction running along the the fibres, both with an uncertainty of 3% of the value [27]. T is the temperature and defined within $T \in [20, 70]$°C. Taking the uncertainty contribution from thermal expansion into account is not trivial for freeform objects. The geometrical shape and internal structure of the object will lead to non-uniform deformations where different parts of the surface will increase or decrease in size differently. The behavior can be accurately estimated either through computer modeling or through repeated measurements of the object at different temperatures. Such a comprehensive estimation is often a contribution in its own right, which is the reason why it is out of the scope of the traceability estimation done here. Instead, a simpler approach is chosen which assigns a realistic, but potentially high, thermal uncertainty contribution. Looking on the blade profile, the leading edge forms a C-shaped arc which encloses a cavity. On the workpiece, the arc length of the leading edge is 135 cm (rounded up to the nearest 5 cm). While the thickness of the shell varies, it is at least 20 times smaller than its length. Using a mean temperature of 24.25°C , the CTE of a rod made of transverse fibers with the same length as the leading edge is $(54.8 + 0.163 \cdot 24.25) = 58.75$ μm/°C/m. This would expand the rod by $58.75(24.25 - 20)1.35 = 337.09$ μm with an uncertainty of $(24.25 - 20)(58.75 \cdot 0.03)1.35 = 10.11$ μm. This uncertainty can be seen as an upper bound of the environmental contribution to the uncertainty of the CMM measurements, u_{eCW}, as the CTE of parallel fibers is much lower.

It was not possible to establish the exact location from where on the blade the workpiece was cut. Therefore, a model of the workpiece could not be made from the blade's CAD model. Instead, it had to be reverse engineered from the CMM measurements. This was done by fitting a Bézier surface to the measured points. First, the bias between the mean positions of the five repeated measurement sets was reduced by applying the Iterative Closest Point (ICP) algorithm [28]. Then, the mean position of the five repetitions were computed at each measured point. Let $(\mathbf{P}^{(i)})_{i=1}^{5}$ be a sequence of the five repetitions of the measured points, with $\mathbf{P}^{(i)} \in \mathbb{R}^{396\times 3}$ $\forall i = 1, \cdots, 5$. From this sequence, the mean positions between the five repetitions at each measurement point were computed and arranged into a matrix $\mathbf{Q} \in \mathbb{R}^{396\times 3}$ with each row computed as $\mathbf{q}_j = 1/5 \sum_{i=1}^{5} \mathbf{p}_j^{(i)}$ where $\mathbf{q}_j$ and $\mathbf{p}_j^{(i)}$ are the vectors corresponding to the j'th row of $\mathbf{Q}$ and $\mathbf{P}^{(i)}$, respectively. The Bézier surface, $\mathbf{s}(u, v) : \mathbb{R}^2 \mapsto \mathbb{R}^3$, is defined as the outer product between two Bézier curves:

$$\mathbf{s}(u, v) = \sum_{i=0}^{d_{\mathrm{u}}} \sum_{j=0}^{d_{\mathrm{v}}} b_{i,d_{\mathrm{u}}}(u) b_{j,d_{\mathrm{v}}}(v) \mathbf{k}_{i,j} \,, \tag{4}$$

where $u, v \in [0, 1]$ spans a unit square plane, and defines the relative position on

the surface. The functions $b_{i,d_\mathrm{u}}(u)$, $b_{j,d_\mathrm{v}}(v) : \mathbb{R} \mapsto \mathbb{R}$ are Bernstein polynomials given by $b_{i,d_\mathrm{u}}(u) = \binom{d_\mathrm{u}}{i} u^i (1-u)^{d_\mathrm{u}-i}$ and $b_{j,d_\mathrm{v}}(v) = \binom{d_\mathrm{v}}{j} u^i (1-v)^{d_\mathrm{v}-j}$. The vectors $\mathbf{k}_{i,j} \in \mathbb{R}^3 \; \forall \; i = 0, \cdots, d_\mathrm{u} \; , \; j = 0, \cdots, d_\mathrm{v}$ are control points in 3D space. The degree of the Bézier surface is defined as $(d_\mathrm{u}, d_\mathrm{v})$ and specifies the number of control points as $(d_\mathrm{u}+1)(d_\mathrm{v}+1)$ in the u and v direction, respectively. The surface is fitted to the measurement means through least squares optimization by minimizing the following:

$$K = \arg\min_{K} \sum_{i=1}^{N} \left\| \mathbf{s}_K(u_i, v_i) - \mathbf{q}_i \right\|^2 \tag{5}$$

where $\mathbf{s}_K(u_i, v_i)$ is the predicted point on the Bézier surface, with control point sequence $K = (\mathbf{k}_{i,j})_{i=0,j=0}^{d_\mathrm{u},d_\mathrm{v}}$, that corresponds to measurement mean point $\mathbf{q}_i$ with surface position (u_i, v_i). The positions of the control points were initially laid out in a grid on a flat plane which spanned the first two principal components of $\mathbf{Q}$.

The surface fitting procedure requires that a forth running pair of (u, v) parametric coordinates are assigned to each point, which can be difficult to get exactly right. The coordinates were initialized such that u indicated which curve the points was on, with 0 corresponding to the first curve and 1 corresponding to the 11'th curve, and v indicated the location of the point on the curve with 0 corresponding to the top most point and 1 corresponding to the bottom most point. This did, however, introduce an error because of the three missing curves which was shadowed by the spheres. The distance between the curves were thus not identical, and therefore it was necessary to also optimize for the (u, v) coordinates, which was done as follows:

$$\mathbf{u}, \mathbf{v} = \arg\min_{\mathbf{u},\mathbf{v}} \sum_{i=1}^{N} \left\| \mathbf{s}_K(u_i, v_i) - \mathbf{q}_i \right\|^2 \tag{6}$$

where the set of control points, K, had been optimized through Equation 5. It was found that alternating between optimizing for the positions of the control points and optimizing for the (u, v) coordinates yielded a much better surface than simply optimizing once for each. Therefore, Equation 5 and Equation 6 were applied iteratively until convergence, which happened after roughly 10 iterations. An example of the fitted surface is showed in Figure 10. Note that the number of target points were $N = 11 \cdot 36 = 396$.

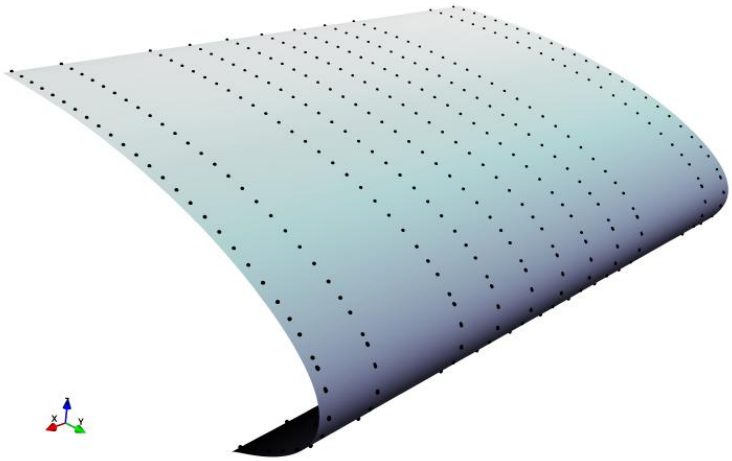

Figure 10: Illustration of the points measured by the CMM on the workpiece together with the fitted Bézier surface. Each point is actually a tight cluster of the five repetitions.

The standard deviation of the signed distance from all $5 \cdot 11 \cdot 36 = 1980$ measured points to the best fit Bézier surface was used to compute the uncertainty of the workpiece.

4.4. Calibration of the scanner system

The now calibrated workpiece was moved to the blade production site and suspended from a forklift with the leading edge oriented towards the floor. Its height over the floor was set such that it best simulated the height of the leading edge as it would have been on an actual blade positioned for measurements. The arrangement is shown in Figure 11.

Figure 11: Photograph of the scanner system measurement process of the calibrated workpiece.

The surface of the calibrated workpiece was cleaned and then allowed to acclimatize. The laser tracker was qualified through repeated measurements of a spherically mounted reflector following the specifications from the manufacturer, and the transformation between the RapidScan and the vProbe was calibrated. The position of the calibrated workpiece was detected and aligned to the scanner system's coordinate frame by measuring its leading edge directly underneath with the scanner pointing straight up. Then, the path planner was used to compute two u-shaped robot trajectories, one forward and one backwards, each with six acquisition positions which were distributed such that the entire intermediate surface was covered. The arclength of each path was 840 mm. The 12 scans were repeated 10 times. In order to investigate if the scanner system's uncertainty was correlated with the distance to the laser tracker, the entire arrangement with scanner system, workpiece and forklift was brought closer to the tracker and the entire process was repeated. The workpiece was measured at 12.5, 10, 7.5 and 4 meters distance. The temperature varied between 20.5°C and 21.3°C during the measurements. The environmental contribution to the uncertainty is estimated through an approach similar to that followed for the CMM measurements.

The point clouds resulting from the measurements were first pre-processed. Noise points situated near edges and in positions where the scanner had observed the surface at a gracing angle was removed. Then, each point cloud was transformed into the global reference frame defined by the laser tracker and combined into a single cloud for each repetition. An example is showed in Figure 12.

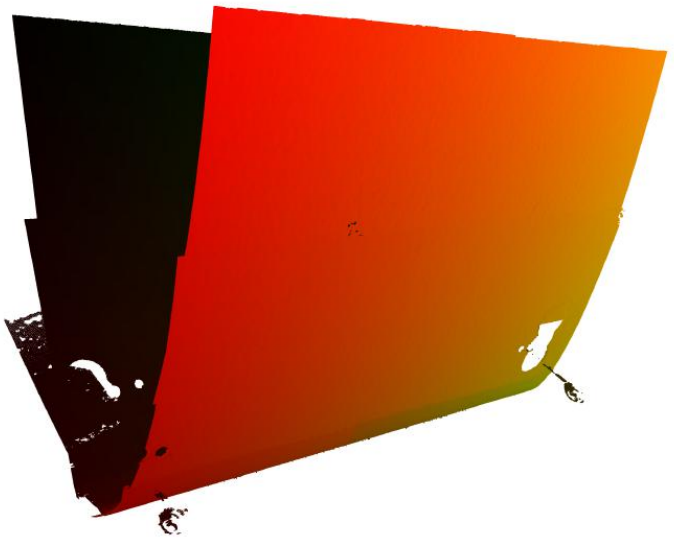

Figure 12: The result of a single measurement of the calibrated workpiece performed by the scanner system at a distance of 12.5 meters from the laser tracker. This scan is composed of 12 individual point clouds and contains just short of 9,000,000 points. Two of the reference spheres, though sparsely sampled, are slightly visible from this angle. The colors indicate the points locations on the surface relative to the first point of the first point cloud and are added here for enhanced comprehensibility.

The distances between the repeated measurements were minimized through ICP in order to remove bias. The measurements were then aligned with the Bézier surface from the CMM measurements, which acted as a calibrated CAD model. The point clouds were roughly aligned with the surface manually and then ICP was used for fine alignment. As it was not feasible to compute the distance between the surface and all nine million points in the point cloud, a subset of points was sampled uniformly over the surface. This was done by sampling the 100 nearest neighbors around each CMM measurement position, which was annotated on the Bézier surface. The standard deviation of the point-to-surface distances was used to estimate the uncertainty of the scanner system.

4.5. Measurements of wind turbine blade

A sanity check of the scanner system's repeatability was done by comparing it with the system's repeatability when measuring a real wind turbine blade. Approximately 20 meters of the leading edge of a 55 m long turbine blade were scanned with the scanner system with four repetitions. Fist, the blade was

allowed to settle and acclimatize and the laser tracker was qualified. Except for the movement of the platform, the measurement process was identical to the one conducted for the calibrated workpiece. The photograph in Figure 3 shows the process. Each full measurement took one hour and 20 minutes and six hours in total for the entire dataset, including handling. The temperature varied between 21.9°C and 23.5°C during the measuring session. The uncertainty contribution from the environment was estimated in a similar way to that used for the calibrated workpiece measurements, but with a leading edge arc length of 1.5 m to account for the larger maximum size of the blade.

An approach similar to the one followed for the calibrated workpiece was employed for estimating the uncertainty of the blade measurements. However, the blade CAD model could not be used directly as a reference surface due to gravity's elastic deformation of the blade. Instead, one of the repeated scans were used as a reference target, first for ridged alignment of the other scans through ICP and secondly for reconstruction of a Bézier surface. This allowed the distance between the surface and the points in the remaining scans to be computed and used for uncertainty estimation.

Though the procedure seems simple, it is complicated by the sheer number of measured points. Each repetition is made up of about 500 individual sub-scans which in turn contains roughly 800,000 points on average. Thus, each repetition contains on the order of 400,000,000 measured points. Figure 13 shows an example. The shown blade was measured in 1 hour and 15 minutes, which is well within the maximum allowed inspection time of two hours.

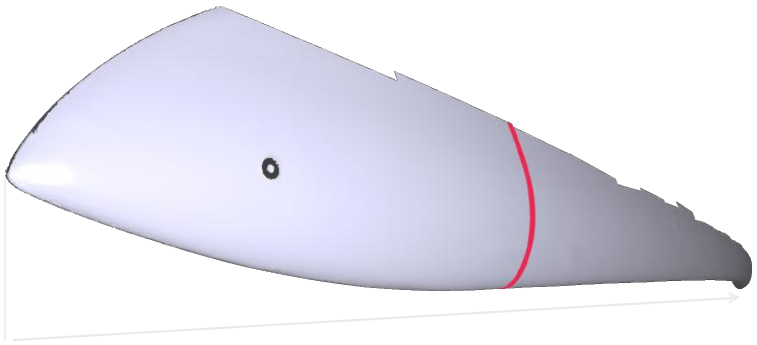

Figure 13: Rendering of the point cloud from a full leading edge scan. The scan is roughly 20 meters long and made up of more than 500 individual sub-scans. The total point count in the scan is over 380,000,000. A profile section is highlighted in order to provide a better feel for the geometry. The ring shaped hole seen near the tip originates from a metal lightning connector which was difficult for the scanner to acquire due to the view angle and specular highlights. Note that this is a view of the raw point set without surface reconstruction.

It was not feasible to reconstruct the entire surface, nor compute the distance

between such a surface and the points, due to limits in available computing power. Instead, the problem was reduced in size by focusing on a set of sampled locations by extracting 100 random points and then the 100 nearest neighbor points around those points as illustrated in Figure 14. Because the laser tracker and blade had been stable throughout the measurement procedure, the four repetitions were more or less aligned from the outset. This allowed for extracting all points from all repetitions inside a given cubic volume surrounding each of the randomly selected sample points. By only focusing on these small regions, it was feasible to build a k-d search tree [29, 30] for each region to be used for ICP alignment.

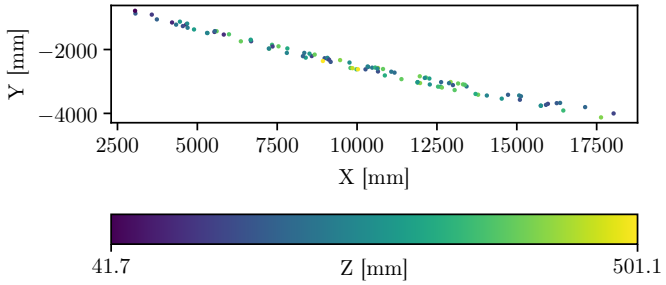

Figure 14: Locations of the 100 sample patches in the coordinate frame defined by the laser tracker as seen from above. The laser tracker is positioned at (0,0,0). The color of each point indicates its height on the z-axis. As seen, the points follow the contour of the blade with the tip being closest to the origin. See Figure 2 for a definition of the coordinate frame.

After the fine alignment, the 300 points closest to the centers of each cubic volume in the first repetition was found by constructing a k-d tree for each volume. A (4,4) order Bézier surface was then fitted to each of these point sets. The 100 points closest to the volume centers of the remaining three repetitions were found in a similar way and the distance between each of these points and their respective surface were computed and used for uncertainty estimation. Figure 15 shows an example of a reconstructed surface patch and an example of the repeated measurements and their respective surface from one volume is shown in Figure 16.

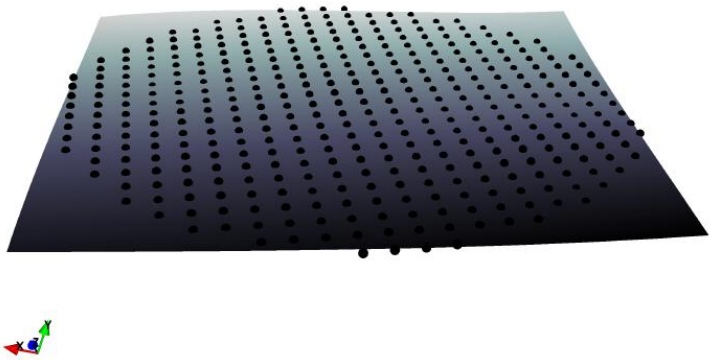

Figure 15: Example of Bézier surface with the 300 target points of one blade patch. The point to point distance is approximately 250 μm.

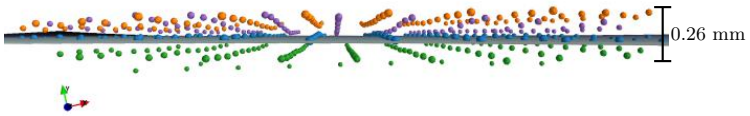

Figure 16: Example of the four repeated measured points around a blade surface patch. The 100 points of each repetition is assigned a different color.

5. Results and discussion

This section presents the results of the uncertainty estimation method. The standard deviation of the repeated CMM measurements of the MFG cylinder was 2.7 μm. Figure 17 shows the distribution of distances between the Bézier surface fitted to the mean CMM measurements and the measured CMM points. As seen, the standard deviation of the measurements 152 μm, which is orders of magnitudes higher than that obtained through the MFG measurements. This is most likely due to the calibrated workpiece's material properties, together with its size, and micrometer imperfections on its surface.

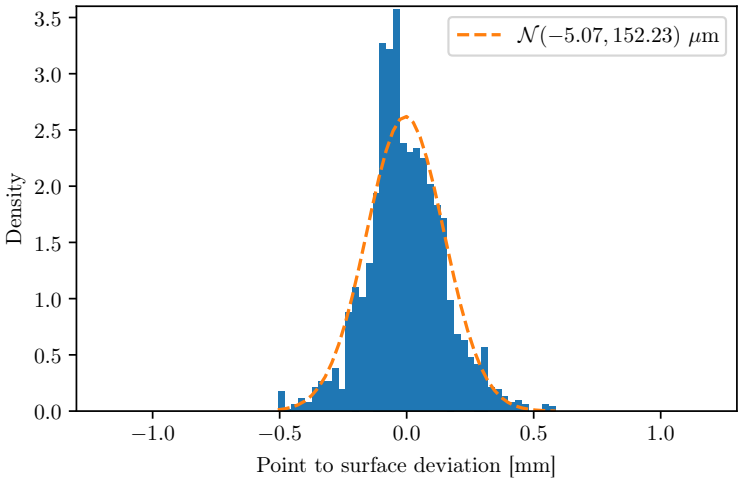

Figure 17: Histogram of the deviations between the Bézier surface and the points measured on the calibrated workpiece by the CMM. The stippled orange line shows a best fit normal distribution. The histogram is based on five repetitions of 396 measurement points. Note that the notation $\mathcal{N}(\mu, \sigma)$ indicates a normal distribution with mean μ and standard deviation σ.

A histogram of the distances between the aligned surface and the extracted points from the repeated scanner measurements of the workpiece is shown in Figure 18. As with the CMM measurements, elastic deformations are expected to be a major contributor to the uncertainty. It was intended to mount the workpiece such that it best resembled an actual blade, but this mounting could not be replicated in the CMM. As described in Section 4.3, the workpiece was lying down in the CMM instead of hanging, which meant that the force of gravity acted with a 90° rotation between the two measuring sessions. This resulted in a discrepancy between the surface model obtained from the CMM measurements and the surface which was measured by the scanner system.

The scanner system measured the workpiece in 12 individual sub-scans, which was transformed into the same reference frame through the positions measured by the laser tracker system. The measurements were repeated 10 times. Uncertainties in the positioning system caused the 12 sub-scans to be positioned a little different at every repetition. Thus, the tracker system's uncertainty propagated through to the overall uncertainty of the scanner system. In addition, the camera system also generally has a larger measurement uncertainty than the CMM [31].

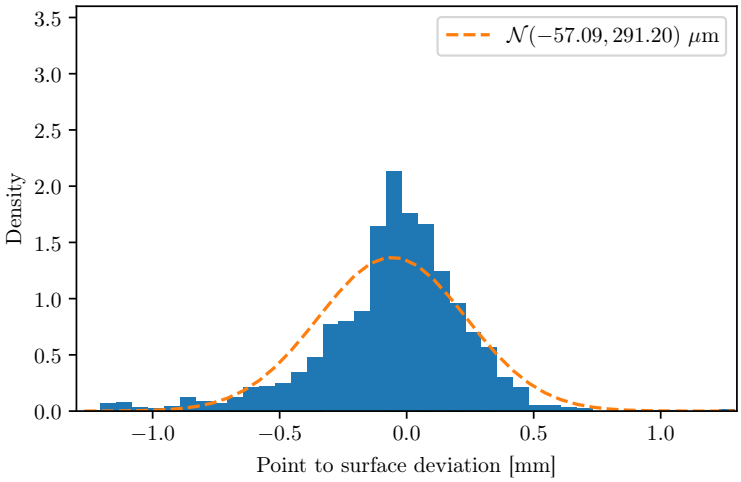

Figure 18: Histogram of the deviations between the Bézier surface, which was fitted to the CMM measurements, and the selected points measured on the calibrated workpiece by the scanner system.

It was speculated that there would be a correlation between the measurement uncertainty and the distance between the scanner system and the laser tracker. This was investigated by measuring the workpiece at four different distances from the tracker. A boxplot of the surface to point distances at each of the four distances is showed in Figure 19. The uncertainty of measuring the (x, y, z) positions of the active target is strongly related to the distance of the laser tracker, but the uncertainty of measuring the orientation (ψ, θ, ϕ) relates only vaguely to the distance. From the measurements conducted at different distances, it was found that there is no apparent relation between the scanner system's measurement uncertainty and the distance between the scanner and the tracker. It is expected that this is because the uncertainty of the orientation measurements is significantly higher than that of the position measurements.

As a feasibility study, the outermost 20 meters of a 55 meter long blade were measured four times with the scanner system. Figure 20 shows a histogram of the deviations between the measurements and their best fit surface for all repeated measurements on the wind turbine. The repeatability of the scanner system's measurements was assessed to 295 μm on the calibrated workpiece and 255 μm on the blade. Thus, the standard deviation of the blade measurements are on the same order of magnitude.

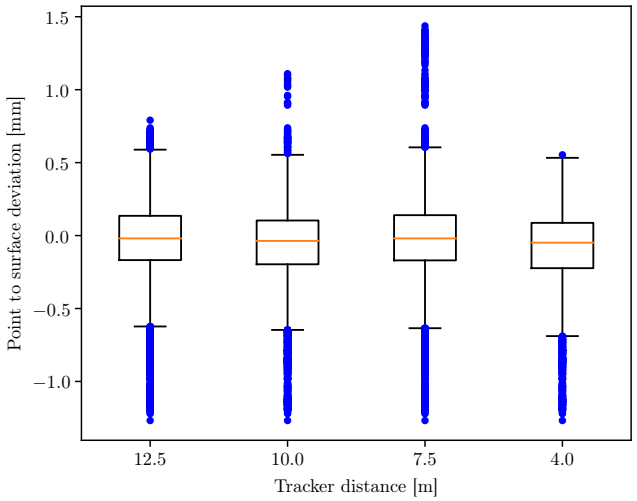

Figure 19: Boxplots of the deviations between the Bézier surface and points measured by the scanner system measured at different distances from the laser tracker. There is no apparent correlation between tracker distance and the point-to-surface deviations.

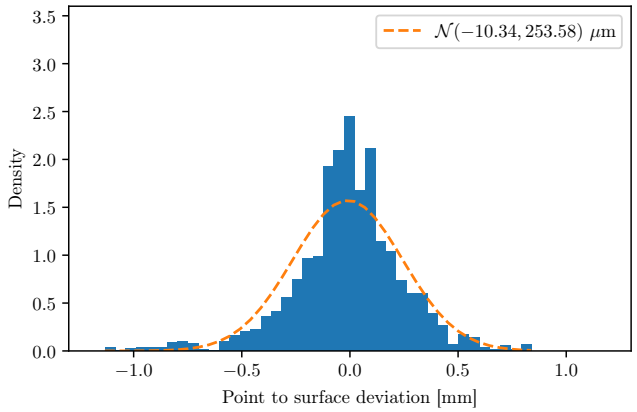

Figure 20: Histogram of the point to surface deviations between the extracted blade patches from all repetitions and the fitted surfaces.

Table 5 shows the results of the estimated measurement uncertainties. The standard uncertainties associated with each link in the traceability chain is documented separately. Following each statement of standard uncertainties, the expanded combined uncertainty for the current and preceding links is documented. The final combined standard and expanded measurement uncertainty of the scanner system is stated in the last two rows of the table, as given by Equation 3.

Table 5: Uncertainty estimations for the blade surface measurements (values in μm, $k = 2$).

Uncertainty Component	**Symbol**	**Uncertainty**
Uncertainty of cylinder radius	u_{rCYL}	0.1
Uncertainty of form	u_{fCYL}	0.13
Expanded uncertainty for MFG	U_{CYL}	0.33
Repeated CMM measurements on CYL	u_{repCYL}	2.73
Temperature	u_{eCYL}	0.16
Expanded uncertainty for CMM	U_{CMM}	5.48
Repeated CMM measurements on CW	u_{repCW}	152.2
Temperature	u_{eCW}	10.1
Expanded uncertainty for CW	U_{CW}	305.2
Repeated SS measurements on CW	u_{repSS}	294.6
Temperature	u_{eSS}	2.1
Combined standard uncertainty for SS	u_{SS}	331.7
Expanded uncertainty for SS and WTB	U_{SS}	663.5

The final, rounded expanded uncertainty ($k = 2$) of measurements on the blade is 665 μm. The CMM is calibrated with an uncertainty of 5.5 μm, while the calibration of the workpiece, with the CMM, yields an uncertainty of 310 μm. The workpiece is thus a major contributor to the uncertainty. It is very likely that its uncertainty can be brought down significantly by replacing the fiberglass blade-piece with one made from a stiffer material, such as carbon fiber. Such a workpiece would be notably more rigid and lighter, which would make it less prone to elastic deformations. As an example, if the repeatability of the measurements done on the calibrated workpiece could be brought down by a factor of 10, the uncertainty of the scanner system would be lowered to 70 μm. In this scenario, the scanner system would then be the primary contributor to the uncertainty, why the uncertainty could possibly be brought further down by using a better 3D scanner.

6. Conclusion

A new optical 3D system for scanning the leading edge of wind turbine blades was presented and its freeform measuring capability demonstrated on a real blade. The scanner system was able to scan 20 meters of the tip of a 55 meter wind turbine blade in a real production environment in just 90 minutes. To the extend of our knowledge, this is the first time such a demonstration has been carried out. Traceability was established through a procedure based on the MFG method and the substitution method from ISO 15530-3. Using a reference steel cylinder, a laboratory CMM was calibrated with an expanded measurement uncertainty of 5.5 μm ($k = 2$). Using the CMM, a workpiece containing the leading edge of a blade was calibrated with an expanded uncertainty of 310 μm. The scanner system was documented to have an expanded measurement uncertainty of 665 μm through the calibrated workpiece. The validity of the estimated uncertainty was tested against measurements done on a real blade.

Acknowledgments

The authors would like to thank the Innovation Fund Denmark for financially supporting the project through grant number 4135-00119B and Siemens Gamesa Renewable Energy A/S for providing the remaining funds. Thank to Christian Brandt Lauritzen and Peder Bent Hansen from FORCE Technology for their contributions to the construction of the scanner system. The reference CMM measurements would not have been possible without the help of Klaus Liltorp, Technical University of Denmark, who we would also like to thank.

References

[1] N. Dalili, A. Edrisy, R. Carriveau, A review of surface engineering issues critical to wind turbine performance, Renewable and Sustainable Energy Reviews 13 (2) (2009) 428 – 438.

[2] J. Lee, E. Lapira, B. Bagheri, H. an Kao, Recent advances and trends in predictive manufacturing systems in big data environment, Manufacturing Letters 1 (1) (2013) 38 – 41.

[3] M. Germani, F. Mandorli, M. Mengoni, R. Raffaeli, CAD-based environment to bridge the gap between product design and tolerance control, Precision Engineering 34 (1) (2010) 7–15.

[4] B. J. Holmes, C. J. Obara, L. P. Yip, Natural Laminar Flow Experiments on Modem Airplane Surfaces, NASA Technical Paper 2256.

[5] M. H. Keegan, D. Nash, M. Stack, On erosion issues associated with the leading edge of wind turbine blades, Journal of Physics D: Applied Physics 46 (38) (2013) 383001.

[6] S. D. Hand, D. B. Ober, B. A. Bond, E. A. Devine, Dimensional measurement of a composite ship hull using coherent laser radar yielding submillimeter results, Journal of ship production 20 (4) (2004) 232–239.

[7] W. Cuypers, N. Van Gestel, A. Voet, J.-P. Kruth, J. Mingneau, P. Bleys, Optical measurement techniques for mobile and large-scale dimensional metrology, Optics and Lasers in Engineering 47 (3-4) (2009) 292–300.

[8] J. C. on Guides for Metrology (JCGM), 200: 2012—International Vocabulary of Metrology—Basic and General Concepts and Associated Terms (VIM), Standard, 2012.

[9] ISO/IEC Guide 98-3:2008, Uncertainty of measurement – Part 3: Guide to the expression of uncertainty in measurement (GUM), Standard, International Organization for Standardization, Geneva, Switzerland, 2008.

[10] ISO 14253-2:2011, Geometrical product specifications (GPS) – Inspection by measurement of workpieces and measuring equipment – Part 2: Guidance for the estimation of uncertainty in GPS measurement, in calibration of measuring equipment and in product verification, Standard, International Organization for Standardization, Geneva, Switzerland, 2011.

[11] E. Savio, L. De Chiffre, An artefact for traceable freeform measurements on coordinate measuring machines, Precision Engineering 26 (1) (2002) 58–68.

[12] ISO 15530-3:2011, Geometrical product specifications (GPS) – Coordinate measuring machines (CMM): Technique for determining the uncertainty of measurement – Part 3: Use of calibrated workpieces or measurement standards, Standard, International Organization for Standardization, Geneva, Switzerland, 2011.

[13] A. Gameros, L. De Chiffre, H. Siller, J. Hiller, G. Genta, A reverse engineering methodology for nickel alloy turbine blades with internal features, CIRP Journal of Manufacturing Science and Technology 9 (2015) 116–124.

[14] E. Savio, L. De Chiffre, R. Schmitt, Metrology of freeform shaped parts, CIRP annals 56 (2) (2007) 810–835.

[15] G. Peggs, P. G. Maropoulos, E. Hughes, A. Forbes, S. Robson, M. Ziebart, B. Muralikrishnan, Recent developments in large-scale dimensional metrology, Proceedings of the Institution of Mechanical Engineers, Part B: Journal of Engineering Manufacture 223 (6) (2009) 571–595.

[16] F. Franceschini, M. Galetto, D. Maisano, L. Mastrogiacomo, Large-scale dimensional metrology (LSDM): from tapes and theodolites to multi-sensor systems, International journal of precision engineering and manufacturing 15 (8) (2014) 1739–1758.

[17] R. Schmitt, M. Peterek, E. Morse, W. Knapp, M. Galetto, F. Härtig, G. Goch, B. Hughes, A. Forbes, W. Estler, Advances in Large-Scale Metrology–Review and future trends, CIRP Annals-Manufacturing Technology 65 (2) (2016) 643–665.

[18] H.-L. Fu, K.-C. Fan, Y.-J. Huang, M.-K. Hu, Innovative optical scanning technique and device for three-dimensional full-scale measurement of wind-turbine blades, Optical Engineering 53 (12) (2014) 122411.

[19] Y. Petryna, A. Künzel, M. Kannenberg, Fault Detection and State Evaluation of Rotor Blades, in: EWSHM-7th European Workshop on Structural Health Monitoring, 2014.

[20] J. Shmueli, M. A. Eder, A. Tesauro, A versatile stereo photogrammetry based technique for measuring fracture mode displacements in structures, Precision Engineering 39 (2015) 38–46.

[21] J. Talbot, Q. Wang, N. Brady, R. Holden, Offshore wind turbine blades measurement using Coherent Laser Radar, Measurement 79 (2016) 53–65.

[22] E. R. Eiríksson, J. Wilm, D. B. Pedersen, H. Aanæs, Precision and accuracy parameters in structured light 3-D scanning, The International Archives of Photogrammetry, Remote Sensing and Spatial Information Sciences 40 (2016) 7.

[23] V. Couture, N. Martin, S. Roy, Unstructured light scanning to overcome interreflections, in: Computer Vision (ICCV), 2011 IEEE International Conference on, IEEE, 1895–1902, 2011.

[24] ISO/TS 15066:2016, Robots and robotic devices – Collaborative robots, Standard, International Organization for Standardization, Geneva, Switzerland, 2016.

[25] P. Schubel, Cost modelling in polymer composite applications: Case study – Analysis of existing and automated manufacturing processes for a large wind turbine blade, Composites Part B: Engineering 43 (3) (2012) 953 – 960.

[26] E. Savio, Reference measurements on cylinders at the Centre for Geometrical Metrology, Report MM99.57, Department of Manufacturing Engineering, Technical University of Denmark, Kgs. Lyngby, Denmark, 1999.

[27] D. McElroy, F. Weaver, C. Bridgman, Thermal expansion of epoxy-fiberglass composite specimens, International Journal of Thermophysics 9 (2) (1988) 233–243.

[28] P. J. Besl, N. D. McKay, Method for registration of 3-D shapes, in: Sensor Fusion IV: Control Paradigms and Data Structures, vol. 1611, International Society for Optics and Photonics, 586–607, 1992.

[29] J. L. Bentley, Multidimensional binary search trees used for associative searching, Communications of the ACM 18 (9) (1975) 509–517.

[30] F. Pedregosa, G. Varoquaux, A. Gramfort, V. Michel, B. Thirion, O. Grisel, M. Blondel, P. Prettenhofer, R. Weiss, V. Dubourg, J. Vanderplas, A. Passos, D. Cournapeau, M. Brucher, M. Perrot, E. Duchesnay, Scikit-learn: Machine Learning in Python, Journal of Machine Learning Research 12 (2011) 2825–2830.

[31] R. A. Lyngby, H. Aanæs, E. Nielsen, A. B. Dahl, Autonomous surface inspection of wind turbine blades for quality assurance in production, in: EWSHM-9th European Workshop on Structural Health Monitoring, BINDT, 2018.